

Experimental and Numerical Investigation of the Damage Response of Ceramic Matrix Composites

by

Pascal Meyer

A dissertation submitted in partial fulfillment
of the requirements for the degree of
Doctor of Philosophy
(Aerospace Engineering)
in The University of Michigan
2015

Doctoral Committee:

Professor Anthony M. Waas, Chair
Associate Professor Samantha H. Daly
Professor John W. Halloran
Associate Professor Veera Sundararagavan

© Pascal Meyer 2015
All Rights Reserved

To my family

ACKNOWLEDGEMENTS

I would like to take the opportunity to thank the people that supported me during my journey toward graduation. I am very grateful that I had the chance to meet and work with so many talented and inspiring people.

First I would like to thank my advisor, Professor Anthony Waas, for his guidance during my time at the University of Michigan. He always took the time to discuss my work and ideas. His enthusiasm, wealth of ideas, creativeness, and his passion for teaching have always inspired me. Working with him has greatly influenced my technical and professional development.

I would like to thank my committee members Professor Samantha Daly and Professor Halloran for their input and ideas during our weekly meetings. I would like to thank Prof. Veera Sundararagavan for his comments and suggestions on my thesis. I would like to express my gratitude toward Dr. Ronald Nimmer for numerous extensive discussions. I will use his inspiring passion for research and constant pursuit of broadening his knowledge as guidance for my future career.

To my fellow colleagues at the University of Michigan: Mark Pankow, Siva Rudraraju, Paul Davidson, Zachary Kier, Pavana Prabhakar, Eugene Kheng, Marianna Maiaru, Dianyun Zhang, Royan DMello, Brian Justusson, Cyrus Kosztowny, Christian Heinrich, Evan Pineda, Scott Stapelton, Jiawen Xie, Armanj Hasanyan, Ashith Joseph, David Singer, Deepak Kumar Patel, Jaspar Marek, Nhung Nguyen, Solver Thorsson, Wu Xu.

I am most grateful for the immense support of my family. This thesis would not have

been possible without the tremendous encouragement of my parents. They taught me from early ages broaden my knowledge and not to give up easily. Being an engineer himself, my dad not only aroused my curiosity to understand and solve engineering problems but also taught me hands on work that made me a better experimentalist today. I am thankful for my mothers perpetual support toward my education and for her guidance during personal and intellectual growth. My sister, Dr. J. Meyer, has been my role-model. She inspired me to go to graduate school and earn my doctorate degree. I would not be the person I am today without Jaimie Sarrault who encouraged me to reach out and discover the world. Her openness to try new things and her pursuit to make the world a better place have always inspired me.

TABLE OF CONTENTS

DEDICATION	ii
ACKNOWLEDGEMENTS	iii
LIST OF FIGURES	viii
LIST OF TABLES	xiii
ABSTRACT	xiv
CHAPTER	
I. Introduction	1
1.1 Ceramic Matrix Composites - Introduction	1
1.1.1 Manufacturing Procedures - Review	3
1.2 Common Failure Mechanisms in Ceramic Matrix Composites	4
1.2.1 Common Damage Models for CMCs	5
1.3 Multi-Scale Modeling	6
1.4 Thesis Objective and Organization	8
II. Experimental Investigation of Ceramic Matrix Composites	10
2.1 Introduction	10
2.2 Experimental Method	12
2.2.1 Laser Speckle Technique Validation	20
2.3 Ambient Temperature Testing	23
2.3.1 [0/90] _{2S} Laminate	23
2.3.2 [90/0] _{2S} Laminate	27
2.3.3 [+45/-45] _{2S} Laminate	29
2.4 Elevated Temperature Testing	31
2.4.1 [0/90] _{2S} Laminate Tested at 1093°C	32
2.4.2 [0/90] _{2S} Laminate Tested at 1204°C	34
2.4.3 [0/90] _{2S} Laminate Tested at 1316°C	36

2.4.4	[90/0] _{2S} Laminate Tested at 1093°C	38
2.4.5	[90/0] _{2S} Laminate Tested at 1204°C	40
2.4.6	[90/0] _{2S} Laminate Tested at 1316°C	42
2.4.7	[+45/ - 45] _{2S} Laminate Tested at 1093°C	44
2.4.8	[+45/ - 45] _{2S} Laminate Tested at 1204°C	46
2.4.9	[+45/ - 45] _{2S} Laminate Tested at 1316°C	48
2.5	Conclusions	50
III. Numerical Model of Micromechanical Failure Mechanisms . . .		57
3.1	Introduction	57
3.2	Analytical Crack Density Formulations	57
3.3	Post-Peak Strain Softening Formulation - Crack Band	63
3.3.1	Characteristic Length Scale	68
3.3.2	Objectivity with Respect to Discretization Size	68
3.4	Crack Band for Interlaminar Failure	72
3.4.1	Double Cantilever Beam Simulation	73
3.5	Transverse Cracking of CMCs under Tensile Loading	76
3.6	Random Fiber Orientation within RUC	77
3.6.1	Influence of Fiber-Interface Packing on Crack Initiation	77
3.6.2	FEM Crack Density Prediction	87
3.6.3	Microscale Modeling of a CMC Laminate	93
3.7	Conclusions	99
IV. Integrated Finite Element Method Multi-Scale Modeling . . .		101
4.1	Introduction	101
4.2	Representative Unit Cell Modeling in a Multi-Scale Framework	104
4.3	IFEM Equations	106
4.3.1	RVE Characteristics	109
4.3.2	Dehomogenization of Displacement Field with Periodic Boundary Conditions (Localization)	111
4.4	Prediction of Elastic Properties of Fiber-Reinforced Composites	112
4.4.1	Influence of Volume Fractions on Composite Properties	115
4.4.2	Influence of Constituent Elastic Properties on Composite Properties	118
4.5	Post-Peak Softening Implementation within IFEM	123
4.5.1	Implementation of Crack Band Failure Scheme within IFEM at the microscale	123
4.5.2	Numerical Calculation of Jacobian Matrix for Implicit Simulations	124
4.6	Single Edge Notch Uniaxial Monotonic Tensile Simulation	126
4.7	Smooth-Bar Uniaxial Monotonic Tensile Simulation	137
4.7.1	Modeling of Material Inhomogeneities	140
4.8	Conclusions	143

V. Fiber Pull-Out Simulations	145
5.1 Introduction	145
5.2 Experimental Measurements of Fiber-Pullout	147
5.3 Fiber-Pullout Micromechanics within the Finite Element Method	150
5.4 Fiber-Pullout Results and Discussion	155
5.5 Conclusions	157
VI. Concluding Remarks	159
6.1 Conclusions	159
6.2 Future Work	161
APPENDICES	165
A.1 Probability Density Function	166
A.2 Mean Intercept Length Tensor	168
BIBLIOGRAPHY	171

LIST OF FIGURES

Figure

1.1	Fracture behavior of <i>a</i>) pure ceramic material <i>b</i>) fiber reinforced ceramic <i>c</i>) coated fiber reinforced ceramic	2
1.2	Schematic representation of the melt infiltration process used for manufacturing SiC/SiC ceramic matrix composites	4
2.1	Experimental setup	13
2.2	Schematic view of the experimental setup	15
2.3	Diffuse reflectance on surface features larger than the wavelength of the coherent illuminating source	16
2.4	<i>a</i>) Speckle pattern at room temperature <i>b</i>) speckle pattern at 1316°C	17
2.5	Typical speckle image on CMC surface (Average speckle diameter is 44 μm)	18
2.6	RMS Error for laser DIC at room temperature and elevated temperature	19
2.7	Reference image for rigid body displacement test to verify laser DIC displacement error	19
2.8	Displacement vs. time comparison of a rigid body motion test on a CMC specimen between DIC and measured displacement	20
2.9	Stress - strain results (strain gage, DIC) on 6061 aluminum at room temperature)	21
2.10	Stress - strain response of 6061 aluminum at 500 F measured with laser DIC setup	22
2.11	CMC tensile sample dimensions	23
2.12	Schematic representation of the single edge notch dimensions	24
2.13	Stress-displacement response of [0/90] _{2S} CMC tensile tests at ambient temperature; A = 100 MPa, B = 150 MPa, C = 225 MPa, D = Ultimate Stress	26
2.14	DIC full-field surface strain maps of cross-ply CMC tensile tests at room-temperature	26
2.15	Stress-displacement response of [90/0] _{2S} CMC tensile tests at ambient temperature; A = 100 MPa, B = 150 MPa, C = 260 MPa for specimens 2098-01-6102-TD4 and 2098-01-6102-TD5 & C = 225 MPa for specimen 2098-01-6100-TD4, D = Ultimate Stress	28

2.16	DIC full-field surface strain maps of $[90/0]_S$ CMC tensile tests at room-temperature	28
2.17	Stress-displacement response of $[+45/-45]_{2S}$ CMC tensile tests at ambient temperature; A = 100 MPa, B = 150 MPa, C = 215 MPa for specimen 2098-01-1345-TD5 & C = 200 MPa for specimen 2098-01-1345-TD2 & C = 195 MPa for specimen 1999-01-0001-TD1, D = Ultimate Stress	30
2.18	DIC full-field surface strain maps of $[+45/-45]_S$ CMC tensile tests at room-temperature	30
2.19	Stress-displacement response of $[0/90]_{2S}$ CMC tensile tests at $1093^\circ C$ (2000 F); A = 100 MPa, B = 150 MPa, C = 250 MPa for specimens 1999-01-0001-TD2 & 1999-01-0001-TD4 and C = 225 MPa for specimen 1999-01-0001-TD5, D = Ultimate Stress	33
2.20	DIC Results of $[0/90]_{2S}$ CMC tensile tests at $1093^\circ C$ (2000 F) . . .	33
2.21	Stress-displacement response of $[0/90]_{2S}$ CMC tensile tests at $1204^\circ C$ (2200 F); A = 100 MPa, B = 150 MPa, C = Ultimate Stress	35
2.22	DIC Results of $[0/90]_{2S}$ CMC tensile tests at $1204^\circ C$ (2200 F) . . .	35
2.23	Stress-displacement response of $[0/90]_{2S}$ CMC tensile tests at $1316^\circ C$ (2400 F); A = 100 MPa, B = 150 MPa, C = 225 MPa for specimen 1999-01-0001-TD9 and C = 180 MPa for specimens 1999-01-0003-TD9 & 2098-01-6100-TD1, D = Ultimate Stress	37
2.24	DIC Results of $[0/90]_{2S}$ CMC tensile tests at $1316^\circ C$ (2400 F) . . .	37
2.25	Stress-displacement response of $[90/0]_{2S}$ CMC tensile tests at $1093^\circ C$ (2000 F); A = 100 MPa, B = 150 MPa, C = 200 MPa, D = Ultimate Stress	39
2.26	DIC full-field strain maps of $[90/0]_{2S}$ CMC tensile tests at $1093^\circ C$ (2000 F)	39
2.27	Stress-displacement response of $[90/0]_{2S}$ CMC tensile tests at $1204^\circ C$ (2200 F); A = 100 MPa, B = 150 MPa, C = 200 MPa, D = Ultimate Stress	41
2.28	DIC full-field strain maps of $[90/0]_{2S}$ CMC tensile tests at $1204^\circ C$ (2200 F)	41
2.29	Stress-displacement response of $[90/0]_{2S}$ CMC tensile tests at $1316^\circ C$ (2400 F); A = 100 MPa, B = 150 MPa, C = 190 MPa, D = Ultimate Stress	43
2.30	DIC full-field strain maps of $[90/0]_{2S}$ CMC tensile tests at $1316^\circ C$ (2400 F)	43
2.31	Stress-displacement response of $[+45/-45]_{2S}$ CMC tensile tests at $1093^\circ C$ (2000 F); A = 100 MPa, B = 150 MPa, C = 185 MPa, D = Ultimate Stress	45
2.32	DIC full-field strain maps of $[+45/-45]_{2S}$ CMC tensile tests at $1093^\circ C$ (2000 F)	45
2.33	Stress-displacement response of $[+45/-45]_{2S}$ CMC tensile tests at $1204^\circ C$ (2200 F); A = 100 MPa, B = 150 MPa, C = 175 MPa, D = Ultimate Stress	47

2.34	DIC full-field strain maps of $[+45/-45]_{2S}$ CMC tensile tests at $1204^{\circ}C$ (2200 F)	47
2.35	Stress-displacement response of $[+45/-45]_{2S}$ CMC tensile tests at $1316^{\circ}C$ (2400 F); A = 100 MPa, B = 150 MPa, C = 170 MPa for specimens 2098-01-1327-TD3 and 2098-01-1327-TD4 & C = 160 MPa for specimen 2098-01-1327-TD1, D = Ultimate Stress	49
2.36	DIC full-field strain maps of $[+45/-45]_{2S}$ CMC tensile tests at $1316^{\circ}C$ (2400 F)	49
2.37	Comparison of ultimate net-section stress for $[0/90]_{2S}$ laminates	50
2.38	Comparison of ultimate net-section strength for $[90/0]_{2S}$ laminates	51
2.39	Comparison of ultimate net-section strength for $[+45/-45]_{2S}$ laminates	52
2.40	Comparison of the average ultimate net-section stress at all temperatures for all tested laminates	53
2.41	Stress-strain response for cross-ply specimens at various temperatures	54
2.42	Schematic crack propagation in a $[0/90]_S$ single edge notch monotonic tensile test	56
3.1	Shear Lag Model	58
3.2	Shear Lag Cracking Sequence	59
3.3	Laws & Dvorak progressive failure; New crack occurs inbetween two existing cracks	60
3.4	Model details used to analyze $[0^{\circ}_m/90^{\circ}_n]_S$ and $[90^{\circ}_m/0^{\circ}_n]_S$ composites (<i>Nairn</i> (1989))	61
3.5	The formation of a new microcrack 2δ dimensionless units above the bottom microcrack of a pair of microcracks separated by 2ρ dimensionless units <i>Nairn</i> (1989)	63
3.6	a) Characteristic element length b) crack-band traction separation law	65
3.7	Joining Element Continuum Stress-Strain law with Traction-Separation law	66
3.8	Boundary conditions for square mesh objectivity study; Red element was given a 10 % lower strain to failure value	69
3.9	Crack path of square model for four distinct mesh sizes	70
3.10	Load P vs. Displacement of square model for four distinct mesh sizes	70
3.11	Boundary conditions for dogbone shape mesh objectivity study; Red element was given a 10 % lower strain to failure value	71
3.12	Crack path of dogbone shape model of four distinct mesh sizes	72
3.13	Load P vs. displacement of dogbone shape model of four distinct mesh sizes	72
3.14	DCB Specimen Geometry	74
3.15	Load vs. Displacement comparison of LEFM solution and crack band of a DCB test	75
3.16	Micrograph of CMC microstructure (White particles are artificial speckle pattern and not part of the CMC material)	78
3.17	Model and Microstructure Overlay (Matrix has been removed from the model for better visibility)	79
3.18	Boundary conditions of microstructure models	80

3.19	Crack paths of random RVE-1 microstructure model	81
3.20	Crack paths of random RVE-2 microstructure model	82
3.21	Crack paths of random RVE-3 microstructure model	82
3.22	Finite element models with randomly located fibers	85
3.23	Ultimate Damage path of randomly generated representative volume elements (RVE's)	86
3.24	Stress-Strain response of randomly generated microstructure models	87
3.25	Four layer cross-ply laminate model	88
3.26	[0/90] _S model details and crack density predictions of finite element model	90
3.27	Comparison of FEM crack density prediction with analytical solutions	93
3.28	Large micromechanics model ([0/90] _{2S}) and boundary conditions . .	94
3.29	Details of the large micromechanics model ([0/90] _{2S})	95
3.30	Maximum principle strain results showing cracks in a 8-Layer finite element model	97
3.31	Stress-Strain response of a 8-Layer finite element model	98
4.1	Flow chart of IFEM implemented using Abaqus	104
4.2	Multi-Scale information exchange between scales	105
4.3	Selection of 3D-IFEM subcells with varying geometrical features . .	110
4.4	Periodic boundary conditions <i>a</i>) undeformed state <i>b</i>) deformed state	112
4.5	Change of <i>a</i>) composite moduli <i>b</i>) composite Poisson's ratios with varying coating & matrix volume fractions	117
4.6	Five fiber RVE used for volumetric & constituent property parameter studies	119
4.7	Change of <i>a</i>) composite moduli <i>b</i>) composite Poisson's ratios with varying coating modulus	120
4.8	Change of <i>a</i>) composite moduli <i>b</i>) composite Poisson's ratios with varying fiber modulus	121
4.9	Change of <i>a</i>) composite Moduli <i>b</i>) composite Poisson's ratios with varying matrix modulus	122
4.10	Notch dimensions of single edge notch tensile simulation	128
4.11	Boundary conditions of a [0/90] _{2S} single edge notch tensile multi-scale simulation	128
4.12	Three meshes of the single edge notch finite element model for mesh convergence study <i>a</i>) coarse mesh <i>b</i>) fine mesh <i>c</i>) fine structured mesh. A field of view was restricted to the area around the notch in order to resolve mesh details	129
4.13	Stress-Strain response and crack paths of a cross-ply [0/90] _S single edge notch monotonic tensile specimen - Experimental results compared with IFEM simulation (three discretization sizes)	134
4.14	Stress-Strain responses and crack paths of the single edge notch monotonic tensile simulation - Comparison of four lay-ups [0/0] _S , [+45/-45] _S , [90/0] _S , and [0/90] _S	135
4.15	Stress-Strain responses and crack paths of the single edge notch monotonic tensile simulation - Comparison of [90/0] _S and [0/90] _S laminates	136

4.16	Simulation details of CMC smooth bar tension model	137
4.17	Stress-Strain response of a $[0/90]_{2S}$ smooth bar tensile specimen . .	138
4.18	Damage propagation in 0° -layer & 90° -layer of a smooth bar $[0/90]_{2S}$ tensile simulation	139
4.19	Weibull matrix strength distribution <i>a)</i> $n=15$ <i>b)</i> $n=20$ <i>b)</i> $n=30$. . .	142
4.20	Effect of Weibull matrix strength distribution on the stress-strain response of CMC smooth bar FEM simulation	143
5.1	Schematic illustrating crack opening, fiber debonding, and fiber pull- out at the crack front and in the crack wave	146
5.2	Investigation of fiber pullout of a CMC specimen tested at 1315° , the top picture shows the surface of the CMC specimen after fracture, bottom left SEM image taken at 100x magnification, bottom right SEM image taken at 500x magnification	148
5.3	SEM micrograph used to measure fiber lengths of a specimen that was tested at 1315°	149
5.4	Histogram of the fiber pullout length for a single layer	150
5.5	Two DCZM interface elements connecting two node pairs in the co- hesive region between the fiber and coating material	151
5.6	Triangular cohesive zone law for DCZM elements	152
5.7	Strategy for creating DCZM elements within the 3D-FEM pullout model; Shown is a single fiber with a dummy material between the fiber and coating material	153
5.8	Fiber-pullout model, <i>a)</i> whole model <i>b)</i> Fiber with Coating <i>c)</i> Fibers only	154
5.9	Fiber pullout response as predicted by the finite element model . . .	155
5.10	Input parameter study of fiber pullout response as predicted by the finite element model	156
A.1	<i>a)</i> Baseline RVE <i>b)</i> randomly generated RVE	167
A.2	Fiber distance calculation for probability density function	167
A.3	Probability density functions of a baseline RVE and a randomly gen- erated RVE	168
A.4	Schematic Drawing of the Mean Intercept Length	169
A.5	Example of mean intercept length of a base RVE and a random subcell	170

LIST OF TABLES

Table

2.1	Comparison for Young’s modulus of aluminum at room temperature	21
2.2	Young’s modulus for aluminum at 500 F	22
2.3	Comparison for Young’s modulus of $[0/90]_{2S}$ specimens at room temperature, $1204^{\circ}C$, $11316^{\circ}C$	55
3.1	Material properties used in mesh objectivity study	71
3.2	Material properties used in mesh objectivity study	74
3.3	Constituent elastic and fracture properties	80
3.4	Constituent elastic and fracture properties for crack spacing analysis	89
3.5	Input properties for Laws & Dvorak analytical crack density model	92
3.6	Input properties for Nairn’s analytical crack density model	92
4.1	Elastic constituent input properties	114
4.2	Comparison of elastic lamina properties	115
4.3	Constituent input properties for varying coating & matrix volume fraction	117
4.4	Constituent input properties for varying coating Young’s modulus .	120
4.5	Constituent input properties for varying fiber Young’s modulus . . .	121
4.6	Constituent input properties for varying matrix Young’s modulus .	122
4.7	Constituent elastic and fracture properties used in single edge notch finite element simulations	127
5.1	Dependence of the pullout strength on the critical Load F_c	157

ABSTRACT

Experimental and Numerical Investigation of the Damage Response of Ceramic Matrix Composites

by

Pascal Meyer

Chair: Anthony M. Waas

Ceramic matrix composites (CMCs) are of interest in the aerospace industry due to their ability to retain high stiffness at elevated temperatures. CMC materials are slated to replace metal alloys currently used in the combustion section of aerospace jet engines, leading to weight savings due to the lower density, and system efficiency due to eliminating complex cooling systems which are not required for CMC components. In this work monotonic tensile tests at room and high temperature are conducted. Three different composite layups are investigated.

Mechanics based numerical models based on finite element analyses are developed to predict the damage behavior of CMCs. The energy based crack band model implemented in Abaqus' user subroutines is used to enforce mesh objectivity. Crack densities are predicted with microstructural FEM models including hundreds of fibers. Geometrical inhomogeneities are included in the model in order to represent the microstructure accurately. Crack-paths and stress-strain responses are compared to experimental results. In order to measure full-field strain at elevated temperatures (excess of 2000F), a novel digital image correlation based technique was developed.

Component level numerical predictions are developed using a multiscale approach referred to as the integrated finite element method (IFEM). In the IFEM, a representative volume element, which includes nonlinear response due to constituent level damage, is embedded within Abaqus user subroutine UMAT. This allows the user to capture the influence of constituent stress-strain relation at the RVE level. This RVE level (subscale) analysis is also conducted using the finite element method. Abaqus is used to calculate the response of a coupon or component level model using the IFEM approach. Energy based fracture mechanics models are implemented in the constitutive relations of the RVE model. Damage of each constituent within the RVE is predicted and volume averaged stresses of the RVE are calculated and returned to the Abaqus model. Macroscopic crack paths are predicted and compared to experimental results. In support of IFEM, micromechanics based models are developed to study the effect of fiber packing and other geometrical features on the transverse response of CMC plies.

Experiments on CMCs at elevated temperature revealed the existence of fiber debonding and subsequent sliding and pullout of the fibers. A numerical model is developed to predict the fiber debonding using discrete cohesive zone elements (DCZM). A surface to surface contact model based on Coulomb friction is used to describe the frictional behavior between the fiber and coating material.

CHAPTER I

Introduction

1.1 Ceramic Matrix Composites - Introduction

Ceramic Matrix Composites (CMCs) have been in existence for nearly four decades. Initial reinforced ceramics appeared in the early 1960's (*Popper (1960)*). Research on manufacturing of stronger ceramics intensified in the 1970's (*Mehan (1978)*, *Forrest et al. (1972)*). However, they have just recently found their application in gas turbine engines. Ceramic materials usually display superior stiffness and higher stability at elevated temperatures when compared to metals. However, monolithic ceramics experience a very low toughness which eliminates this material from use in high strain applications. Typically, a single crack grows instantaneously through a component when the critical stress is reached. This is shown schematically in figure 1.1a. Adding fiber reinforcements, which have a high melting point, low density, high modulus and high strength, to a monolithic ceramic material does not increase the stiffness or toughness (figure 1.1b) of a ceramic material due to the similarity in elastic properties of the fibers. To increase the toughness and therefore increase the usability of ceramic materials, a compliant interface between the fiber and matrix is added. The interface material tends to have a noticeable volume fraction in the range of 6-10 %. A crack front deflects at or is arrested by the compliant fiber coating and crack saturation sets in before ultimate fracture of the component. This leads to a

stress-strain response which is comparable to metals as shown in figure 1.1c. However, CMCs experience a lower macroscopic strain to failure than metals. Many reinforcements have been tested, such as fibers, whiskers or particles. Typical reinforcement materials include carbon, silicon carbide (SiC), titanium diboride, silicon nitride and alumina. Continuous-fiber-reinforced CMCs show a preferable failure behavior compared to discontinuous reinforcements. The major difference between the two is that the continuous-fiber-reinforced CMCs do not fail catastrophically which make them more desirable for component manufacturing. The ratio of elastic modulus of the reinforcement material to the matrix is commonly low and can frequently be equal to unity. Of particular importance to the technology of toughened ceramics has been the development of high-temperature silicon carbide reinforcements. Although other reinforcement materials are available, such as glass and carbon fiber, metal whiskers, and alumina-based products, this work focuses on SiC-based products due to their utilization in high-temperature applications. SiC offers a unique combination of properties such as creep resistance, low porosity, low density, high thermal conductivity and low thermal expansion (*Corman and Luthra (2005)*).

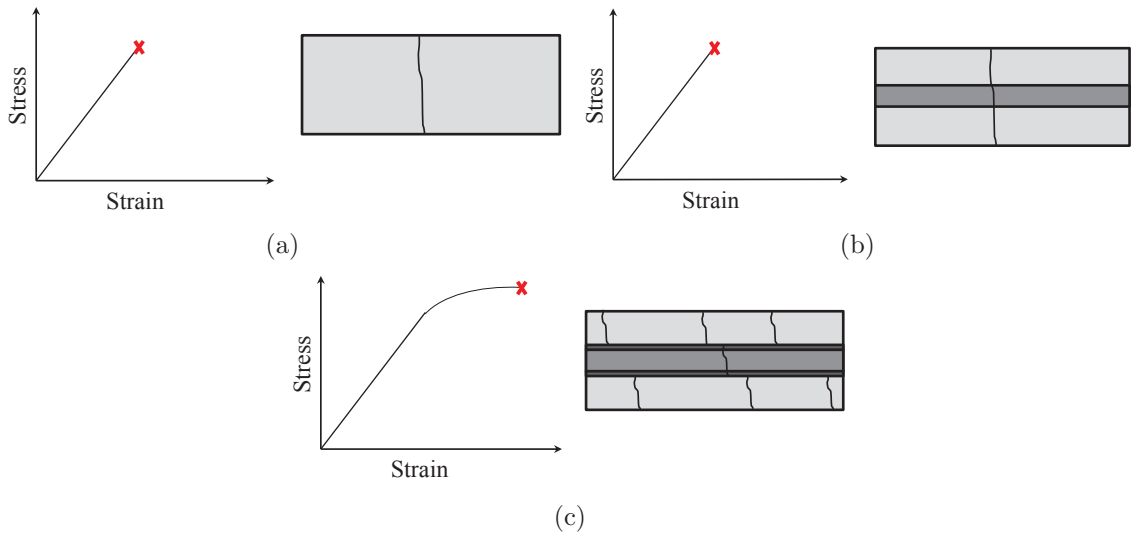


Figure 1.1: Fracture behavior of a) pure ceramic material b) fiber reinforced ceramic c) coated fiber reinforced ceramic

Typically, a fiber coating is applied in CMCs to prevent chemical attack of the fiber during processing. The coating also provides a weak interface between the fiber and the matrix which enhances the toughness and improves the failure behavior. Boron Nitride (BN) coatings are most widely used and applied by chemical vapor deposition (CVD). Unfortunately, BN is susceptible to degradation by contact with molten silicon which necessitates an additional coating with Silicon Carbide or Silicon Nitride to protect the BN-layer. An important consideration when using a BN coating is its degradation due to oxidation in the presence of matrix cracks. Especially in environments at high temperature with a high water vapor content in the air, as can be found in the hot sections of gas turbines, oxidation must be considered. Typically, a silicon-doped BN coating is applied which forms a boron silicon oxidation product that greatly slows the oxide volatilization.

1.1.1 Manufacturing Procedures - Review

Traditionally, there are a number of different methods to manufacture ceramic matrix composites, such as chemical vapor, liquid phase infiltration, hot press sintering techniques, polymer infiltration, and pyrolysis (PIP). This thesis is focused on silicon melt-infiltrated ceramic matrix composites (MI-CMCs). This type of CMC consists of three major components, the reinforcing fibers, the fiber coating, and the silicon carbide matrix. *Corman et al.* (2003) provides an overview of the possible processes. Typically, the SiC fibers are first coated with the BN-based fiber-matrix interphase and a protective overcoat, and then formed into unidirectional prepreg sheets via wet drum winding. The prepreg sheets are then laid-out in the directions needed, comparable to the manufacturing process of polymer matrix composites. At this stage the matrix consist of powders which are then burned out and parts are converted to free carbon which maintains the preform shape. In a final step the preform is densified. Liquid silicon, at temperatures above its melting point of 1414° C, wets

the surface of the prepreg. Capillary forces drive the liquid silicon into the porous prepreg where it reacts with the free carbon to form a continuous silicon carbide (SiC) phase. Commonly, some residual free silicon is left in the SiC matrix. This process requires the porosity of the preform to be within a tight range. Large pores simplify the infiltration process but may result in an incomplete chemical reaction leaving higher amounts of free silicon and carbon. Pore density below a particular limit may result in a complete reaction but could result in an incomplete infiltration of the prepreg.

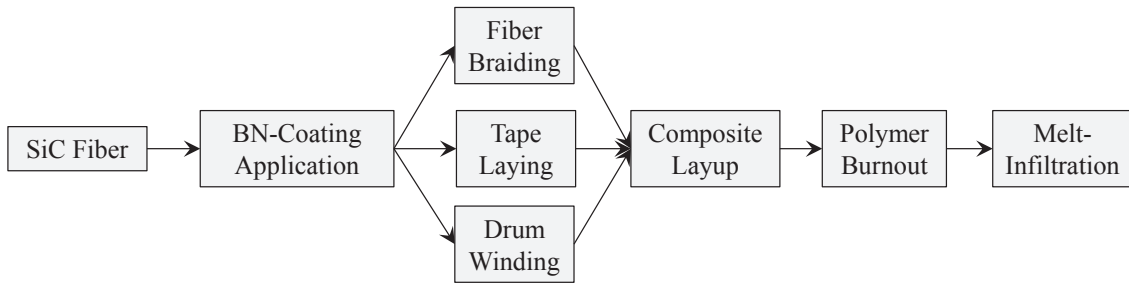


Figure 1.2: Schematic representation of the melt infiltration process used for manufacturing SiC/SiC ceramic matrix composites

1.2 Common Failure Mechanisms in Ceramic Matrix Composites

Ceramic Matrix Composites have been studied for decades. These composites are most commonly reinforced with Silicon Carbide (SiC) fibers. Fiber coatings, such as Carbon (C) or Boron-Nitride (Bn), are typically used to protect the fibers, to ensure bonding, and induce ductility. Such composites usually exhibit non-linearity in the stress-strain response before fracture due to accumulation of matrix cracks. Non-linearity manifests in reduced Young's modulus (E) with increasing tensile strain. Understanding and predicting the onset of matrix cracking, especially in the vicinity of geometrical stress risers such as holes and notches is imperative for the design of

components. Models representing matrix cracking have been developed in the past. *Budiansky et al.* (1986) studied the critical conditions for onset of widespread matrix cracking analytically based on fracture mechanics. *Marshall et al.* (1985) used a stress intensity factor based approach to analyze fracture in brittle fiber-matrix composites. Short and long cracks were distinguished. *Beyerle et al.* (1992) conducted research on mechanical characteristics of a unidirectional fiber-reinforced calcium aluminosilicate matrix composite. They found that the model was adequate to predict initial matrix cracking and the ultimate strength of the composite. However, deficiencies were noted in the ability to predict the evolution of matrix cracks, and associated changes in the modulus. However, comparison with experiment, especially with regard to matrix cracking, has led to contradictory conclusions (*McCartney* (1987)). The apparent discrepancies arise either from widely differing choices of the properties of the composite constituents (fiber, matrix, interface), in situ properties in the composite, or from differing assumptions about the flaw distributions in the matrix. In addition these models, which analyze failure mechanisms in isolation, are not capable of capturing interaction among mechanisms, which is key to understanding the overall deformation response and failure of CMC's.

1.2.1 Common Damage Models for CMCs

Classic one dimensional models are typically based on the so-called steady state cracking condition. In this condition a long matrix crack extends from a free edge of a unidirectional composite. The crack bridges the fiber and is perpendicular to the loading direction. *Aveston and Kelly* (1973) introduced simple ideas to predict crack spacing and stress-strain responses in fibrous composites. The authors developed analytical solution for the stress-strain response assuming the fiber-matrix bond remains intact after the matrix has cracked.

Commonly, damage modeling in unidirectional CMCs address fiber/matrix debonding

and fiber sliding. Many modified shear lag theories have been reported in the literature (*Evans and Zok (1994); Hutchinson and Jensen (1990); Sauder et al. (2010)*). Two characterizations of interface friction are generally used to handle the interaction between the fiber/matrix during fiber-pullout: Coulomb friction and constant friction stress models. *Lissart and Lamon (1997)* included a probabilistic-statistical approach for modeling matrix and fiber damage and failure. The authors used the two parameter Weibull equation in an attempt to recognize the statistical nature of brittle failure in the matrix and fiber material. *Charalambides and Evans (1989)* investigated the mechanics of debonding of brittle-matrix composites including residual stresses due to manufacturing processes. They found that subsequent to fiber failure some crack closure along the fiber occurs and therefore fiber-pullout affects the mechanical properties of the composite.

1.3 Multi-Scale Modeling

The term multi-scale modeling has been widely used in the literature (*Efendiev and Hou (2009)*). It can be divided into three main techniques, e.g. hierarchical, synergistic, and concurrent. For the scope of this work multi-scale modeling is understood to be the concurrent information exchange between multiple scales. In terms of fiber reinforced composites generally two scales of interest exist. A macroscopic scale which entails the prediction of damage of coupons, structural parts, or components which are on the order of 1 m scale. Information on this scale, usually displacement or strain fields, are transferred to a smaller scale (this is the RVE scale which is usually several mm's) through localization techniques. Material softening or degradation at the macro scale is informed by the RVE scale, denoted as microscopic scale. At the RVE scale, e.g. fiber-matrix scale, a number of different analytical, semi-analytical or numerical models can be used to predict damage. Different damage models are used to predict material behaviors. Homogenization techniques are used to update,

e.g. stress fields or stiffness tensor, which are passed to the macroscopic scale. Many theories have been developed over the last decade and published in review papers and books [*Kwon et al. (2008)*].

Ghosh et al. (1995) introduced a multiscale finite element method using Voronoi cells (VCFEM) to find homogenized material coefficients. Periodic boundary conditions were used on the base cell. The mesh generation relies on the Dirichlet tessellation. Multi-sided convex Voronoi polygons form a network to discretize a microstructural material element. Each polygon contains a single inclusion at most. Multiple formulations have been developed for, e.g. linear elastic problems *Ghosh and Mukhopadhyay (1993)*, micropolar thermo-elasticity problems *Ghosh and Liu (1995)*, and elastic plastic problems *Moorthy et al. (1994)*. *Bacarreza et al. ((2012)* developed a progressive damage multi-scale model for woven composites. A semi-analytical homogenization method, equivalent to the generalized method of cells, is used to derive effective properties of the composite. The authors differentiate between matrix damage, which is assumed to be isotropic, and damage in the yarn assumed to be anisotropic.

Non-local theories are widely used in multi-scale methodologies. Generally, homogenization is accomplished by solving the fine-scale boundary value problem (BVP). *Fish et al. (1999)* derived a homogenization technique based on double-scale asymptotic expansions. The authors introduced closed-form expressions to relate local phase fields to the macroscopic strain and damage. *Fish and Yu (2002)* further expanded the theory to fatigue damage predictions of composite materials. Recently, (*Zhang et al. (2015)*) have developed a two-scale model, referred to as the NCYL model for studying fiber reinforced composites. A main advantage of this model is the use of an analytical closed-form solution for the subscale problem which leads to a distinct computational advantage.

1.4 Thesis Objective and Organization

The objective of this thesis is to investigate in-plane damage and failure of laminated ceramic matrix composites. Laminated CMCs exhibit large strain to failure compared to the bulk strain to failure of the constituents. The predominant damage mechanism that leads to strain accumulation in this type of material is microcracking of the matrix. In this work three main objectives were addressed. These are the development of a high temperature DIC setup, micromechanics based finite element model, and multi-scale finite element model. The following four chapters and appendices are a discussion of the achievements toward this development.

Chapter II marks the progress toward the development of a very high temperature Digital Image Correlation (DIC) setup. Single edge notch tensile specimens are tested in a temperature range from room temperature to 1316° C. Blue light illumination in conjunction with a naturally emerging laser speckle pattern are used to solve multiple problems generally associated with elevated temperature DIC measurements. Crack paths and stress-strain response of these specimens are discussed in detail.

In an attempt to further understand the influence of microcracking of the matrix material, chapter III introduces an energy based damage model. Multiple FEM models including a large number of explicitly modeled fibers are created to predict crack paths in the microstructure under transverse tension conditions. It is shown that sufficiently large models can be used to predict crack densities. Influences of microstructural details such as fiber packing and interface thicknesses are investigated. Most important is the development of tools for predictions of parts and components. FEM is well suited for this type of work. However, damage in laminated composites is highly dependent on microstructural details. Current computational facilities do not allow to explicitly model fibers within component level models. Chapter IV introduces a concurrent multi-scale framework that is based on two finite element models. The commercial finite element suite Abaqus is used to solve FEM equations for the

macroscopic (coupon level) model. More advanced material models are needed to accurately capture matrix cracking on the microstructure scale. Therefore, a second finite element code has been implemented using Fortran and included in Abaqus' user material subroutines. It predicts the response of a RVE under multi-axial loading conditions. An energy based damage methodology has been included in the constitutive equations which ensures mesh objectivity within the microscale model. The combined approach is referred to as IFEM.

At elevated temperatures SiC/SiC CMCs show a significant amount of fiber-pullout. This phenomenon is discussed in chapter V. Two-, and three-dimensional finite element models are used to study the mechanisms involved in the fiber-pullout process. Discrete Cohesive Zone (DCZM) elements are used to simulate the initial bonding behavior between the fiber and coating. Fiber pullout lengths are determined from post experimental scanning electron microscopy (SEM). The finite element models recognize a random fiber orientation and variations in fiber diameters. Surface to surface contact formulation is used in order to capture frictional behaviors and investigate the influence of friction parameters.

The last chapter discusses final conclusions and gives a short introduction to future work. A comparison is made to connect the work presented in all previous chapters and link the different methodologies. Suggestions are given for improvements which could be pursued in the future.

CHAPTER II

Experimental Investigation of Ceramic Matrix Composites

2.1 Introduction

With the demand for faster but at the same time more efficient air transportation, new materials will have to be introduced into future propulsion systems. In an effort to make aerospace engines more efficient, the temperatures of the turbine sections will be raised to a level which exceeds the limit of current metallic materials. New materials will have to be tested and validated at very high temperatures that surpass $1300^{\circ}C$. New techniques that allow the observation of material behavior and damage evolution at these elevated temperatures need to be developed. Strain measurements using extensometers can be applied at very-high temperatures but only provide a single value averaged over the volume of material that is local to the extensometer. Especially for non-metallic composite materials, such as ceramic matrix composites (*Gowayed et al. (2011)*), this technique will not capture the damage initiation and will subsequently lead to inaccurate proportional limits with no meaning in terms of damage initiation. Digital Image Correlation (DIC), principally developed by *Sutton et al. (1983)*, is a good tool to measure full-field displacement maps and in theory has no limitation at very high temperatures provided the image quality and speckle

contrast are sufficient. DIC, as used in experimental strain analysis, is an optical method to measure deformation on an object surface by correlating images of that surface, which contains a speckle pattern, that are supposed to represent the deformation of that surface. This technique has been proven for applications at slightly elevated temperatures but faces several issues at very high temperatures that have to be considered in order to measure displacement fields. Black-body radiation emanating from the heated sample makes it impossible with standard lighting and camera equipment to image the surface of the test specimen. Speckle patterns, usually in form of paint, that are applied to the surface tends to de-bond within a short amount of time at very-high temperatures. It also requires additional steps to be carried out before testing and results might be error-prone due to poor adhesion between the paint and sample. Precautions have to be in place to account for heat haze. *Liu et al.* (1998) used aluminum-oxide and boron nitride ceramic coatings to create a speckle pattern on the sample surface. The maximum temperature that was demonstrated to achieve good DIC results was 704°C . *Novac and Zok* (2011) employed a CO_2 Laser to locally heat up a test specimen. An air knife was positioned to blow across the sample surface in an effort to minimize thermal turbulence. A speckle pattern, using alumina or zirconia paints, was applied with an airbrush. They showed analytically that blue light illumination and filtering systems could provide contrast at temperatures up to 1700°C . *Vest et al.* (2009) showed that blue light illumination could be used for DIC measurements up to 1000°C . The authors measured Youngs modulus and coefficient of thermal expansion for RR1000 samples. However, the reference image was updated frequently during the cross-correlation which may introduce strain errors. *Lyons et al.* (1996) demonstrated DIC at temperatures up to 650°C . The specimens were heated in a box furnace equipped with a window. Boron nitride- and aluminum oxide-based ceramic coatings were used to create the speckle pattern. The present work describes a simple, yet effective setup for room and high-temperature DIC measurements which

employs the technique of blue light illumination with an appropriate bandpass filter used in combination with a two zone furnace for accurate and stable temperature control over a large volume of the tested sample. It is shown that this technique can be used to detect the onset of damage, appearing as regions of high strain gradients. The surface strain concentrations can result from interior damage that manifests as high strain fields on the surface, or because of cracks occurring on the surface. Final determination requires post-experiment inspections to ascertain the origin of surface strain gradients. The experimental focus of this thesis was monotonic uni-axial tensile tests on a variety of lay-ups and geometries. In this chapter, geometric effects are studied and comparisons between room and elevated temperature are presented. Tensile tests on single edge notch specimens were conducted to study the effects of stress concentrations on failure mechanisms. The notched specimens give the opportunity to study crack initiation carefully since the initiation site is predetermined. Smooth bar specimens were tested to determine failure mechanisms based purely on material inhomogeneities. Parts of this chapter have been published in *Meyer and Waas* (2015).

2.2 Experimental Method

The thermo-mechanical testing was performed on a hydraulic test frame capable of controlling the displacement of both the bottom and top grip of the uniaxial tensile test sample. This configuration is preferable since the specimen center, when aligned correctly, will show less rigid body movement relative to the camera which will allow for a lower correlation error when performing DIC on recorded images. Figure 2.1 shows the load frame and camera set-up. Hydraulic grips with 25.4 mm (1 inch) wide smooth wedges were employed and a grip pressure of 4448.2 N (1000 lbf) was used to clamp the specimens. Aluminum mesh was used between the smooth grip surfaces and the rough specimen surface to ensure uniform loading. Heating was accomplished

with a 3.5 inch tall two-zone hot rail furnace with horizontal sliding action supplied by Amteco Incorporated. A viewing port, specially manufactured for visualizing very-high temperature surfaces was incorporated in the center of the furnace. The viewing port consisted of an alumina housing and a window holder with a thin sapphire glass window about 3 inches away from the specimen surface with a viewing port opening of 25.4 mm x 50.8 mm. It should be mentioned that the sapphire glass window has to be of high quality otherwise an uneven refractive index could induce errors on the measured displacement fields. Figure 2.2 visualizes the path of the light from the Laser to the specimen from which it reflects back to the camera. This setup ensures easy specimen access and temperature control over a large volume due to the two heating zones. The small window, good insulation properties of the viewing port, and insulation of all gaps minimized turbulent air caused by temperature differences.

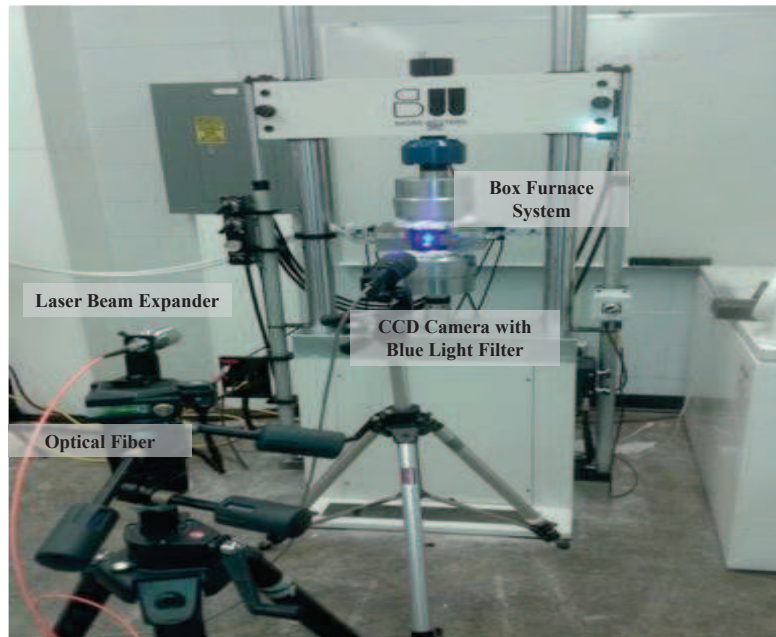


Figure 2.1: Experimental setup

Each heating zone was individually controlled using feedback from a type-R thermocouple. The thermocouples were placed about 2.5 mm above and below the center of the sample at a distance of about one tenth of a millimeter away from the spec-

imen surface. Heating of the sample was split into three steps. First, the sample was heated to 538°C (1000 F) at a ramp rate of 34°C (60 F) per minute. A five minute dwell time at 537.7°C (1000 F) was included to allow the temperature to fully stabilize. Second, the temperature was ramped up to 1093°C (2000 F) at 28°C (50 F) per minute followed by a five minute dwell time. Finally, the specimen was heated to 1316°C (2400 F) at 17°C (30 F) per minute. To allow the specimen to be in a thermally equilibrated state, a dwell time of fifteen minutes at 1316°C (2400 F) followed the last ramp-up. This heating procedure was used to ensure an even heating of the sample. The specimen was then loaded to failure in a displacement controlled test. The displacement rate was set to 0.16 millimeter per minute. Compressed air in combination with air amplifiers were used during heat-up to avoid overheating of the grips. It was turned off for the duration of the testing procedure to avoid any air circulation around the furnace. Turbulent air caused by temperature differences leads to local changes of the refractive index and subsequently to a higher DIC correlation error. The specimen was illuminated with a blue light laser with a wavelength of 447.5 nm. The laser has a nominal output energy of 300 mW as reported by the supplier. An optical multimode fiber in combination with a large beam expander was used to simplify the setup and expand the beam from initially 1 mm diameter to approximately 40 mm. The laser beam expander was mounted slightly above the lens camera assembly. Images for digital image correlation were acquired using LaVisions Imager E-Lite 5M with 2448×2048 pixel resolution. One 2x magnifying lens and a 200 mm focal length Nikor lens were connected to the camera. Best depth of field for the measurements was achieved with the F stop set to 8.

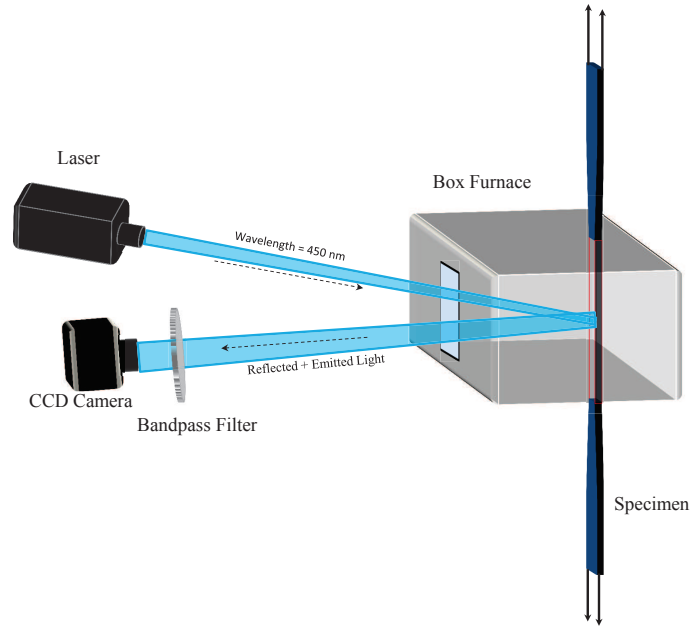


Figure 2.2: Schematic view of the experimental setup

This camera-lens combination yielded a field of view of 12 mm x 10 mm providing a final resolution of 205 pixels/mm. The camera assembly was mounted on a precision alignment stage which allowed for easy adjustments. In order to minimize vibrations, the camera setup was mounted on an optical table. A blue light band-pass filter, with a center wavelength of 450 nm and a bandwidth of 80 nm, was built into the system. Images were post-processed with LaVisions DIC correlation software DaVis. This software is based on a Fourier-transform cross-correlation algorithm to determine the relative displacement of sub regions of the images. Several subset sizes were tested for the given images out of which the final subset size of 35 pixels with a step size of 9 pixels was chosen. The proposed method will not use any artificial speckle pattern but rather rely on the natural surface roughness (deviation from flatness) to generate speckles. The tested samples contain a sufficiently rough surface as a result of the manufacturing process. That is, the typical wave-length of surface roughness undulations are much larger than the wave length of the illumination source. As a result, the image of the surface on the image plane, due to diffuse reflectance at the surface,

results in a speckle pattern due to destructive interference as schematically illustrated in Figure 2.3. This phenomenon is well known and is described for example, in, *Vest* (1979), and used by many, for example in studies that use holographic interferometry to measure out-of-plane displacements, *Fago and Waas* (1998) . Each point on the object surface scatters some light to the observer. Due to the laser lights high coherence, the light scattered by one object point interferes with the light scattered by each of the other object points. The interference is observed as a random speckle pattern of bright and dark regions. The randomness is dictated by the local surface height of the object surface. The typical speckle size can be calculated as,

$$b_s = 1.22 \frac{\lambda z}{D} \tag{2.1}$$

where D is the diameter of the lens pupil and the image is formed at a distance z from the lens. The wavelength of the laser light is denoted by λ . The formula shows that the speckle size can be influenced by choosing the appropriate aperture stops [16]. Here a lens with a focal length of 200 mm and an f-stop of 8 is used resulting in a lens pupil diameter of 25 mm. The camera was placed 2 m apart from the specimen surface giving an average speckle diameter of 44 μm .

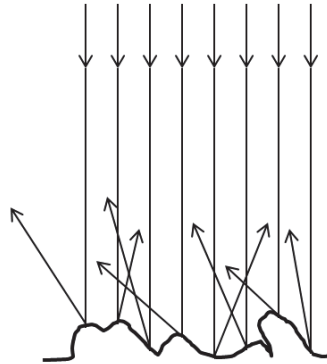


Figure 2.3: Diffuse reflectance on surface features larger than the wavelength of the coherent illuminating source

Reliable DIC calculations require a suitable carrier of surface deformations. In

the past [*Chen et al. (2012)*; *Pan et al. (2011)*], researchers have used artificial high-temperature speckle patterns that require additional work in advance of the actual experiment. Figure 2.4 depicts the surface of a single notch SiC/SiC specimen at room temperature and at 1316°C (2400F) with the laser speckle technique discussed here. No additional surface treatment was carried out. A surface pattern from the specimen manufacturing process is noticeable. The edges of the notch were highlighted in white for better visibility. It can be observed that images with sufficient grayscale intensity can be obtained and no significant difference between room temperature and 1316°C is visible

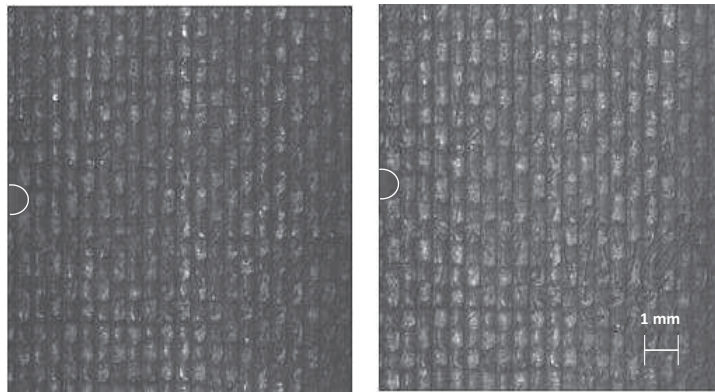


Figure 2.4: a) Speckle pattern at room temperature b) speckle pattern at 1316°C

The surface of the CMC specimens is covered with a layer of SiC matrix. The roughness visible in Figure 2.4 is a remnant of the manufacturing process and should not be confused with woven CMCs. Figure 2.5 shows an example of a magnified region of Figure 2.4. A uniform speckle size is created when the laser beam interferes with microscopic elements on the specimen surface.

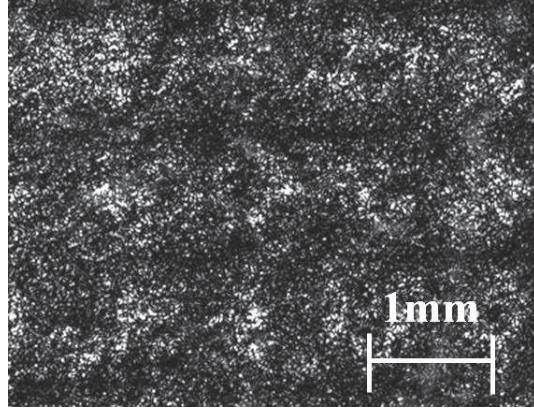


Figure 2.5: Typical speckle image on CMC surface (Average speckle diameter is $44\ \mu\text{m}$)

DIC systems are excellent tools for surface displacement measurements. However, small errors in the displacement field are typically found with every DIC system. Different methods have been used in the past to quantify the error associated with a particular DIC system. In this work the root mean square error, as presented in *Rajan et al. (2012)*, is used. The RMS error can be calculated for static image pairs as

$$v_{RMS} = \sqrt{\frac{1}{n} \sum_{j=1}^n (v_j)^2} \quad (2.2)$$

where v_j is the displacement at every data point. Figure 2.6 shows the effects of temperature on the RMS error. The error displayed is the average error of 10 consecutive images taken under a zero load condition. The displacement errors obtained at room temperature (0.0032) agrees with results found in other studies *Rajan et al. (2012)*. The RMS displacement error increases at elevated temperatures to approximately 0.013 pixels.

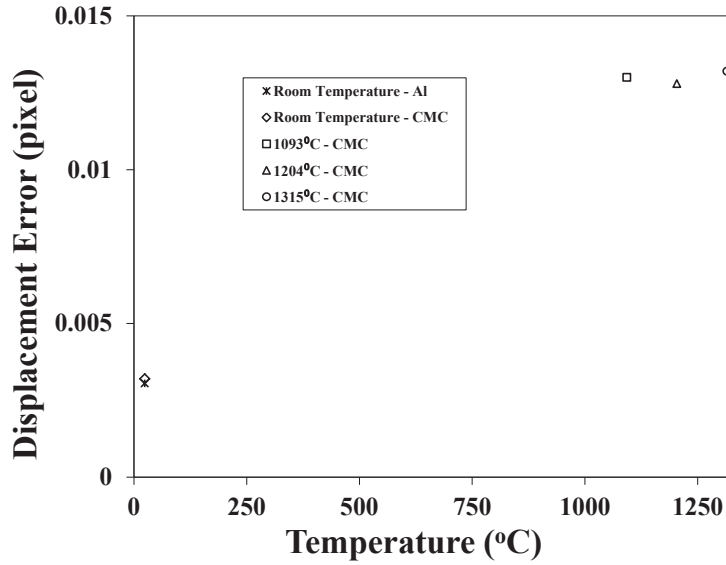


Figure 2.6: RMS Error for laser DIC at room temperature and elevated temperature

In addition to the RMS error calculations a rigid body motion test was conducted on a CMC specimen. The displacement rate was chosen to be 1.2 mm/min. A millimeter scale was attached to the back surface of the specimen. The CMC specimen surface covered the lower two-thirds of the field of view and the upper third was reserved for the millimeter scale as shown in figure 2.7. DIC calculations were conducted on the CMC surface. The calculated displacement was verified against the displacement measured based on the attached scale. The comparison of both measurements of the displacement-time response is shown in figure 2.8.

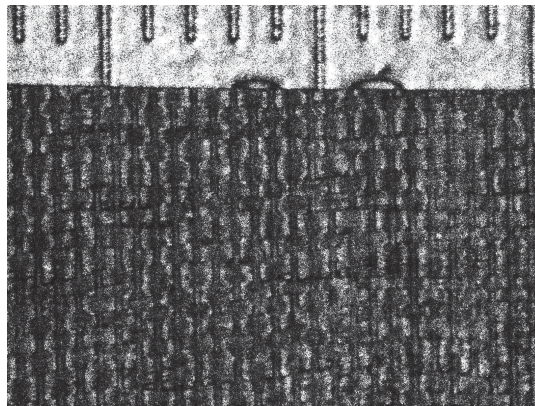


Figure 2.7: Reference image for rigid body displacement test to verify laser DIC displacement error

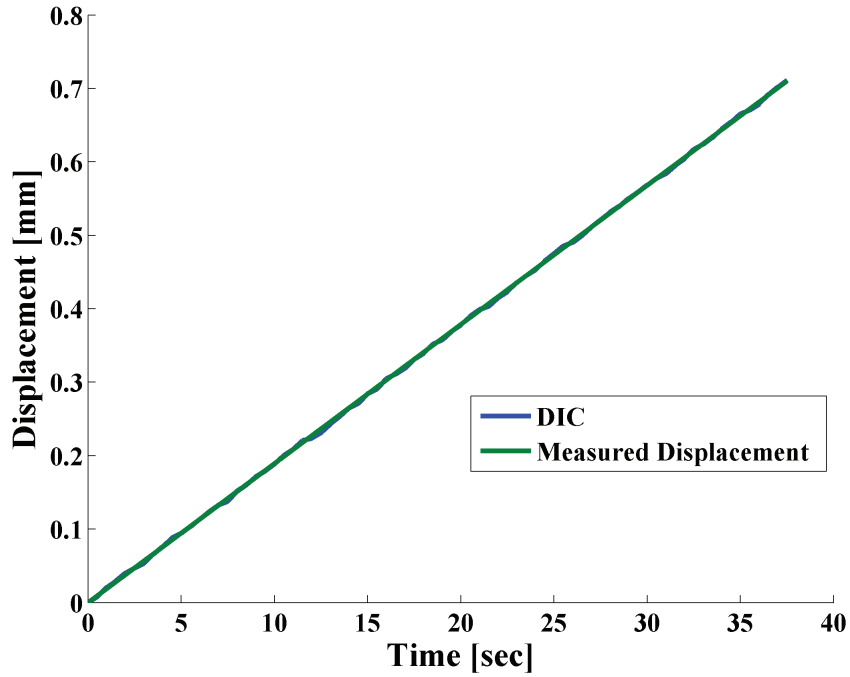


Figure 2.8: Displacement vs. time comparison of a rigid body motion test on a CMC specimen between DIC and measured displacement

2.2.1 Laser Speckle Technique Validation

Awander et al. (2000) used a digital laser speckle correlation technique (LSCT) to build an optical strain gage. Limitations of the DIC technique have been studied in the past. *Bornert et al.* (2008) investigated the performance and has provided practical rules for users. It was shown that this technique could be used to resolve strains on the order of 20 microstrains. The range of values for Young's modulus for 6061-T6 aluminum are well established and tabulated for a wide temperature range. Hence, the measurement of Young's modulus for this material was chosen in order to establish the validity of the proposed method. A single strain gage was attached on the back surface of a room temperature smooth bar sample to record the strain component in the load direction (ϵ_{yy}). The optical setup was focused on the same area on the front surface. The laser DIC strain values in load direction were averaged over a small area comparable to the area of the strain gage. In addition, a second

test was carried out with a commonly used paint speckle pattern. Figure 2.9 shows the comparison between the three strain measurements. Young's modulus is extracted from the stress-strain curve and reported in Table 2.1. Both speckle techniques are in excellent agreement and match with the well-established strain gauge stress-strain curve.

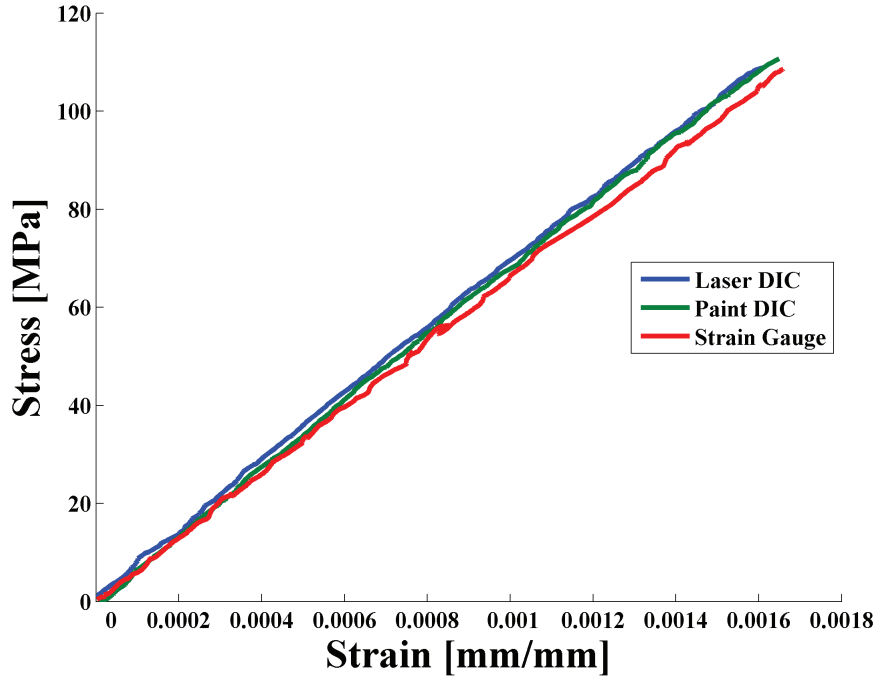


Figure 2.9: Stress - strain results (strain gage, DIC) on 6061 aluminum at room temperature)

Table 2.1: Comparison for Young's modulus of aluminum at room temperature

Method	Young's Modulus E [GPa]
Literature	68.6
Strain Gage	67.9
Laser Speckle DIC	68.1
Paint Speckle DIC	68.1

To establish that the proposed method is well suited for elevated temperature,

Young's modulus was measured for 6061-T6 Aluminum at 500 Fahrenheit (260°C). Artificial speckle patterns for high temperature application often suffer from degradation, such as chipping or oxidation [Grant et al. (2009); Sutton et al. (2009)], within a short period of time and the application is time consuming. Figure 2.10 shows the stress-strain curve for the tested aluminum sample and Young's modulus for this test is reported in table 2.2. The measured value is in agreement with values reported in the literature (Boyer (2002)).

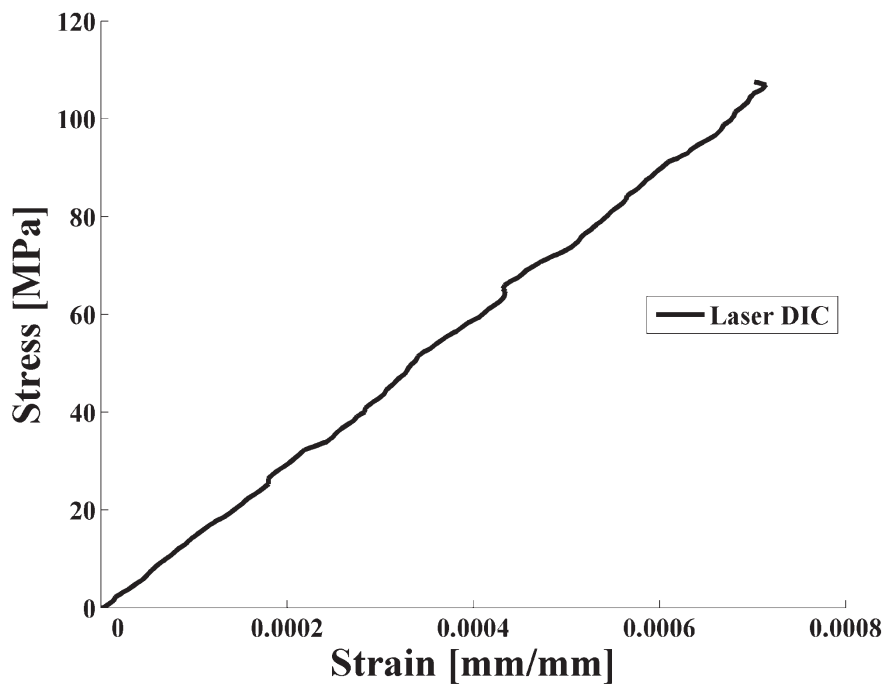


Figure 2.10: Stress - strain response of 6061 aluminum at 500 F measured with laser DIC setup

Table 2.2: Young's modulus for aluminum at 500 F

Method	Young's Modulus E [GPa]
Literature	68.6
Strain Gage	67.9

2.3 Ambient Temperature Testing

Although CMCs are intended for very high temperatures in excess of 1316°C , initial studies were conducted at room temperature in order to establish baseline data. The experimental setup was identical to the high temperature setup with the exception that the furnace was removed. Single edge notch monotonic tensile tests were conducted on the Shore Western load frame displayed in figure 2.1. A blue light laser was used for illumination of the sample and speckle pattern creation. The blue light bandpass filter was built in the camera-lens setup. The CMC test samples were gripped directly between the hydraulic wedge grips. All tests were conducted with a loading rate of 0.15 mm (0.0001) per minute. In the following discussions a crack is defined as a visible local increase in strain as seen in the DIC data.

2.3.1 $[0/90]_{2S}$ Laminate

Dog-bone shaped single edge notch cross-ply $[0/90]_{2S}$ CMC samples were tested at room-temperature. The specimens were 152.4 mm (6 in) in length with a grip section width of 12.7 mm (0.5 in). The gage section width was tapered down to 10.16 mm (0.4 in) with a gage section length of 76.2 mm (3 in) as shown in Figure 2.11. The tested notch geometry is given in Figure 2.12. The notch tip consisted of a single curved surface with a radius of 0.03 mm (0.012 in) and a notch depth of 0.91 mm (0.036 in).

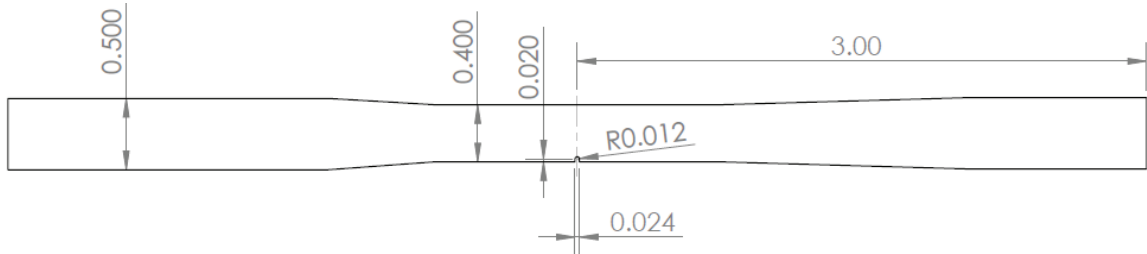


Figure 2.11: CMC tensile sample dimensions

All tested samples had a thickness of 2.03 mm (0.08). The surface fiber direction was lined up with the tensile direction. One inch wide hydraulic wedge grips with

serrated surfaces were used to clamp the gauge section of the specimens. A grip pressure of 800 psi was used to ensure slip-free displacement conditions while not introducing any damage to the specimen. Specimen designations consist of four main groups, e.g. 1999-01-0001-TD9. The second last group stands for the panel number and the designation TD implies a tensile dogbone with the corresponding specimen number.

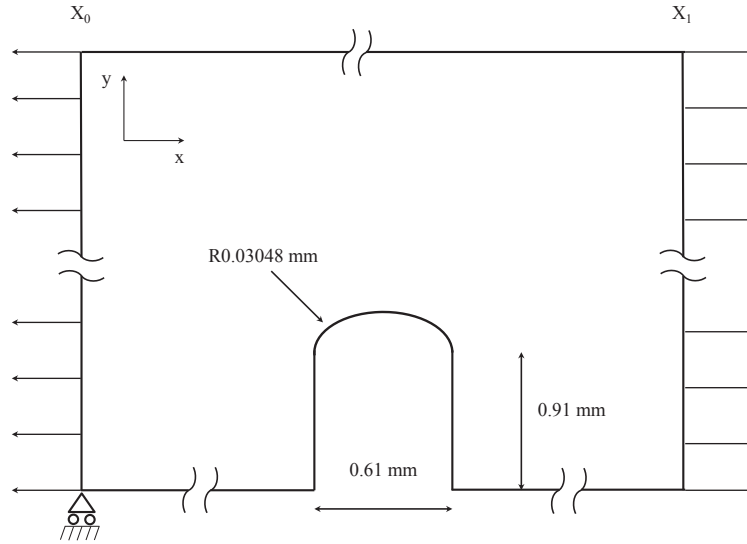


Figure 2.12: Schematic representation of the single edge notch dimensions

Strain measurements based on the DIC results are inherently difficult on materials which experience small surface displacements as is the case for CMCs. The correlation error of the system was measured by taking static consecutive images of a CMC specimen without applied loading. The images were then correlated and displacement and strain fields calculated. In theory, all surface displacement fields are equal to zero. However, 2D-DIC is subject to multiple errors that originate from various sources, e.g. vibrations, non-perpendicular camera alignment, etc. (*Bruck et al. (1989); Pankow et al. (2010); Vendroux and Knauss (1998)*). The noise level of the used system was determined to be on the order of $200\mu\epsilon$. The expected strain for *SiC/SiC* CMCs is in the range of $1000 - 2000\mu\epsilon$ resulting in a noise/strain ratio of $\frac{1}{5} - \frac{1}{10}$. The used

furnace did not permit the use of an extensometer to measure surface strains. Selected stress-strain responses based on DIC strain measurements are shown in figure 2.41. Figure 2.14 shows the DIC results of three experiments with the corresponding crack propagation carried out on $[0/90]_{2S}$ laminates. Specimens TD6 and TD7 failed at a maximum net-section stress of 286 MPa and 289 MPa, respectively. Specimen TD1 failed prematurely at 251 MPa. The limited number of specimens does not allow for a statistical analysis at this point. The crack propagation in all three tests was similar. A single crack initiated at the notch and progressively propagated outward. The field of view (FOV) was not sufficient enough for a detailed analysis of the crack initiation around the notch. Typically, two initial cracks are observed in close proximity of the notch when small fields of view are used (*Tracy (2014)*). Both cracks develop initially until one propagates faster and overtakes the other one. The faster growing crack usually determines the ultimate fracture path. The initial cracks usually appear to be aligned with the direction that is perpendicular to the the maximum principle strain directions.

The $[0/90]_{2S}$ laminates display a lower crack density on the surface, as visualized with DIC, compared to the $[90/0]_{2S}$ laminates discussed in section 2.3.2. It is expected that the density of transverse cracks in the 90-layers is higher compared to 0-layers. Hence more cracks will be visible on specimens with the weaker 90-layer on the outside surface.

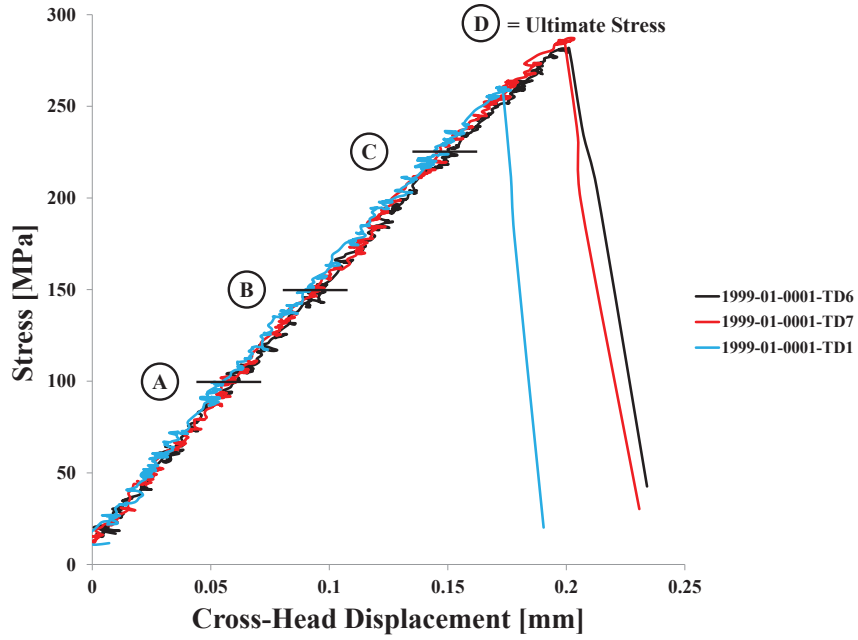


Figure 2.13: Stress-displacement response of $[0/90]_{2s}$ CMC tensile tests at ambient temperature; A = 100 MPa, B = 150 MPa, C = 225 MPa, D = Ultimate Stress

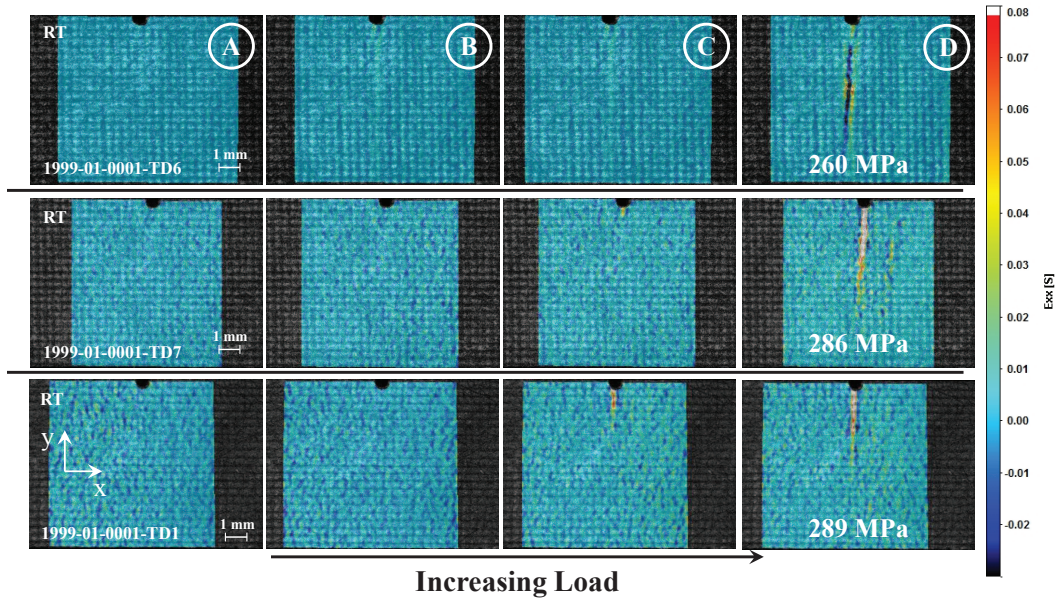


Figure 2.14: DIC full-field surface strain maps of cross-ply CMC tensile tests at room-temperature

2.3.2 $[90/0]_{2S}$ Laminate

In this section results for the eight layer cross-ply $[90/0]_{2S}$ laminates tested at ambient temperature are reported. Three tests were carried out and the stress-displacement response is shown in figure 2.15. These laminates exhibit a more diverse crack propagation compared to the $[0/90]_{2S}$ lay-up as shown in figure 2.16. No damage was observed at 100 MPa corresponding to point A in figure 2.15. Two strain concentrations can be seen at point B corresponding to 150 MPa slightly off-set from the notch tip in all three experiments. This matches well with the DIC results of the $[0/90]_{2S}$ -specimens. However, multiple cracks developed in these specimens before the ultimate strength is reached. Crack initiation and a higher crack density are expected to be found in the 90-layers of the composite as will be confirmed in section III with a micro-scale finite element approach. The field of view for specimen 2098-01-6100-TD4 was reduced to half the size compared to the other two tests. This was done to capture more details of the crack initiation in the vicinity of the notch. At this magnification, three cracks can be identified around the notch tip. Two cracks span the entire field of view. A fourth crack is evident approximately 2 mm to the left of the center line of the notch. This specimen fractured at a lower net-section stress of 245 MPa compared to the other two specimens. Specimen 2098-01-6102-TD4 and 2098-01-6102-TD5 exhibit a slight non-linear stress response before fracturing at 281 MPa and 277 MPa, respectively. The onset of non-linearity corresponds to the occurrence of additional cracks to the left of the notch center line, indicated at point C of figure 2.15. In order for new cracks to appear away from an existing crack, fibers in the zero layers have to bridge the existing crack and hence transfer load across the crack surface. Further investigation is needed to clarify the exact location of the observed cracks with respect to the specimen thickness. The final fracture surface of all tested specimens was found to be perpendicular to the loading direction in the plane of the notch. Point D in figure 2.16 shows the last image before final fracture.

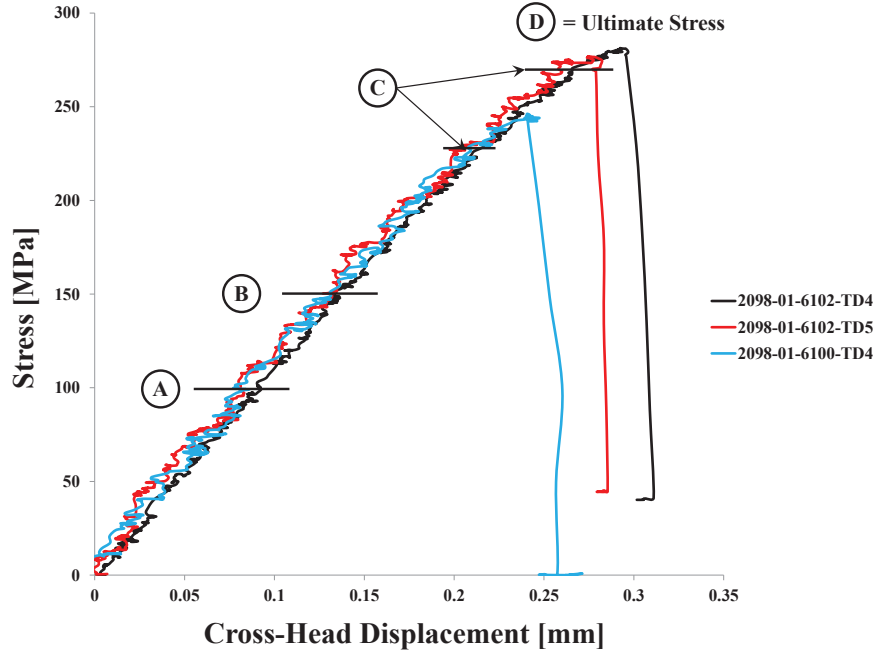


Figure 2.15: Stress-displacement response of $[90/0]_{2S}$ CMC tensile tests at ambient temperature; A = 100 MPa, B = 150 MPa, C = 260 MPa for specimens 2098-01-6102-TD4 and 2098-01-6102-TD5 & C = 225 MPa for specimen 2098-01-6100-TD4, D = Ultimate Stress

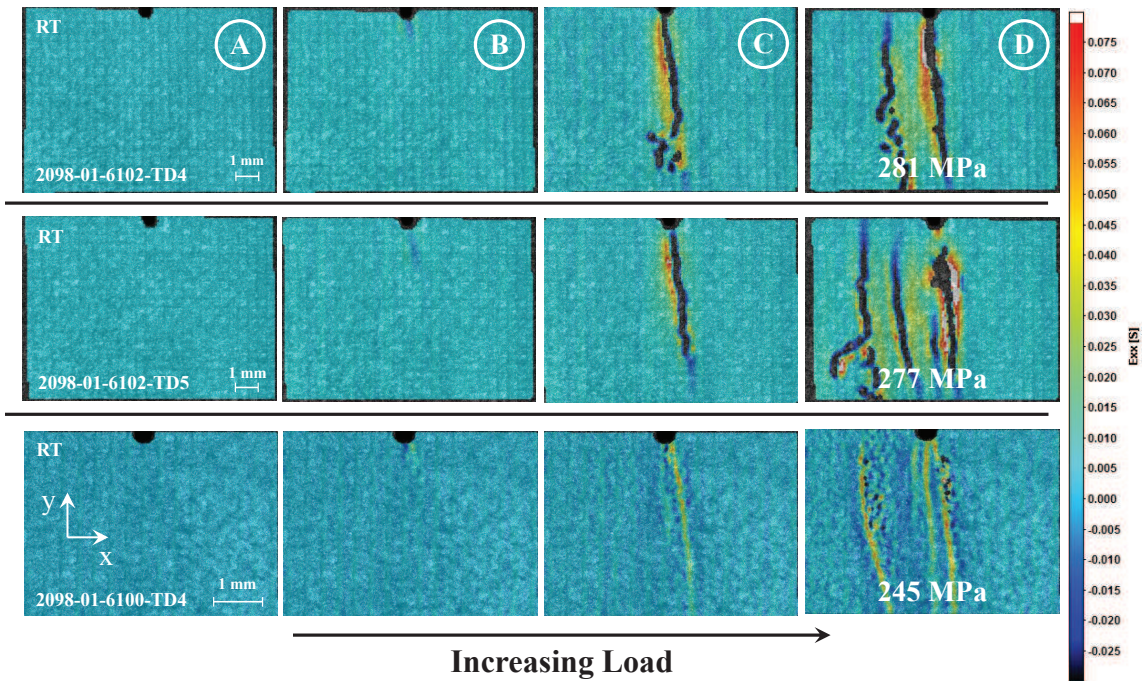


Figure 2.16: DIC full-field surface strain maps of $[90/0]_S$ CMC tensile tests at room-temperature

2.3.3 $[+45/-45]_{2S}$ Laminate

In addition to the cross-ply laminates discussed in sections 2.3.1 and 2.3.2, three experiments at ambient temperature on 8-layer $[+45/-45]_{2S}$ laminates were carried out. The damage propagation is depicted in figure 2.18. The field of view of the third test was reduced to half the size of the previous two experiments in order to achieve a higher resolution of the crack initiation in the vicinity of the notch. Crack initiation is observed at the notch tip. This behavior is similar to the damage initiation exhibited by the $[0/90]_{2S}$ and $[90/0]_{2S}$ laminates. However, strain concentrations occur at the notch tip as depicted at point B in figure 2.17. A single crack forms perpendicular to the loading direction (x-direction) and spans the entire width before additional cracks can be observed on both sides of the existing crack. Point C in figure 2.17 represents the damage stage before any non-linear stress response can be observed. Point C corresponds to a net-section stress of 215 MPa for specimen 2098-01-1345-TD5, 200 MPa for specimen 2098-01-1345-TD2 and 195 MPa for specimen 1999-01-0001-TD1. In contrast to the $[0/90]_{2S}$ composite specimens the $[+45/-45]_{2S}$ specimens exhibit a crack-band type behavior and extended non-linear stress-response. Point D in figure 2.17 represents the last captured image (ultimate strength) before the specimens fractured catastrophically. Additional cracks have formed in between existing cracks. This observation can be explained by fibers bridging matrix crack surfaces and thus transferring load across the crack. The crack density and extend of non-linear stress response is higher compared to the $[90/0]_{2S}$ specimens. The final fracture surface of all three specimens extended from the notch tip perpendicular (in y-direction) across the width of the sample. Post-failure analysis of the fracture surface revealed no fiber-pull out was present. It was found that the crack was tilted by approximately 10 degrees with respect to the z-axis of the specimen(through thickness direction).

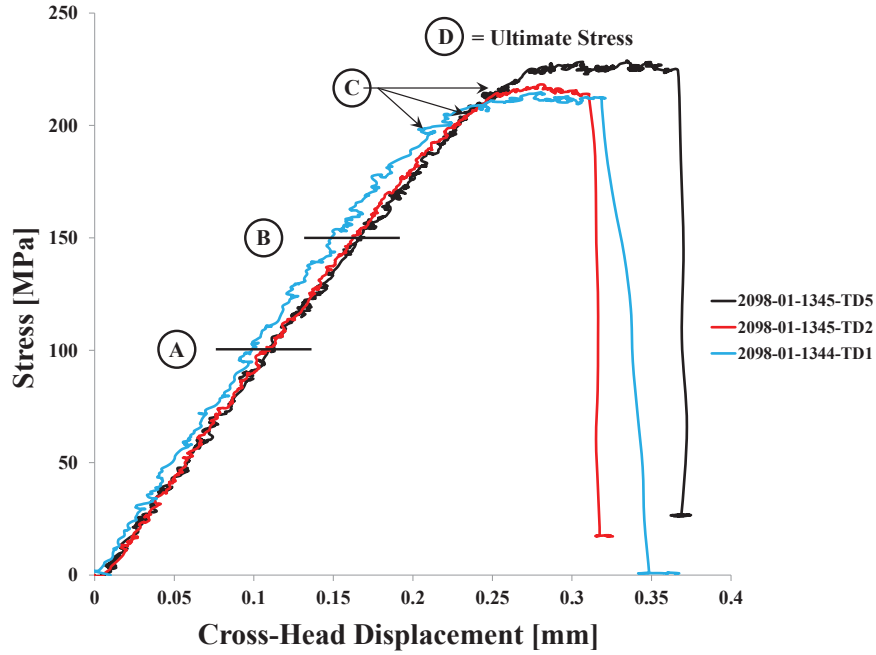


Figure 2.17: Stress-displacement response of $[+45/-45]_{2S}$ CMC tensile tests at ambient temperature; A = 100 MPa, B = 150 MPa, C = 215 MPa for specimen 2098-01-1345-TD5 & C = 200 MPa for specimen 2098-01-1345-TD2 & C = 195 MPa for specimen 1999-01-0001-TD1, D = Ultimate Stress

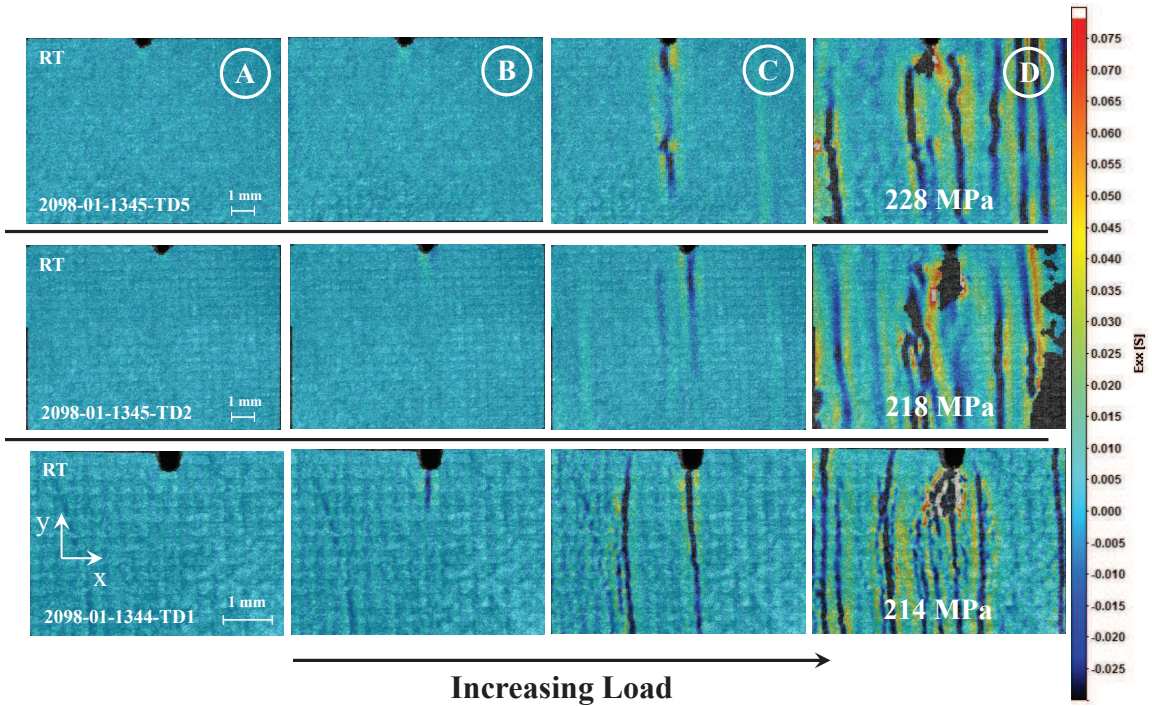


Figure 2.18: DIC full-field surface strain maps of $[+45/-45]_S$ CMC tensile tests at room-temperature

2.4 Elevated Temperature Testing

Monotonic tensile tests were conducted on Ceramic-Matrix-Composite (CMC) specimens, *Corman and Luthra* (2005), with the following dimensions at 1093°C (2000 F), 1204°C (2200 F), and 1316°C (2400 F): total length of 152.4 mm (6), gage length of 76.2 mm (3), gage width of 10.16 mm (0.4), and a thickness of 2.032 mm (0.08). A notch with a radius of 0.3048 mm (0.012) and a depth of 0.9144 mm (0.036) was cut on one side. The notch corresponded to a stress concentration factor of 3.6, as computed with a three dimensional linear elastic homogenous finite element simulation. The experiments were conducted in a displacement controlled mode. The bottom grip was displaced at a constant rate of 0.15 mm (0.0001) per minute. The grip section of the specimen and an additional 12.7 mm (0.5) were outside the furnace. Two thermocouples, as described in section 2.2, were used to ensure a constant temperature in the vicinity of the notch. After positioning the equipment in place and completing the heating cycle, the temperature of the sample was equilibrated over a period of 15 minutes. Subsequently, the bottom grip was closed. It had been kept in the open position during the heating cycle to avoid loading of the sample due to thermal expansion. All air amplifiers, which were used for grip cooling during heat-up cycle, were turned off in order to minimize air movement in front of the furnace, in an effort to reduce the occurrence of schlieren (*Settles* (2001)). Light deviations (differences in the optical pathlength) caused by schlieren in the line of sight between the furnace and camera would increase the error of the DIC calculation.

In order to study the effects of temperature on the elastic and fracture properties three tests on single edge notch tensile specimens ($[0/90]_{2S}$, $[90/0]_{2S}$, $[+45/-45]_{2S}$) were conducted at 1093°C (2000 F), 1204°C (2200 F), and 1316°C (2400 F) each. The specimen and notch dimensions were equal to those discussed in chapter 2.3.1.

2.4.1 $[0/90]_{2S}$ Laminate Tested at $1093^{\circ}C$

Three single edge notch $[0/90]_{2S}$ CMC laminates were subjected to monotonic tensile loading at $1093^{\circ}C$ (2000 F). Figure 2.20 displays the crack propagation at four stress levels. Point A represents a net-section stress of 100 MPa, point B = 150 MPa, point C = 250 MPa for specimens 1999-01-0001-TD2 & 1999-01-0001-TD4. Point C = 225 MPa for specimen 1999-01-0001-TD5 due to premature fracture of this sample at 236 MPa. The maximum load as well as the crack path are comparable to the room temperature tests. A detailed discussion of the temperature dependence on the ultimate strength is given in the conclusions section (chapter 2.5). Specimens TD2 and TD4 failed at a net-section stress of 286 MPa and 291 MPa, respectively. In addition, both samples showed extensive fiber-pullout in a post-fracture analysis of the crack surface. Specimen 1999-01-0001-TD5 failed prematurely, compared to the other two samples, at 236 MPa. The post failure observation of the crack surface of this sample did not reveal any evidence of fiber pull-out. This phenomenon will be discussed further in chapter 5.2. Damage evolution, as observed by the DIC strain contour plots shown in figure 2.20, is comparable in all three specimens. Initial damage is visible slightly offset from the notch tip at a stress of 150 MPa (Point B). Specimen 1999-01-0001-TD2 and 1999-01-0001-TD4 developed a crack that spans the width of the sample before catastrophic fracture occurred. It is assumed that a macroscopic matrix crack develops and fibers are bridging the crack surfaces and transfer load through the sample.

Due to the small number of specimens, no statistical analysis can be conducted. It is assumed that the first two tests represent the mean failure load for this particular temperature and specimen geometry. However, test results of a minimum of 15 samples is suggested in order to establish a value for the standard deviation.

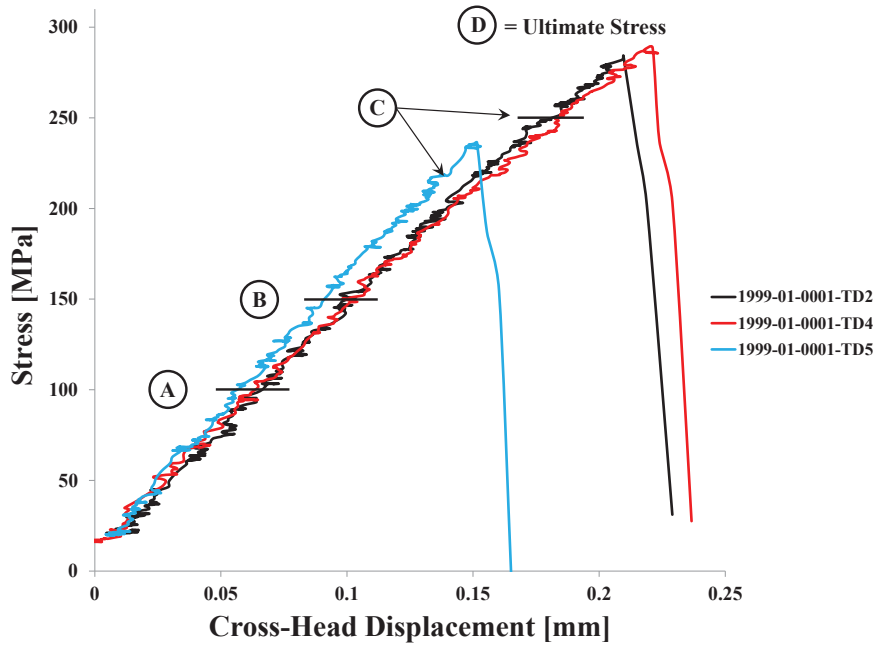


Figure 2.19: Stress-displacement response of $[0/90]_{2S}$ CMC tensile tests at $1093^{\circ}C$ (2000 F); A = 100 MPa, B = 150 MPa, C = 250 MPa for specimens 1999-01-0001-TD2 & 1999-01-0001-TD4 and C = 225 MPa for specimen 1999-01-0001-TD5, D = Ultimate Stress

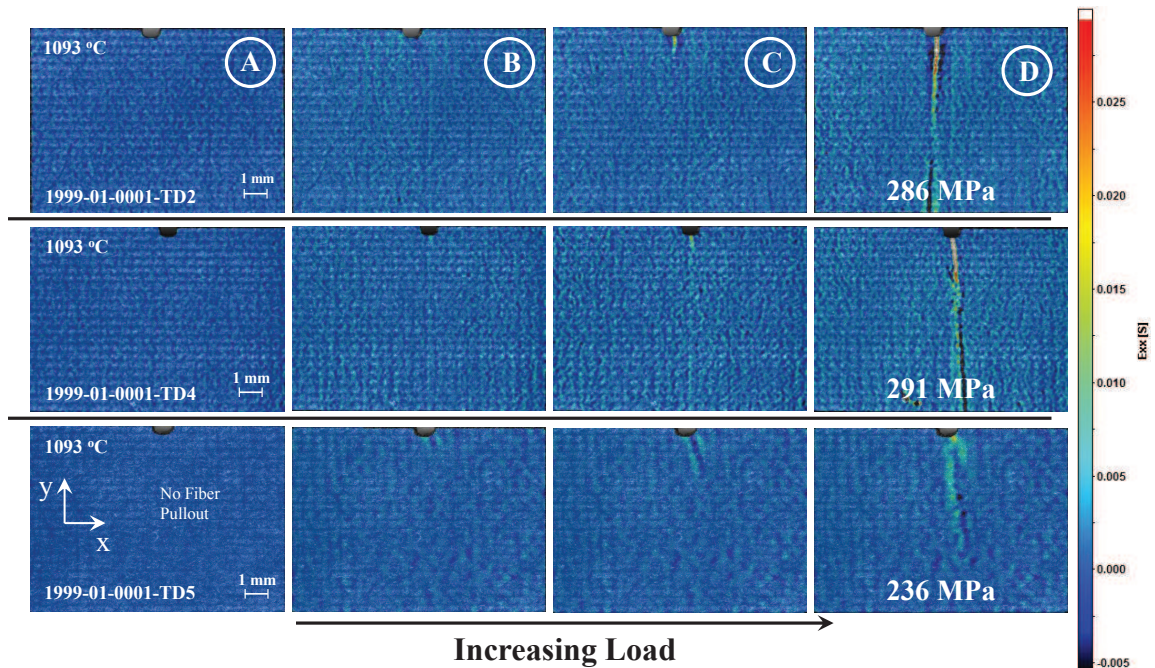


Figure 2.20: DIC Results of $[0/90]_{2S}$ CMC tensile tests at $1093^{\circ}C$ (2000 F)

2.4.2 $[0/90]_{2S}$ Laminate Tested at $1204^{\circ}C$

Figure 2.22 compares the damage evolution of three $[0/90]_{2S}$ specimens tested at $1204^{\circ}C$ (2200 F). Point A shows the axial strain field at a stress of 100 MPa. Strain localization indicating damage is not observed in the vicinity of the notch. At a stress of 150 MPa specimens 1999-01-0001-TD11 and 1999-01-0001-TD10 have a clear indication of localized damage at the notch tip. No damage can be observed in the DIC results for specimen 1999-01-0001-TD11 at this load. All three specimens exhibit high strains at the notch tip at a stress level of 200 MPa. Damage appears to be more localized in specimen 1999-01-0001-TD11. The width, expansion in x-direction, of the strain localization in specimen 1999-01-0001-TD3 is larger. This might be an indication of two separate macroscopic cracks evolving simultaneously. Further indication of this phenomenon can be seen in the strain contour plot at point D. It appears that two cracks originally initiated slightly off-set of the notch tip and joined approximately 3.4 mm in y-direction away from the notch tip. Specimen 1999-01-0001-TD11 exhibited the smallest ultimate strength of 230 MPa. It also showed the shortest visible crack length of all three tested specimens at the ultimate strength. The scatter of the three tested specimens was small compared to the series of test conducted at room temperature and $1093^{\circ}C$. Further discussion of the reduction in ultimate strength is given in the conclusion section.

Post-fracture investigation of the fracture surface revealed a large amount of fiber-pullout in all three specimens. This will be further discussed in chapter V.

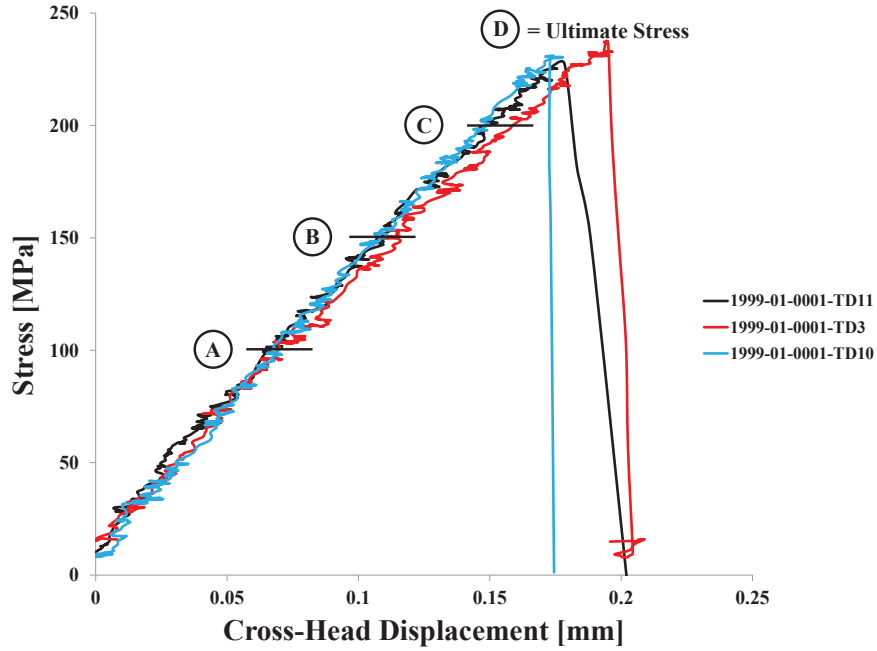


Figure 2.21: Stress-displacement response of $[0/90]_{2S}$ CMC tensile tests at $1204^{\circ}C$ (2200 F); A = 100 MPa, B = 150 MPa, C = Ultimate Stress

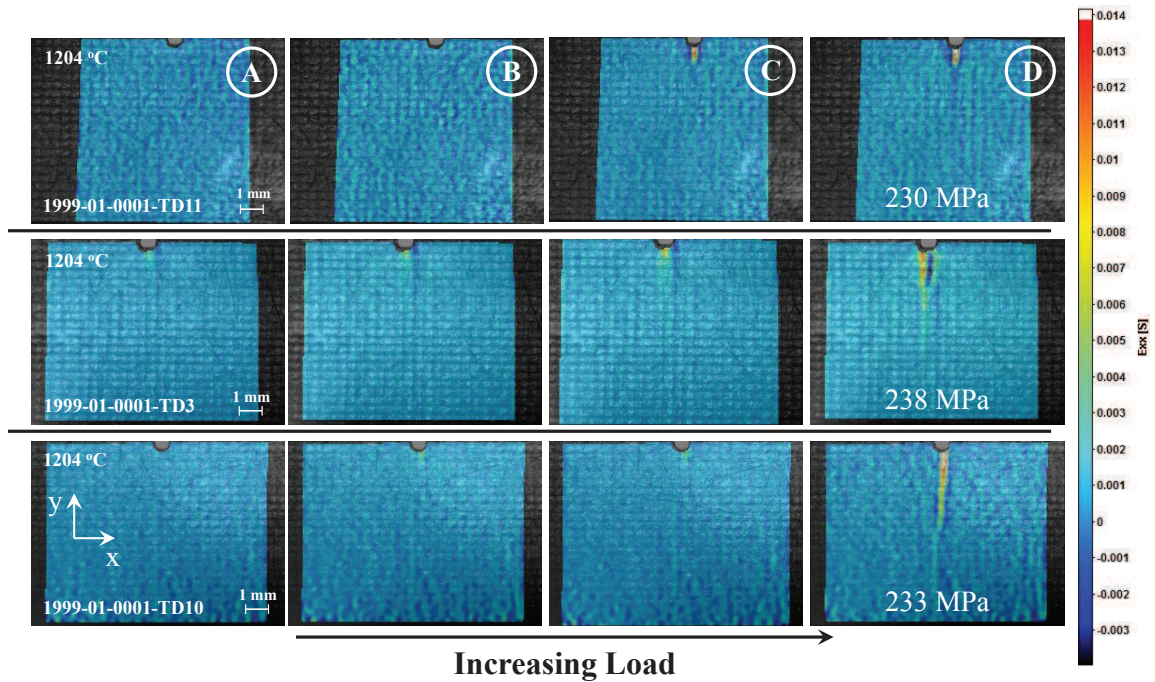


Figure 2.22: DIC Results of $[0/90]_{2S}$ CMC tensile tests at $1204^{\circ}C$ (2200 F)

2.4.3 $[0/90]_{2S}$ Laminate Tested at $1316^{\circ}C$

Experimental results of three single edge notch specimens tested at $1316^{\circ}C$ (2400 F) are presented in figure 2.24. The ultimate crack path and ultimate load are almost identical to the results found at $1204^{\circ}C$ (2200 F). However, the observable crack extension in y-direction just before fracture, point D, is shorter compared with the results at ambient temperature, $1093^{\circ}C$, and $1204^{\circ}C$. Initial damage is observable at point A (100 MPa) for specimens 1999-01-0001-TD9 and 1999-01-0003-TD9. No significant crack growth was observed at point C of figure 2.24 ($C = 225\text{MPa}$ for specimen 1999-01-0001-TD9 and $C = 180\text{MPa}$ for specimens 1999-01-0003-TD9 & 2098-01-6100-TD1,). The average ultimate strength of the three specimens was decreased compared with measurements at $1204^{\circ}C$. Specimen 1999-01-0001-TD9 sustained a significantly higher ultimate strength of 240 MPa, 32 MPa higher, when compared with specimen 1999-01-0003-TD9 and 27 MPa above the ultimate strength sustained by specimen 1999-01-0001-TD8.

Post-failure investigation under a light microscope revealed that fiber pull-out was present in two specimens in the damage evolution process. No fiber-pullout was observed for specimen 1999-01-0001-TD8. Initial steps toward a deeper understanding of the influence of fiber-pullout on the stress-strain response of CMCs is discussed in chapter V.

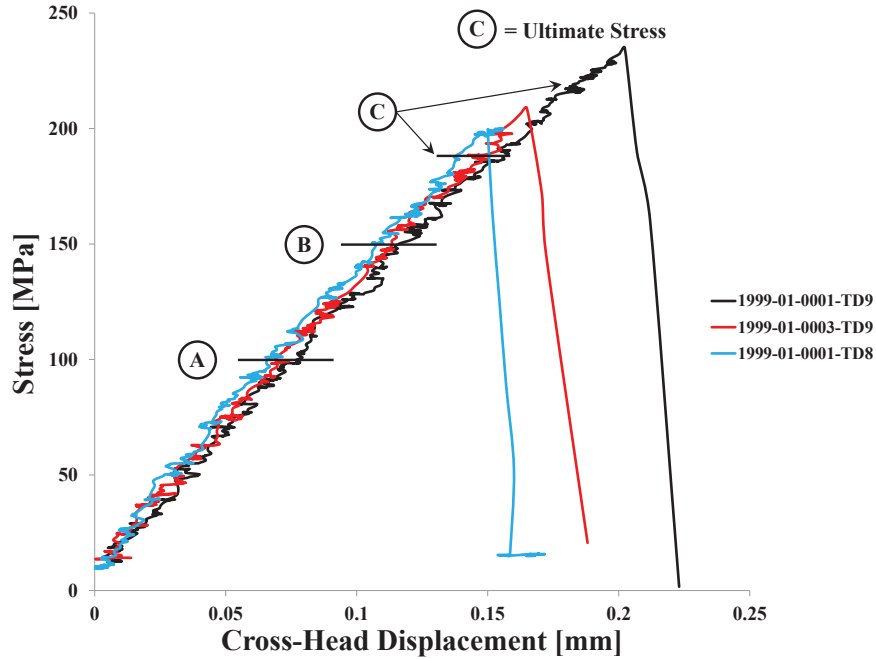


Figure 2.23: Stress-displacement response of $[0/90]_{2S}$ CMC tensile tests at $1316^{\circ}C$ (2400 F); A = 100 MPa, B = 150 MPa, C = 225 MPa for specimen 1999-01-0001-TD9 and C = 180 MPa for specimens 1999-01-0003-TD9 & 2098-01-6100-TD1, D = Ultimate Stress

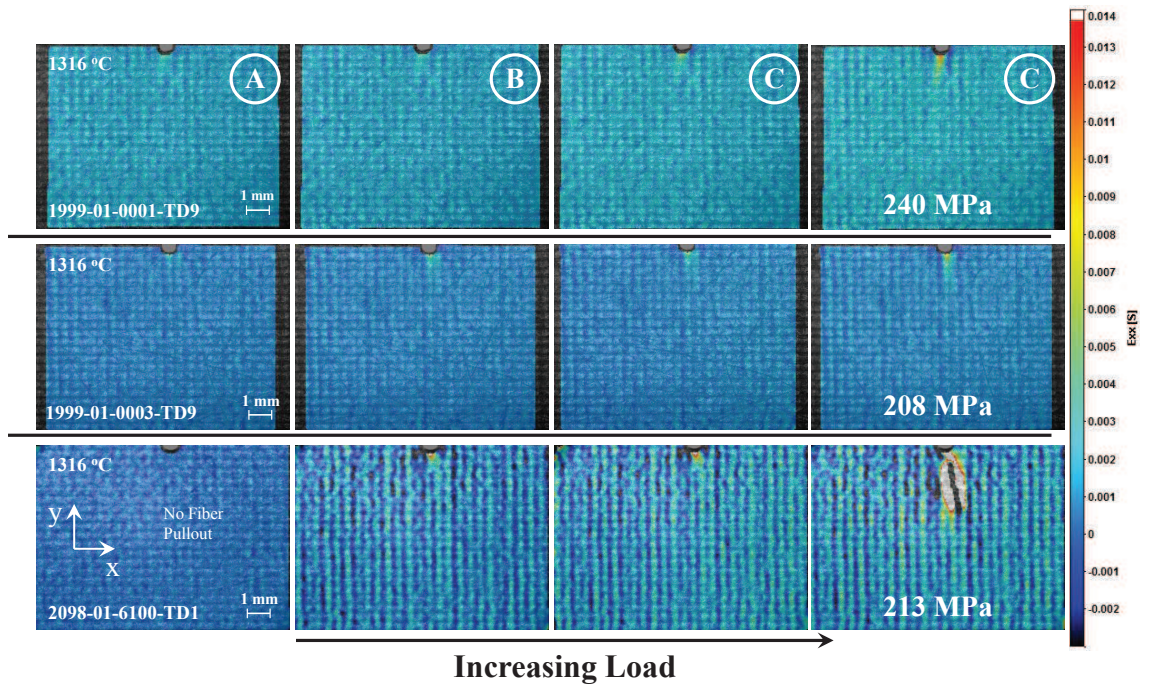


Figure 2.24: DIC Results of $[0/90]_{2S}$ CMC tensile tests at $1316^{\circ}C$ (2400 F)

2.4.4 $[90/0]_{2S}$ Laminate Tested at $1093^{\circ}C$

Two $[90/0]_{2S}$ composite samples were tested at a temperature of $1093^{\circ}C$. Longitudinal strain (ϵ_{xx}) maps depict the damage development for both tests at four stress levels in figure 2.26. A higher magnification of 2x was used during the second experiment (specimen 2098-01-6101-TD3) in order to resolve the strain field in the vicinity of the notch in more detail. Both specimens did not show signs of damage at a net-section stress of 100 MPa, corresponding to point A in figure 2.25. A strain concentration at the notch tip is observable on specimen 2098-01-6101-TD3 at a net-section stress of 150 MPa (point B). Specimen 2098-01-6100-TD2 did not show signs of damage at this stress level. A single crack can be observed on both specimens at point C corresponding to a stress of 200 MPa. Specimen 2098-01-6100-TD2 fractured at a net-section stress of 221 MPa. Specimen 2098-01-6101-TD3 failed catastrophically at 233 MPa. The longitudinal strain fields just before fracture are shown at point D in figure 2.26. In contrast to the specimens tested at ambient temperature both samples tested at $1093^{\circ}C$ showed only a single crack at the ultimate strength. The crack in both samples developed at an angle of approximately 5° to the y-axis. The difference in damage and fracture behavior of the elevated temperature specimens is expected to be influenced by the degradation of the fiber coating material. It is expected that the elastic stiffness has reduced significantly, limiting the ability of the fiber coating to transfer shear stresses from the fiber to the matrix. As a result, the stress level in the matrix material will not reach critical values away from the notch and existing crack. Further research is required to examine the temperature dependent elastic and fracture properties of the fiber coating material. Post-failure examination of the fracture surfaces did not show fiber-pullout at this temperature.

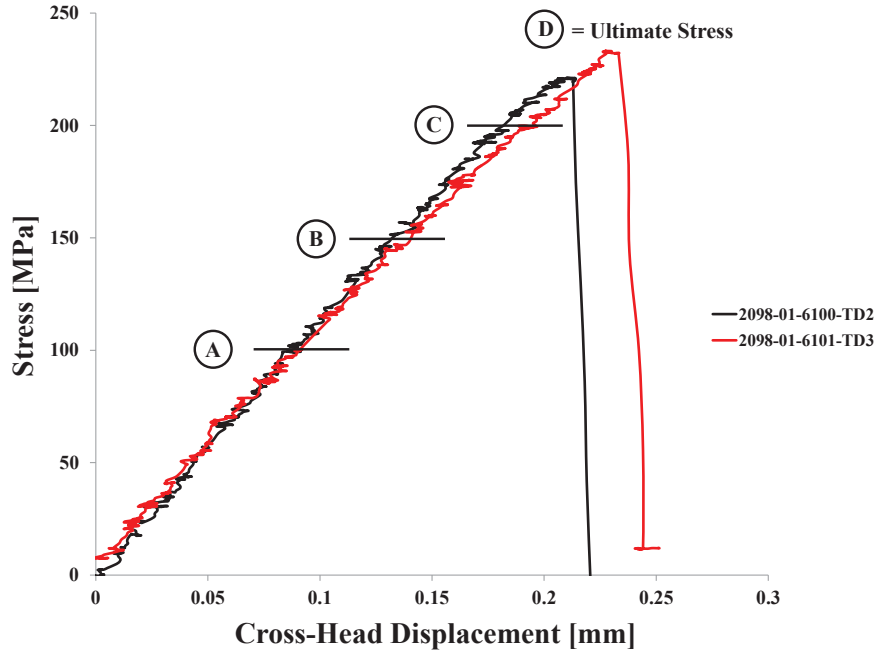


Figure 2.25: Stress-displacement response of $[90/0]_{2S}$ CMC tensile tests at 1093°C (2000 F); A = 100 MPa, B = 150 MPa, C = 200 MPa, D = Ultimate Stress

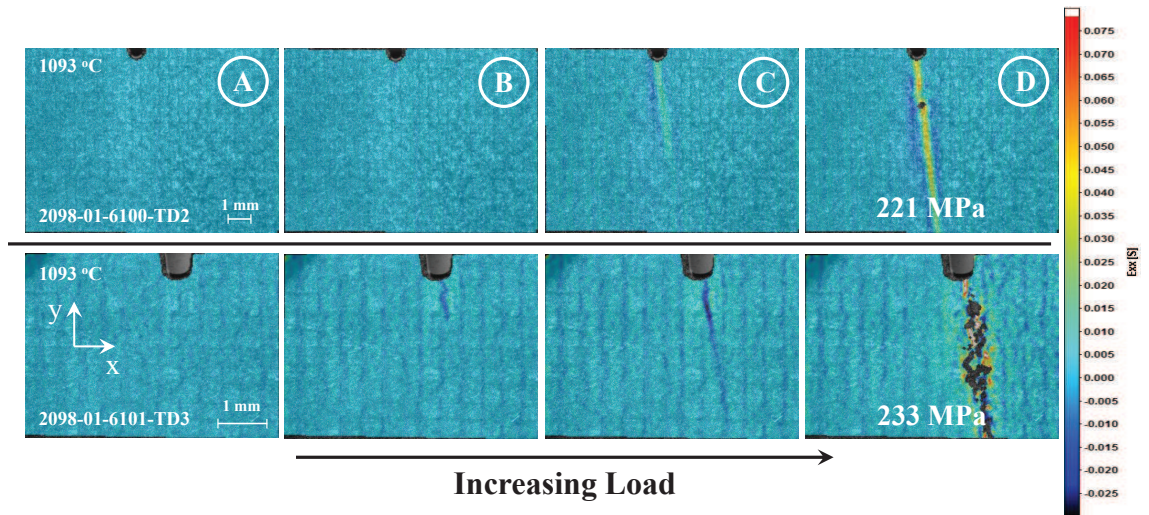


Figure 2.26: DIC full-field strain maps of $[90/0]_{2S}$ CMC tensile tests at 1093°C (2000 F)

2.4.5 $[90/0]_{2S}$ Laminate Tested at $1204^{\circ}C$

Two $[90/0]_{2S}$ cross-ply specimens were tested at $1204^{\circ}C$ (2000 F). Figure 2.28 shows the longitudinal strain field, ϵ_{xx} . The test setup for specimen 2098-01-6100-TD5 was extended by an additional 2x magnifying lens compared to the setup used for specimen 2098-01-6101-TD2. This yielded a smaller field of view and hence a higher resolution of the strain field of the notch region. As was observed in previous experiments on the same composite lay-up at lower temperatures, damage is not observable at a net-section stress of 100 MPa. First indications of strain concentration are visible at point B of figure 2.28 corresponding to a stress level of 150 MPa. A single crack is present at a stress level of 200 MPa. This is consistent with the findings discussed in section 2.4.4. The damage mode at elevated temperature changes from a crack-band type behavior at room temperature to the development of a single fracture site at elevated temperatures above $1093^{\circ}C$. Further experimental studies should be carried out at temperatures below $1093^{\circ}C$ to determine the critical temperature range at which a shift in the damage mode can be observed. Crack propagation in both tested specimens occurred at an angle of 4° and 5° with respect to the y-axis, respectively. This is consistent with the specimens tested at $1093^{\circ}C$. The crack observed in specimen 2098-01-6100-TD5 appears to turn back to a perpendicular growth path with respect to the loading axis (x-axis). Images D in figure 2.28 show the strain field at the respective ultimate strength. Specimen 2098-01-6101-TD2 fractured at 208 MPa, 15 MPa lower than the fracture stress of 223 MPa of specimen 2098-01-6100-TD5. No non-linear stress response was observed which is consistent with the lack of toughening due to distributed damage. This suggests that the fibers and matrix are carrying load as separate entities without a composite action. Post-experiment examination of the fracture surfaces did not reveal any signs of fiber-pullout supporting the finding that there is little to no load transfer through the BN coating.

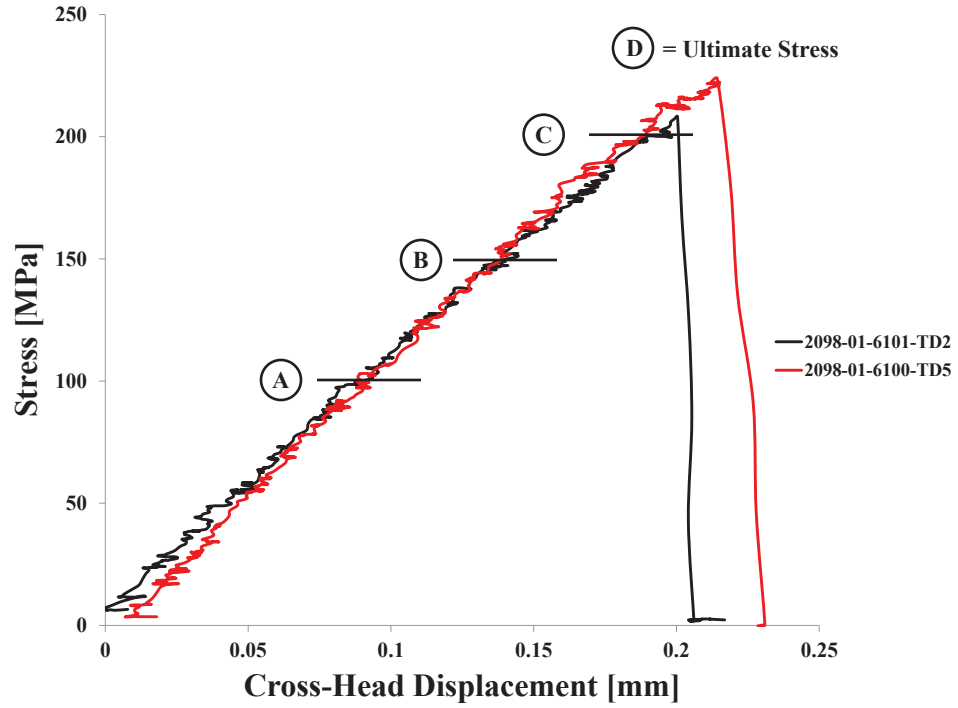


Figure 2.27: Stress-displacement response of $[90/0]_{2S}$ CMC tensile tests at $1204^{\circ}C$ (2200 F); A = 100 MPa, B = 150 MPa, C = 200 MPa, D = Ultimate Stress

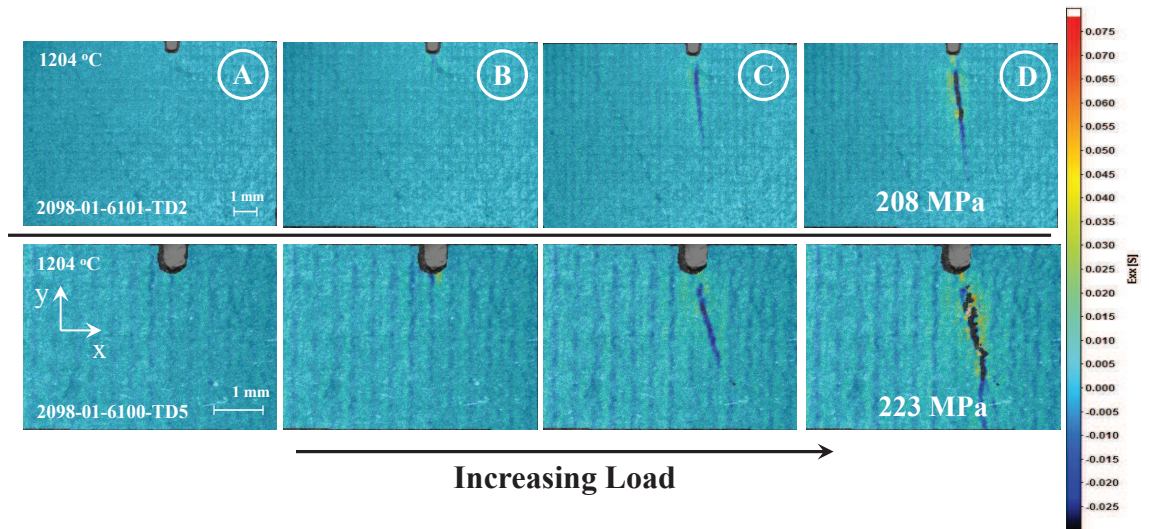


Figure 2.28: DIC full-field strain maps of $[90/0]_{2S}$ CMC tensile tests at $1204^{\circ}C$ (2200 F)

2.4.6 $[90/0]_{2S}$ Laminate Tested at $1316^{\circ}C$

Three $[90/0]_{2S}$ specimens were tested at $1316^{\circ}C$, the maximum temperature used in this series of experiments. As before, two tests were conducted with a camera-lens setup that yielded a field of view (fov) of approximately 12 mm x 10 mm. An additional 2x magnifying lens was added to the optical setup before conducting the third experiment. This yielded a field of view of approximately 6 mm x 6 mm. DIC results at four stress levels are shown in figure 2.30 for the three tested specimens. Point A represents the strain field at a net-section stress of 100 MPa. A strain localization at the notch tip is visible on specimen 2098-01-6101-TD4 at this stress state. However, no strain localization is visible for both specimen 2098-01-6100-TD3 and 2098-01-6100-TD1, respectively. Subsequently, the strain concentration at the notch tip of specimen 2098-01-6101-TD4 remains unchanged up to a net-section stress of 190 MPa. At this stress signs of localized damage are noticeable on all specimens. The extend and location of damage is consistent in all tests. However, crack growth continues in specimen 2098-01-6101-TD4 as can be seen at point D in figure 2.30. At this point the crack extends approximately 9 mm in length across the specimen width. The crack is angled with respect to the loading axis comparable to the angle observed at test temperatures of $1093^{\circ}C$ and $1204^{\circ}C$. This specimen exhibits the highest ultimate strength out of the three tested samples of 211 MPa. Progressive crack growth cannot be observed and the crack length remains constrained to the vicinity of the notch in specimens 2098-01-6100-TD3 and 2098-01-6100-TD1, respectively. Specimen 2098-01-6100-TD1 exhibits the lowest stress at fracture of 194 MPa, 17 MPa lower compared to the first tested specimen. A comparison of all fracture stresses at all temperatures and laminates is given in the conclusion section of this chapter.

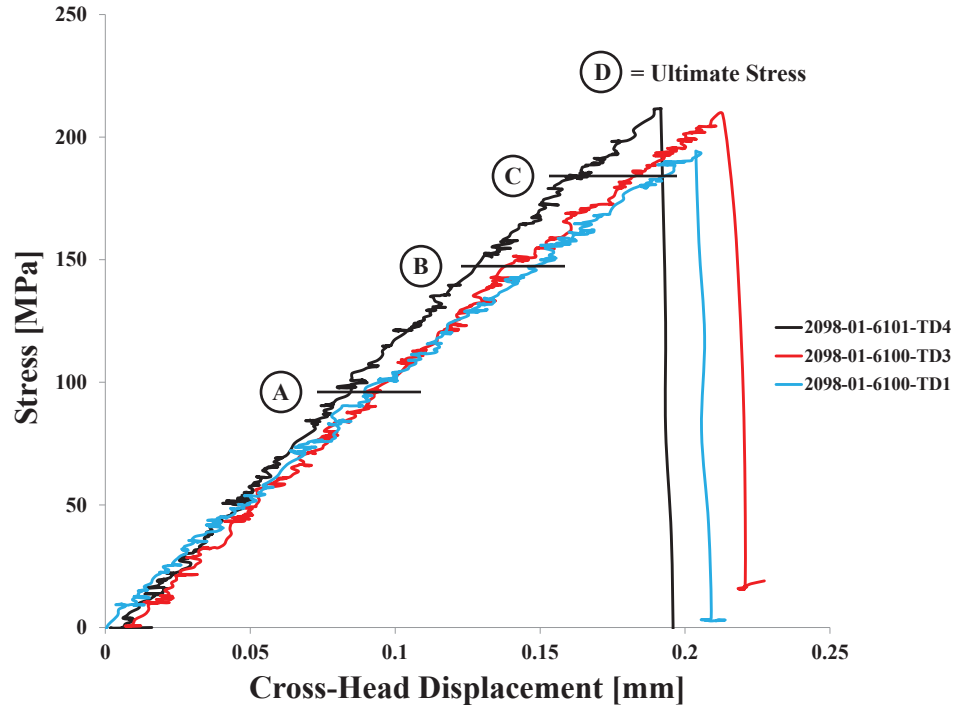


Figure 2.29: Stress-displacement response of $[90/0]_{2S}$ CMC tensile tests at 1316°C (2400 F); A = 100 MPa, B = 150 MPa, C = 190 MPa, D = Ultimate Stress

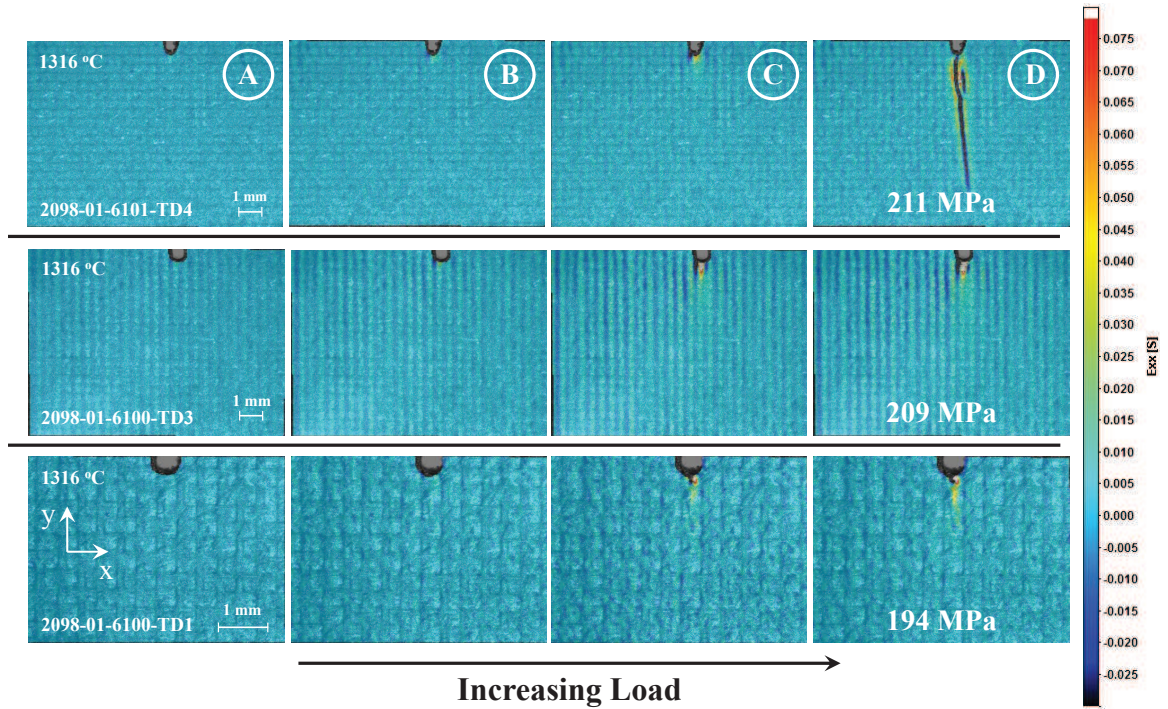


Figure 2.30: DIC full-field strain maps of $[90/0]_{2S}$ CMC tensile tests at 1316°C (2400 F)

2.4.7 $[+45/-45]_{2S}$ Laminate Tested at $1093^{\circ}C$

In addition to the experimental study at elevated temperature on cross-ply specimens a test series of eight layer off-axis $[+45/-45]_{2S}$ specimens was also conducted. Three samples were exposed to a temperature of $1093^{\circ}C$ and then subsequently subjected to monotonic tensile load. Figure 2.32 shows the development of the axial strain field, ϵ_{xx} , with increasing load for all three specimens. The field of view for specimens 2098-01-1345-TD1 and 2098-01-1345-TD4 was approximately 12 mm x 10 mm whereas an additional magnifying lens was added to the optical setup for specimen 2098-01-1344-TD2. The field of view was reduced to 6 mm x 6 mm whilst maintaining a resolution of 5 megapixels. The stress-displacement response is shown in figure 2.31. Four points of interest are marked and the corresponding axial strain contour plots are shown in figure 2.32. Specimens 2098-01-1345-TD1 and 2098-01-1345-TD4 exhibit strain localization at point B (150 MPa net-section stress). The crack tip extends 1.5 mm in y-direction from the notch tip. No damage is recognizable at this stress state in specimen 2098-01-1344-TD2. At a net-section stress of 185 MPa the crack tip in specimen 2098-01-1345-TD1 has propagated approximately 5 mm outward from the notch tip. At the same stress level the cracks in specimens 2098-01-1345-TD4 and 2098-01-1344-TD2 had propagated through the entire width of the sample. At the ultimate load, specimen 2098-01-1345-TD4 shows signs of additional cracks to the left of the existing center crack. At point D, e.g. ultimate strength, the center crack extends perpendicular to the loading direction through the entire width of all three samples.

The higher resolution of the third specimen reveals that damage appears to have initiated at the notch tip. This differs from the observation of damage initiation in both $[0/90]_{2S}$ and $[90/0]_{2S}$ specimens. This phenomenon will be verified with a finite element prediction in chapter IV that is based on modeling microstructural features and includes an energy based damage methodology.

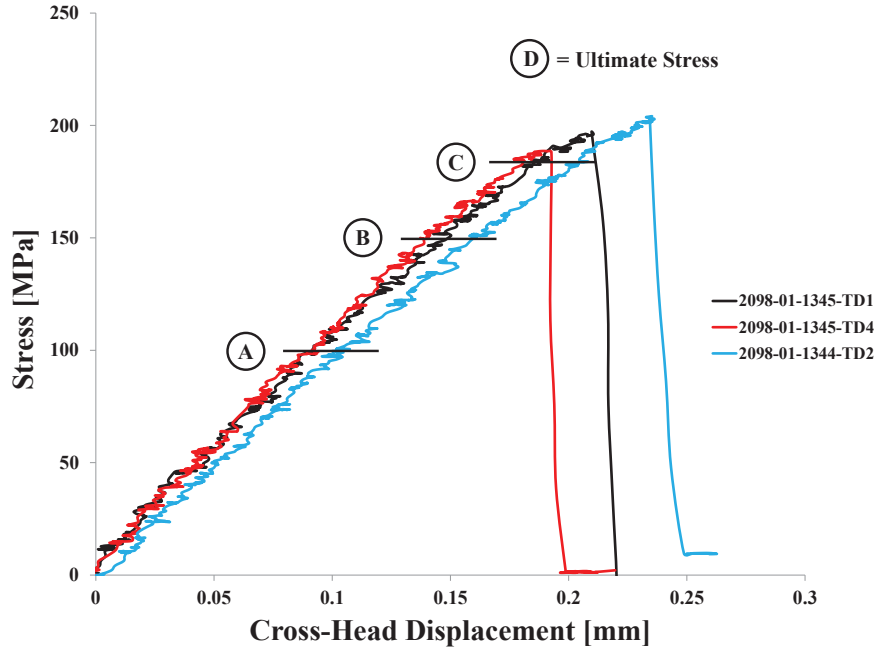


Figure 2.31: Stress-displacement response of $[+45/-45]_{2S}$ CMC tensile tests at $1093^{\circ}C$ (2000 F); A = 100 MPa, B = 150 MPa, C = 185 MPa, D = Ultimate Stress

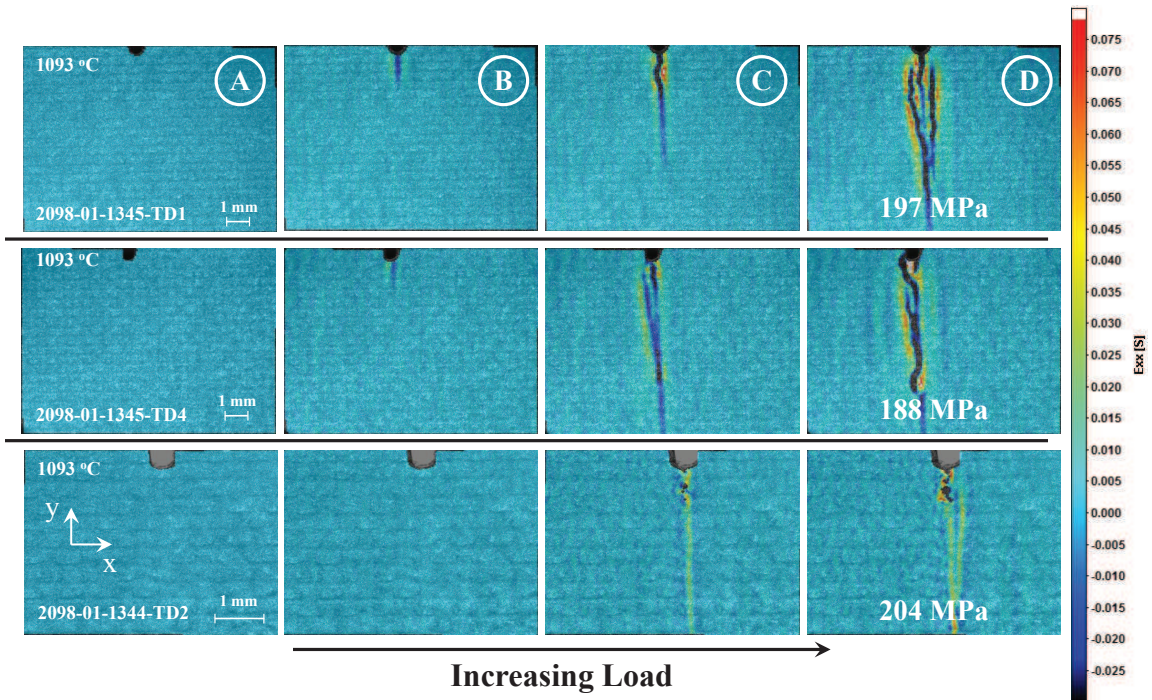


Figure 2.32: DIC full-field strain maps of $[+45/-45]_{2S}$ CMC tensile tests at $1093^{\circ}C$ (2000 F)

2.4.8 [+45/ - 45]_{2S} Laminate Tested at 1204°C

A series of three tests were performed to study the crack propagation of [+45/ - 45]_{2S} laminate at an elevated temperature of 1204°C (2200 F). The field of view for the first two specimens was approximately 12 mm x 10 mm. The third test was conducted with an additional 2x magnifying lens built into the optical setup. As was observed at a temperature of 1093°C no damage or strain localization could be seen at a net-section stress of 100 MPa, point A in figure 2.34. Damage was visible at point B in all three samples at a stress level of 150 MPa. The single crack in sample 2098-01-1345-TD3 extended the furthest with a length of approximately 7 mm. The crack length measured 2.2 mm and 0.9 mm in sample 2098-01-1327-TD5 and in sample 2098-01-1327-TD2, respectively. The strain contour plot of the last recorded image before catastrophic fracture is shown at point D in figure 2.34. The crack length in specimens 2098-01-1345-TD3 measured 8.9 mm. Specimen 2098-01-1327-TD5 exhibited a smaller crack length of 3.2 mm. The crack length in specimen 2098-01-1327-TD2 at the ultimate load could not be determined due to the crack extending past the field of view. At this temperature, the crack path was perpendicular to the loading direction as was seen in previous tests at 1093°C for the same composite lay-up. The average ultimate strength of the three tested samples was 183.6 MPa, 13 MPa lower compared to the average stress measured at 1093°C. A more detailed discussion on the ultimate strength evolution with respect to temperature is given in the conclusion section of this chapter (2.5).

Post fracture examination of the crack surface under a light microscope revealed no signs of fiber-pullout.

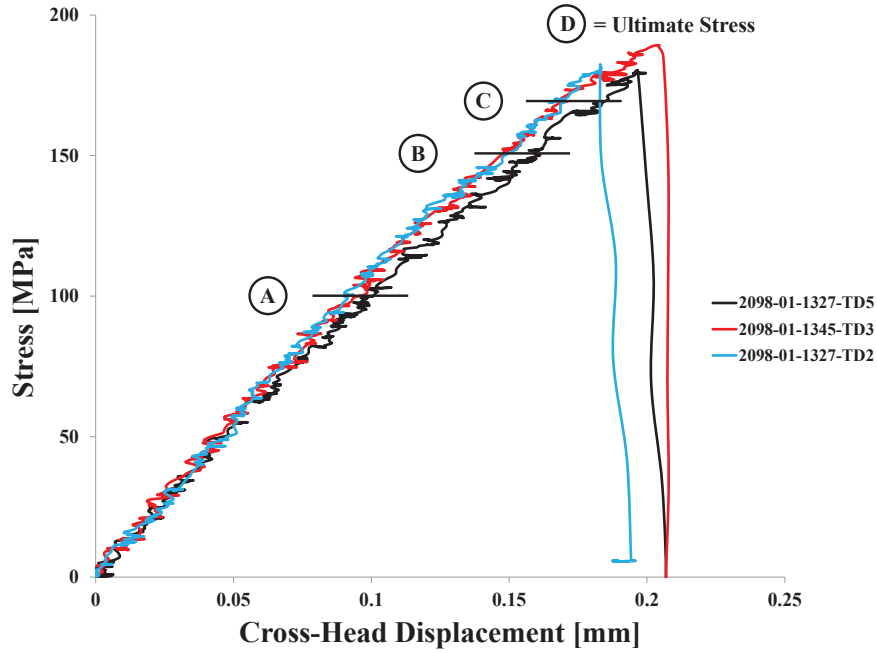


Figure 2.33: Stress-displacement response of $[+45/-45]_{2S}$ CMC tensile tests at 1204°C (2200 F); A = 100 MPa, B = 150 MPa, C = 175 MPa, D = Ultimate Stress

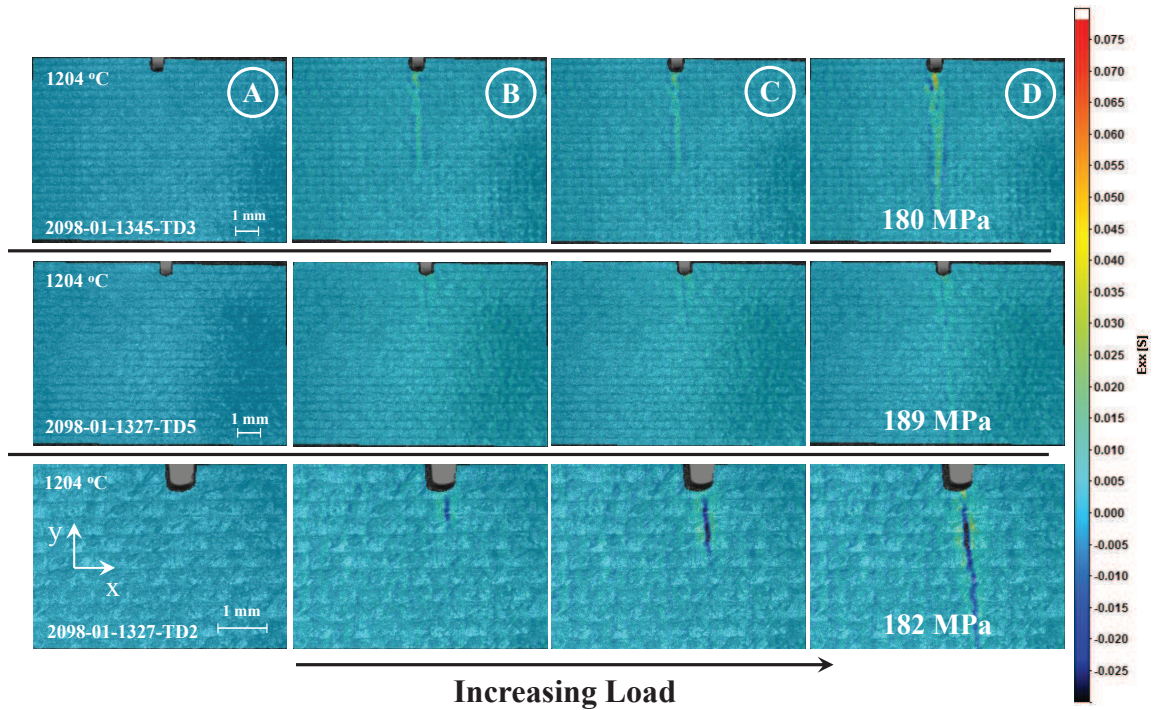


Figure 2.34: DIC full-field strain maps of $[+45/-45]_{2S}$ CMC tensile tests at 1204°C (2200 F)

2.4.9 $[+45/-45]_{2S}$ Laminate Tested at $1316^{\circ}C$

In this chapter the stress response and damage propagation of $[+45/-45]_{2S}$ laminates at $1316^{\circ}C$ subjected to monotonic tensile loading are discussed. The optical setup for the third test (specimen 2098-01-1327-TD1) was changed to achieve a smaller field of view compared to the other two specimens. An additional 2x magnifying lens was added to achieve a field of view of 6 mm x 6 mm. The axial strain contour plots, ϵ_{xx} , are given in figure 2.36. At point A, representing a net-section stress of 100 MPa, no damage was observable. The damage evolution in specimens 2098-01-1327-TD4 and 2098-01-1327-TD1 was comparable to the crack propagation of the samples tested at $1204^{\circ}C$ and discussed in section 2.4.8. Specimen 2098-01-1327-TD3 sustained the highest fracture stress of 175 MPa. Crack initiation was detected at 132 MPa net-section stress. The crack advanced instantaneously to a length of 3.1 mm and remained constant up to the ultimate strength. Specimen 2098-01-1327-TD1 exhibited the lowest ultimate strength of 164 MPa. The strain contour plot at point C in figure 2.35 shows the crack advancement at a stress of $C = 170$ MPa for specimens 2098-01-1327-TD3 and 2098-01-1327-TD4 and $C = 160$ MPa for specimen 2098-01-1327-TD1. The crack in specimen 2098-01-1327-TD1 extends past the field of view and appeared instantaneously at a stress of 140 MPa. Overall, crack evolution growth speeds appear to be increased at this temperature. More specimens should be tested in the future to verify this finding. The fracture surfaces of all three specimens were found to be perpendicular to the loading direction. The average ultimate strength was calculated as 170 MPa. It was lower compared to the average stress of the experiments conducted at $1204^{\circ}C$.

Post fracture examination of the crack surface under a light microscope revealed no sign of fiber-pullout.

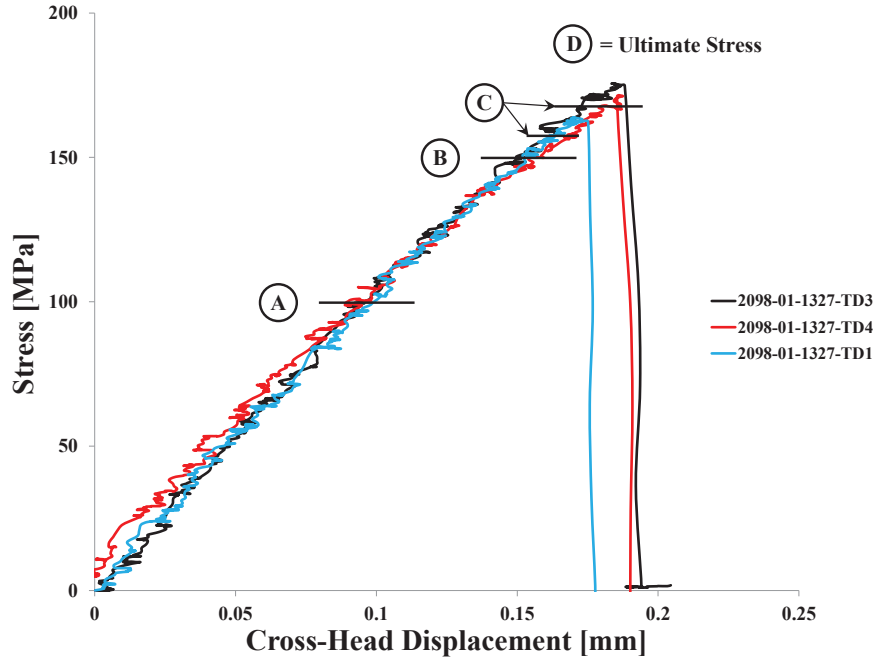


Figure 2.35: Stress-displacement response of $[+45/-45]_{2S}$ CMC tensile tests at 1316°C (2400 F); A = 100 MPa, B = 150 MPa, C = 170 MPa for specimens 2098-01-1327-TD3 and 2098-01-1327-TD4 & C = 160 MPa for specimen 2098-01-1327-TD1, D = Ultimate Stress

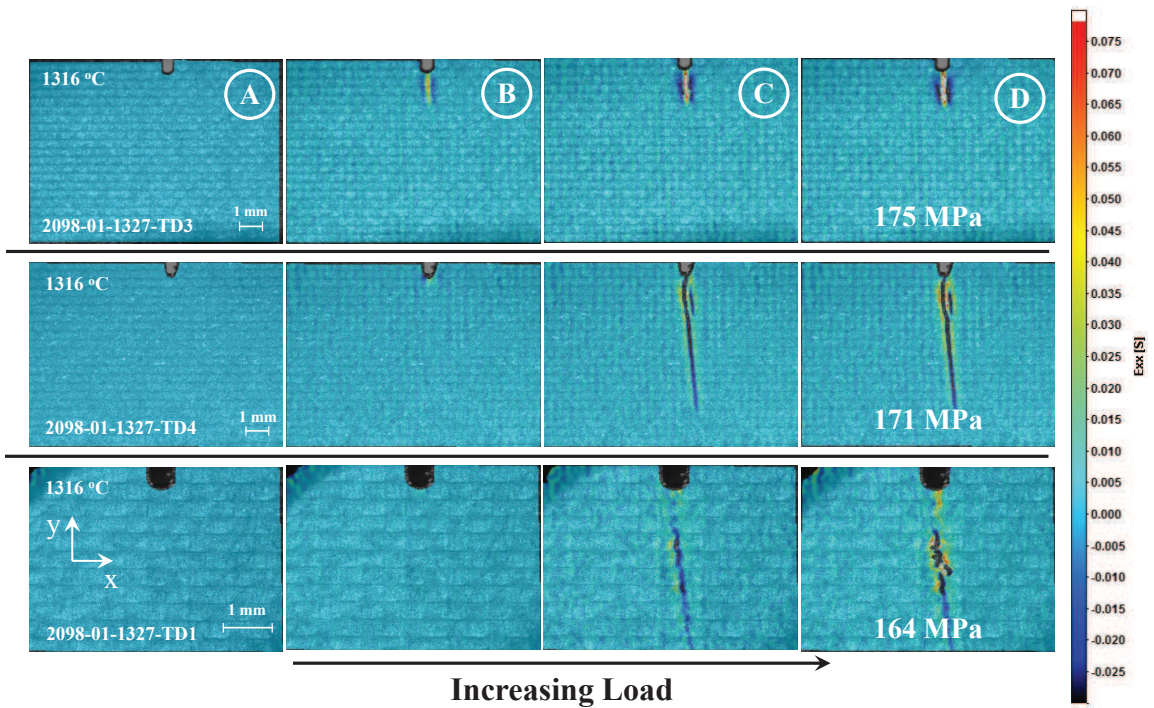


Figure 2.36: DIC full-field strain maps of $[+45/-45]_{2S}$ CMC tensile tests at 1316°C (2400 F)

2.5 Conclusions

An experimental setup for monotonic tensile tests at ambient and elevated temperature was discussed in this chapter. A low intensity blue light laser in combination with a blue light filter was used to illuminate the specimen surface and create a non-contact speckle pattern. This setup results in reduced setup time, elimination of the most common problems associated with high temperature DIC, and increased fidelity. Single edge notch CMC specimens with three composite lay-ups ($[0/90]_{2S}$, $[90/0]_{2S}$, $[+45/-45]_{2S}$) were tested at various temperatures. Figure 2.37 gives an overview of the ultimate net-section stress sustained by the $[0/90]_{2S}$ specimens at the tested temperatures. A minimal reduction in the average stress was calculated between ambient temperature (278 MPa) and 1093°C (271 MPa). However, the difference lies within the range of scatter. A significant decrease in sustained net-section stress was observed between 1093°C (2000 F) and 1204°C (2200 F), from 271 MPa to 233 MPa. The scatter of the three tested specimens at 1204°C was smaller compared with the test series at other temperatures. A further average ultimate strength reduction to 220 MPa was observed at a test temperature of 1316°C .

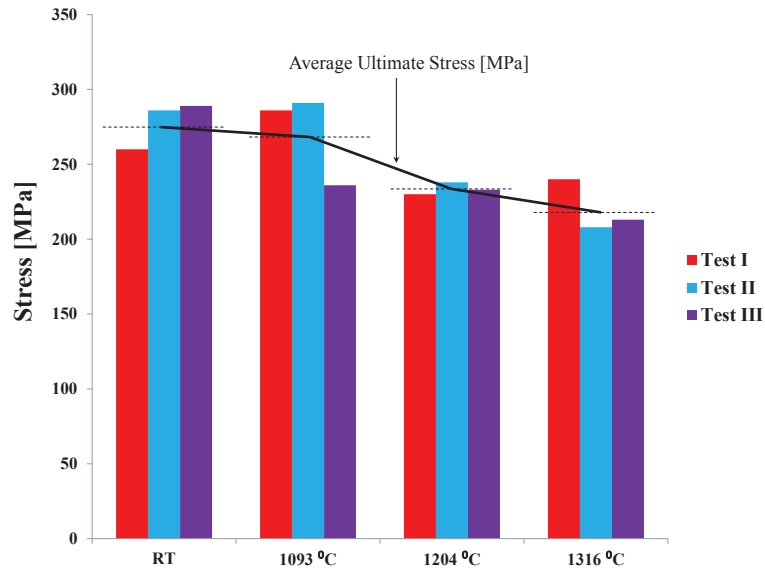


Figure 2.37: Comparison of ultimate net-section stress for $[0/90]_{2S}$ laminates

Future research is required to investigate the physical and chemical changes occurring at the material level that leads to an explanation of the strength reduction between 1093°C and 1204°C . It is assumed that the interface material (BN) response plays a significant role. It should be noted that one specimen each at room temperature and 1093°C failed at a much lower stress compared to the two other tests, carried out under nominally identical conditions. However, due to limited number of available specimens no statistical analysis can be provided in this study.

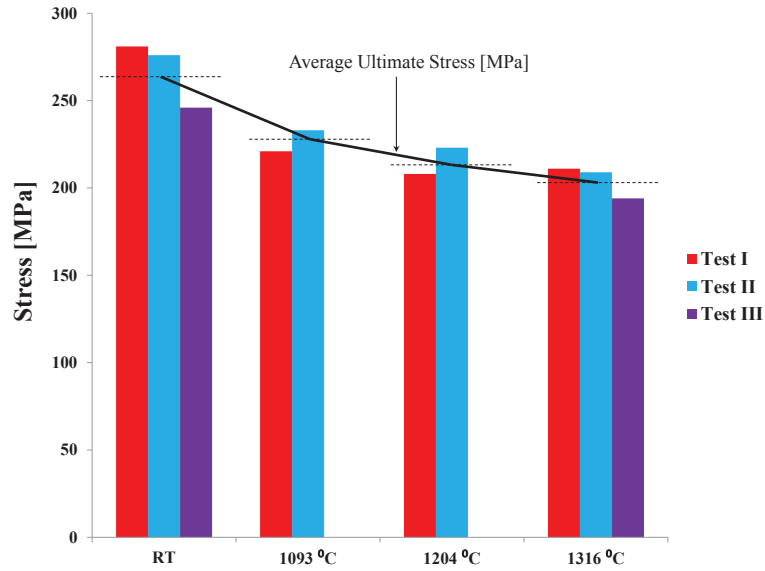


Figure 2.38: Comparison of ultimate net-section strength for $[90/0]_{2S}$ laminates

A clear strength reduction between the ambient temperature experiments and elevated temperature tests is visible in the experimental results of the $[90/0]_{2S}$ laminates, as shown in figure 2.38. The average ultimate strength reduces from 267 MPa at room temperature to 227 MPa at 1093°C . The average stress was calculated as 215 MPa and 204 MPa at a temperature of 1204°C and 1316°C , respectively. However, the strength variation between the elevated temperature experiments falls within the range of scatter.

Figure 2.39 shows the ultimate strength of all experiments conducted on $[+45/-45]_{2S}$ specimens. The average ultimate strength reduced from 220 MPa at room temper-

ature to 196 MPa at 1093°C. A further reduction to an average stress level was observed from 183 MPa to 169 MPa at 1204°C and 1316°C respectively. The trend seems to indicate a reduction of strength with increased temperature. However, as discussed before the variation of the elevated temperature experiments fall within the range of scatter. More experimental results at each temperature are required.

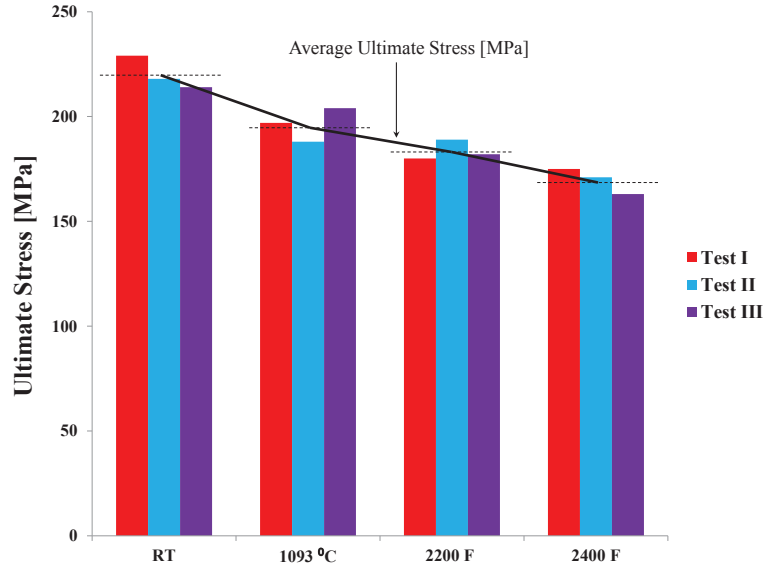


Figure 2.39: Comparison of ultimate net-section strength for [+45/-45]_{2S} laminates

A comparison of the average strength of each composite lay-up at all tested temperatures is given in figure 2.40. Each bar represents 3 experiments with the exception of two tests with [90/0]_{2S} specimens where only two experiments were conducted at 1093°C and 1204°C. Error bars indicate the scatter of each test series. At room temperature, the average stress for both [0/90]_{2S} and [90/0]_{2S} laminates match perfectly. The stress was calculated as 278 MPa and 276 MPa, respectively. However the strength of the [90/0]_{2S} laminates decreased to 227 MPa at 1093°C whereas the strength of the [0/90]_{2S} laminates remained almost unchanged at 271 MPa. A drop was noticeable for the [0/90]_{2S} laminates between 1093°C and 1204°C from 271 MPa to 233 MPa. The results showed a minimal reduction of the average ultimate strength at 1316°C to 220 MPa.

The lowest average ultimate strength at room temperature of 220 MPa was measured for the $[+45/-45]_{2S}$ laminates. It reduced to 196 MPa at $1093^{\circ}C$, 183 MPa at $1204^{\circ}C$, and 169 MPa at $1316^{\circ}C$.

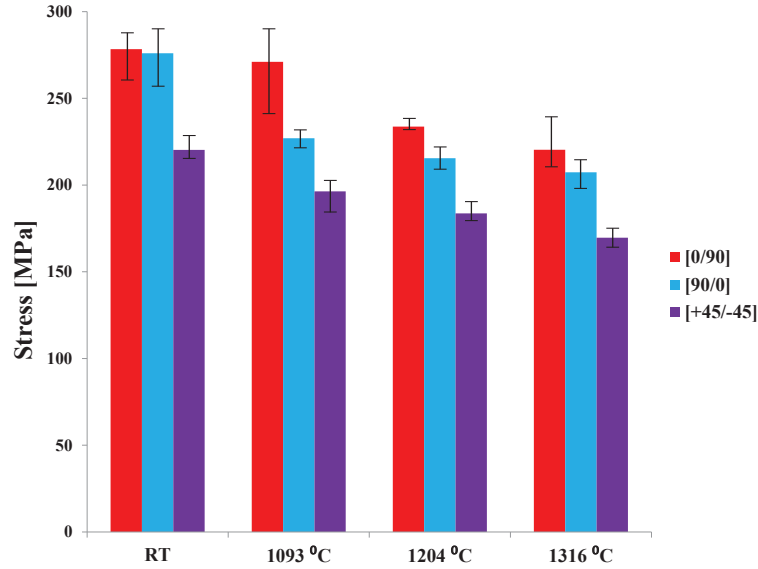


Figure 2.40: Comparison of the average ultimate net-section stress at all temperatures for all tested laminates

DIC results of the $[90/0]_{2S}$ and $[+45/-45]_{2S}$ laminates showed the formation of crack bands at ambient temperature. However, at elevated temperature only single cracks were observed. In order for crack bands to form, the load that is carried across a crack surface by the fibers needs to be transferred back into the matrix material. In theory this is achieved through shear stresses along the fiber-matrix interface. However, it is likely that the fiber coating material degrades at elevated temperatures and is therefore unable to carry these loads. This phenomenon is likely causing a lack of load transfer from the fibers back into the matrix away from the existing crack surface. The stress level in the matrix does not reach critical values and therefore no new damage sites occur.

DIC results at all tested temperatures revealed that damage of the CMC specimens occurred progressively. Initially, strain concentrations can be observed in the vicinity of the notch with further propagation outward until catastrophic fracture of

the sample. This behavior is beneficial for the design of components as no instantaneous catastrophic failure occurs. Damage can be detected before the load carrying capability of a component vanishes. Tests with a reduced field of view showed that for the tested notch geometry two cracks occur slightly off-set of the notch tip for the cross-ply specimens. Finite element simulations as further discussed in chapter IV show that the crack direction appears to be aligned perpendicular to the maximum principle strain direction. The cracks turn perpendicular to the loading direction within a characteristic distance away from the notch. Ultimately, one single crack overtakes the other one which then defines the final fracture path. It is likely that damage initiates at the matrix rich regions between the inner 90° plies as shown in Figure 2.42. Upon increased loading these cracks increase in size and spread into the adjacent 0° plies. This theory is supported by the numerical predictions discussed in chapter III. Off-axis $[+45/-45]_{2S}$ specimens exhibited a single crack originating from the notch tip.

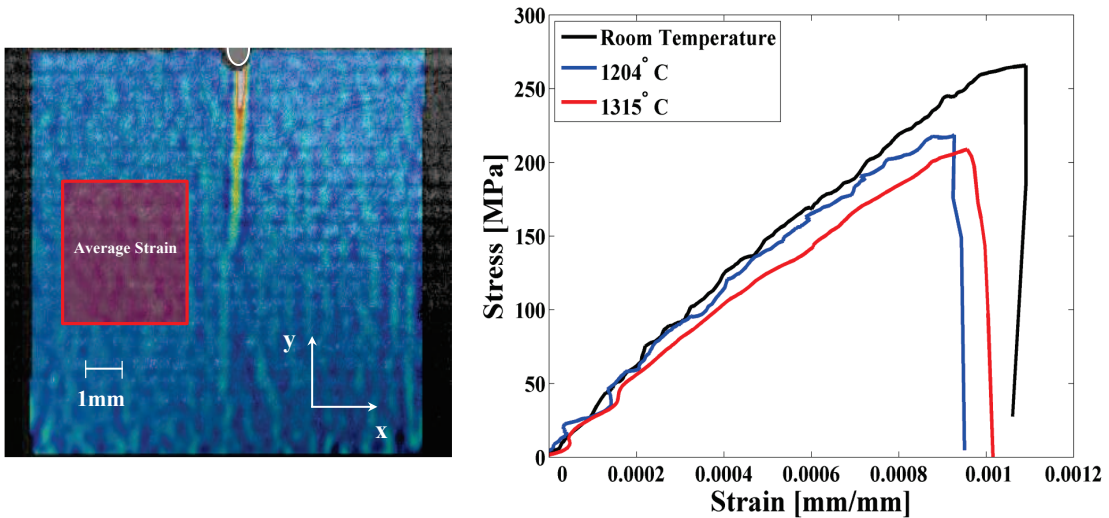


Figure 2.41: Stress-strain response for cross-ply specimens at various temperatures

Selected stress-strain curves at various temperatures of the cross-ply laminates are shown in Figure 2.41. Due to the elevated noise level at temperatures above 1204°C strain measurements based on DIC can contain large outliers.

Table 2.3: Comparison for Young's modulus of $[0/90]_{2S}$ specimens at room temperature, $1204^{\circ}C$, $1316^{\circ}C$

	Room Temperature	$1204^{\circ}C$	$1316^{\circ}C$
Young's Modulus [MPa]	248.3	231.1	204.6

These outliers can be filtered out in most cases and valuable strain data can be computed. CMC materials have the advantage of retaining a high elastic modulus at very high temperatures. Young's modulus calculated from the stress-strain data is shown in figure 2.41 and is given in table 2.3. A slight material softening can be observed with Young's modulus ranging from 290 MPa at room temperature to 210 MPa at $1316^{\circ}C$. This corresponds to a 30% loss of elastic stiffness in the tested temperature domain.

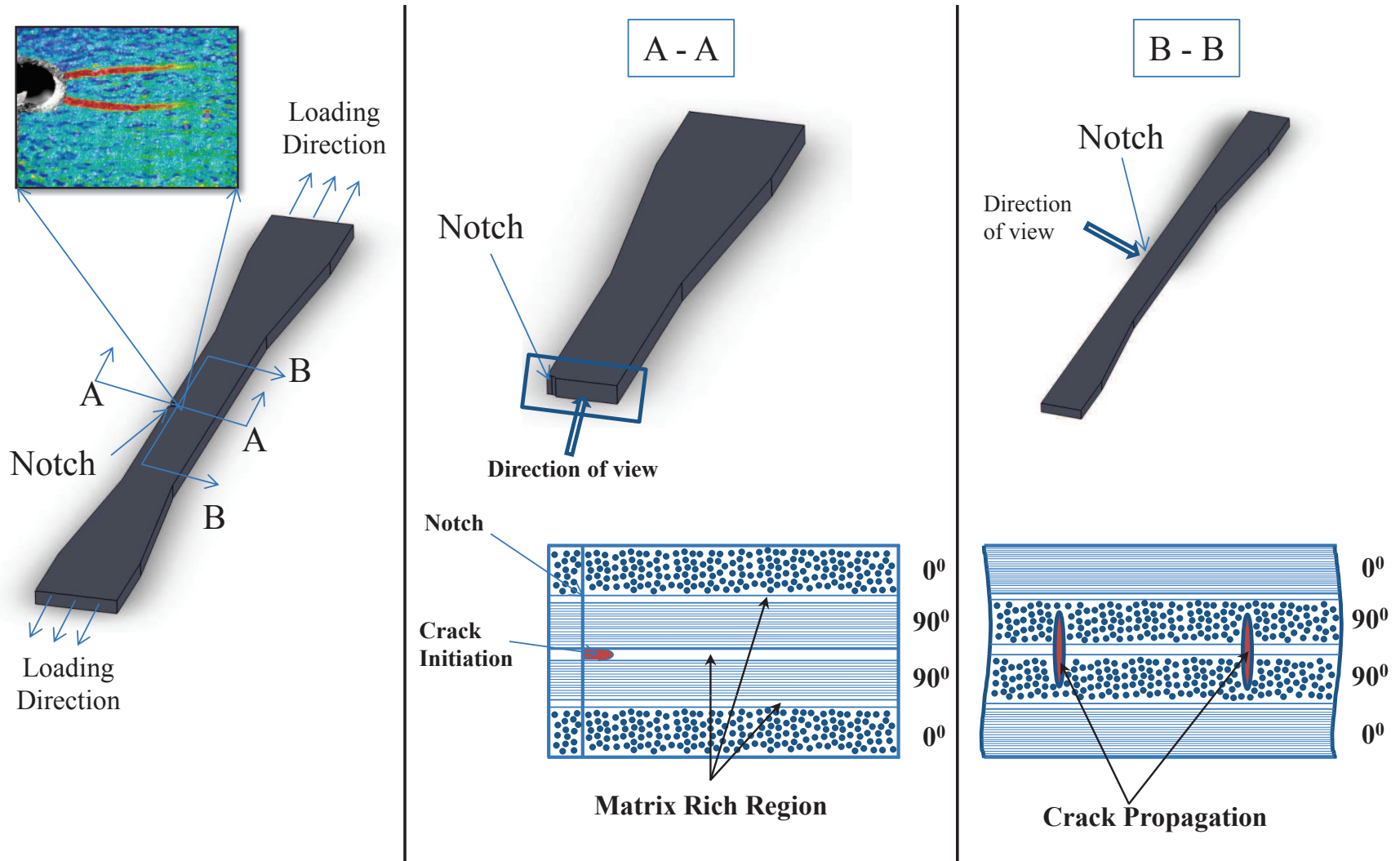


Figure 2.42: Schematic crack propagation in a $[0/90]_S$ single edge notch monotonic tensile test

CHAPTER III

Numerical Model of Micromechanical Failure Mechanisms

3.1 Introduction

In this chapter a crack band failure scheme is introduced for modeling damage on a microstructural scale. Detailed models including fiber-, interface- and matrix materials are developed and crack paths are predicted. It is shown that the component failure behavior is influenced by controlling features at the fiber/matrix level. Transverse cracking of 90° laminae as well as cracking of multi-layer models are shown and discussed. In this thesis the term Representative Volume Element (RVE) is used to describe the smallest entity of the composite selected to represent the correct physics of damage evolution. Thus, the size of the RVE has to be chosen such that multiple damage and failure modes and their interactions are captured.

3.2 Analytical Crack Density Formulations

Traditionally, two groups of analytical modeling approaches can be identified. Strength based models assume that a crack forms when the local stress (or strain) reaches a particular critical value in a ply. Energy based models generally assume the existence of a flaw and that the flaw growth initiates when the energy release rate is

greater or equal to the fracture toughness which is assumed to be a material property. A summary of the most common models can be found in *Talreja and Singh (2012)*. A classic model was developed by *Garret and Bailey (1977)*. They applied the shear lag analysis to cross-ply laminates. They considered the model shown in Fig. 3.1.

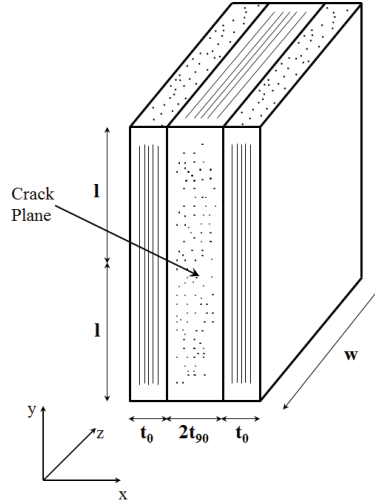


Figure 3.1: Shear Lag Model

The load shed by the transverse (90°) plies in the crack plane and transferred back to the transverse plies over the distance y is given as,

$$F = 2t_0w\Delta\sigma_0[1 - e^{-\beta y}] \quad (3.1)$$

where β^2 is the shear lag parameter,

$$\beta^2 = G_{xz0}^{90} \left[\frac{1}{E_{x0}^{90}} + \frac{1}{\lambda E_{x0}^0} \right] \quad (3.2)$$

where $\lambda = \frac{t_0}{t_{90}}$ is the ply thickness ratio. The transverse ply will fail in tension when

$$F = 2t_{90}w\sigma_{tu} \quad (3.3)$$

where σ_{tu} is the failure stress of a ply in transverse tension and w is the specimen

width. Assuming that the first crack will form in the middle of the specimen length at $\Delta\sigma_0 = \frac{t_{90}}{t_0}\sigma_{tu}$. Next, the cracking process will cause second and third cracks to form simultaneously above and below the first crack. From Eq. 3.1 and Eq. 3.3 with $y = l$ where $2l$ is the crack spacing, $\Delta\sigma_0$ will be

$$\Delta\sigma_0 = \frac{1}{\lambda} \frac{\sigma_{tu}}{1 - e^{-\beta l}} \quad (3.4)$$

These cracks will perturb the force transferred such that the new cracking process will occur at.

$$\Delta\sigma_0 = \frac{1}{\lambda} \frac{\sigma_{tu}}{1 + e^{-\beta l} - 2e^{-\beta l/2}} \quad (3.5)$$

Similarly the $(N + 2)$ th crack formation will occur when,

$$\Delta\sigma_0 = \frac{1}{\lambda} \frac{\sigma_{tu}}{1 + e^{-\frac{\beta l}{N}} - 2e^{-\frac{\beta l}{2N}}} \quad (3.6)$$

The cracking sequence assumed in this model is shown in figure 3.2.

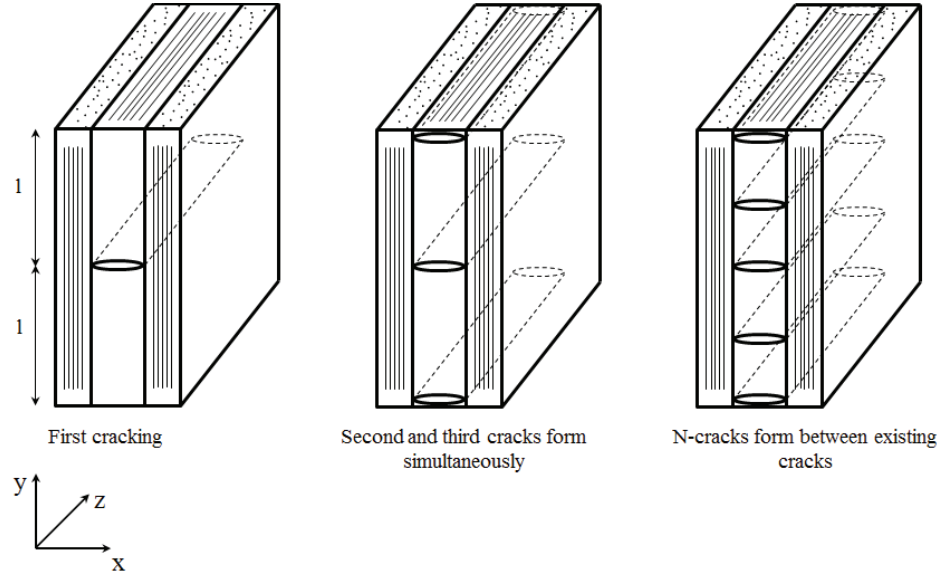


Figure 3.2: Shear Lag Cracking Sequence

This model predicts the general trends but underestimates the average crack spac-

ing. Furthermore, the model assumes uniform crack spacing.

Laws and Dvorak (1988) predicted progressive ply cracking using an energy based analysis. The authors calculated the released energy during cracking as,

$$\Delta\Gamma = \frac{2t_{90}^2 whE_c}{\beta t_0 E_{x0}^0 E_{x0}^{90}} \left(\sigma_{xxR}^{90} + \frac{E_{x0}^{90}}{E_{x0}^0} \sigma_c \right)^2 \left[\tanh \frac{\beta l_1}{2t_{90}} + \tanh \frac{\beta l_2}{2t_{90}} - \tanh \frac{\beta l}{2t_{90}} \right] \quad (3.7)$$

where β is the shear lag parameter. A new crack will form if

$$\frac{t_{90} h E_c}{\beta t_0 E_{x0}^0 E_{x0}^{90}} \left(\sigma_{xxR}^{90} + \frac{E_{x0}^{90}}{E_{x0}^0} \sigma_c \right)^2 \left[\tanh \frac{\beta l_1}{2t_{90}} + \tanh \frac{\beta l_2}{2t_{90}} - \tanh \frac{\beta l}{2t_{90}} \right] \geq \gamma \quad (3.8)$$

Equation 3.8 yields the first-ply fracture stress for the limiting case $\lim_{l \rightarrow \infty}$

$$\sigma_c^{fpf} = \left(\frac{\beta E_{x0}^0 E_c \gamma}{t_{90} h E_{x0}^{90}} \right)^{1/2} - \frac{E_c}{E_{x0}^{90}} \sigma_{xxR}^{90} \quad (3.9)$$

Laws & Dvorak regard the first ply fracture stress as experimentally measurable and therefore determined the shear lag parameter from equation 3.9.

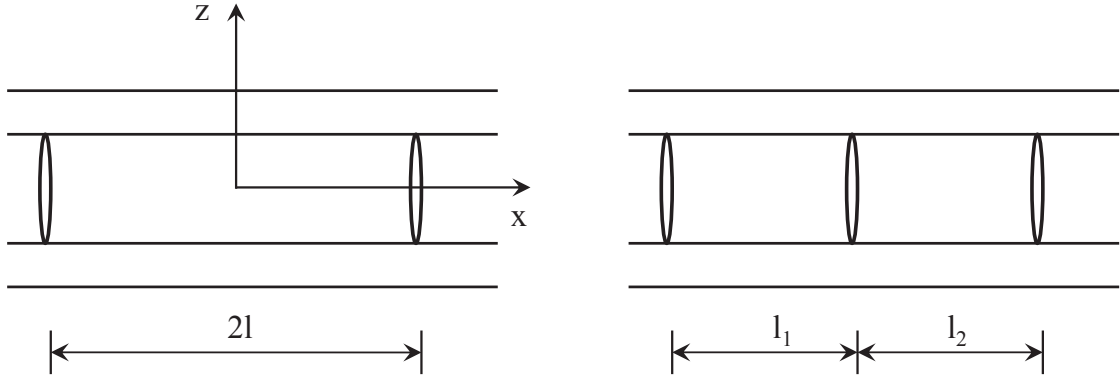


Figure 3.3: Laws & Dvorak progressive failure; New crack occurs inbetween two existing cracks

Once the shear lag parameter is known the critical applied stress that causes cracking at a new location can be determined from equation 3.8. Assuming that two cracks already exist in the material, the onset stress for additional cracking can be

calculated as

$$\sigma_c(\rho_c) = \int_0^{2l} p(x)\sigma_c(x)dx \quad (3.10)$$

Assuming that the next crack occurs midway between two existing cracks as shown in figure 3.3

$$p(x) = \delta(x - l) \quad (3.11)$$

the solution to equation 3.10 can be found as

$$E[\sigma_c(\rho_c)] = \left(\sigma^{fpf} + \frac{E_c}{E_{x0}^{90}} \sigma_{xxR}^{90} \right) \left[2 \tanh \frac{\beta}{2\rho_c} - \tanh \frac{\beta}{\rho_c} \right]^{-1/2} - \frac{E_c}{E_{x0}^{90}} \sigma_{xxR}^{90} \quad (3.12)$$

Nairn (1989) used the variational approach for cracked cross-ply laminates in conjunction with the energy release rate criterion to predict crack densities in cracked cross-ply laminates. He considered sections of the $[0_m^{\circ}/90_n^{\circ}]_S$ and the $[90_m^{\circ}/0_n^{\circ}]_S$ laminates as shown in Fig. 3.4. The load, σ_0 , is an axial load applied parallel to the fibers.

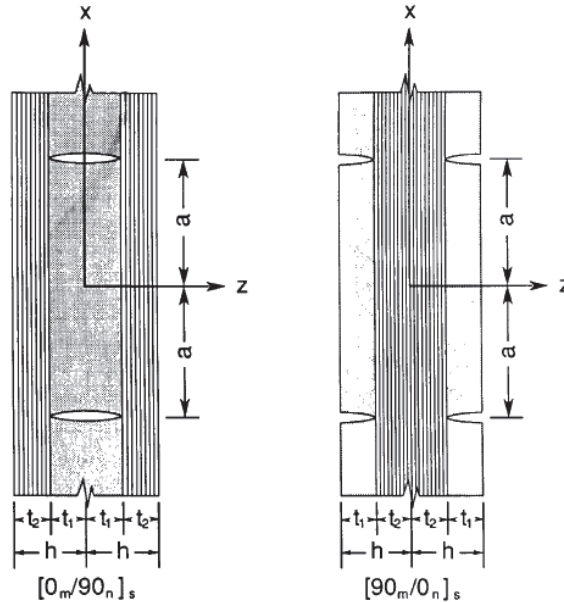


Figure 3.4: Model details used to analyze $[0_m^{\circ}/90_n^{\circ}]_S$ and $[90_m^{\circ}/0_n^{\circ}]_S$ composites (*Nairn* (1989))

Nairn's fracture criterion for $[0_n/90_m]$ laminates is,

$$G_m = \left(\sigma_c^2 \frac{E_2^2}{E_c^2} + \frac{\Delta\alpha T^2}{C_{00}^2} \right) t_{90} C_{22} [2\chi(\rho/2) - \chi(\rho)] \quad (3.13)$$

with,

$$\chi(\rho_n) = 2\alpha_1\alpha_2(\alpha_1^2 + \alpha_2^2) \frac{\cosh(2\alpha_1\rho_n) - \cos(2\alpha_2\rho_n)}{\alpha_1 \sin(2\alpha_2\rho_n) + \alpha_2 \sinh(2\alpha_1\rho_n)} \quad (3.14)$$

where $\rho_n = l_n/t_{90}$ is the normalized crack spacing. In equation 3.13 G_m is the matrix fracture toughness which he suggested could be determined through fitting experimental data for ply cracking. The material parameters are calculated as

$$\begin{aligned} \alpha &= q^{\frac{1}{4}} \cos\left(\frac{\theta}{2}\right) \\ \beta &= q^{\frac{1}{4}} \sin\left(\frac{\theta}{2}\right) \\ q &= \frac{C_{00}}{C_{22}} \\ p &= \frac{C_{02} - C_{11}}{C_{22}} \\ \theta &= \tan^{-1} \left(\sqrt{\frac{4q}{p^2} - 1} \right) \\ C_{00} &= \left(\frac{1}{E_2} \right) + \left(\frac{1}{\lambda E_1} \right) \\ C_{11} &= \frac{1}{3} \left(\frac{1}{G_T} + \frac{1}{\lambda G_A} \right) \\ C_{02} &= \frac{\nu_T}{E_T} \left(\lambda + \frac{2}{3} \right) - \frac{\nu_A}{3E_A} \lambda \\ C_{22} &= (\lambda + 1)(3\lambda^2 + 12\lambda + 8) \end{aligned} \quad (3.15)$$

This formulation can be adjusted for a probabilistic crack formation. Fig. 3.5 shows the formation of new microcracks. For cracking in $[90_m/0_n]$ laminates, the expressions for energy release rate remain the same except that the constant C_{22} is now given by $C_{22} = (\lambda + 1)(3 + 12\lambda + 8\lambda^2)$.

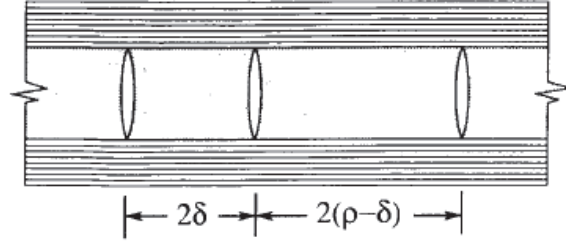


Figure 3.5: The formation of a new microcrack 2δ dimensionless units above the bottom microcrack of a pair of microcracks separated by 2ρ dimensionless units *Nairn* (1989)

Nairn's predictions showed good agreement with experiments when the critical energy release rate for matrix cracking was deduced from test data rather than evaluated independently.

3.3 Post-Peak Strain Softening Formulation - Crack Band

As could be seen in chapter 2.3, SiC/SiC ceramic matrix composites show large deviation from linear stress-strain relation in the performed monotonic tensile tests. This strain-softening is the result of formation of micro-cracks in the matrix material. Many techniques have been used by authors in the past to estimate microcracking. The smeared crack approach has been used by *Heinrich and Waas* (2013) to predict cracking of polymer matrix composites with various lay-ups. *Pineda et al.* (2013) used the crack band method in a multi-scale scheme based on the generalized method of cells. In the context of this work, the same differentiation between damage and failure as defined by *Pineda et al.* (2013) is used. Damage denotes the release of energy due to microcracking. It is the regime between the critical strain ϵ_{cr} and the maximum strain ϵ_f . Microcracking starts at ϵ_{cr} and a clean separation of surfaces occurs at ϵ_f . Failure denotes the post-peak regime after all energy has been released resulting in a total loss of secant stiffness. This regime occurs for $\epsilon > \epsilon_{cr}$. Loss of positive-definiteness of the tangent stiffness tensor leads to a material instability, which manifests as a localization of damage into the smallest length scale in the continuum problem

[*Bažant and Cedolin (1991)*]. In order to satisfy numerical stability the failure secant stiffness is set to $E_{secant} = 0.0001$.

In this chapter, we restrict attention to Mode I cracks, i. e., cracks (straight or curved) which have no shear stress at their front. This does not detract much from practical usefulness since cracks in CMCs seem to propagate in most situations along the direction that are perpendicular to the maximum principle strain direction in which Mode I prevails at the front. In finite element analysis damage initiation, e.g. entering the traction-separation law, is based on a simple but physical criterion:

$$\frac{\epsilon'}{\epsilon_{cr}} = 1 \quad (3.16)$$

where ϵ' is the maximum principle strain, ϵ_{cr} is the strain to initiate damage in the material and assumed to be a material parameter. The crack-band failure method falls into the category of smeared failure approaches. Cracks are not explicitly modeled inside an element but rather incorporated in the element constitutive law. After damage has been initiated, the stiffness perpendicular to the crack, e.g. in maximum principle strain direction, is reduced according to a traction separation law. The stiffness in the local crack direction is assumed to be unaffected. As a result a previously isotropic element becomes orthotropic after damage initiation. Once a crack has been initiated, the crack band orientation is fixed. The crack normal is aligned with the maximum principle strain direction. In most numerical applications, the secant stiffness in maximum principle direction is chosen such that the traction will follow the curve of the traction separation law shown in figure 3.6b. In this work a triangular traction-separation law is employed. The area under the curve corresponds to the mode I fracture toughness (G_{IC}) of the material. Objectivity with respect to the discretization size of the microscale model is achieved through introduction of a characteristic element length as further discussed in chapter 3.3.1. It is assumed that

the total element strain can be written as

$$\epsilon = \epsilon_{cont} + \epsilon_{cr} \quad (3.17)$$

where ϵ_{cont} represents the continuum strain of the element and ϵ_{cr} represents the additional "effective" strain due to cracking. The strain is a result of the crack opening normalized by the length, residing within the element and normal to the crack plane. This is shown schematically in figure 3.6a. One can rewrite equation 3.17 for an isotropic material in the principal frame as,

$$\begin{Bmatrix} \epsilon_{11} \\ \epsilon_{22} \\ \epsilon_{33} \end{Bmatrix} = \begin{bmatrix} \frac{1}{E} & \frac{-\nu}{E} & \frac{-\nu}{E} \\ \frac{-\nu}{E} & \frac{1}{E} & \frac{-\nu}{E} \\ \frac{-\nu}{E} & \frac{-\nu}{E} & \frac{1}{E} \end{bmatrix} \begin{Bmatrix} \sigma_{11} \\ \sigma_{22} \\ \sigma_{33} \end{Bmatrix} + \begin{Bmatrix} \epsilon_{nn}^{cr} \\ 0 \\ 0 \end{Bmatrix} \quad (3.18)$$

It is assumed that the continuum part and the crack part are in an iso-stress state and can be thought of as two springs in series. This leads to the condition

$$\sigma_{nn} = \sigma_{11} \quad (3.19)$$

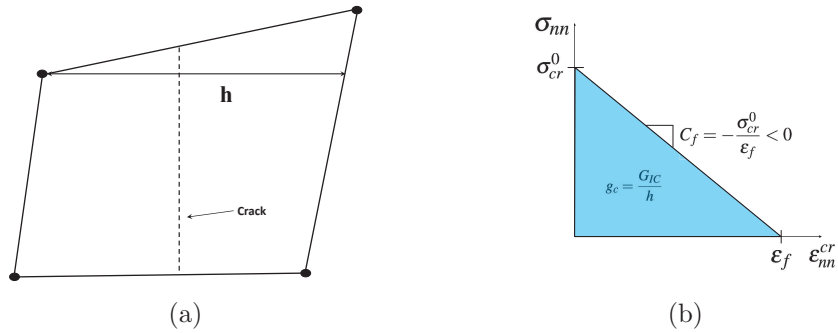


Figure 3.6: a) Characteristic element length b) crack-band traction separation law

The crack strain can be calculated from the traction-separation law (Figure 3.6b),

$$\epsilon_{nn}^{cr} = \epsilon_F + \frac{\sigma_{11}}{C_f} \quad (3.20)$$

Substituting equation 3.20 into equation 3.18 leads to

$$\begin{Bmatrix} \epsilon_{11} - \epsilon_f \\ \epsilon_{22} \\ \epsilon_{33} \end{Bmatrix} = \begin{bmatrix} \frac{1}{E} + \frac{1}{C_f} & \frac{-\nu}{E} & \frac{-\nu}{E} \\ \frac{-\nu}{E} & \frac{1}{E} & \frac{-\nu}{E} \\ \frac{-\nu}{E} & \frac{-\nu}{E} & \frac{1}{E} \end{bmatrix} \begin{Bmatrix} \sigma_{11} \\ \sigma_{22} \\ \sigma_{33} \end{Bmatrix} + \begin{Bmatrix} \epsilon_{nn}^{cr} \\ 0 \\ 0 \end{Bmatrix} \quad (3.21)$$

Next, the element continuum stress-strain curve can be combined with the traction-effective strain law as shown in figure 3.7. σ_{11} and ϵ_{11} are written in the local crack coordinate system. E denotes the undamaged Young's modulus in the principle frame. A fracture variable D is introduced which corresponds to zero if damage has not initiated. D equals to one if ϵ_{11} exceeds ϵ_f . When $\epsilon_{11} > \epsilon_f$ the element has failed catastrophically and no load can be transferred normal to the crack direction.

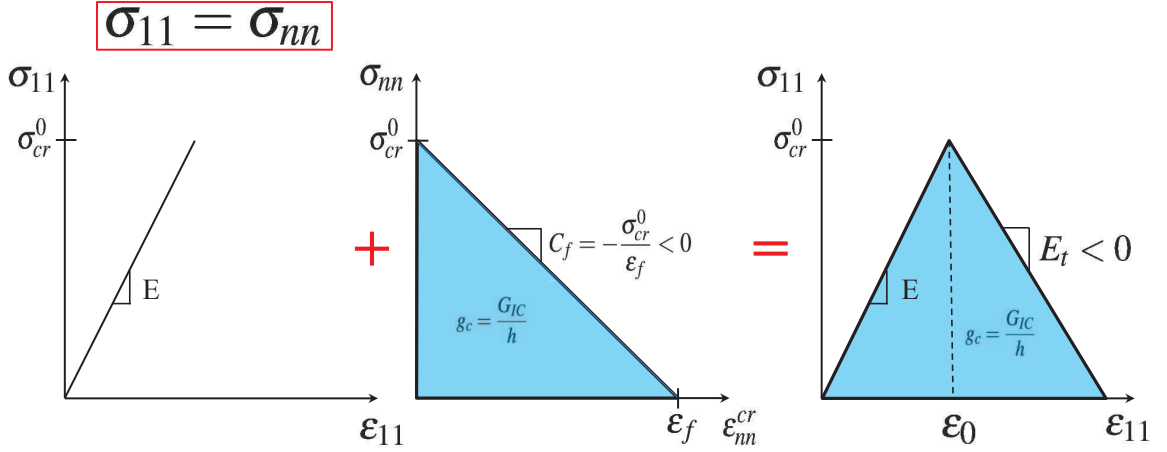


Figure 3.7: Joining Element Continuum Stress-Strain law with Traction-Separation law

The total stress-strain law in the principal frame can be rewritten as,

$$\begin{Bmatrix} \epsilon_{11} - \epsilon_f \\ \epsilon_{22} \\ \epsilon_{33} \end{Bmatrix} = \begin{bmatrix} \frac{1}{(1-D)E} & \frac{-\nu}{E} & \frac{-\nu}{E} \\ \frac{-\nu}{E} & \frac{1}{E} & \frac{-\nu}{E} \\ \frac{-\nu}{E} & \frac{-\nu}{E} & \frac{1}{E} \end{bmatrix} \begin{Bmatrix} \sigma_{11} \\ \sigma_{22} \\ \sigma_{33} \end{Bmatrix} \quad (3.22)$$

The damage parameter D can be determined from the stress-strain relation in Figure 3.7.

$$E_t = \frac{\sigma_{cr}^0}{\epsilon_0 - \epsilon_f} \quad (3.23)$$

and

$$(1 - D)E = \frac{E_t(\epsilon_{11} - \epsilon_f)}{\epsilon_{11}} \quad (3.24)$$

Using equations 3.23 and 3.24 the failure parameter D can be calculated as

$$D = 1 - \frac{\sigma_{cr}^0}{\epsilon_f - \epsilon_0 E} \left(\frac{\epsilon_f}{\epsilon_{11}} - 1 \right) \quad (3.25)$$

It is assumed that only the normal and shear directions at the crack interface are traction free. Therefore, the entries S_{11} , S_{55} , and S_{66} of the compliance matrix in the principle frame are affected and will be degraded.

$$[S] = \begin{bmatrix} \frac{S_{1111}}{(1-D)} & S_{1122} & S_{1133} & & & \\ S_{1122} & S_{2222} & S_{2233} & & & \\ S_{1133} & S_{2233} & S_{3333} & & & \\ 0 & 0 & 0 & S_{2323} & 0 & 0 \\ 0 & 0 & 0 & 0 & \frac{S_{1313}}{(1-D)} & 0 \\ 0 & 0 & 0 & 0 & 0 & \frac{S_{1212}}{(1-D)} \end{bmatrix} \quad (3.26)$$

Finally, the degraded compliance matrix has to be transformed back into the global

x-,y-,z-coordinate system.

$$[S] = [T]^{-1}[S][T^T]^{-1} \quad (3.27)$$

3.3.1 Characteristic Length Scale

Bažant (1983) introduced a characteristic length based on material elastic and fracture properties. Independent of the element size the released energy due to damage in a particular finite element needs to be preserved. Satisfying the restriction of the mesh size guaranties a mesh objective simulation as will be shown in chapter 3.3.2. As can be seen in figure 3.7 the strain softening modulus E_t must be negative. Therefore, the following equation holds true

$$\frac{1}{E_t} = \frac{1}{E} + \frac{1}{C_f} \leq 0 \quad (3.28)$$

C_f can be replaced by $\sigma_{cr}^0/\epsilon f$ and thus equation 3.28 can be rewritten as

$$\frac{1}{E} - \frac{2G_{IC}}{h\sigma_{cr}^2} \leq 0 \quad (3.29)$$

This condition leads to a maximum characteristic finite element length of

$$h \leq \frac{2EG_{IC}}{\sigma_{cr}^2} \quad (3.30)$$

As *Bažant* (1983) noted h should be smaller but at least half of that value in practical FEM problems. The limiting case is given by $E_t^{-1} = 0$ which corresponds to a sudden drop in the stress-strain response.

3.3.2 Objectivity with Respect to Discretization Size

Smearred crack damage models were developed with the intention of introducing mesh independence into finite element damage evolution methods. As mentioned

above, section 3.3.1, the characteristic length, h is introduced to effectively scale the dissipated energy. Four mesh sizes were studied for two different models in order to establish mesh objectivity. Model A has square dimensions with a side length of 0.001 mm. Displacement boundary conditions were used with simple supports on the left edge and an applied monotonic tensile displacement of 0.0015 mm on the right edge as shown in Figure 3.8.

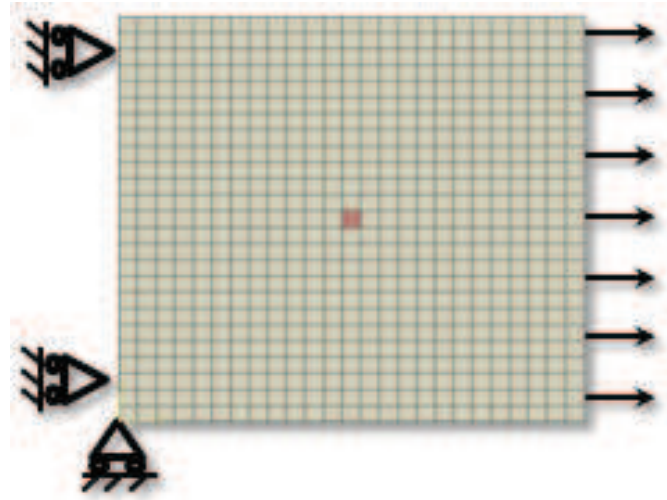


Figure 3.8: Boundary conditions for square mesh objectivity study; Red element was given a 10 % lower strain to failure value

The discretization size of the model ranged from: 25 elements x 25 elements, 35 elements x 35 elements, 45 elements x 45 elements, and 65 elements x 65 elements. The bottom left corner was also restricted to move in vertical direction to avoid rigid body movement. In order to not trigger failure based on numerical inaccuracies the center element in all models was assigned a 10 % lower strain to failure value compared to all other elements. It should be mentioned that a material inhomogeneity is not required for models with stress gradients caused by geometrical features, such as fibers or notches. Table 3.1 gives an overview of the elastic and fracture properties.

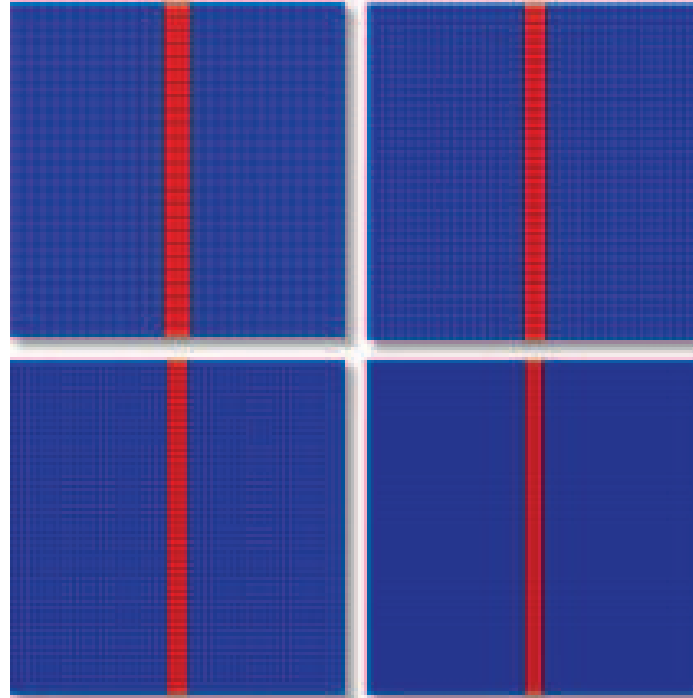


Figure 3.9: Crack path of square model for four distinct mesh sizes

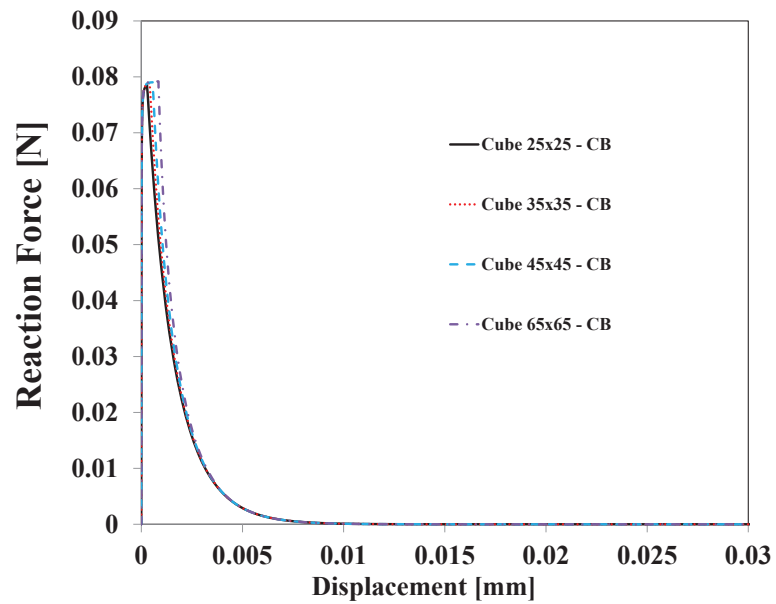


Figure 3.10: Load P vs. Displacement of square model for four distinct mesh sizes

As can be seen in Figure 3.9 the crack path is identical in all four meshes. The crack width can not be identical due to the intrinsic property of smeared crack schemes to localize failure within an element. The resulting load P in x-direction is plotted

against the applied displacement in Figure 3.10. A marginal difference between the discretization sizes due to more refined stress gradients is to be expected. It is evident that the post-peak dissipated energy does not depend on the level of model refinement.

Table 3.1: Material properties used in mesh objectivity study

Property	Value
E (N/mm^2)	3700
ν	0.35
ϵ_{cr}	0.01216
G_{IC} (N/mm)	0.075

A second dogbone shape model was created to further examine mesh objectivity for other geometrical shapes. The mesh sizes were chosen to be: 25 elements x 85 elements, 35 elements x 95 elements, 45 elements x 105 elements, and 75 elements x 135 elements. Displacement boundary conditions were used with simple supports on the left edge and an applied monotonic tensile displacement of 0.004 mm on the right edge as shown in figure 3.11.

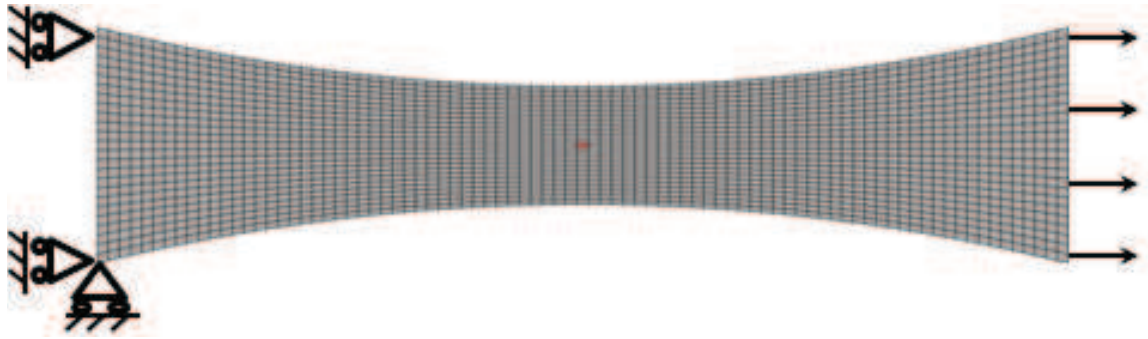


Figure 3.11: Boundary conditions for dogbone shape mesh objectivity study; Red element was given a 10 % lower strain to failure value

Material properties are given in table 3.1. As before, a 10 % lower strain to failure value was assigned to the center element. The left bottom corner was restricted from movement in the vertical direction to avoid rigid body movement. The crack propagation was not further controlled and followed the direction perpendicular to

the maximum principle strain direction. The crack paths are given in figure 3.12. As can be seen in figure 3.13, the Load versus Displacement response of the four meshes match each other and therefore objectivity with respect to the discretization size is demonstrated.



Figure 3.12: Crack path of dogbone shape model of four distinct mesh sizes

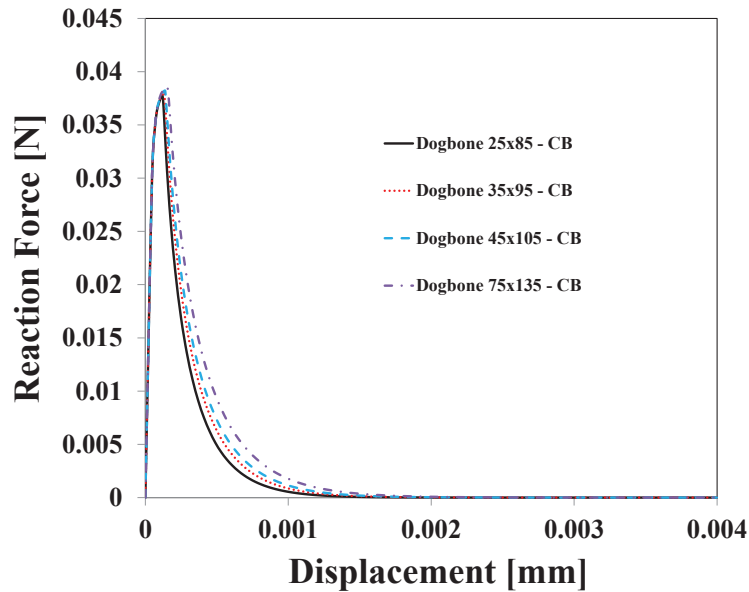


Figure 3.13: Load P vs. displacement of dogbone shape model of four distinct mesh sizes

3.4 Crack Band for Interlaminar Failure

Several methods have been developed in recent years to predict interlaminar failure. *Xie and Waas* (2006) developed the discrete cohesive zone model (DCZM) within

a finite element environment, based on prior work by *Song and Waas* (1993). The authors implemented a special element and showed that crack initiation and growth could be captured. DCZM elements, in general, are mixed-mode elements. However, the use of DCZM elements require that the the crack path be known a-priori and is modeled explicitly. *Heinrich and Waas* (2013) used the smeared crack approach (SCA) to describe post-peak softening in composite materials. They compared numerical predictions to a linear elastic fracture mechanics analysis. The crack-band model used in this work is related to the SCA. However, the crack-band model is currently only implemented for mode I fracture. Hence, the technique in the current form can only be used to model normal crack opening as is present in a typical double cantilever beam test as described next.

3.4.1 Double Cantilever Beam Simulation

Heinrich and Waas (2013) compared finite element predictions of a double cantilever beam (DCB) to the analytical linear elastic fracture mechanics (LEFM) solution. The crack-band method, in a slightly modified form, will be used to predict the mode I fracture of the same model. It is assumed that the thickness of the interlaminar layer is very small ($\leq 10 * t_{beam}$) compared to the beam thickness. Hence, if a crack occurs in the the adhesive layer it is assumed that the compliance in all directions is affected as shown in equation 3.31,

$$[S] = \frac{1}{(1 - D)} \begin{bmatrix} S_{1111} & S_{1122} & S_{1133} & & & \\ S_{1122} & S_{2222} & S_{2233} & & & \\ S_{1133} & S_{2233} & S_{3333} & & & \\ 0 & 0 & 0 & S_{2323} & 0 & 0 \\ 0 & 0 & 0 & 0 & S_{1313} & 0 \\ 0 & 0 & 0 & 0 & 0 & S_{1212} \end{bmatrix} \quad (3.31)$$

No rotation of the compliance matrix is required in this case since there is no directional dependence. For this discussion and better comparability to the LEFM solution, a maximum principle stress criterion is used. A summary of the model geometry is given in figure 3.14. Elastic and fracture material properties are given in table 3.2.

Table 3.2: Material properties used in mesh objectivity study

Beam	
Young's Modulus E	70 GPa
Poisson's ratio ν	0.3
Adhesive	
Mode I Energy Release Rate G_{IC}	7.48 (N/mm)
Critical Stress	503 MPa

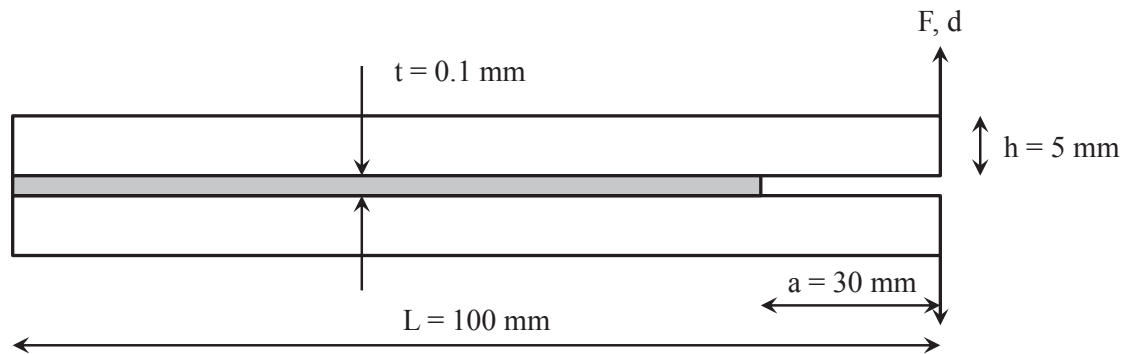


Figure 3.14: DCB Specimen Geometry

Analytically, the applied force at the ends of the beam can be calculated as

$$F = \sqrt{\frac{G_{IC}EIb}{a^2}} \quad (3.32)$$

where G_{IC} is the fracture toughness, E is Young's Modulus, I is the area moment of inertia, b is the beam width, and a is the crack length. The crack length of the FEM

predictions can be computed as

$$a = \sqrt[3]{\frac{3\delta EI}{F}} \quad (3.33)$$

A comparison of the analytical and numerical solution is given in figure 3.15. The FEM predictions show initially higher loads. Both curves approach each other for increasing crack lengths. These results confirm that the crack-band method is well suited for mode I dominant interlaminar fracture problems. Future work should include a multitude of comparisons.

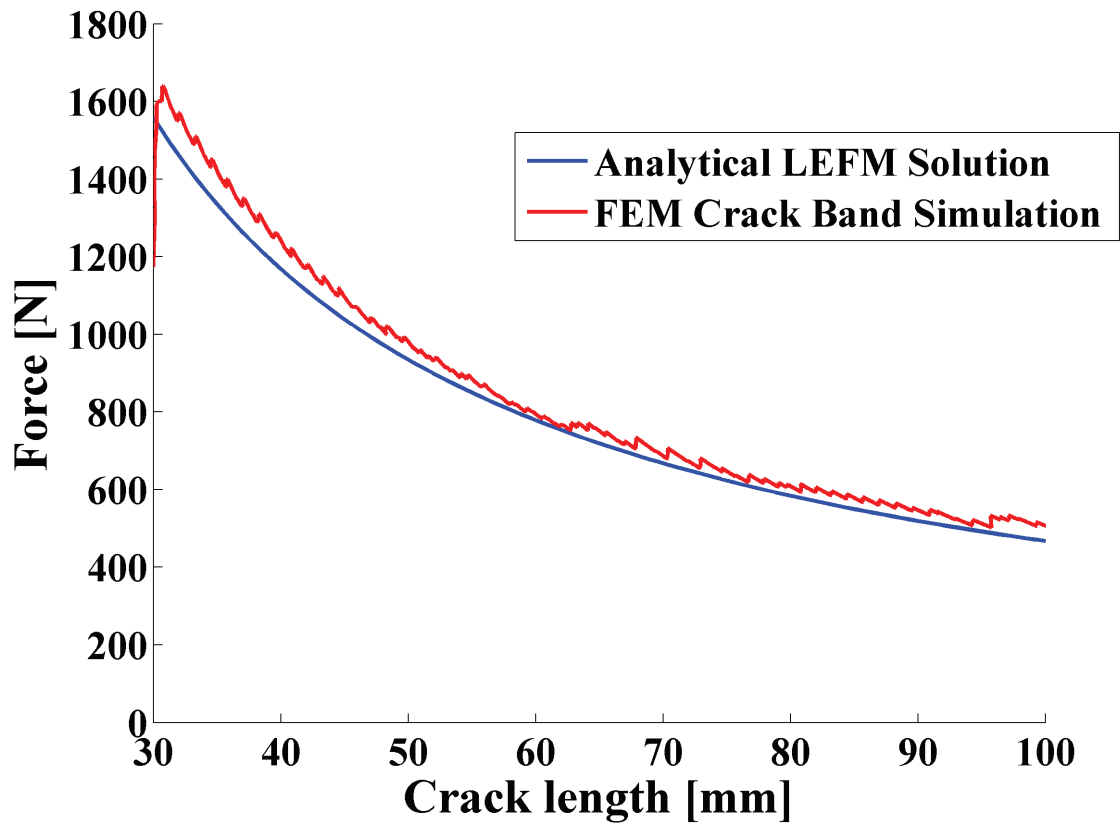


Figure 3.15: Load vs. Displacement comparison of LEFM solution and crack band of a DCB test

3.5 Transverse Cracking of CMCs under Tensile Loading

In the past, a single fiber surrounded by matrix material with a fiber volume fraction matching that of the lamina was often used (*Berger et al. (2005)*, *Mahmoodia and Aghdamb (2011)*). Structured RUCs with 2-4 fibers in a hexagonal or square array were investigated by *Shoukry et al. (2007)*. The representative unit cell plays a central role in the mechanics and physics of random heterogeneous materials with a view to predicting their effective properties, damage initiation and crack propagation. Many researchers have investigated the effects of the size of the RUC (*Dal Corso and Deseri (2013)*, *Gusev (1997)*, *Soni et al. (2014)*, *Drugan and Willis (1996)*). *Kanit et al. (2003)* showed that a bias in the estimation of the effective properties is observed for too small volumes for all types of boundary conditions. *Totry et al. (2008)* predicted the mechanical response of a composite lamina made up of PEEK matrix unidirectionally reinforced with 60 vol% C fibers subjected to transverse compression and longitudinal shear using computational micromechanics. The authors showed that the failure locus given by the envelope of the loading curves under different biaxial loading conditions was in excellent agreement with the experimental results. *Heinrich et al. (2012)* investigated the influence of fiber packing and RVE size on the residual stresses created during the curing process of the epoxy matrix material. They concluded that at least 25 fibers should be used for the numerical damage and failure predictions. It was found that average values can be used for stiffness predictions. In the present work, the crack band method is used to investigate the behavior of a ceramic matrix composite representative volume element (RVE) under monotonic transverse tensile loading. The RVE size is chosen such that at least 40 fibers are modeled.

3.6 Random Fiber Orientation within RUC

Fiber volume fractions in CMCs tend to be in the range between 15 – 30%. These low volume fractions result in large variations in distribution of fibers within a lamina. These geometrical inhomogeneities affect the performance of the composite material. Fiber clustering can serve as local stress risers which might lead to pre-mature matrix cracking. In addition, non-uniform fiber coatings, resulting from poor control during the manufacturing process, affect the stress and strain fields in the surrounding matrix material. In order to investigate the influence of geometric inhomogeneities, micromechanics models were developed and the Crack-Band methodology was used to identify microstructural features that support pre-mature matrix damage.

This subsection is divided into two parts. Chapter 3.6.1 shows the influence of fiber-coating packing on damage propagation under transverse loading conditions. Multiple randomly generated microstructures are compared and features that cause local damage are identified. Chapter 3.6.3 uses a large scale model to predict the behavior of cross-ply laminates. It captures multiple transverse cracks and shows differences between $[0/90]_{2S}$ and $[90/0]_{2S}$ laminates. A four layer model is used to predict crack spacing and a comparison is drawn with analytical models.

3.6.1 Influence of Fiber-Interface Packing on Crack Initiation

In order to model realistic features a model based on the real microstructure is needed. Automated model generation based on micrographs is inherently difficult for CMCs due to the low contrast between the main constituent materials. In this work a Matlab script was developed to manually fit circles to fibers and interfaces of a micrograph. The total size of the micrograph and the locations of the fiber- and interface coordinates within the micrograph was stored in a text file. This information was then used in a python script that automatically generated an Abaqus model. This technique allowed a simple solution for generating realistic models.

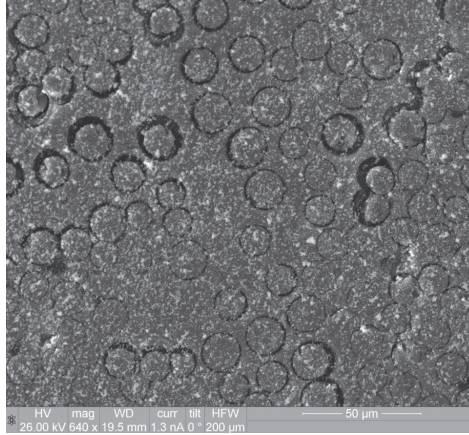


Figure 3.16: Micrograph of CMC microstructure (White particles are artificial speckle pattern and not part of the CMC material)

In addition, a second Matlab script was developed to randomly re-orient the fibers within the RVE. Following, each micrograph model and its random variations will be denoted as representative volume elements (RVE's). The Matlab script allows the definition of minimum fiber distances and included a code to simulate fiber clustering. Randomly placed artificial fibers, which are not included in the FEM model, are inserted during the randomization process. The space occupied by these fibers cannot be taken by real fibers and therefore clustering occurs. If the minimum distance between fibers was set to be larger than zero, no fibers were allowed to interfere with each other. Coatings on the other hand were always allowed to interfere with each other. This is often observed in CMCs, as can be seen in Figure 3.16. White particles were added to the surface for DIC measurement purposes and are not part of the CMC material. Large variations in coating thickness and random orientation of the fibers within the transverse ply can be observed. Figure 3.17 shows an overlay of the Abaqus model over the micrograph.

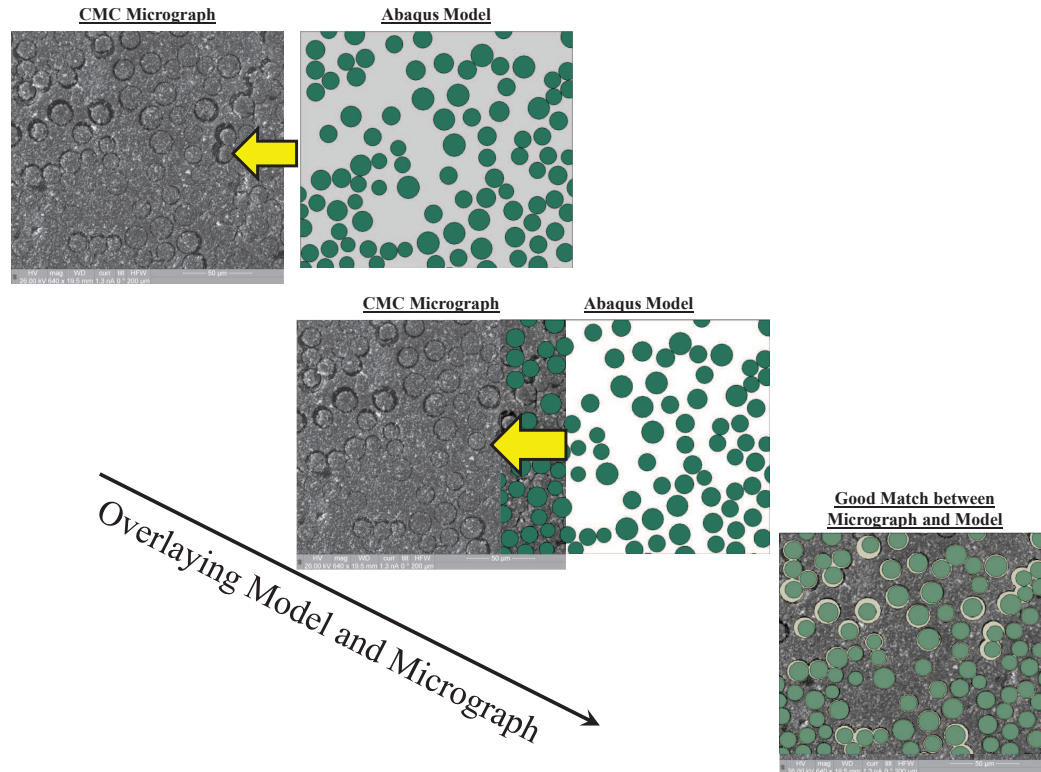


Figure 3.17: Model and Microstructure Overlay (Matrix has been removed from the model for better visibility)

The matrix material has been removed from the model plot to allow the observation of the fiber and interface locations of the model compared to the microstructure. A good match between the model and the micrograph is apparent. A second model was created with the same technique. These two models will be used as the baseline models in the following comparisons. The volume fractions of the two baseline models as well as the randomly created models range between, 19-21 vol % fibers, 9-10 vol % interface, and 70-73 vol % matrix. Random models were created and the crack-band user subroutines were used in Abaqus to predict the damage behavior of each RVE. Plane strain elements (CPE in Abaqus) were used. On average, the models consisted of 90,000 degrees of freedom. In this study, the RVE does not represent a repeating unit of the microstructure. Hence, simple transverse tension boundary conditions were chosen over periodic boundary conditions. A positive transverse displacement,

u_x , was applied on the edge X_1 of all models as shown in figure 3.18. Edges Y_0 and Y_1 are traction free and Corner X_0 - Y_0 was constrained in y -direction to avoid rigid body movement. Ultimate load, post-peak behavior, and crack paths are dependent on the location of the fibers as can be seen from Figures 3.23 and 3.24, respectively.

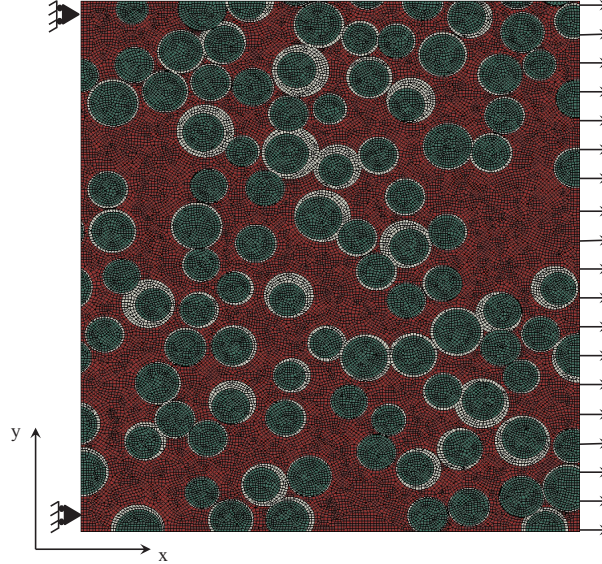


Figure 3.18: Boundary conditions of microstructure models

Further investigation of the crack initiation sites revealed that damage in all RVE's initiated around fiber clusters with thick coatings. Typically, damage initiates at the top or bottom of the matrix surrounding a fiber. The BN coating is compliant compared to the fiber and matrix. The elastic and fracture constituent properties are given in table 3.3. Figures 3.19 - 3.21 depict damage in three different RVE's. The

Table 3.3: Constituent elastic and fracture properties

Material	Young's Modulus (MPa)	Poisson's Ratio ν	Critical Stress σ_{cr} (MPa)	Fracture Toughness G_{IC} (N/mm)
Matrix	340000	0.14	200	0.05
Coating	10000	0.19	200	0.05
Fiber	380000	0.14	2600	0.005

crack path has been rendered with a black line for better visibility. Upon damage initiation a redistribution of the current stress field occurs which can lead to new

damage initiation sites.

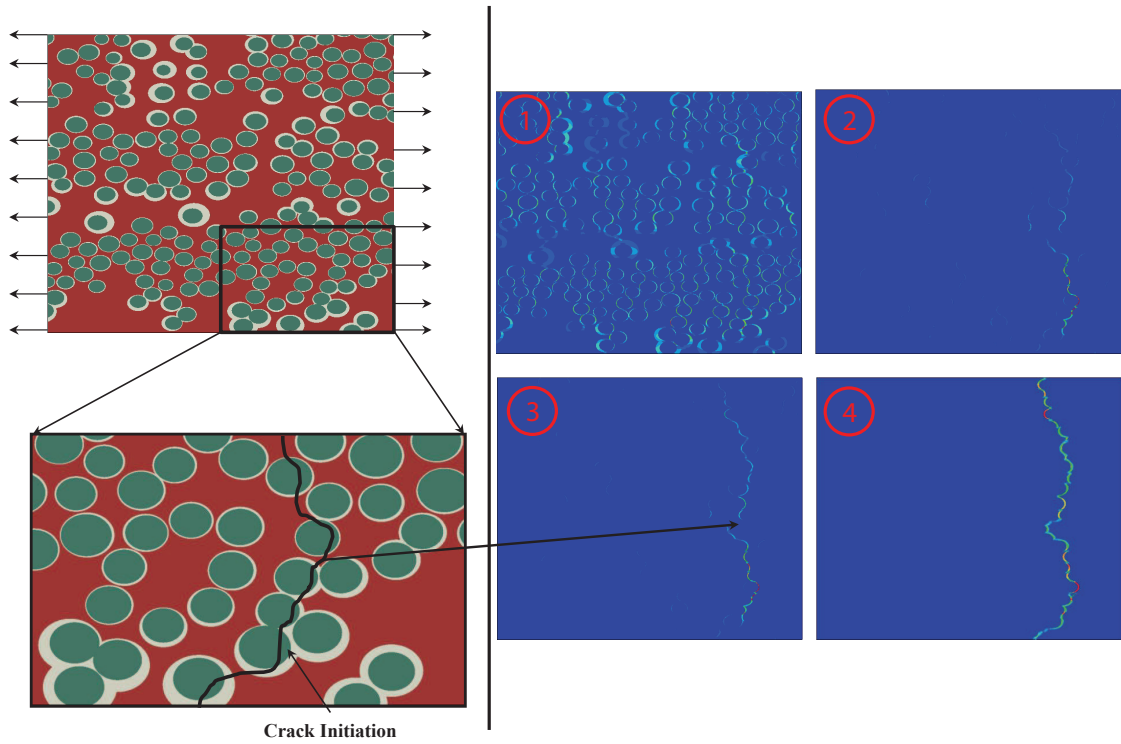


Figure 3.19: Crack paths of random RVE-1 microstructure model

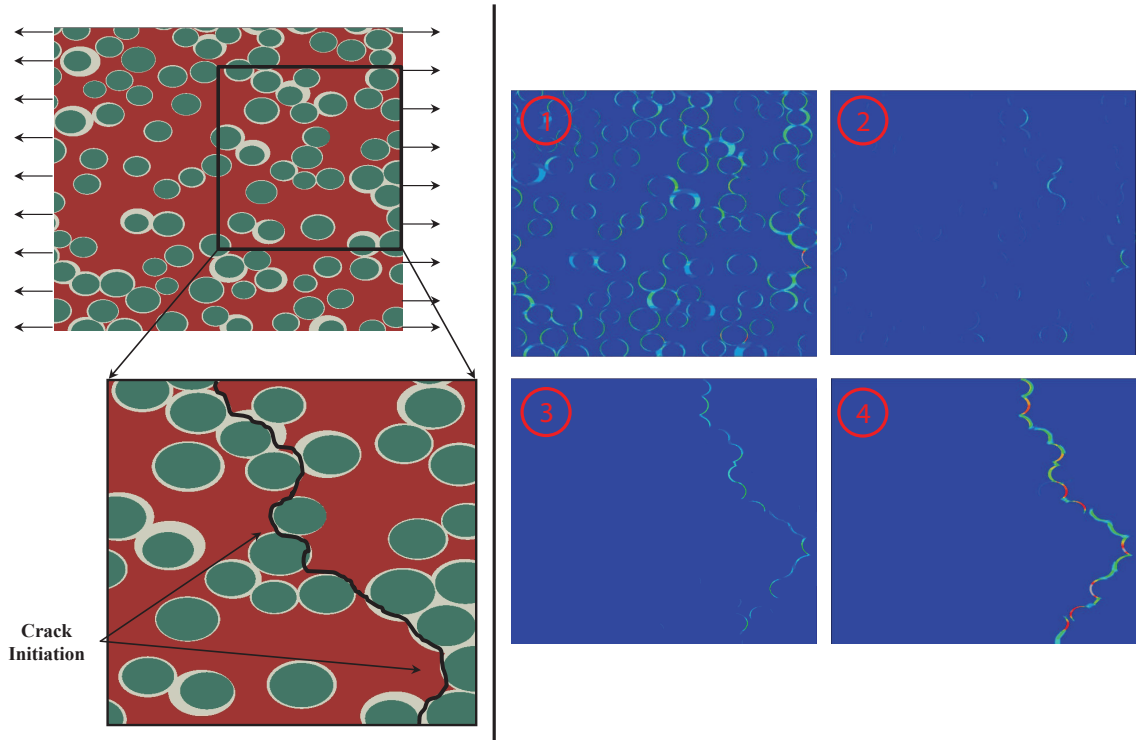


Figure 3.20: Crack paths of random RVE-2 microstructure model

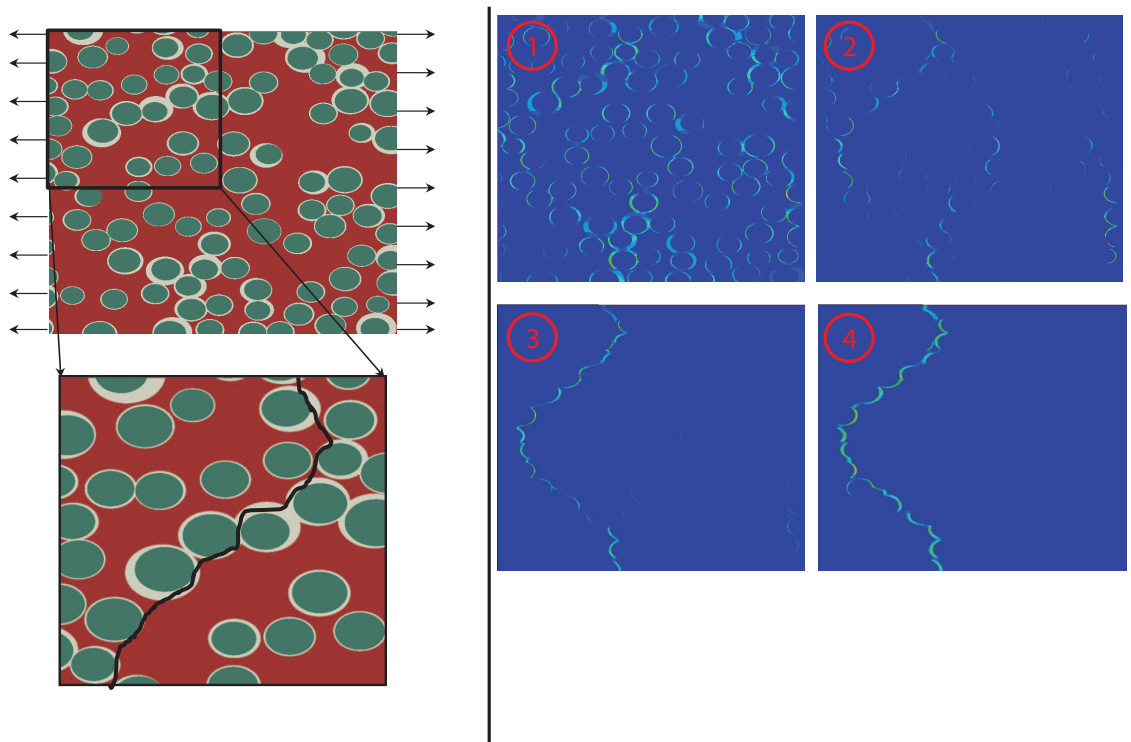


Figure 3.21: Crack paths of random RVE-3 microstructure model

By evaluating the strain-field at various times of the simulation it is visible that the crack opening in certain areas of the model begin to close during the simulation due to new cracks appearing in other locations of the model. This can be explained by the redistribution of load transfer throughout the model and is very consistent with experimental results (*Tracy (2014)*). Drastic reductions in the post-peak stress-strain response can usually be associated with sudden crack-growth or further crack opening of an existing crack. Once a single crack has developed from the top to bottom of a RVE and all elements within the crack have exhausted their load carrying capability it is expected that the reaction force of the RVE's reduces to zero. However, if the ultimate crack path is not perpendicular to the load direction or two cracks developed in the model, it is possible that a small residual stress can be observed as seen for RVE's 2 and 3, respectively. Nine representative RVE's and two baseline models based on micrographs are discussed in this chapter. Noticeable in all RVE's is the crack deflection when the crack tip reaches a fiber or fiber bundle. The local orientation of the crack tip changes and subsequently the crack deviates around the obstacle (fiber). All crack predictions showed a similar initiation behavior. Multiple cracks occur and grow initially until two or more cracks join to form a macro-crack which then defines the final crack path. Figure 3.24 shows the stress-strain response of the RVE's. All models deviate from linearity before the peak stress is reached. Load drops in the stress-strain response are associated with additional crack growth. The post-peak response of all RVE's is characterized by stepwise stress degradation due to crack growth and arrestment in the vicinity of fibers in the crack path. A significant scatter in the peak stress and post-peak behavior can be observed. Baseline model 1 sustained an ultimate load of 89.1 MPa whereas baseline model 2 peaked at 84.2 MPa. The maximum stress of 92.14 MPa was achieved in RVE 9. The lower bound is represented by RVE 6 where the peak stress was computed at 79.29 MPa and is 15% lower compared to RVE 9. The average ultimate stress of all RVE's was 87.15 MPa

with a standard deviation of 4.22 MPa. The strain at peak stress ranges from $\epsilon = 0.0006$ to $\epsilon = 0.0011$ with an average strain at ultimate load of $\epsilon = 0.0008$ and a standard deviation of $\epsilon = 0.00001$. Damage initiates in all RVE's before a deviation from linearity is observed in the stress-strain response and therefore a definition of a proportional limit in terms of damage initiation becomes difficult. The arrangement of fibers within a lamina has a profound impact on the overall performance of the composite as can be seen from this study. Crack initiation as well as propagation are significantly controlled by fiber-fiber distances and coating thickness. A more specific manufacturing process, aimed at eliminating features that lead to increased crack growth, could improve the overall performance of parts and components significantly.

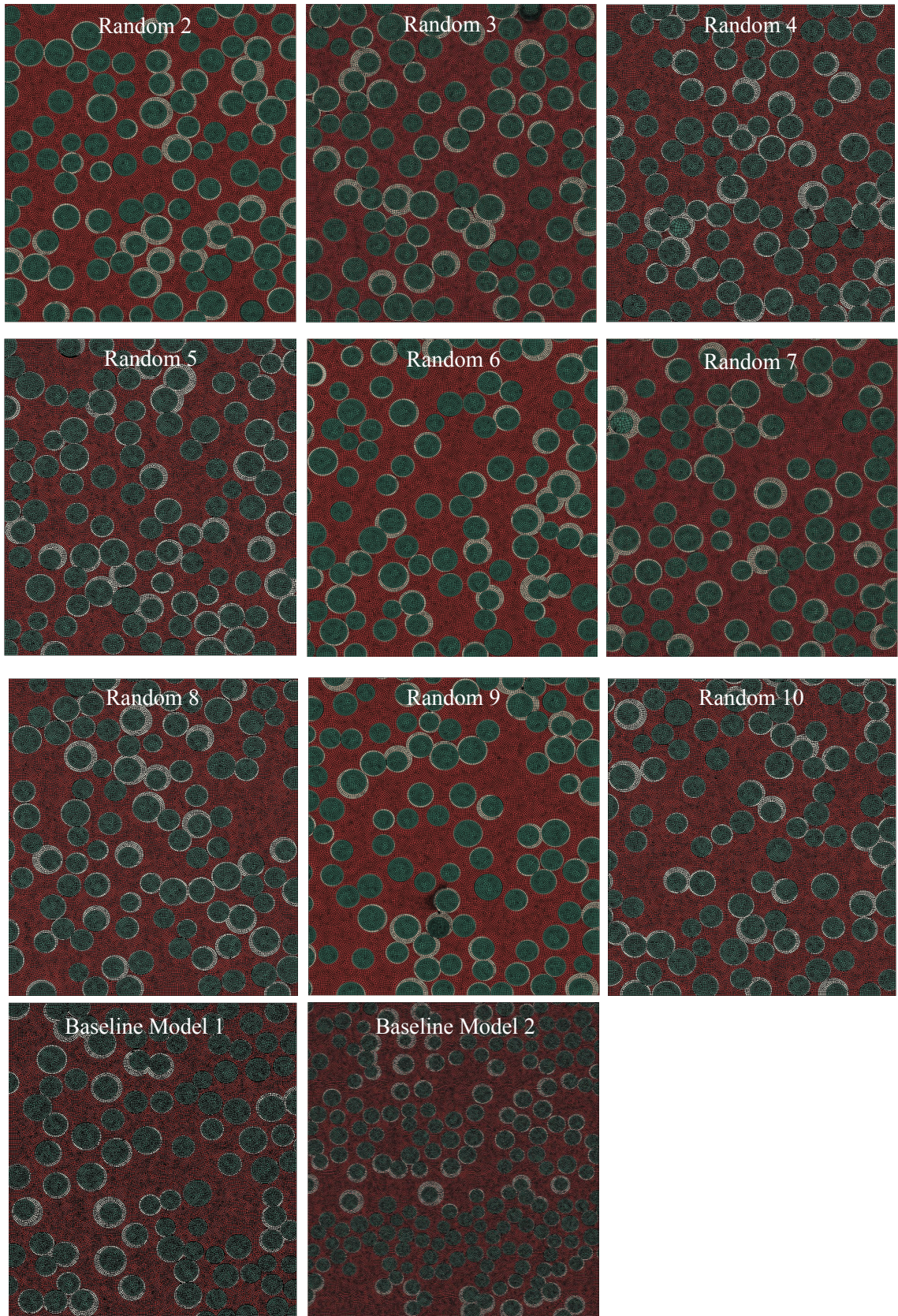


Figure 3.22: Finite element models with randomly located fibers

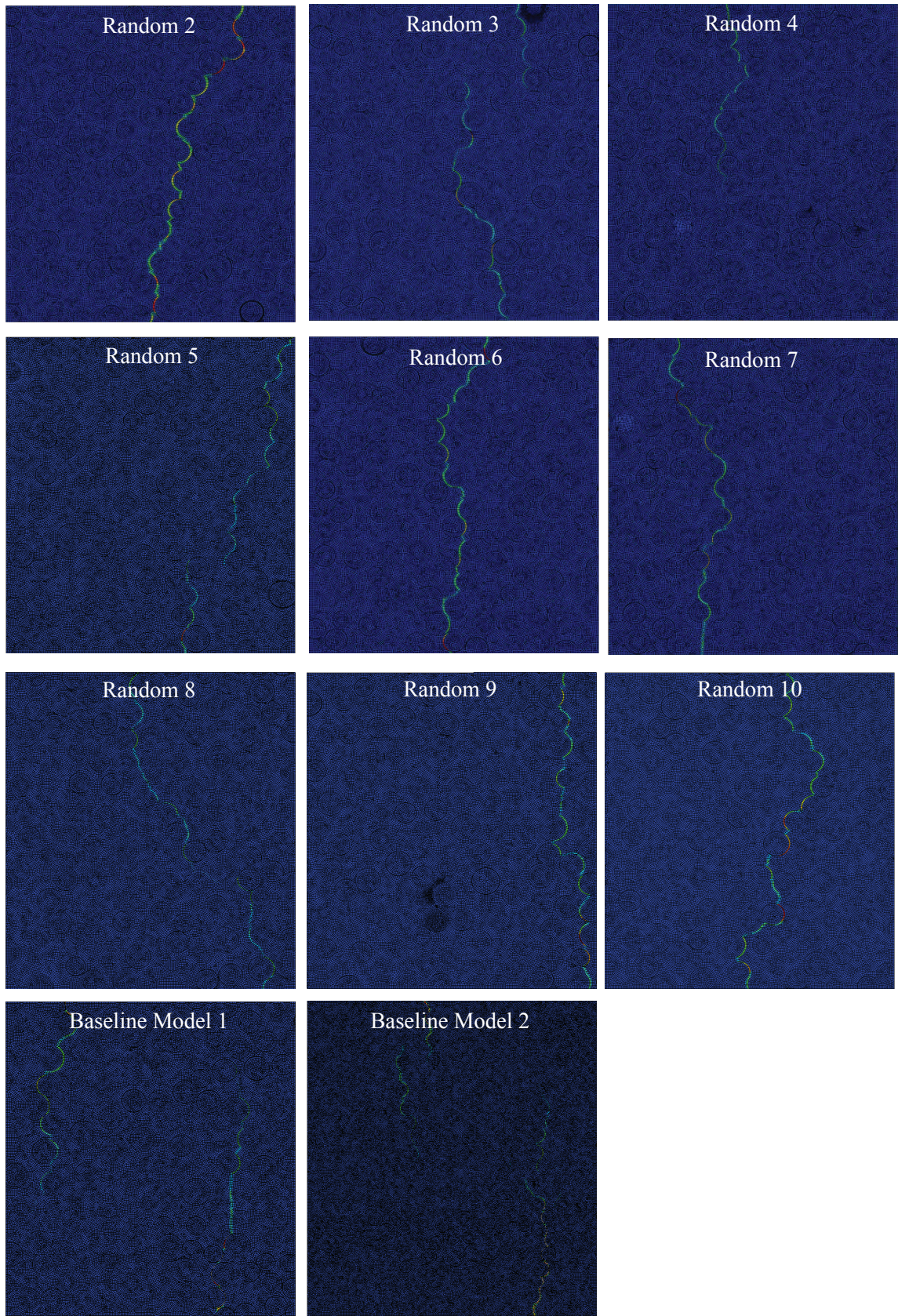


Figure 3.23: Ultimate Damage path of randomly generated representative volume elements (RVE's)

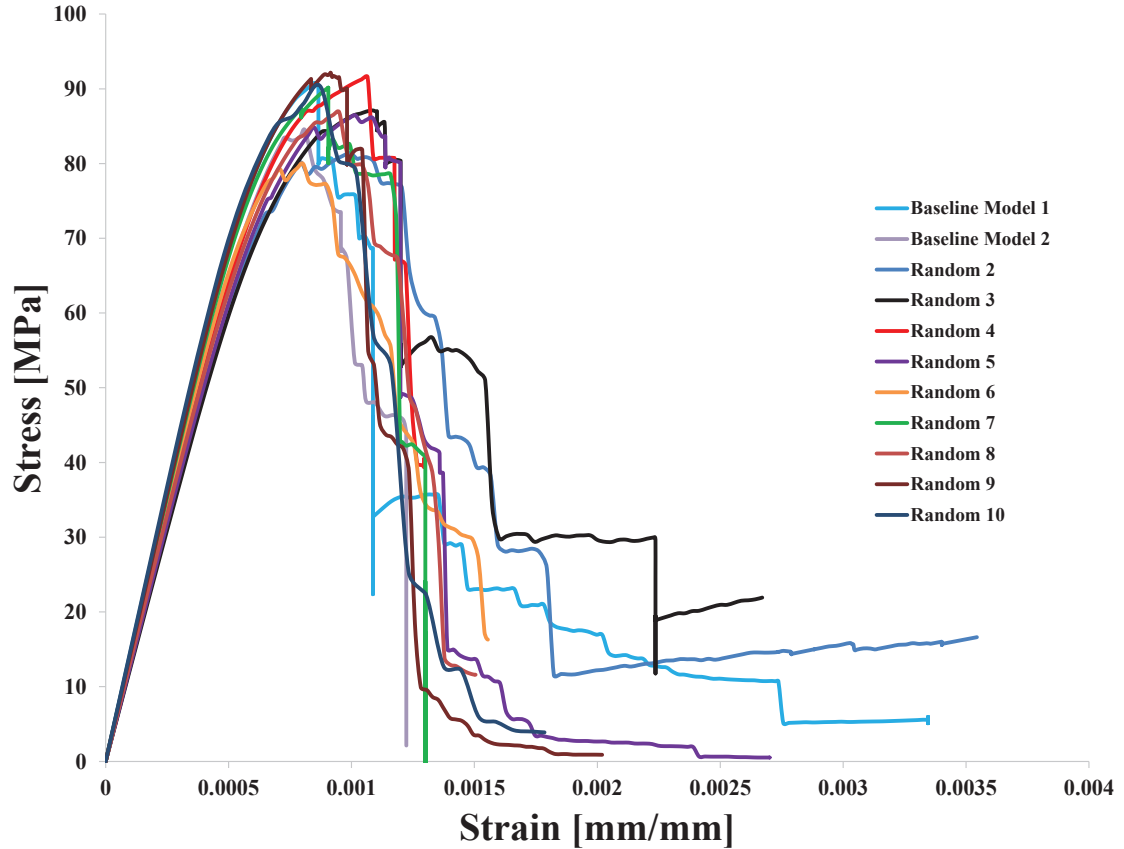


Figure 3.24: Stress-Strain response of randomly generated microstructure models

3.6.2 FEM Crack Density Prediction

Most analytical crack density theories introduced in chapter 3.2 assume a double ninety-lamina in between two single zero-layers or vice versa. Crack density is defined as the inverse of crack spacing and indicates how many cracks are present per unit length. Although some of those models are capable of both $[0/90]_S$ and $[90/0]_S$ laminates only cross-ply laminates with two inner 90-degree layers are discussed here. In an effort to compare crack density predictions a two-dimensional plane strain element model (CPE4 in Abaqus) that has a four layer cross-ply configuration was created. Each transverse ply contains 578 fibers at random locations. Fiber diameters are constant at $10\ \mu\text{m}$. The model includes fiber clusters as well as touching fibers and coatings as shown in figure 3.25.

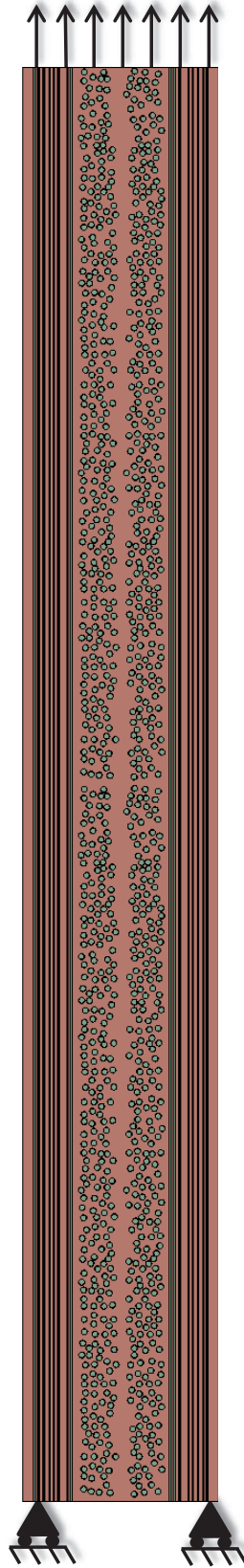


Figure 3.25: Four layer cross-ply laminate model

The crack band theory is used to dictate the damage behavior of the model. All input parameters are given in table 3.4. Fiber damage in the zero plies is activated, however the simulation is aimed toward the investigation of transverse cracks in the transverse plies. Results of the numerical finite element predictions are displayed in

Table 3.4: Constituent elastic and fracture properties for crack spacing analysis

Material	Young's Modulus (MPa)	Poisson's Ratio ν	Critical Stress σ_{cr} (MPa)	Fracture Toughness G_{IC} (N/mm)
Matrix	340000	0.14	200	0.05
Coating	10000	0.19	200	0.05
Fiber	380000	0.14	2600	0.005

figure 3.26. In order to compare crack densities of the FEM simulation to analytical models, a definition of "cracks" is needed. The crack band theory uses a damage parameter D as an indication of the amount of energy dissipated by each element, where $D = 0$ indicates an undamaged element. In this work it is assumed that a physical crack has occurred in every element which exceeded $D = 0.99$. Elements, that are shown in red in figure 3.26 have exceeded this threshold. It can be seen that six discrete cracks were predicted for this laminate. The cracks initiate within the ninety-ply and eventually grow through the matrix rich region between the two layers. Furthermore, it can be observed that cracks meander around fibers in the transverse plies.

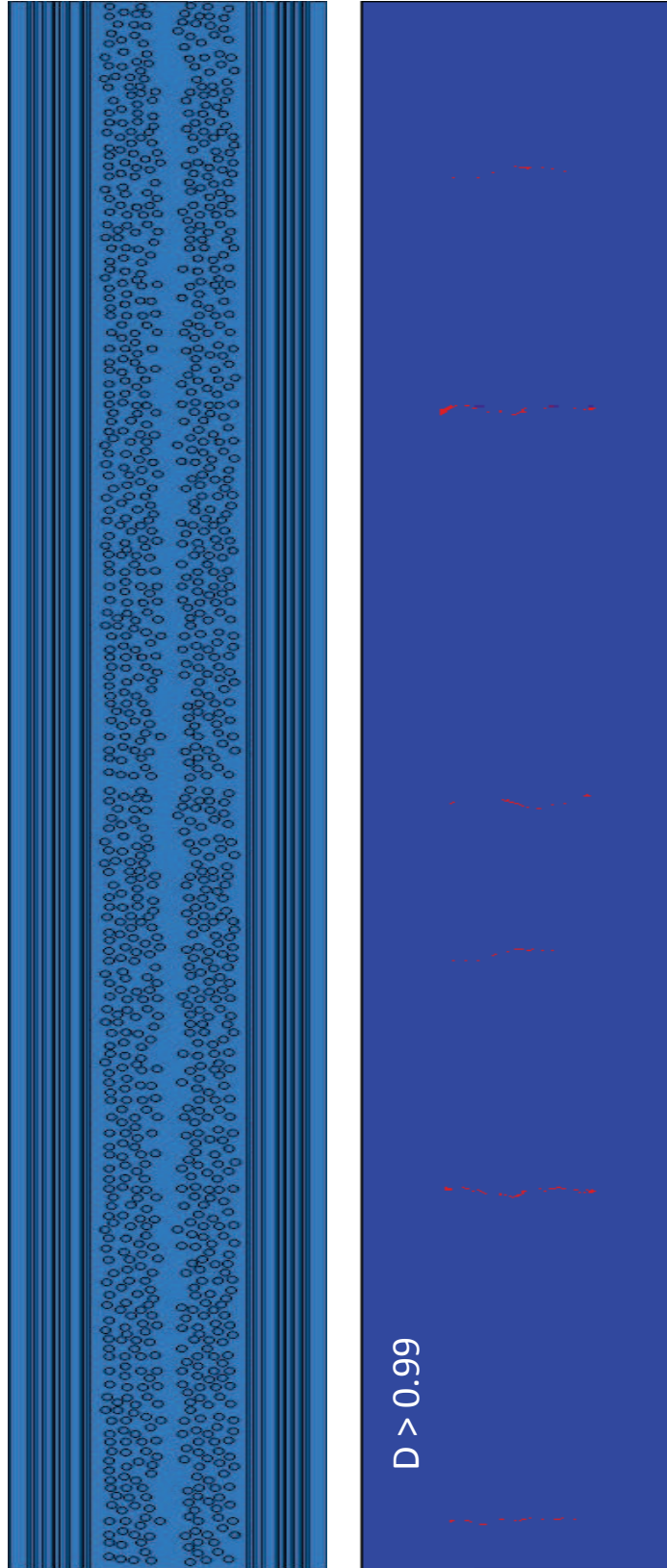


Figure 3.26: $[0/90]_S$ model details and crack density predictions of finite element model

Figure 3.27 shows a comparison of the crack density predicted by the finite element model, Nairn, and Laws and Dvorak model. The input parameters for the Laws and Dvorak model and Nairn model are given in table 3.5 and 3.6, respectively. The first ply fracture stress is an input parameter to the Laws and Dvorak model and chosen to match the first ply fracture stress predicted by the finite element model. In Laws and Dvorak's model it is used to calculate the shear lag parameter β . Nairn's analytical model can be used to calculate the first ply fracture stress as seen in figure 3.27 for crack density equal to zero. This model underpredicts the first ply fracture stress for the input parameters given in table 3.6 as $\sigma^{fpf} = 180MPa$. The finite element predictions are in good agreement with the Laws and Dvorak analytical model. Equation 3.12 was used to calculate the crack density. It is assumed that no residual thermal stresses are present in the composite. Fiber failure in the zero plies occurs at a crack density of approximately 2.5 cracks/mm in the numerical model which terminates the development of transverse cracks in the inner ninety laminae. All three models show similar behavior during initial crack development. Cracks develop rapidly at an almost constant stress level. This observation is plausible for brittle materials. Cracks occur in multiple locations simultaneously. More energy is needed to force further cracking in between existing cracks which is seen in figure 3.27 as a reduced slope.

Table 3.5: Input properties for Laws & Dvorak analytical crack density model

Laws & Dvorak	
First Ply Failure Stress σ^{fpf}	194 GPa
Fracture Toughness G_C	0.05 N/mm
Composite Modulus E_C	290 GPa
Axial Ply Modulus E_0	327 GPa
Transverse Modulus E_t	216 GPa
Longitudinal Ply Thickness b	0.25 mm
Double Transverse Ply Thickness b	0.25 mm

Table 3.6: Input properties for Nairn's analytical crack density model

Nairn	
Matrix Fracture Toughness G_C	0.05 N/mm
Composite Modulus E_C	290 GPa
Axial Ply Modulus E_0	327 GPa
Transverse Modulus E_t	216 GPa
Transverse Shear Modulus G_t	90 GPa
Axial Shear Modulus G_a	90 GPa
Transverse Poisson's Ratio ν_t	0.14
Axial Poisson's Ratio ν_a	0.14
Longitudinal Ply Thickness b	0.25 mm
Double Transverse Ply Thickness b	0.25 mm

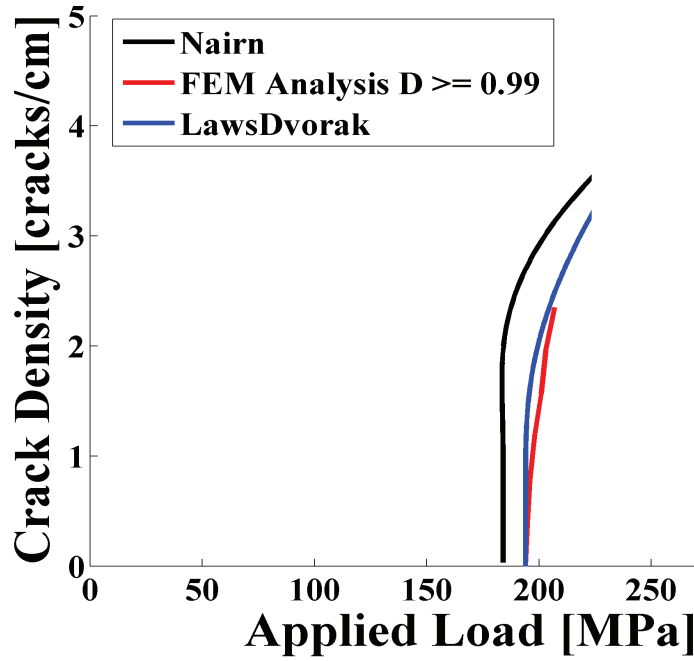


Figure 3.27: Comparison of FEM crack density prediction with analytical solutions

3.6.3 Microscale Modeling of a CMC Laminate

In order to predict the non-linear behavior of brittle laminated composites accurately, multiple dominant cracks must be captured. During initial loading a large number of microcracks form in the matrix. On further loading, microcracks join to form macrocracks. Some microcracks deflect along fiber/matrix interfaces or get arrested. This cracking behavior usually leads to the non-linear stress-strain relation observed in experiments of CMC specimens. At some loading level, matrix cracking reached saturation after which only the fibers are carrying the load. *Zok and Spearing* (1992) developed a model to describe the evolution of matrix cracks in unidirectional continuous fiber, brittle matrix composites. The authors used the steady state strain energy release rate available for crack extensions in terms of the constituent properties, the applied stress and the distances to the neighboring cracks. *Li et al.* (2014) showed that the classical Budiansky-Hutchinson-Evans shear lag model could be used to determine the micro-stress field of damaged composites. They calculated the crack

spacing in SiC/CAS composites and showed that crack saturation occurs at a particular stress level. Capturing the matrix crack spacing correctly requires a large scale model including hundreds of fibers.



Figure 3.28: Large micromechanics model ($[0/90]_{2S}$) and boundary conditions

Fig.3.28 shows the finite element model used in this study. It represents an 8-layer $[0/90]_{2S}$ lay-up. Each 90° layer consisted of 578 fibers and every 0° layer consisted of 8 fibers. The overall fiber volume fraction was 21 % and the interface volume fraction was 5 %. Two dimensional plane strain elements in Abaqus were used to discretize the model resulting in 1,011,274 degrees of freedom. Nodes on the left edge were assigned with a zero displacement in the horizontal direction. The node located at the left bottom corner was also constrained from movement in the vertical direction to avoid rigid body movements. Nodes on the right-hand vertical edge were subjected to a displacement of 0.2 mm. The All fibers were randomly located within each layer and fiber clustering, touching fibers, eccentric coatings, and varying coating thicknesses were modeled (figure 3.29). These details naturally lead to non-uniform stress and strain fields in the model which determine crack initiation and growth. Modeling a large number of fibers is essential for capturing crack growth as cracks tend to get arrested when they are intercepted by a fiber. Crack arresting contributes to the material ability to redistribute stress fields which leads to new crack initiation sites. Increasing stress in one location of a lamina or laminate automatically leads to a relaxation in another region. Crack closing can be observed as a result and is shown in Figure 3.31. It shows an enlarged region of the inner transverse ply. Results at

increasing time (load) of the same region are shown. Crack-closure at one location can be observed due to increased crack-opening of a nearby crack.

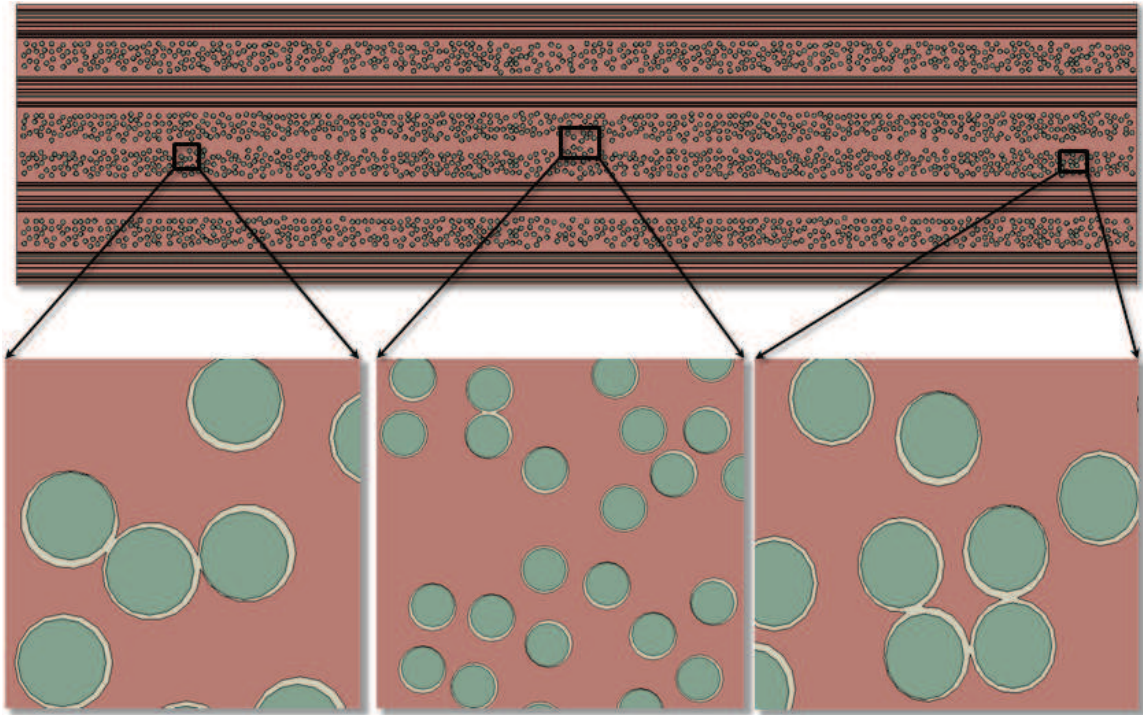


Figure 3.29: Details of the large micromechanics model ($[0/90]_{2s}$)

Figure 3.30 depicts the maximum principle strain plot of the last increment of the simulation. Multiple cracks with a crack spacing of approximately $600 \mu\text{m}$ are evident in the two inner transverse plies. A higher crack density, e.g. lower crack spacing can be observed in the outer transverse plies. It is approximately $1/4$ times the crack spacing of the inner transverse plies. Due to the nature of a 2-dimensional simulation cracks are inhibited from growing around fibers in the zero plies. The crack growth is instead deflected in the load direction. As can be seen in figure 3.30 multiple longitudinal cracks can be seen along fibers in the zero plies. This phenomenon is also evident in real materials, however, in an increasing load environment these cracks generally tend to grow transverse to the zero fibers. After the crack has completely traversed perpendicular through the zero ply fiber pull-out releases additional energy. This phenomenon is further discussed in chapter V. More energy can be released

through frictional sliding which leads to an apparent toughening effect of the CMC material. Future work should include fiber pull-out in the zero plies in addition to the crack band method. The stress-strain response of the the model prediction is compared to the stress-strain response of an eight ply $[0/90]_{2S}$ smooth bar specimen tested in monotonic tension, shown in figure 3.31. The specimen was heat treated prior to the experiment to reduce the impact of residual stresses on the experimental results. The deviation from linearity in the stress-strain response is captured accurately.

Experimental results of a heat-treated CMC smooth bar tensile test shown in figure 3.31 were supplied by the specimen manufacturer. Details of the heat-treatment are proprietary and can not be given here. The predicted response of the FEM model, shown in red, in the strain range between $\epsilon = 0.0007 - 0.0025$ matches well with the experimental results (black). In the strain regime $\epsilon \geq 0.0025$, it is assumed that the load carrying capability of the transverse plies has decreased significantly. Damage and fiber-pullout in the longitudinal plies controls the specimen response. It is therefore expected that the model predictions will deviate from the experimental results.

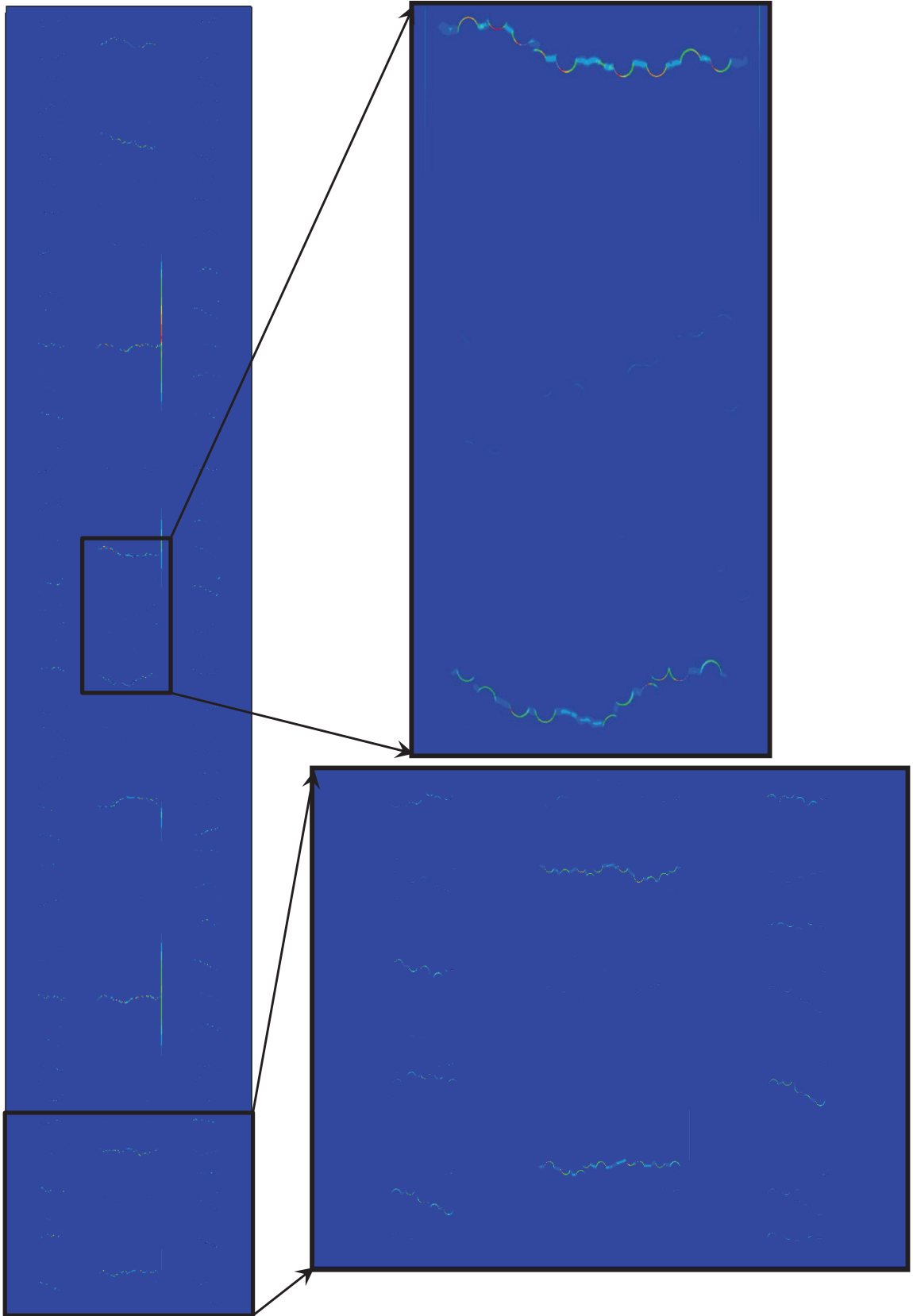
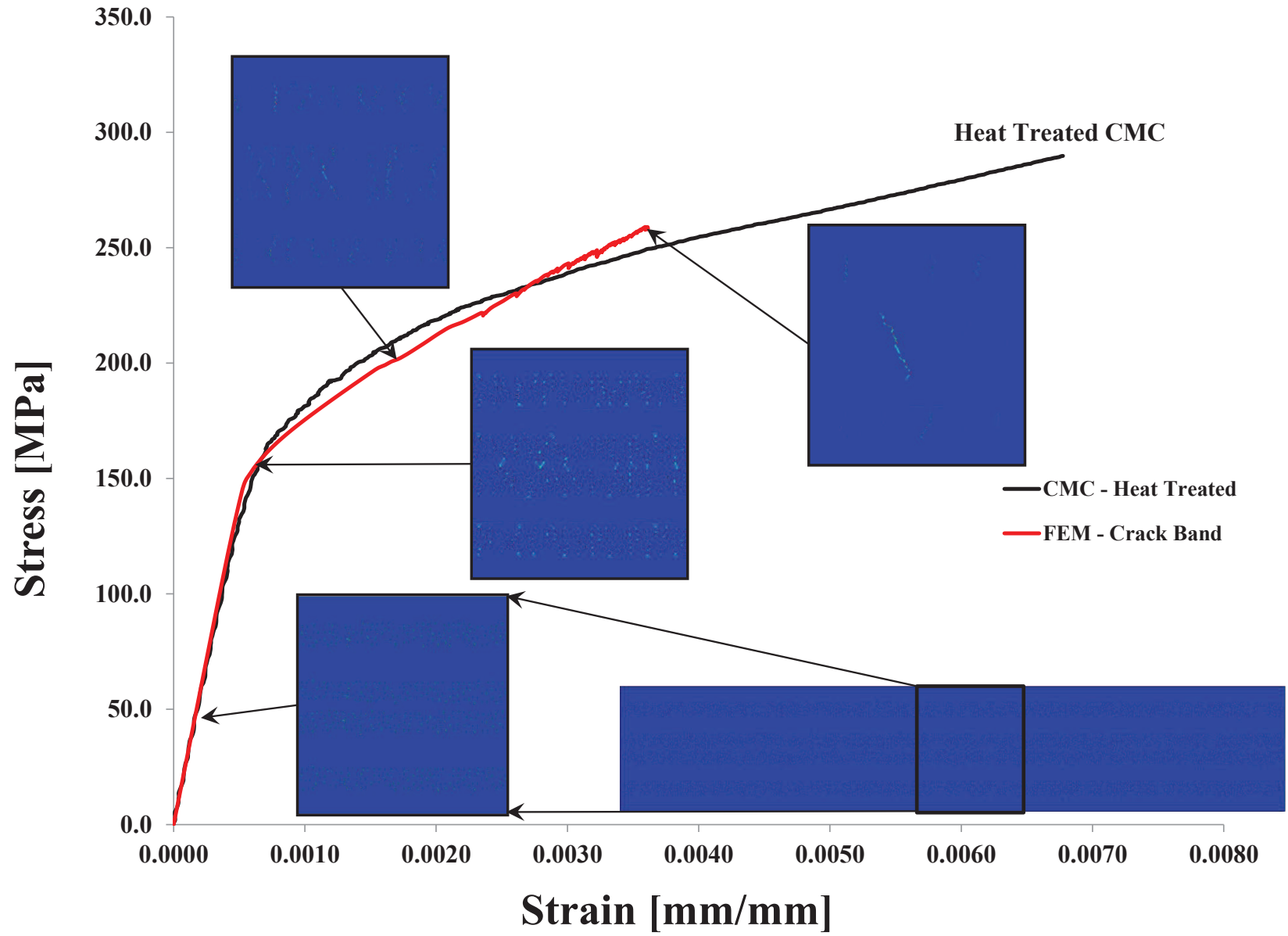


Figure 3.30: Maximum principle strain results showing cracks in a 8-Layer finite element model

Figure 3.31: Stress-Strain response of a 8-Layer finite element model



3.7 Conclusions

The energy based crack band method was introduced in this chapter. It was shown that this method can provide mesh independent results assuming the characteristic length of the elements is smaller than the maximum length defined by the material properties. Mesh independence was established by using a square and dogbone shaped model. The influence of fiber packing was investigated by creating a model based on a micrograph of the CMC microstructure. It was found that the ultimate load varied significantly. It is expected that good control of fiber placement within a lamina can yield an improvement of the ultimate load that can be sustained by the material.

Furthermore crack density studies were carried out on symmetric four ply $[0/90]_s$ laminates. It could be shown that the crack band methodology is suitable to predict crack spacing. An eight layer large scale model with over one million degrees of freedom was created to predict the damage behavior of a smooth bar CMC specimen. Damage initiated between the inner transverse plies. A characteristic crack spacing was observed in the simulation. Due to more complex damage modes of the zero-ply only the damage initiation and early post-peak stiffness can be predicted accurately. Further work is required to include mode-II crack growth in the coating material and subsequent fiber-coating debonding. Furthermore, fiber-pullout models in the zero-ply are required to capture the correct damage modes in the longitudinal plies after matrix crack saturation has set in.

The crack-band model can be used in the future to identify if a randomly generated RVE is suitable to examine e.g. transverse damage behavior in a multi-scale methodology. Furthermore, a quick measure of the geometric properties of each RVE would be needed to assess the suitability. Similarities between RVE's could be identified and objectively evaluated. Two possible methods are further discussed in appendix A. For transverse plies, the stress-strain response from detailed transverse tension

models could be used in the future to replace the time consuming concurrent multi-scale scheme, as discussed in chapter IV. Results from multiple random RVEs could be used to randomize the microstructure of a component.

CHAPTER IV

Integrated Finite Element Method Multi-Scale Modeling

4.1 Introduction

The deformation response, subsequent damage development and failure of multi-constituent materials such as ceramic matrix composites is dependent on microstructural details such as variations in fiber packing arrangement, properties at fiber-matrix interfaces, and interactions between neighboring fibers. This dependency of failure modes on the microstructure is well known for composite materials which led to the development of numerous homogenized theories. *Kanoute et al.* (2009) reviewed various multi-scale methods for mechanical and thermomechanical responses of composites. *Heinrich and Waas* (2013) utilized the smeared crack approach to describe the post-peak softening in laminated materials. They predicted the cracking behavior of an open hole tensile specimen and recorded crack directions for various fiber angles. Accurate numerical predictions for layered, fiber reinforced materials are inherently difficult due to the intricate mechanisms that tie global component failure to microstructural degradation. Modeling strategies based on homogenized material properties neglect the importance of the physical behavior at the microstructural level, and thus homogenized models fail to predict critical parameters accurately that

are observed experimentally, e.g. maximum load, strain to failure, crack spacing and other salient features. Often times the material direction is used as the failure direction. This might lead to erroneous crack paths for materials with similar fiber and matrix properties such as CMCs. Hence, multi-scale methods have become the focus of many research papers in recent years. These models dehomogenize the strain and stress state for each constituent. Typically, a Representative Unit Cell (RUC) that preserves the microstructural dimensions is identified. *Yuan and Fish* (2008) developed a computational homogenization approach for linear and nonlinear solid mechanics problems. In this work two commercial solvers were bridged by a python code. The authors showed that linear problems could be accurately modeled. *Key et al.* (2004) used multicontinuum technology in a multi-scale simulation to analyze the separation of rib to skin interfaces. Multicontinuum theory decomposes the stress and strain field for each constituent using volume averages. This method is numerically fast with the cost of inaccuracy particularly for shear components. *Aboudi et al.* (2001) introduced the generalized method of cells (GMC), a semi-analytical method, which discretised the microstructure with rectangular subcells. *Pineda et al.* (2013) achieved mesh objectivity with a thermodynamics based approach within GMC as well as High-Fidelity Generalized Method of Cells (HFGM). Multi-scaling methods often suffer from lower computational efficiency compared to homogenized models. This disadvantage can usually be overcome by using the multi-scale method in areas where microstructural failure is to be expected, e.g. at stress concentrators (notches, etc.). Homogenized element stress-strain relation can be utilized in regions of low failure probability. In recent years significant improvements have been made in terms of fidelity and computational efficiency (*Feyel and Chaboche* (2000); *Ladevze and Nouy* (2003); *Michel et al.* (1999); *Smit et al.* (1998)). Recently, *Zhang et al.* (2015) have introduced a 2-scale method in which the subscale RVE is a concentric cylinder model and the stress and strain fields are provided by a closed form solution, leading to sig-

nificant computational savings.

In this chapter the commercial Finite Element software suite Abaqus is used to generate lamina-level models. A second Integrated Finite Element Method (IFEM) has been developed and fully integrated with the main Abaqus solver through a user material subroutine, denoted as UMAT. IFEM calculates the reaction of a microstructural model to an imposed displacement field. The microstructural model consists of a Representative Volume Element (RVE) which includes all constituents of the real material, e.g. fiber, matrix, and fiber/matrix interfaces, details of packing, non-uniformities in properties etc. The energy based Crack Band Theory (CBT), first introduced by *Bažant* (1983), is implemented within IFEMs constitutive laws to predict micro-cracking in all constituents that are included in the micromechanics model. Figure 4.1 displays a flow chart of the integration of IFEM within Abaqus FEM suite. IFEM is called at every Gauss point of a large scale model, e.g. tensile coupon or component. The current strain state is applied on a subcell model and the corresponding stress field is calculated. A damage check for every element within the subcell is carried out. If damage has occurred in one or more elements the stress and strain fields within the subcell are re-equilibrated. Hence, the communication between the micro- and macro-scale is achieved through the exchange of strain, stress, and stiffness tensors. Important failure parameters, e.g. crack path, proportional limit, etc. are part of the solution and predicted with a high level of accuracy. Numerical predictions are validated against experimental results. An overview of the IFEM is schematically shown in figure 4.1.

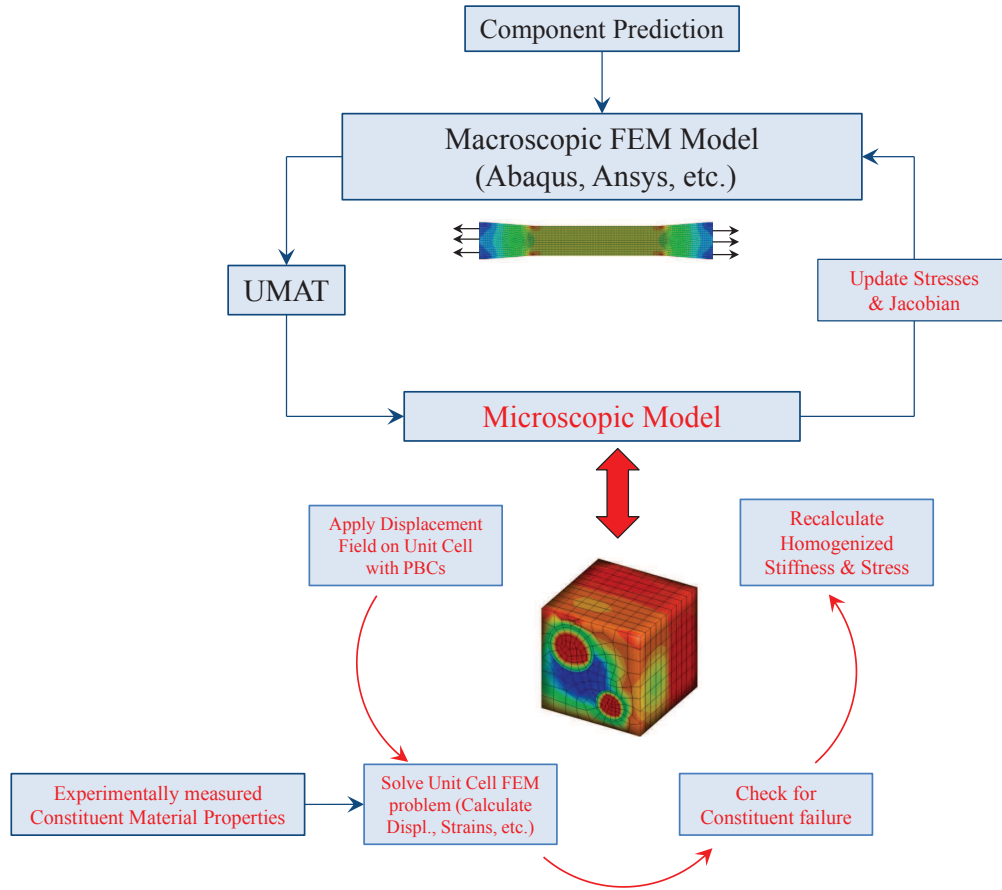


Figure 4.1: Flow chart of IFEM implemented using Abaqus

4.2 Representative Unit Cell Modeling in a Multi-Scale Framework

Most commercially available finite element suites offer the user to implement custom constitutive material laws. In this work Abaqus has been chosen to solve the macroscopic scale (e.g. lamina level) finite element problem. User material subroutines, called UMAT (*Abaqus User Manual Abaqus* (2008)), are readily accessible through the computer language Fortran. The UMAT subroutine is called at each integration point of the Abaqus macroscopic model for each element within an element set that has been defined with a user material. In a multi-scale scheme information

are exchanged between multiple length and/or time scales. Here the focus lies on a concurrent technique that exchanges essential stiffness, stress, and strain information between a lamina-level simulation and a microstructure level simulation. This technique employs FEM at both the Fiber/Matrix scale and the macroscopic, e.g. lamina level scale. It is often referred to as *FEM*². The constitutive response at the coarse scale is purely dictated by what is computed at the Fiber/Matrix level model. Localization techniques, as discussed below and referenced in equation 4.12 are employed for transforming displacement fields from a global state to a local state. Back-transformation is achieved through a homogenization step according to equation 4.11. The concurrent information exchange between the scales is shown figure 4.2.

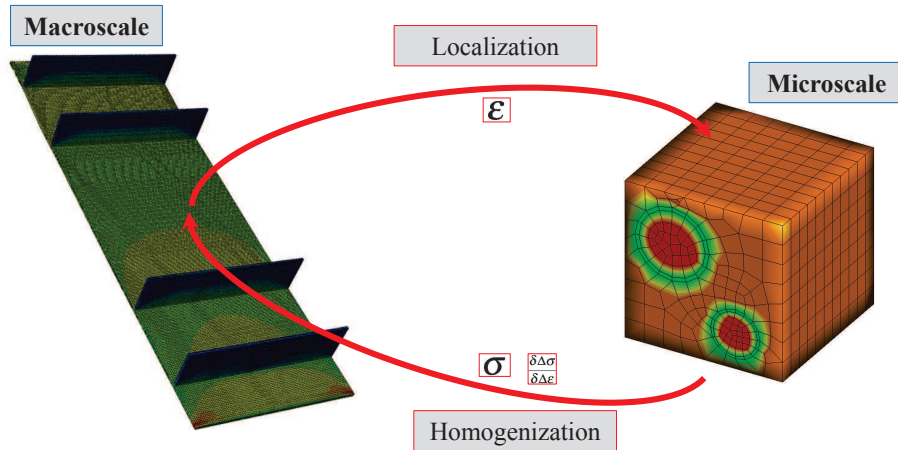


Figure 4.2: Multi-Scale information exchange between scales

A homogenized strain field from the component FEM model at the macroscale is passed to the user defined material definition and applied on the boundaries of the RVE at the microscale. This process is denoted as the localization step. The RVE problem is solved and subsequently the volume averaged stress and stiffness tensors are calculated and passed back to Abaqus. This step is denoted as the homogenization step. Multi-scale methodologies attempt to find an optimum between the

computational effort and accuracy of the predictions. Theoretically, each RVE can consist of an unlimited number of constituent materials, fibers, etc. The complexity of each RVE should be chosen wisely and typically requires user experience to find the ideal RVEs. In order to keep computational costs at a minimum in the current study the number of fibers is limited to three in the RVE microscale model. In this work three phase (fiber/interface/matrix) RVEs are used. It is assumed that the bonding properties between the fiber/coating and coating/matrix are perfect, e.g. nodes are shared between these constituents. No limitation exists for volume fractions of the included materials. A major advantage of multi-scale models is the ability to randomize the microstructure by using RVE with varying geometrical features. Figure 4.3 depicts six example RVE. Fiber touching and clustering as well as differences in fiber-diameter can be simulated. Elastic properties of the RVEs are similar but differences exist in terms of the RVE strengths. Fiber clusters amplify the local stress field and are sites for damage initiation. These phenomena are commonly found in low volume fraction composites such as CMCs.

4.3 IFEM Equations

Two versions of IFEM have been developed. 3D-IFEM uses a linear 8-noded element formulation as can be found in *Chandrupatla and Belegundu (2002)*. As is well known three dimensional finite element codes deliver a higher accuracy over two dimensional codes. However, they suffer from higher computational effort due to more degrees of freedom in the model. Hence, a two dimensional generalized plane strain finite element code, denoted as 2D-IFEM, has also been developed to reduce the required simulation time while maintaining a good level of accuracy. This version is based on a linear 4-noded element formulation. In the following, the equations for the three dimensional formulation are presented. The geometry of each element is described by cartesian coordinates (X_i, Y_i, Z_i) of the nodes. Each node i has three

displacement degrees of freedom (u_i, v_i, w_i) and the nodal degree of freedom vector \mathbf{q} can be written as

$$\{q\}^T = \{u_1, v_1, w_1, u_2, v_2, w_2, \dots, \dots, \dots, u_8, v_8, w_8\} \quad (4.1)$$

The corresponding nodal force vector is

$$\{f\}^T = \{f_{x1}, f_{y1}, f_{z1}, f_{x2}, f_{y2}, f_{z2}, \dots, \dots, \dots, f_{x8}, f_{y8}, f_{z8}\} \quad (4.2)$$

The displacement components at any point (X,Y,Z) can be interpolated by the nodal displacements

$$\{u\} = [N]\{q\} \quad (4.3)$$

where

$$[N] = \left\{ \begin{array}{cccccccccccc} N_1 & 0 & 0 & N_2 & 0 & 0 & \dots & \dots & \dots & N_8 & 0 & 0 \\ 0 & N_1 & 0 & 0 & N_2 & 0 & \dots & \dots & \dots & 0 & N_8 & 0 \\ 0 & 0 & N_1 & 0 & 0 & N_2 & \dots & \dots & \dots & 0 & 0 & N_8 \end{array} \right\} \quad (4.4)$$

is the matrix of shape functions. The eight shape functions can be written as

$$N_i = \frac{1}{8}(1 + \xi\xi_i)(1 + \zeta\zeta_i)(1 + \eta\eta_i) \quad (4.5)$$

The isoparametric transformation is given by

$$\begin{aligned} x &= N_1x_1 + N_2x_2 + \dots + N_8x_8 \\ y &= N_1y_1 + N_2y_2 + \dots + N_8y_8 \\ z &= N_1z_1 + N_2z_2 + \dots + N_8z_8 \end{aligned} \quad (4.6)$$

Next, the Jacobian matrix of the derivative transformation from real coordinates (X,Y,Z) to isoparametric coordinates can be written as

$$J = \begin{bmatrix} \frac{\partial x}{\partial \xi} & \frac{\partial y}{\partial \xi} & \frac{\partial z}{\partial \xi} \\ \frac{\partial x}{\partial \eta} & \frac{\partial y}{\partial \eta} & \frac{\partial z}{\partial \eta} \\ \frac{\partial x}{\partial \zeta} & \frac{\partial y}{\partial \zeta} & \frac{\partial z}{\partial \zeta} \end{bmatrix} \quad (4.7)$$

The stresses and strains are then given by,

$$\begin{aligned} \sigma &= [\sigma_x, \sigma_y, \sigma_z, \tau_{xy}, \tau_{xz}, \tau_{yz}]^T \\ \epsilon &= [\epsilon_x, \epsilon_y, \epsilon_z, \gamma_{xy}, \gamma_{xz}, \gamma_{yz}]^T \end{aligned} \quad (4.8)$$

The linear strain-displacement relations are given by

$$\epsilon = \left[\frac{\partial u}{\partial x}, \frac{\partial v}{\partial y}, \frac{\partial w}{\partial z}, \frac{\partial u}{\partial y} + \frac{\partial v}{\partial x}, \frac{\partial u}{\partial z} + \frac{\partial w}{\partial x}, \frac{\partial v}{\partial z} + \frac{\partial w}{\partial y} \right] \quad (4.9)$$

Finally, a matrix relating the element strains and nodal displacements can be derived

$$\{\epsilon\} = [B]\{q\} \quad (4.10)$$

At the end of each RVE calculation, the current stress and stiffness tensors of the RVE are required to complete the information exchange between the two scales. These quantities are passed back to the macroscale. In the present work, volume averaged stresses are used to calculate the homogenized stress field. Each component within an element of the RVE is integrated over the element volume and finally averaged with the total RVE volume as shown in equation 4.11.

$$\sigma_{ij}^V = \frac{1}{V} \int \sigma_{ij}^e dV \quad (4.11)$$

Implementing an FEM code in Fortran was essential for a highly efficient multi-scale

framework. It allows the macroscopic model to be run in a cluster environment and hence solving multiple material integration points simultaneously.

4.3.1 RVE Characteristics

The objective of multi-scale analyses is to decompose a general homogenized stress- and strain field of a lamina-level model into constituent stress- and strain states. Post-peak softening is based on these decomposed stresses and strains and therefore failure is dependent on geometrical features and constituent material response within the RVE. Theoretically, there are no geometrical limitations on the RVE. However, as stated earlier, the choice of RVE size and features are predicated on experimental observations that provide qualitative and quantitative insight on damage and failure mechanisms. In this research the maximum number of fibers per RVE was limited to three. This number of fibers resulted in a runtime of several hours using 12 processors within a cluster environment. However, future work will focus on the influence of detail within a subcell on the runtime and accuracy of numerical predictions. Furthermore, the discretization size should be selected to arrive at a minimum number of degrees of freedom within the RVE. Further restrictions might be imposed by the failure models used within the sub-scale. The crack-band method for example requires a minimum characteristic element length as further discussed in section 3.3.1. Often overlooked is the importance of microstructural details on the failure mechanisms in numerical models. Detailed views of microstructures of composite materials reveal a random organization of fibers. Perfectly hexagonal packed RVE's, as they are often used in numerical models due to the simple architecture, can merely be an approximation. Many different deviations of the perfect packing are found in real materials, e.g. fiber touching, varying fiber diameter, etc. Multi-scale methods are well suited to implement a random microstructure by using several RVE's with varying architectures randomly distributed throughout the macroscopic model.

Hence, each element within the macroscopic model will use a RVE that slightly differs from the neighboring RVE's. Figure 4.3 shows examples of six geometrically different three dimensional three phase (fiber,matrix,interface) RVE's. It should be noted for completeness that material properties (critical stress, toughness, etc.) can also exhibit spatial variations in a deterministic or random manner. Uniform properties are assumed in this study preliminary study, and other cases will be addressed in the future.

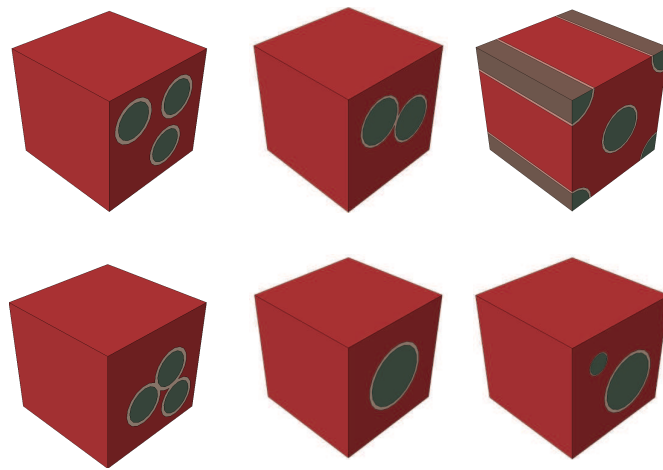


Figure 4.3: Selection of 3D-IFEM subcells with varying geometrical features

The choice of the three phase RVE's, including fiber, interface and, matrix, created to represent the microstructure of Ceramic Matrix Composites (CMCs) is based on observations from experiment, however, the approach developed here is not limited to these types of materials. Two phase (Polymer Matrix Composites) or one phase material (pure matrix) RVE's for example are possible and can be used. The objective here is to demonstrate that RVE features are an integral part of developing physics based multi-scale strategies that fall within the realm of predictive science.

4.3.2 Dehomogenization of Displacement Field with Periodic Boundary Conditions (Localization)

One essential step in multi-scale simulations is the transformation from the homogenized strain field to a local strain field. This step is denoted as the localization step. Load has to be transferred at each material point of the component level model to the microscopic RVE. In this work Periodic Boundary Conditions (PBCs) are used to convert the homogenized strain state at each integration point of the macroscale model into a displacement field that is applied on the boundaries of the RVE. PBCs enforce displacement continuity on all outer surface nodes of the RVE (*Heinrich et al. (2012); Xia et al. (2003)*) with the assumption that the RVE is part of a infinite continuum. Equations 4.12 represent the three dimensional formulation. These equations can be easily simplified to two dimensions. For compactness only the three dimensional periodic boundary conditions are explicitly discussed here.

$$\begin{aligned}
u_1(L_1, x_2, x_3) - u_1(0, x_2, x_3) &= \epsilon_{11}L_1 \\
u_2(L_1, x_2, x_3) - u_2(0, x_2, x_3) &= 2\epsilon_{12}L_1 \\
u_3(L_1, x_2, x_3) - u_3(0, x_2, x_3) &= 2\epsilon_{13}L_1 \\
u_1(x_1, L_2, x_3) - u_1(x_1, 0, x_3) &= 2\epsilon_{21}L_2 \\
u_2(x_1, L_2, x_3) - u_2(x_1, 0, x_3) &= \epsilon_{22}L_2 \\
u_3(x_1, L_2, x_3) - u_3(x_1, 0, x_3) &= 2\epsilon_{23}L_2 \\
u_1(x_1, x_2, L_3) - u_1(x_1, x_2, 0) &= 2\epsilon_{31}L_3 \\
u_2(x_1, x_2, L_3) - u_2(x_1, x_2, 0) &= 2\epsilon_{32}L_3 \\
u_3(x_1, x_2, L_3) - u_3(x_1, x_2, 0) &= \epsilon_{33}L_3
\end{aligned} \tag{4.12}$$

where ϵ_{ij} are the macroscopic strain quantities which are passed down from Abaqus at each integration point of the component level model. L_1 , L_2 , and L_3 are the corresponding side lengths of the RVE in x-, and y-, and z-directions. Using the

PBC approach in the localization step poses the requirement of mesh equality on opposite surfaces of RVE. Each node on one boundary surface must have a partnering node with the same in-plane coordinates on the opposite boundary surface. The PBC constraints are implemented using the Penalty Approach (PA) (*Chandrupatla and Belegundu (2002)*). Compared with the elimination approach the PA offers the simplicity of implementation with only a minor set back in terms of time required to solve the FEM problem.

$$\beta_1 Q_1 + \beta_2 Q_2 = \beta_0 \quad (4.13)$$

where Q_1 and Q_2 are the degrees of freedom (DOF) to be coupled and β_0 the applied distance between Q_1 and Q_2 . β_1 and β_2 are integer parameters with a value of 1 and -1, respectively.

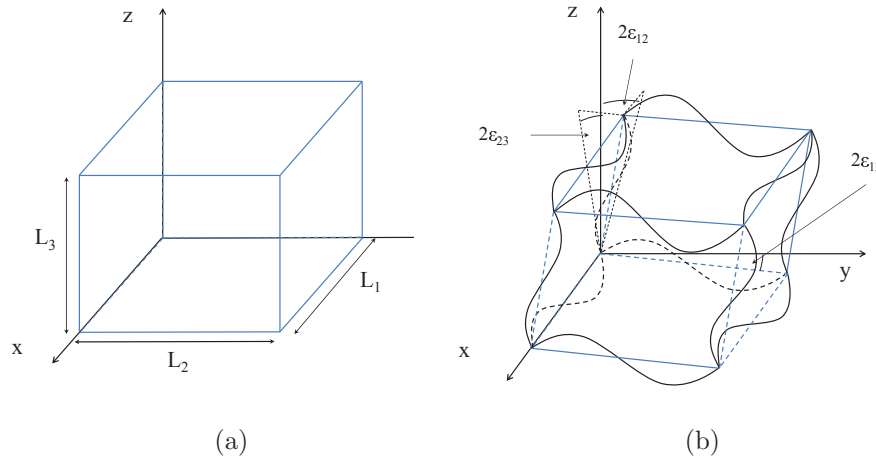


Figure 4.4: Periodic boundary conditions *a)* undeformed state *b)* deformed state

4.4 Prediction of Elastic Properties of Fiber-Reinforced Composites

In the past, theoretical derivations of elastic properties of fiber-reinforced composites have been developed (*Hashin and Rosen (1964)*, *Hill (1964)*) where the rule of mixtures represents the most basic model to predict elastic properties, however

it lacks accuracy for transverse properties. In this work the well known and widely accepted concentric cylinder model (CCM) is used for a comparison of the elastic lamina properties. The CCM equations can be found in the appendix. In the following equations, it is assumed that the fiber direction is denoted as the local 1-direction. Hence, directions 2 and 3 are transverse to the fiber. A standalone version of IFEM has been developed to predict the elastic properties of fiber reinforced composites. An orthotropic material model is assumed and all nine homogenized constants are calculated.

$$\begin{pmatrix} \sigma_{11} \\ \sigma_{22} \\ \sigma_{33} \\ \sigma_{12} \\ \sigma_{23} \\ \sigma_{13} \end{pmatrix} = \begin{bmatrix} C_{11} & C_{12} & C_{13} & 0 & 0 & 0 \\ C_{21} & C_{22} & C_{23} & 0 & 0 & 0 \\ C_{31} & C_{32} & C_{33} & 0 & 0 & 0 \\ 0 & 0 & 0 & C_{44} & 0 & 0 \\ 0 & 0 & 0 & 0 & C_{55} & 0 \\ 0 & 0 & 0 & 0 & 0 & C_{66} \end{bmatrix} \begin{pmatrix} \epsilon_{11} \\ \epsilon_{22} \\ \epsilon_{33} \\ \epsilon_{12} \\ \epsilon_{23} \\ \epsilon_{13} \end{pmatrix} \quad (4.14)$$

Three IFEM calculations with varying boundary conditions in form of displacement fields are necessary in order to calculate all entries of the stiffness matrix C (equation 4.15). Entries in the first column (C_{11}, C_{21}, C_{31}) and the shear entry C_{44} are calculated by applying the global strain field as follows,

$$\begin{pmatrix} \sigma_{11} \\ \sigma_{22} \\ \sigma_{33} \\ \sigma_{12} \\ \sigma_{23} \\ \sigma_{13} \end{pmatrix} = \begin{bmatrix} C_{11} & C_{12} & C_{13} & 0 & 0 & 0 \\ C_{21} & C_{22} & C_{23} & 0 & 0 & 0 \\ C_{31} & C_{32} & C_{33} & 0 & 0 & 0 \\ 0 & 0 & 0 & C_{44} & 0 & 0 \\ 0 & 0 & 0 & 0 & C_{55} & 0 \\ 0 & 0 & 0 & 0 & 0 & C_{66} \end{bmatrix} \begin{pmatrix} \epsilon_{11} \\ 0 \\ 0 \\ \epsilon_{12} \\ 0 \\ 0 \end{pmatrix} \quad (4.15)$$

where the strain field ϵ is converted to a displacement field using periodic boundary

conditions as described above (section 4.3.2). In order to calculate the remaining entries of the stiffness matrix C two additional global strain fields are applied in separate IFEM calculations.

$$\left\{ \begin{array}{c} 0 \\ \epsilon_{22} \\ 0 \\ 0 \\ \epsilon_{23} \\ 0 \end{array} \right\}, \left\{ \begin{array}{c} 0 \\ 0 \\ \epsilon_{33} \\ 0 \\ 0 \\ \epsilon_{13} \end{array} \right\} \quad (4.16)$$

All nine elastic properties can be readily calculated by inverting the resulting stiffness matrix C to arrive at the compliance matrix S for orthotropic materials which is commonly written as,

$$S = \begin{bmatrix} \frac{1}{E_1} & -\frac{\nu_{21}}{E_2} & -\frac{\nu_{31}}{E_3} & 0 & 0 & 0 \\ -\frac{\nu_{12}}{E_1} & \frac{1}{E_2} & -\frac{\nu_{32}}{E_3} & 0 & 0 & 0 \\ -\frac{\nu_{13}}{E_1} & -\frac{\nu_{23}}{E_2} & \frac{1}{E_3} & 0 & 0 & 0 \\ 0 & 0 & 0 & \frac{1}{G_{23}} & 0 & 0 \\ 0 & 0 & 0 & 0 & \frac{1}{G_{31}} & 0 \\ 0 & 0 & 0 & 0 & 0 & \frac{1}{G_{12}} \end{bmatrix} \quad (4.17)$$

Elastic constituent (matrix, fiber, interface) input properties are assumed to be isotropic and are given in table 4.1 A limited number of experimentally determined

Table 4.1: Elastic constituent input properties

Material	Young's Modulus E [$\frac{N}{mm^2}$]	Poisson's Ratio ν
Matrix	340000	0.14
Fiber	380000	0.14
Interface	10000	0.19

elastic lamina constants can be found in *Dunn* (2010). Transversely isotropic con-

stants based on the CCM model are shown in column two of table 4.2. It can be seen that a good match is achieved between IFEM and CCM predictions and the experimentally measured Young’s modulus in the fiber direction.

Table 4.2: Comparison of elastic lamina properties

Property	Experimental	CCM	IFEM
$E_{11}[GPa]$	318	329	332
$E_{22}[GPa]$	257	195	254
$E_{33}[GPa]$	n/a	n/a	254
ν_{12}	n/a	0.14	0.14
ν_{13}	n/a	n/a	0.14
ν_{23}	n/a	n/a	0.107
$G_{12}[GPa]$	n/a	107	111
$G_{23}[GPa]$	n/a	75	91
$G_{13}[GPa]$	n/a	n/a	111

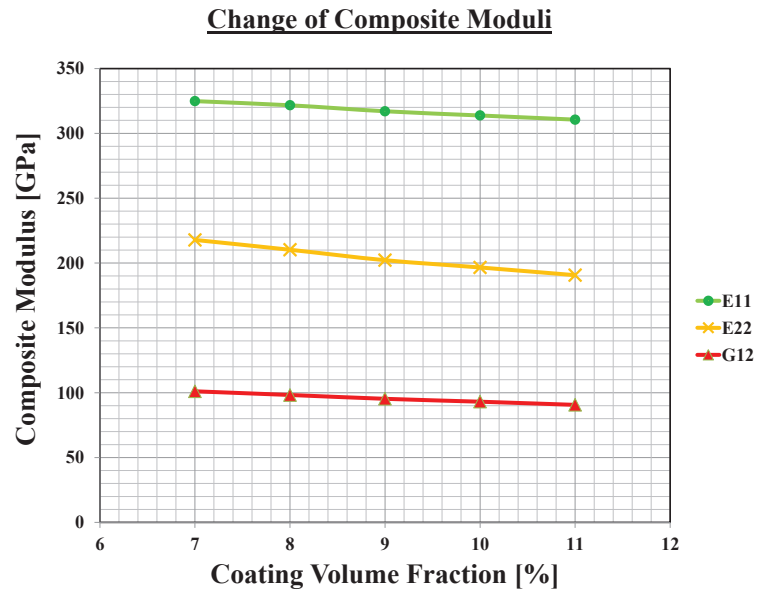
4.4.1 Influence of Volume Fractions on Composite Properties

Perfect control of constituent volume fractions within CMCs is inherently difficult especially for the fiber coating material. A numerical volumetric parameter study has been conducted to study the effects of varying constituent volume fractions on the composite properties. A five fiber RVE was used in this study as shown in Figure 4.6. A constant fiber volume fraction of 21% was used. The coating volume fraction varies from 7 - 11% leading to a matrix volume fraction within the range of 68 - 72%. All engineering constants show a linear dependence on the coating volume fraction except for ν_{12} . The constituent material properties are given in table 4.3. Young’s modulus of the fiber was 380 GPa, Young’s modulus of the matrix was 340 GPa. Uncertainty exists with respect to the elastic stiffness of the coating. However, experiments suggest that it is an order of magnitude lower than the fiber and matrix stiffness and lies within the range of 4 GPa to 12 GPa. In this study it was chosen to be 10 GPa. As expected from a simple rule of mixture analysis, an increased coating volume fraction decreases the composite stiffness. The longitudinal modulus decreases from 325 MPa

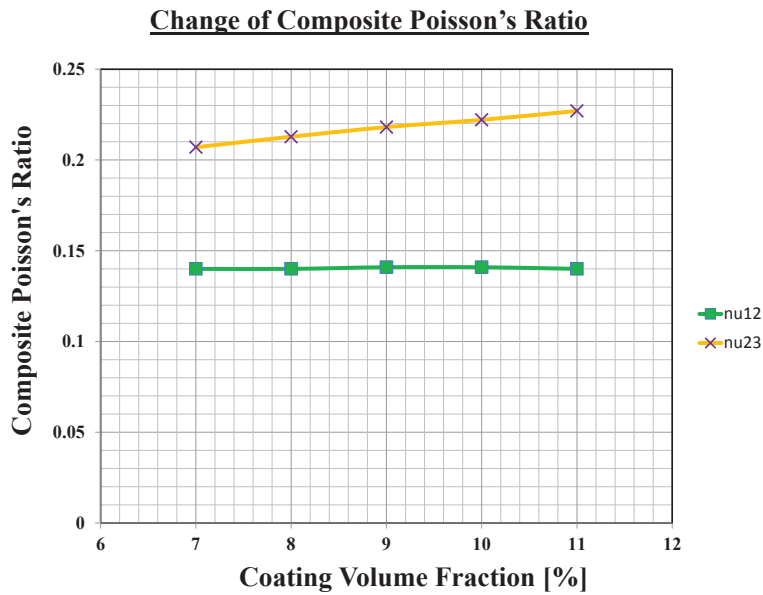
at $v_c = 7\%$ to 310 MPa at $v_c = 11\%$. The transverse modulus varies within the range of 219 MPa to 191 MPa. The shear modulus decreases from 101 MPa to 92 MPa. ν_{23} increases from 0.208 to 0.228. ν_{12} remains constant for the range of coating and matrix volume fractions studied here.

Table 4.3: Constituent input properties for varying coating & matrix volume fraction

Material	Young's Modulus E [MPa] [$\frac{N}{mm^2}$]	Poisson's Ratio ν	Volume Fraction %
Matrix	340000	0.14	68 - 72 vol%
Fiber	380000	0.14	21
Coating	10000	0.19	7 - 11 vol%



(a)



(b)

Figure 4.5: Change of *a*) composite moduli *b*) composite Poisson's ratios with varying coating & matrix volume fractions

4.4.2 Influence of Constituent Elastic Properties on Composite Properties

In-situ constituent properties are generally intrinsically difficult to measure experimentally. A numerical study can be used to determine the effects of varying elastic composite properties. In this chapter the focus lies on Young's modulus for the three main constituents, e.g. fiber, fiber-coating, and matrix. Table 4.4 shows the input parameters used in the parameter study with varying coating Young's modulus. Transversely isotropic composite properties are assumed, e.g. $E_{22} = E_{33}$, $G_{12} = G_{13}$, and $\nu_{12} = \nu_{13}$. In CMC materials, there is a uncertainty in the coating properties. Figure 4.7 shows the influence on the lamina elastic properties with a change of the coating Young's modulus. As could be expected, based on a simple rule of mixture estimation, the lamina Young's modulus in fiber direction E_{11} is not affected since the stiffness of the fiber and matrix are orders of magnitudes larger compared to the coating. The transverse stiffness ranges between 150 GPa to 230 GPa with a change of the coating modulus between 1 GPa to 12 GPa. Transverse to the fiber the load can only be transferred between the matrix and the fiber through the coating. Hence, the transverse lamina stiffness E_{22} is more affected with a change of the coating stiffness. The shear moduli G_{12} and G_{23} change only slightly and range between 80 GPa to 90 GPa and 90 GPa to 100 GPa, respectively. Poisson's Ratio ν_{12} remains constant as can be seen from Figure 4.7b. However, ν_{23} ranges from 0.35 to 0.21 for the tested range of the coating stiffness.

Next, the influence of the fiber stiffness on the lamina properties are investigated. Young's modulus of the fiber was varied between 340 GPa and 400 GPa. Figure 4.8a depicts the change of lamina moduli. E_{11} changes slightly between 325 GPa and 335 GPa. Due to the low fiber volume fraction the influence of the fiber is small since the matrix has a comparable stiffness. The contribution of the fiber stiffness to the composite stiffness transverse to the fiber direction, E_{22} , is negligible since the compliant

coating does not transfer much load to the fibers. The shear moduli G_{12} and G_{23} are not affected due to the same reason. Figure 4.8b depicts the change of Poisson's ratio with a change in fiber Young's modulus. ν_{12} remains constant and ν_{23} shows minimal changes.

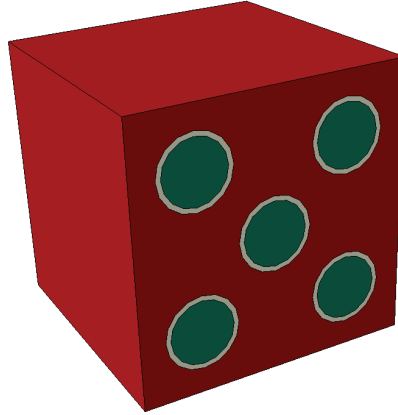
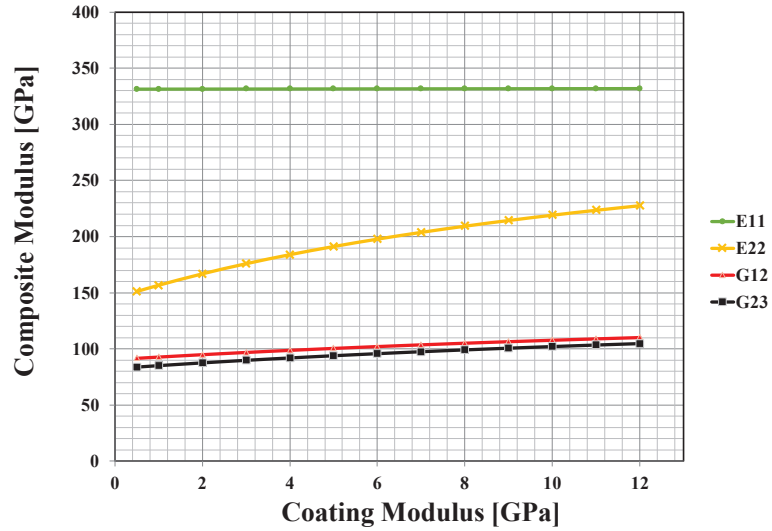


Figure 4.6: Five fiber RVE used for volumetric & constituent property parameter studies

Table 4.4: Constituent input properties for varying coating Young's modulus

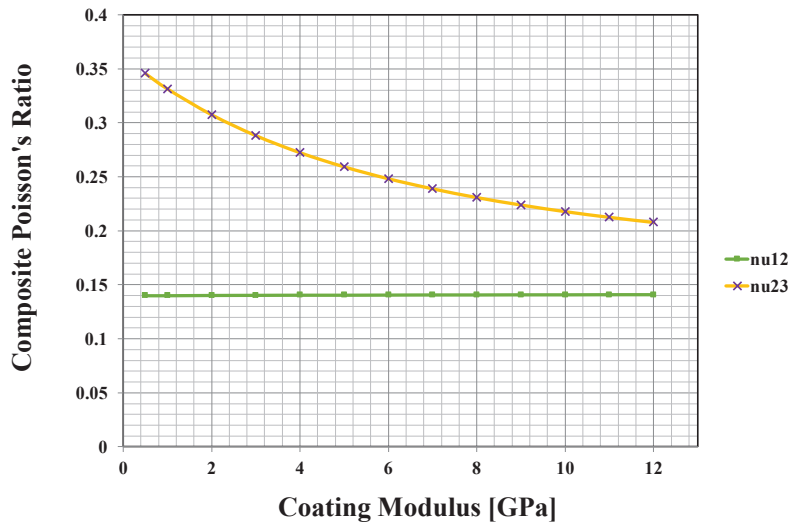
Material	Young's Modulus E [MPa] [$\frac{N}{mm^2}$]	Poisson's Ratio ν	Volume Fraction %
Matrix	340000	0.14	75
Fiber	380000	0.14	20
Coating	variable	0.19	5

Change of Composite Moduli



(a)

Change of Composite Poisson's Ratio



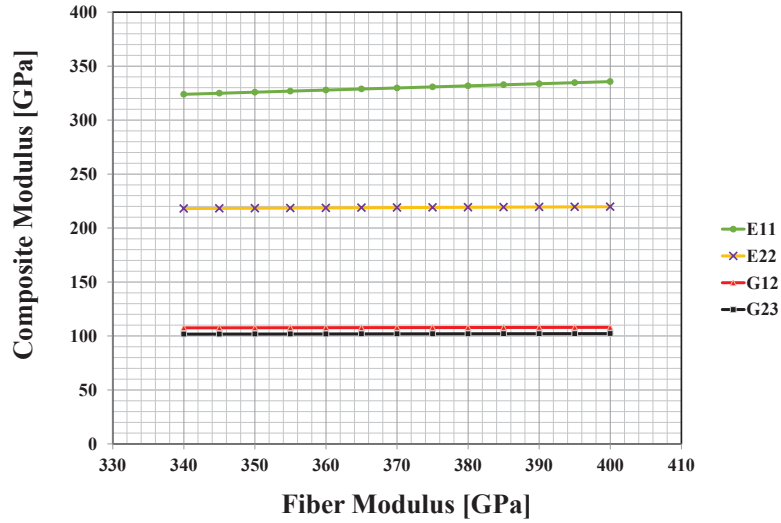
(b)

Figure 4.7: Change of *a)* composite moduli *b)* composite Poisson's ratios with varying coating modulus

Table 4.5: Constituent input properties for varying fiber Young's modulus

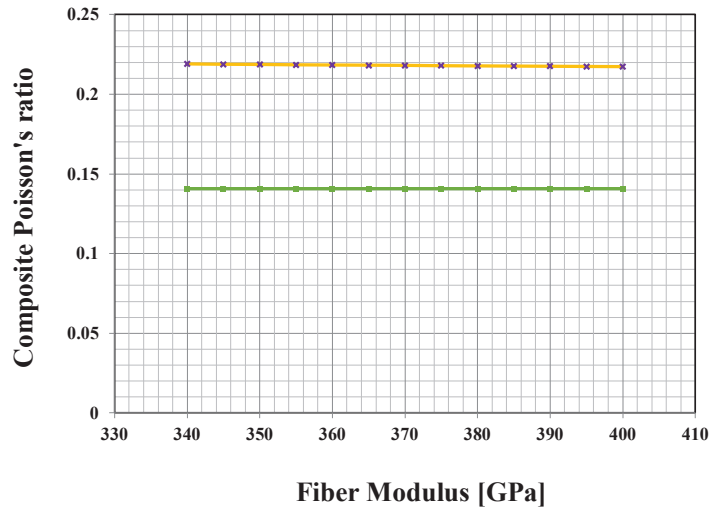
Material	Young's Modulus E [MPa] [$\frac{N}{mm^2}$]	Poisson's Ratio ν	Volume Fraction %
Matrix	340000	0.14	75
Fiber	variable	0.14	20
Coating	10000	0.19	5

Change of Composite Moduli



(a)

Change of Composite Poisson's Ratio



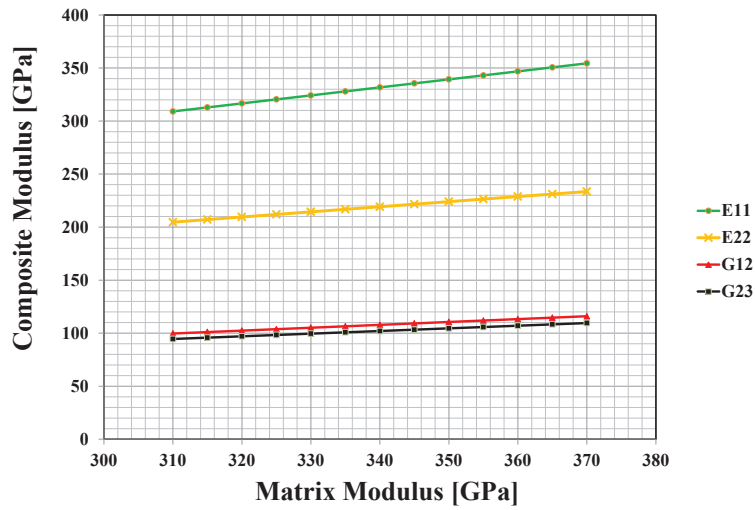
(b)

Figure 4.8: Change of *a)* composite moduli *b)* composite Poisson's ratios with varying fiber modulus

Table 4.6: Constituent input properties for varying matrix Young's modulus

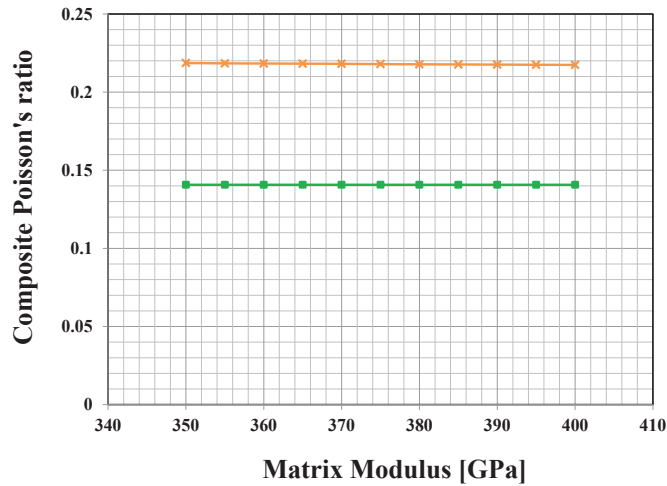
Material	Young's Modulus E [MPa] [$\frac{N}{mm^2}$]	Poisson's Ratio ν	Volume Fraction %
Matrix	variable	0.14	75
Fiber	380000	0.14	20
Coating	10000	0.19	5

Change of Composite Moduli



(a)

Change of Composite Poisson's Ratio



(b)

Figure 4.9: Change of a) composite Moduli b) composite Poisson's ratios with varying matrix modulus

4.5 Post-Peak Softening Implementation within IFEM

In this chapter the energy based crack band method is introduced on an elemental basis of the IFEM calculations. Damage and failure, as introduced in 3.3, are modeled for each constituent material separately. In addition to the elastic properties fracture properties, such as fracture toughness G_{IC} and material strength σ_{cr} , have to be supplied by the user for each constituent. The damage history for each element within the subcell model is stored in the user defined state variable space for all integration points of the macroscopic model. This ensures consistent progressive failure within the overall IFEM.

4.5.1 Implementation of Crack Band Failure Scheme within IFEM at the microscale

The post-peak strain softening model used within IFEM at the microscale is similar to the formulation covered in section 3.3 with the exception of the crack orientation. A maximum principle strain criterion is employed to predict the onset of damage.

$$\frac{\epsilon'}{\epsilon_{cr}} = 1 \quad (4.18)$$

It is assumed that once damage has initiated within a subcell the compliance of the element is degraded isotropically. There is no preferred crack direction within elements of the RVE, however the macroscopic response e.g. homogenized compliance of a subcell, remains orthotropic. This method yields an increased computational efficiency which is of great importance to multi-scale modeling approaches. The use of the crack band method results in mesh objective predictions within the RVE's. However, the component level simulation remains mesh dependent. This needs to be taken into account when choosing a discretization size of the global model. Equations

3.26 are changed as follows,

$$[S] = \frac{1}{(1-D)} \begin{bmatrix} S_{1111} & S_{1122} & S_{1133} & 0 & 0 & 0 \\ S_{1122} & S_{2222} & S_{2233} & 0 & 0 & 0 \\ S_{1133} & S_{2233} & S_{3333} & 0 & 0 & 0 \\ 0 & 0 & 0 & S_{1212} & 0 & 0 \\ 0 & 0 & 0 & 0 & S_{2323} & 0 \\ 0 & 0 & 0 & 0 & 0 & S_{1313} \end{bmatrix} \quad (4.19)$$

4.5.2 Numerical Calculation of Jacobian Matrix for Implicit Simulations

All numerical predictions in this work were carried out with an implicit solution methodology in Abaqus. Due to the nature of the backward Euler scheme used in Abaqus implicit simulations a Jacobian matrix $\frac{\delta \Delta \sigma}{\delta \Delta \epsilon}$ has to be supplied at the end of the user defined material law (*Abaqus* (2008)). In implicit FEM calculations it is used to find the next converged solution. In case of the undamaged subcell the Jacobian matrix is constant and calculated only once in advance of the actual multi-scale simulation. It is stored in a fortran compiled file and can be called at any time during the IFEM simulation. In case of damage in the subcell model a new Jacobian matrix should be calculated to guarantee fast convergence of the macroscopic model. It should be noted that a constant Jacobian matrix might lead to convergence but at the cost of losing a quadratic convergence rate during the Newton-Raphson scheme used in the Abaqus FEM solution process. *Stein and Sagar* (2008) showed that fewer numbers of equilibrium iterations are needed at each increment to arrive at the desired solution accuracy. Since IFEM leads to a numerical material law for composite materials, the Jacobian matrix, denoted in Abaqus UMATs as DDSDD, must be

determined numerically. The procedure is as described in section 4.4.

$$\left\{ \begin{array}{c} \epsilon_{11} \\ 0 \\ 0 \\ \epsilon_{12} \\ 0 \\ 0 \end{array} \right\}, \left\{ \begin{array}{c} 0 \\ \epsilon_{22} \\ 0 \\ 0 \\ \epsilon_{23} \\ 0 \end{array} \right\}, \left\{ \begin{array}{c} 0 \\ 0 \\ \epsilon_{33} \\ 0 \\ 0 \\ \epsilon_{13} \end{array} \right\} \quad (4.20)$$

Three separate IFEM calculations on the damaged subcells have to be carried out with three global strain vectors, Eq. 4.20, applied on the boundaries of the damaged subcell separately and the corresponding stress state is determined. Equations 4.21 depict the calculation of the first column of the Jacobian matrix as well as the entry S_{1212} .

$$\left\{ \begin{array}{c} \sigma_{11} \\ \sigma_{22} \\ \sigma_{33} \\ \sigma_{12} \\ \sigma_{23} \\ \sigma_{13} \end{array} \right\} = \left[\begin{array}{cccccc} S_{1111} & S_{1122} & S_{1133} & 0 & 0 & 0 \\ S_{1122} & S_{2222} & S_{2233} & 0 & 0 & 0 \\ S_{1133} & S_{2233} & S_{3333} & 0 & 0 & 0 \\ 0 & 0 & 0 & S_{1212} & 0 & 0 \\ 0 & 0 & 0 & 0 & S_{2323} & 0 \\ 0 & 0 & 0 & 0 & 0 & S_{1313} \end{array} \right] \left\{ \begin{array}{c} \epsilon_{11} \\ 0 \\ 0 \\ \epsilon_{12} \\ 0 \\ 0 \end{array} \right\} \quad (4.21)$$

This scheme requires additional numerical effort on the micro-scale model but ultimately leads to a reduction of time required to solve the macroscopic finite element problem due to better convergence.

4.6 Single Edge Notch Uniaxial Monotonic Tensile Simulation

In this section a single edge notch model is simulated and the stress-strain response and crack paths are predicted for three different lay-ups. The notch dimensions are presented in Figure 4.10. A notch width of 0.18 mm with a notch radius of 0.09 mm is used. The notch depth was approximately 1/15th of the specimen gauge section width. Figure 4.11 shows the boundary conditions and loading on the model. The edges X_0 and X_1 are subjected to a displacement in negative and positive x-direction, respectively. The corner A at X_0 is prevented from moving in y- and z-direction to avoid rigid body movement. All models are meshed with three dimensional 8-noded elements (C3D8R). Important to note here is that like any real specimen no strict symmetry in geometry with respect to the center line of the notch exists which leads to unsymmetrical failure as described below. In addition, the microstructure was randomized by using six geometrically unique RVEs which are randomly distributed throughout the model. The RVEs include 1-, 2-, or 3-fibers each. One RVE was modeled with touching fibers. Although the RVEs result in comparable elastic composite properties, e.g. pre-peak behavior, differences exist for the post-peak regime. RVEs with clustering fibers exhibit higher stress concentrations and tend to initiate damage at a lower stress state compared to other RVEs. The constituent elastic and fracture properties are given in table 4.7. A maximum principle strain criterion was used for each constituent (equation 4.18).

By introducing a characteristic element length to the microscale constituent model it was shown in chapter 3.3.2 that mesh objectivity is preserved. However, the current multi-scale model does not transfer the mesh objectivity across scales. A mesh convergence study is therefore necessary. Three mesh renditions of the same single edge notch model are compared as depicted in figure 4.12. Mesh I consists of 37140

degrees of freedom (dof), mesh II consisted of 110260 dofs, and mesh III consisted of 269835 dofs. All models were run in a cluster environment on a single node with 12 processors. Due to the increased number of integration points, the model runtime increased from 1042 min for the coarse mesh to 3105 min for mesh III, an increase of 297%. The memory usage rose from 689 Mb to 4638 Mb representing an increase of 673%.

Table 4.7: Constituent elastic and fracture properties used in single edge notch finite element simulations

Material	Young's Modulus (MPa)	Poisson's Ratio ν	Critical Strain ϵ_{cr} (MPa)	Fracture Toughness G_{IC} (N/mm)
Matrix	340000	0.14	0.001	0.05
Coating	10000	0.19	0.04	0.05
Fiber	380000	0.14	0.012	0.005

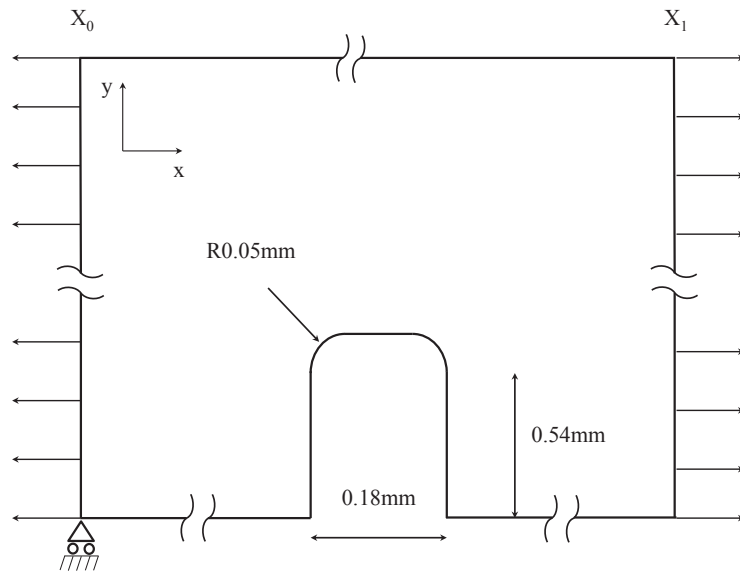


Figure 4.10: Notch dimensions of single edge notch tensile simulation

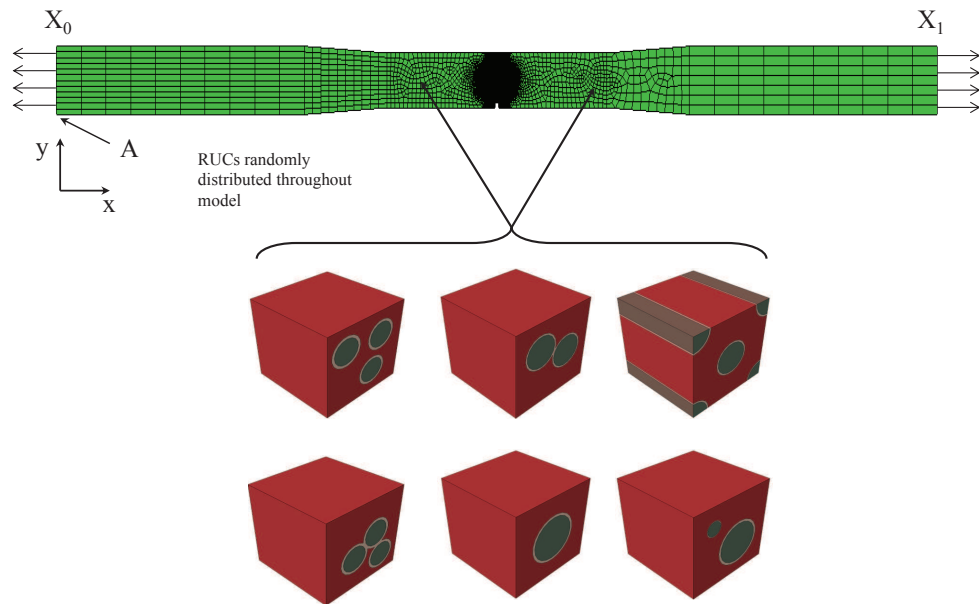
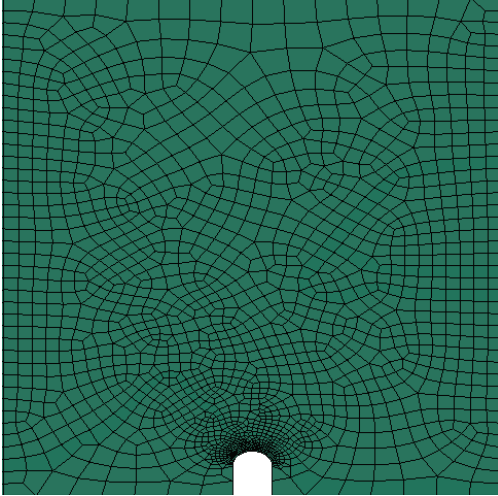
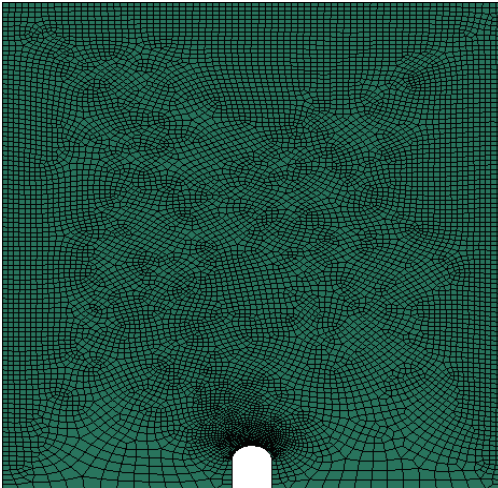


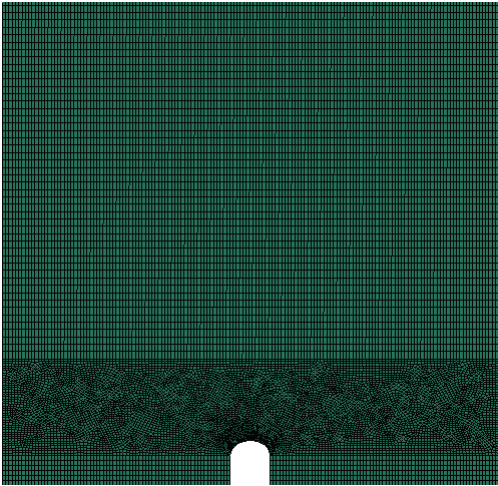
Figure 4.11: Boundary conditions of a $[0/90]_{25}$ single edge notch tensile multi-scale simulation



(a)



(b)



(c)

Figure 4.12: Three meshes of the single edge notch finite element model for mesh convergence study *a)* coarse mesh *b)* fine mesh *c)* fine structured mesh. A field of view was restricted to the area around the notch in order to resolve mesh details

Figure 4.13 shows the stress-strain response of a single edge notch specimen at room temperature and results from IFEM predictions with three discretization sizes. The experiments were conducted on "as received" specimens. It is assumed that residual stresses from the manufacturing process were present in the specimen. A disparity between the IFEM predictions and the experimental results is therefore expected.

As mentioned above, mesh objectivity is not transferred between the macroscopic and microscopic scale. The introduction of a characteristic element length into the crack-band formulation guarantees mesh independence of the IFEM-RVE models provided that the maximum characteristic element length is smaller than the critical length as described in chapter 3.3.1 . However, the ultimate load and post-peak behavior of the macroscopic response will depend on the discretization size used on the macroscopic scale model. Larger elements and therefore larger volumes will increase the apparent dissipated energy. This dispute is suggested to be addressed in future work. The pre-peak elastic composite stiffness is not affected by the mesh size as can be seen from figure 4.13. The stress reported here is the net section stress, e.g. reaction force/net section area. The reported strain is the average measure of the surface strain field in the tensile direction (ϵ_{xx}) comparable to the area used in figure 2.41. The ultimate net section stress decreases by 2% from 240 MPa predicted with mesh I to 230 MPa as predicted by the discretization size used in mesh III. Mesh convergence has been achieved with mesh II since the ultimate load does not change significantly between mesh II and mesh III. Minor differences in the predicted strain to failure are observable and can be attributed to the location change of the measured strain values due to the discretization size of the elements. The initial elastic stiffness is in good agreement with the experiment. Both, the ultimate load and strain to failure match with the experimental results. The strain to failure of the matrix was increased in this study to account for residual stresses which effect the experimentally measured

stress-strain response. A deviation from linearity can be observed before the ultimate load is reached for both, the IFEM prediction and experimental results. Damage initiation can be observed before the onset of non-linearity in the stress-strain response. Damage initiation observations based on the DIC results tend to be subjective due to the resolution restrictions and are regarded as approximate measures. Localized damage, in form of microcracks, might occur before it can be detected with the DIC system. Damage onset during the IFEM multi-scale simulation is easily measurable and corresponds to the first element that exceeds the critical strain within an IFEM RVE. Damage initiation is predicted at 47 MPa, 48 MPa, and 48 MPa for mesh I, mesh II, and mesh III, respectively. Initially cracking can be observed in two distinct regions slightly offset of the notch-tip. These cracks evolve under further increased loading until one crack dominates. The angle spanned between the simultaneously occurring cracks is determined by the composite layup. It is larger for unidirectional laminates and smaller for cross-ply composite lay-ups. Upon increased growth of the dominant crack the stress field around this crack intensifies and simultaneously decreases around the second crack. This leads to a reduction of the crack opening of the less dominant crack as was shown experimentally by *Tracy* (2014). The phenomenon of a single dominant crack advancing can only be observed numerically if antisymmetry is introduced in the finite element model. In the IFEM multi-scale methodology this is achieved through the use of multiple geometrically different RVEs and a non-symmetric mesh, as mentioned above. A material property based randomization is introduced in chapter 4.7.1. Figure 4.13 shows the crack development at three stress levels, e.g. 150 MPa, 250 MPa, and at the ultimate stress of each simulation. The crack path is similar for the three mesh sizes investigated in this chapter. The crack width is determined by the element width. Smaller elements will result in smaller crack width as can be observed in the illustrations of the crack paths in figure 4.13. Due to the small element size of the models only the specimen edges are shown. In

order to resolve the crack details, the field of view of the plots was restricted to the area within the vicinity of the notch.

The response of single edge notch tensile models is investigated for four composite lay-ups. Input properties for the IFEM model as well as the used subcell were identical throughout the models and are given in table 4.7. Only the element directional assignments of the layers were set to create the following laminates: $[0/0]_S$, $[+45/-45]_S$, $[90/0]_S$, and $[0/90]_S$. Mesh III, as discussed above, was chosen for this study. Figure 4.14 depicts the stress-strain response and crack paths on the surface for $[0/0]_S$, $[+45/-45]_S$, and $[0/90]_S$ laminates. The elastic stiffness of the $[0/0]_S$ laminate is predicted as 290 GPa. Elastic stiffnesses for the $[90/0]_S$ and $[0/90]_S$ lay-ups are identical as expected based on the principles of the lamination theory and were predicted as 290 GPa. Young's modulus of the $[+45/-45]_S$ laminate was predicted to be lower compared to the other three laminates as 290 GPa. Longitudinal strain, ϵ_{xx} , calculated as total displacement / the length of the specimen, is used for this comparison.

Laminate $[0/0]_S$ sustained the highest fracture stress of 330 MPa. A noticeable non-linear stress-strain response before fracture can be seen in figure 4.14 for this laminate. Non-linearity corresponds to fibers bridging existing matrix cracks. Hence, matrix cracks in all four layers can develop before fracture of the fibers occurs. This leads to a larger combined crack opening and hence a non-linear stress-strain behavior. The fiber strength is an order of magnitude larger compared to the matrix strength. Hence, it is expected to observe higher ultimate stresses for laminates that contain high amounts of fibers that are oriented with the loading direction. The weakest laminate in this comparison is the $[+45/-45]_S$ lay-up which matches with the experimental observations discussed in chapter II. The ultimate stress was predicted as 170 MPa. The crack path of this prediction is given at lower stresses compared to the other three laminates, due to the comparably low ultimate stress. Point A in figure 4.14 represents a composite stress of 100 MPa. Crack growth of the $[+45/-45]_S$

laminates differs from the one observed for the other three laminates. A single crack initiates at the notch tip. This observation matches with the experimental results discussed in chapter II. On further loading splitting at the crack tip is observed before a single crack advances. The crack grows under a 45° -angle for approximately 1.5 mm before turning perpendicular to the loading direction. The numerical prediction showed two cracks before catastrophic fracture. Multiple cracks were observed in the experimental study in section 2.3.2. It is expected that a randomization of the microstructure will improve the model prediction. This will be further investigated in ongoing research.

Despite identical elastic responses of the $[90/0]_S$ and $[0/90]_S$ lay-ups, the ultimate crack paths and ultimate stress vary. Both models predict two sites of damage initiation slightly off-set of the notch tip and comparable crack propagation at point B (250 MPa). A single crack advances on the surface of the $[0/90]_S$ laminate before turning perpendicular to the loading direction. A single crack occurs at the notch tip, in-between the two existing cracks, of the $[90/0]_S$ model. It advances to a length of approximately 0.9 mm before splitting of the crack tip into two distinct cracks occurs. Figure 4.15 shows the propagation of damage in the outer-most layer of both $[90/0]_S$ and $[0/90]_S$ laminates in more detail. Damage initiates for both laminates well below any non-linearity in the stress-strain response can be detected. The damage initiates at two locations in the vicinity of the notch tip. The stress-strain response and crack propagation are similar in both laminates at a stress of 250 MPa. However the ultimate stress of the $[90/0]_S$ laminate was predicted to be higher. The post-peak crack path clearly shows that multiple cracks form in the outer 90-degree layer of the $[90/0]_S$ laminate (Points I and J). A second crack initiates at the opposite side of the notch and grows parallel to the existing crack until it ultimately joins with the second crack at the notch tip. The damage propagation in the $[0/90]_S$ laminate is predicted as a single crack, which originated at the notch.

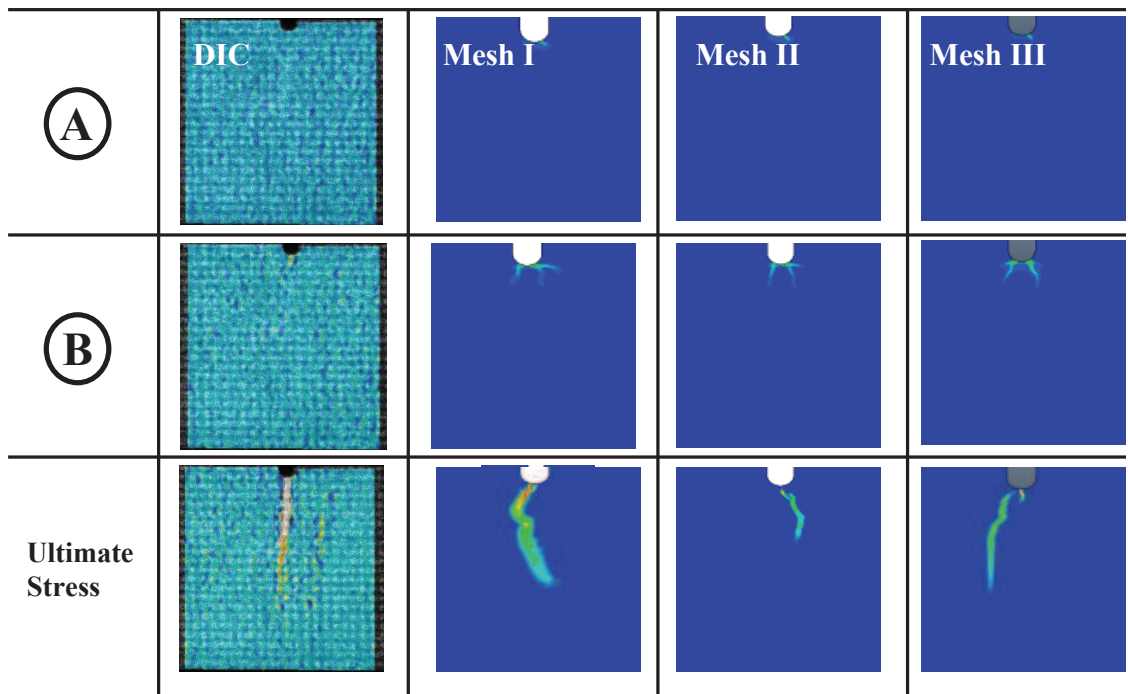
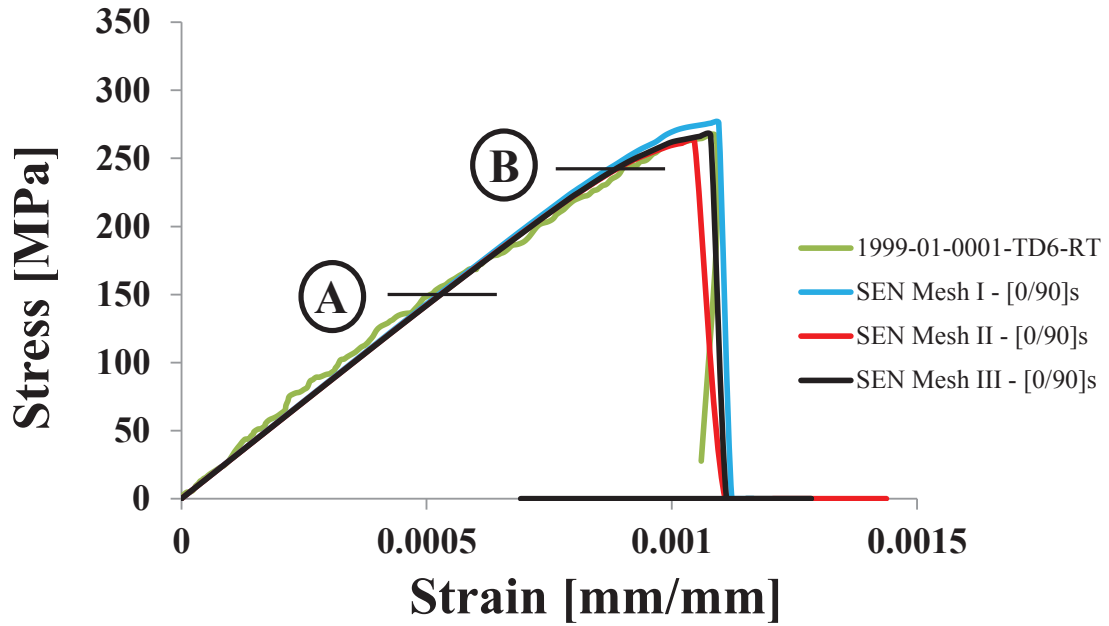


Figure 4.13: Stress-Strain response and crack paths of a cross-ply $[0/90]_s$ single edge notch monotonic tensile specimen - Experimental results compared with IFEM simulation (three discretization sizes)

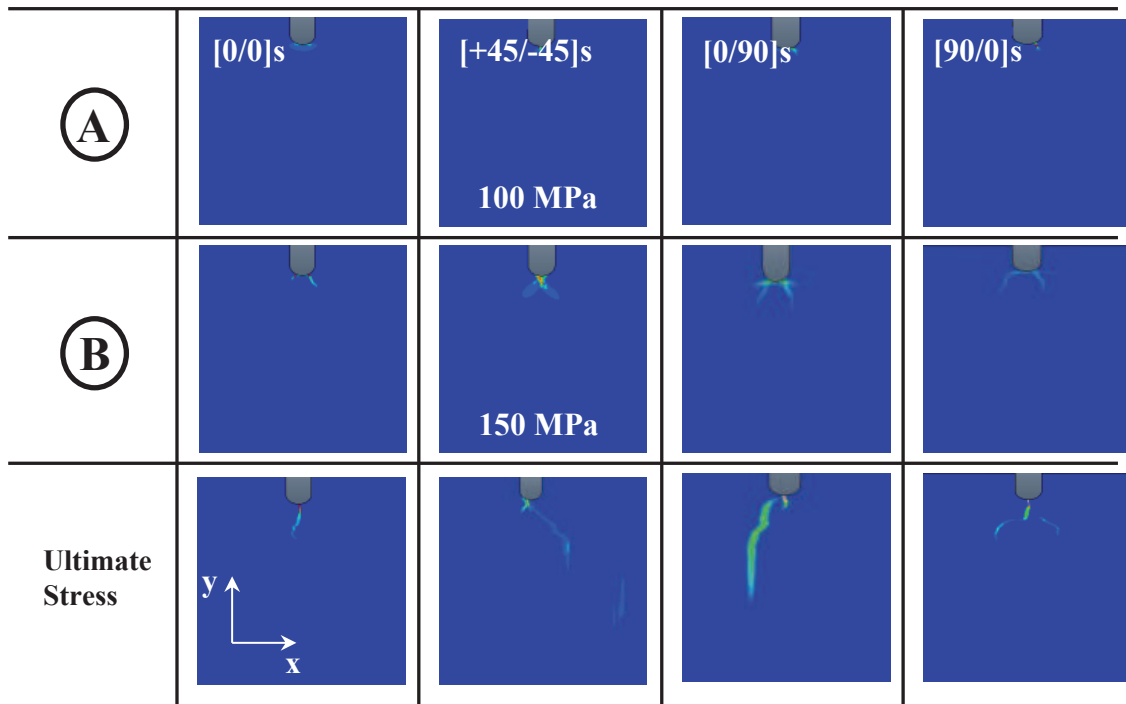
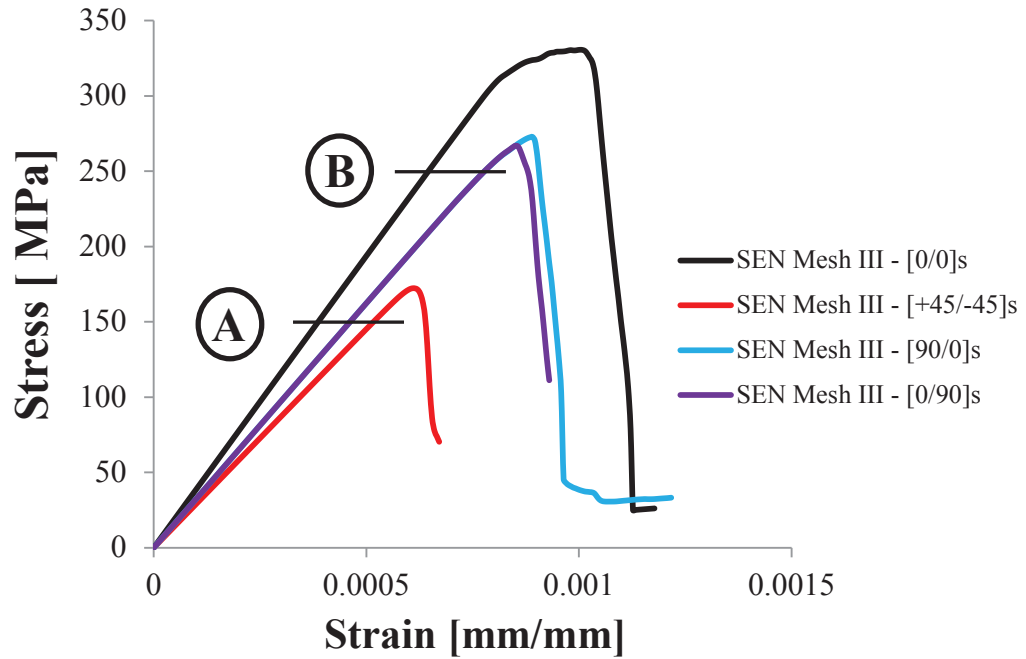


Figure 4.14: Stress-Strain responses and crack paths of the single edge notch monotonic tensile simulation - Comparison of four lay-ups $[0/0]_s$, $[+45/-45]_s$, $[90/0]_s$, and $[0/90]_s$

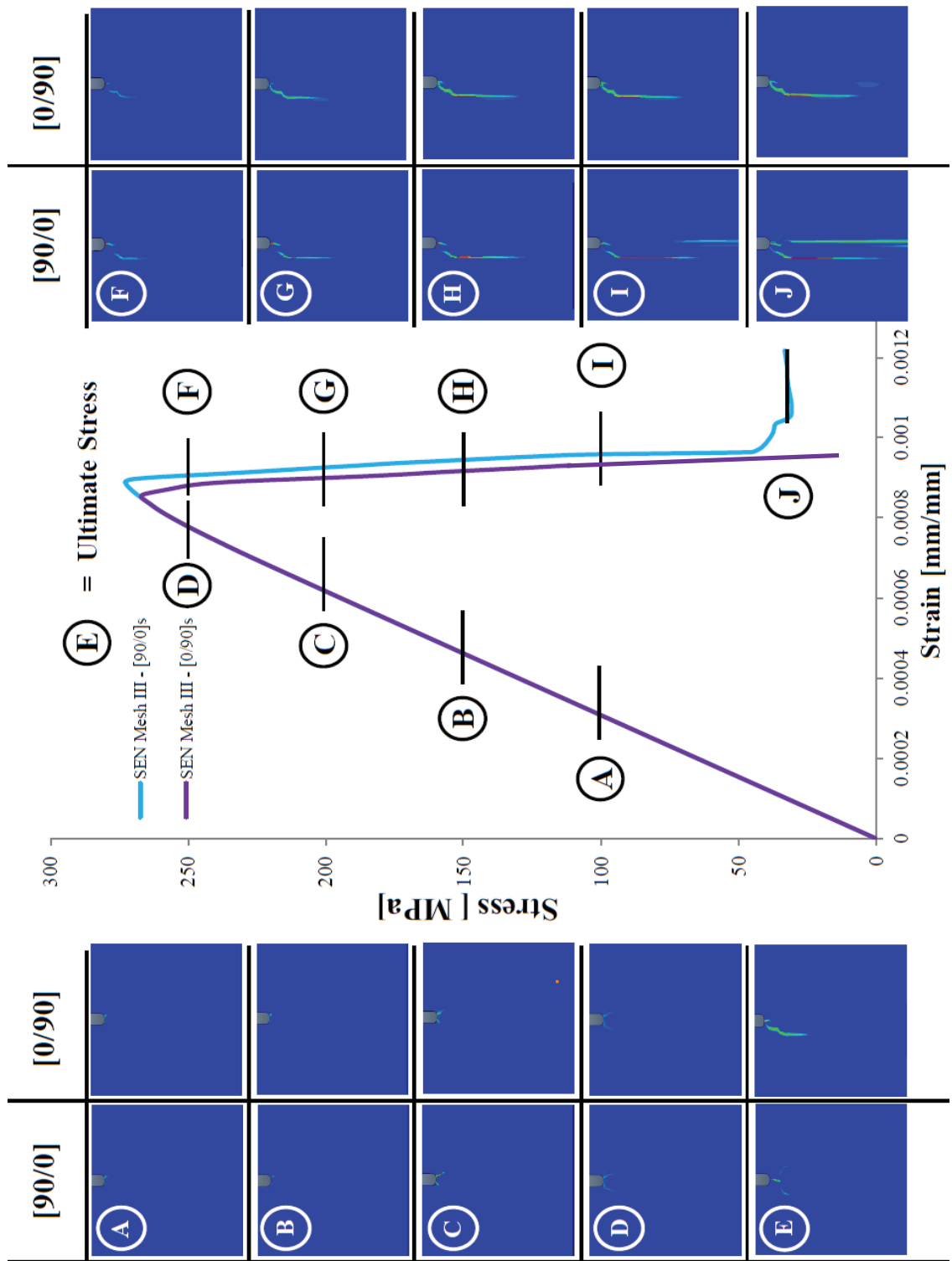


Figure 4.15: Stress-Strain responses and crack paths of the single edge notch monotonic tensile simulation - Comparison of $[90/0]_S$ and $[0/90]_S$ laminates

4.7 Smooth-Bar Uniaxial Monotonic Tensile Simulation

In this section 3D-IFEM will be used to analyze the failure of an eight layer $([0/90]_{2S})$ cross-ply smooth bar ceramic matrix composite specimen. The specimen dimensions are: 152.4 mm long, 10.16 mm wide at the gage section, and 12.7 mm wide at the grip section. Figure 4.16 depicts the boundary conditions. The left vertical edge was simply supported with a displacement restriction in x-direction. The right edge was displaced in x-direction by 0.1 mm. Each layer was modeled with one element through the thickness resulting in 400000 degrees of freedom. Orientations were assigned to each layer of the macroscopic model. Six randomly distributed subcells containing 1-, 2-, and 3-fibers each were used in order to accurately represent the real microstructure. Two of these subcells contained touching fibers, a phenomenon which is often observed in this type of CMCs.

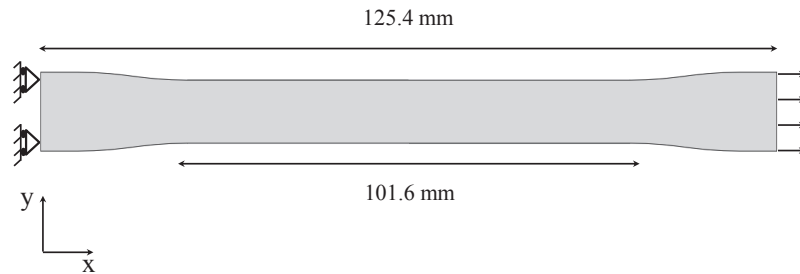


Figure 4.16: Simulation details of CMC smooth bar tension model

The stress-strain responses for both the numerical prediction and experimental result are shown in Figure 4.17. The strain corresponds to the accumulated strain over the gage section and was measured using a 1 inch extensometer. It can be seen

that the onset of non-linearity in the simulation appears to be more abrupt. This might be a result of small residual stresses still present in the real specimen. In an effort to minimize the effects of residual stresses in the experiment, specimens were heat treated before testing. The initial response and beginning of the post-peak stiffness predicted with 3D-IFEM is in good agreement with the experimental results, shown in figure 4.17. At a strain of 0.2% the prediction deviates from the experimentally measured response. The ongoing softening can likely be attributed to fiber-pullout. This effect is currently not modeled within the IFEM framework. A further discussion of this phenomenon is presented in chapter V.

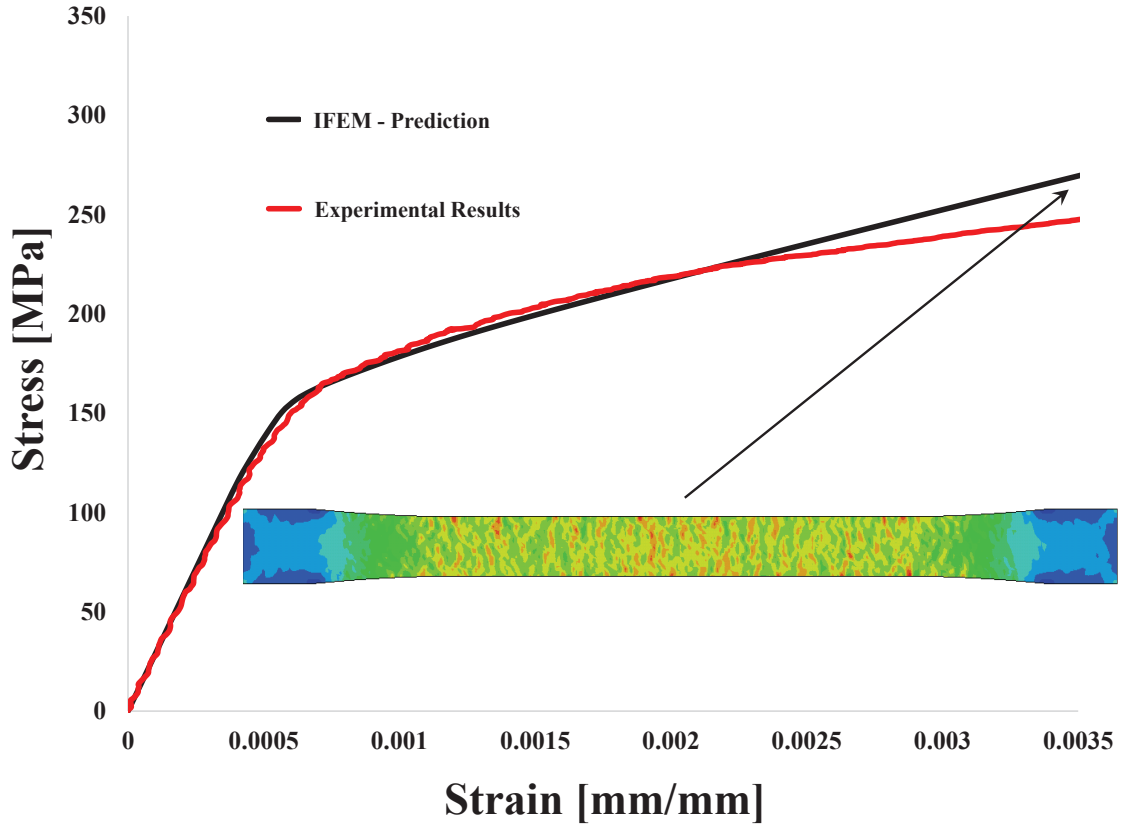


Figure 4.17: Stress-Strain response of a $[0/90]_{2S}$ smooth bar tensile specimen

No distinctive strain localizations are observed at the lamina level due to the lack of geometric stress concentrations. Generally impurities can be found in ceramic ma-

materials resulting in local changes of the matrix strength or fracture toughness. In an attempt to investigate the propagation of damage within each lamina the damage parameter D_{lamina} is introduced. $D_{lamina} = 0$ if no damage has occurred and $D_{lamina} = 1$ if an element has entered the post-peak regime. Figure 4.18 shows the development of damage in a $[0/90]_{2S}$ specimen in both 90° and 0° lamina with blue elements representing $D_{lamina} = 0$ and red elements representing $D_{lamina} = 1$. Damage initiates in the 90° -layers first before it spreads into the 0° -layers. Damage is also distributed throughout the 90° -layers whereas distinctive crack-bands form in the 0° -layers. This phenomenon can be explained with a shear-lag type analysis as discussed in chapter 3.2. Stresses in the immediate vicinity of a matrix crack in a 0° -layer are below the matrix strength. Stresses build up to a critical value within a characteristic length at which a new crack can form. This characteristic length diminishes with an increased loading of the specimen resulting in damage accumulating in-between the existing cracks.

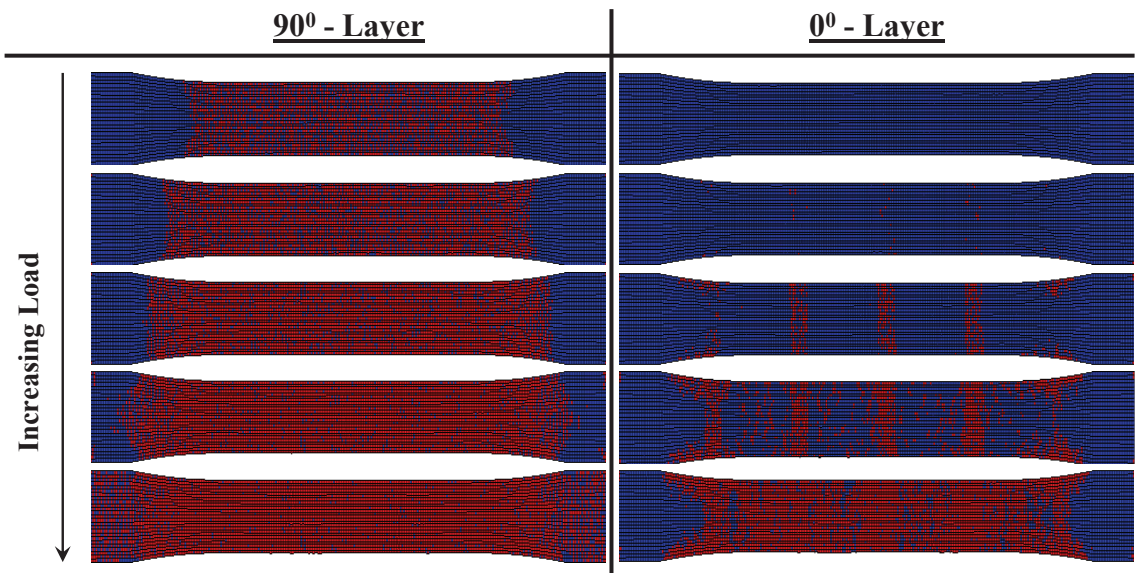


Figure 4.18: Damage propagation in 0° -layer & 90° -layer of a smooth bar $[0/90]_{2S}$ tensile simulation

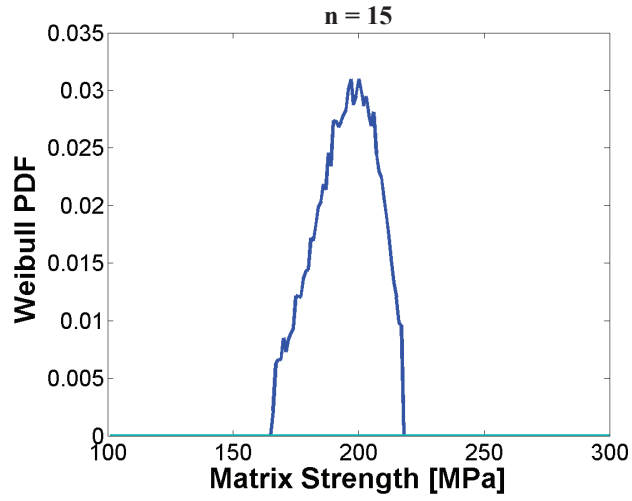
4.7.1 Modeling of Material Inhomogeneities

In the absence of geometrical stress risers such as notches it is important to include randomness in numerical models as shown in chapter 4.7. Material inhomogeneities are present in every specimen and this needs to be captured in multi-scale models. As shown before randomness can be included by using a fixed number of geometrically different subcells. In order to increase computational efficiency, a distribution of the material strength can be used instead of geometrical random subcells. One subcell with a small number of elements can be chosen and used throughout the macroscopic model optimizing the computational costs. In this chapter a two-parameter Weibull probability distribution is used to assign varying values of matrix strength to every element of the macroscopic model.

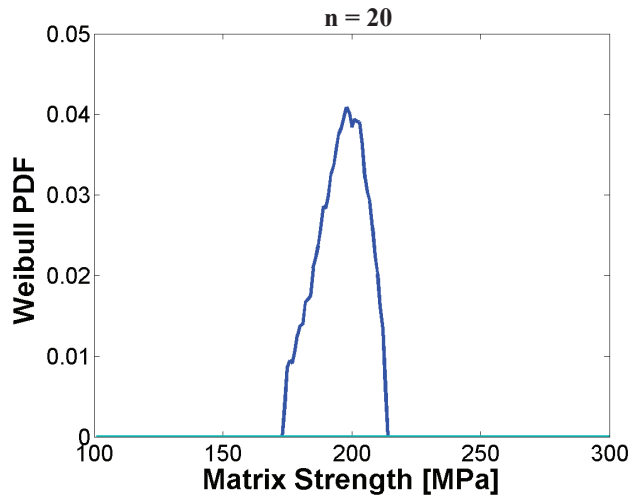
$$f = 1 - e\left(\frac{\sigma}{\sigma_0}\right)^n \quad (4.22)$$

where n is the Weibull modulus and σ_0 is the center strength. Generally, the parameters of the Weibull-Strength distribution are difficult to measure experimentally. Therefore it must be shown that variations of the shape parameter n will not impact the FEM predictions significantly. Three simulations, similar to the smooth bar simulation in chapter 4.7, were carried out. One single fiber subcell was used and the Weibull modulus was chosen as $n = 15$, $n = 20$, and $n = 30$. The distributions are shown in figure 4.19. An increase in the Weibull modulus leads to a more narrow strength distribution with an increase in probability for a particular strength. The smallest critical stress increases from $\sigma_{cr} = 160$ MPa for $n = 15$ to $\sigma_{cr} = 175$ MPa for $n = 30$. The maximum critical stress decreases from $\sigma_{cr} = 220$ MPa for $n = 15$ to $\sigma_{cr} = 210$ MPa for $n = 30$. Variations in the mean strength σ_0 will affect the onset of damage and therefore will shift the stress-strain response along the ordinate without affecting the shape. The following simulations were carried out with $\sigma_0 = 200$ MPa.

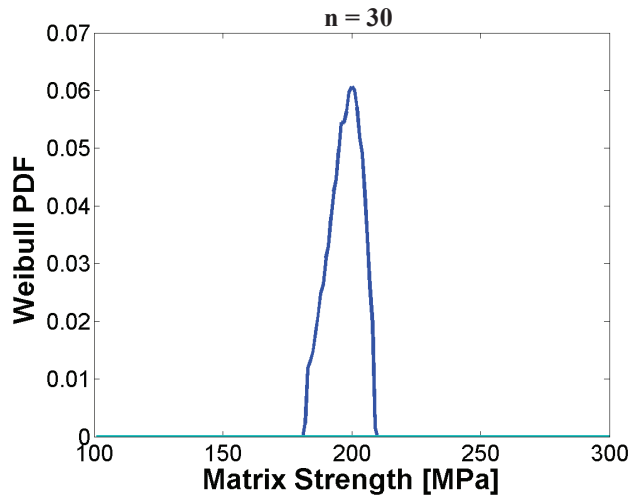
Figure 4.20 shows the stress-strain response as predicted by the IFEM models. No significant difference can be observed. The minimum strength for a Weibull modulus of $n = 15$ is lower compared to $n = 30$ however, the effect is minimal due to an increase in the number of elements with the lowest strength for $n = 30$. As can be seen from these results, a Weibull strength distribution is a viable tool to model material inhomogeneities. It is useful for numerical predictions that lack physical stress risers. Optimizations with respect to the model run-time can be achieved by choosing a RVE with a minimum number of features (elements) that captures the expected material non-linear response correctly. This technique does not address the damage behavior in the zero plies at strains larger than $\epsilon = 0.0025$ as discussed in chapter 4.7. It is assumed that fiber pull-out occurs which leads to strain softening in the stress-strain response (figure 4.20). Future work will include a combination of material strength variation and a distribution of geometrically different RVE's.



(a)



(b)



(c)

Figure 4.19: Weibull matrix strength distribution a) $n=15$ b) $n=20$ c) $n=30$

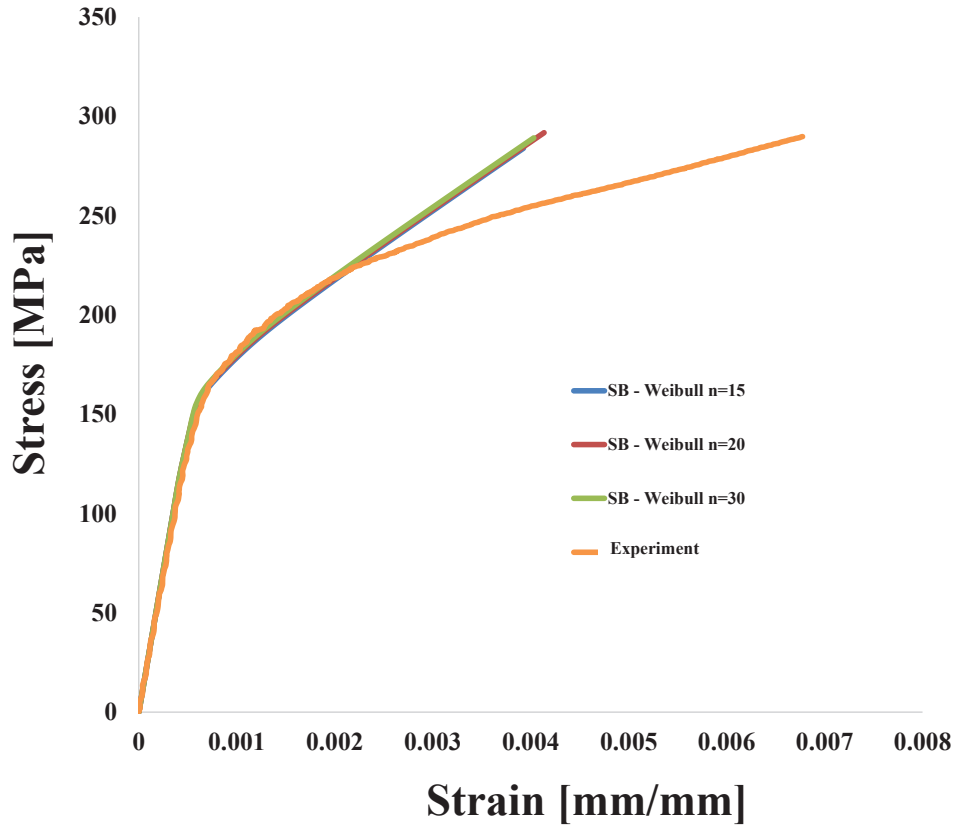


Figure 4.20: Effect of Weibull matrix strength distribution on the stress-strain response of CMC smooth bar FEM simulation

4.8 Conclusions

Finite element predictions of coupon level models were discussed in this chapter and a multi-scale method was introduced. A dehomogenization technique of a global strain field is used to transfer information at every integration point of a part level model (global model) to the microscopic model. Volume averaged stresses are used to homogenize the stress-field in the representative volume element (RVE). The homogenized stress field is passed back up to the global scale model. The stiffness tensor for each RVE is re-calculated upon damage initiation to retain a quadratic convergence with the Abaqus implicit solving scheme. It was shown that crack paths and

stress-strain responses of single edge notch specimens and smooth bar specimens can be predicted accurately. The energy based crack band method has been implemented in the constitutive equations of a finite element model to predict constituent damage within the RVE. Single edge notch predictions showed matrix damage initiated at two locations slightly off-set of the notch tip. Both cracks grow until fiber damage occurs and one crack overtakes the other and subsequently determines the final crack path. Damage of cross-ply smooth bar specimens was shown to exhibit matrix crack bands which lead to a non-linear strain softening stress-strain response. The ultimate strain to failure is determined by fiber fracture in the zero plies.

It was shown that the damage initiation and growth in the 0-ply is captured inadequately. Matrix cracks were shown to grow perpendicular to the fibers in mode I. However, if a crack tip encounters a fiber in a longitudinal ply, the crack tip deviates from pure mode I growth. If the crack propagates in the coating material along a fiber, the fracture mode changes to mixed mode behavior, e.g. mode I and mode II. A mixed mode damage initiation criterion, e.g. in equation 4.23, should therefore be considered for the coating material in the future.

$$\left(\frac{\epsilon_{11}}{\epsilon_{cr11}}\right)^2 + \left(\frac{\epsilon_{12}}{\epsilon_{cr12}}\right)^2 = 1 \quad (4.23)$$

Furthermore, an energetic mixed mode powerlaw should be used for the damage propagation in the coating as shown in equation 4.24.

$$\left(\frac{G_I}{G_{IC}}\right)^n + \left(\frac{G_{II}}{G_{IIC}}\right)^m = 1 \quad (4.24)$$

where n and m are experimentally determined parameters (*Johnson and Mangalgiri (1985)*).

CHAPTER V

Fiber Pull-Out Simulations

5.1 Introduction

The enhanced toughness of CMCs has led to more versatile engineering composite properties and has had a profound impact on their usefulness in industrial applications. Increased toughness is a result of the ability of the fibers to release energy through debonding and sliding. Propagating matrix cracks must be deviated along a fiber, rather than introducing premature fiber rupture, in order to increase the overall performance of the composite. This requires that an upper bound is placed on the interface toughness between the fiber/matrix or fiber/coating. Fiber debonding occurs at both the crack front and in the crack wake as shown in figure 5.1. Pure matrix cracks are mode I dominated whereas fiber debonding occurs in mixed mode. Many analytical models have been developed over the years to describe the mechanisms during fiber-pullout (*Hutchinson and Jensen (1990)*). Analytical models usually assume either a constant friction stress or Coulomb friction to predict interfacial sliding. *Evans (1988)* reviews damage behaviors of CMCs and gives an overview of damage parameters associated with mode I, mode II and mixed mode I-II damage behaviors. *Evans (1988)* states that the debond resistance of a bimaterial interface is characterized by two parameters: the critical strain energy release rate G_{IC} and the phase angle of loading ψ_i . The extent of debonding is influenced by

the residual stress field. Residual radial tension tends to increase debonding whereas residual radial compression reduces the extent of the debonded interface. *Sigl and Evans* (1989) studied the effects of residual stresses in detail on a simple composite cylinder model. It was suggested that an optimum residual strain exists to maximize the matrix cracking stress. *Thouless and Evans* (1988) used a statistical analysis of the location of fiber failure to establish the influence of pull-out on the mechanical properties of the composite. Fiber debonding effects were neglected and the findings were limited to CMCs that exhibit low interfacial bonding.

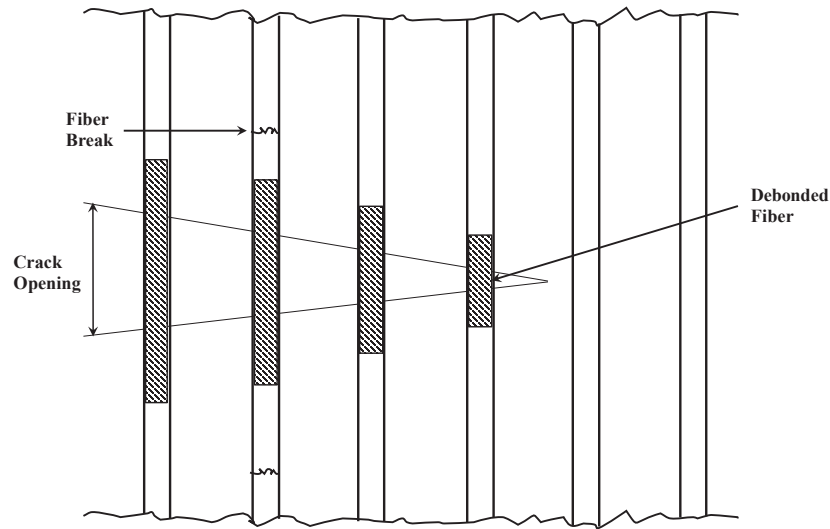


Figure 5.1: Schematic illustrating crack opening, fiber debonding, and fiber pullout at the crack front and in the crack wave

Experimental measurements of interfacial properties are inherently difficult. Two approaches have been developed to determine the constant sliding stress τ : Fiber-pushout tests and crack opening hysteresis tests. *Marshall and Oliver* (1987) used the indentation method to investigate properties of the fiber/matrix interface in SiC/glass ceramic composites. A nano-indenter pushes into a single fiber. The total displacement, a combination of the sliding displacement and indentation, and reaction force were measured. The frictional stress fell within the range of 2.8 - 3.5 MPa.

In the previous chapters, the effect of fiber-pullout in longitudinal plies was discussed.

The present chapter focuses on experimental observations of post-failure fiber pullout and addresses finite element modeling techniques that are able to capture interface debonding through cohesive elements. After initial debonding has occurred between two constituent materials Abaqus surface to surface contact formulation is used to simulate frictional effects. The Coulomb friction model is employed to describe the tangential sliding behavior. It is characterized by the friction coefficient μ

5.2 Experimental Measurements of Fiber-Pullout

The experimental procedures for high temperature testing of CMCs was discussed in chapter II. It was mentioned that the tested cross ply $[0/90]_{2S}$ CMC samples exhibited fiber-pullout at elevated temperatures. However, no significant pullout was observed at room temperature. Furthermore, no difference of the pullout length at the tested temperatures of $1093^{\circ}C$, $1204^{\circ}C$, and $1316^{\circ}C$ was noticeable. Figure 5.2 depicts the CMC specimen after the pullout test had been completed. The specimen has separated into two pieces and no fibers are bridging the crack surface. Two images at magnifications of 100x and 500x show the fiber pullout in the plies lined up with the tension direction. It is apparent that a variation in pullout length exist. The existence of fiber pullout clearly shows that the shear resistance of the coating material degrades at elevated temperature. The SEM images show that the coating remains attached to the matrix and fibers pull out of the coating. It is assumed that matrix cracking typically occurs in mode I until the crack tip reaches the fiber coating. If the crack is deflected along the fiber, mode II dominates.

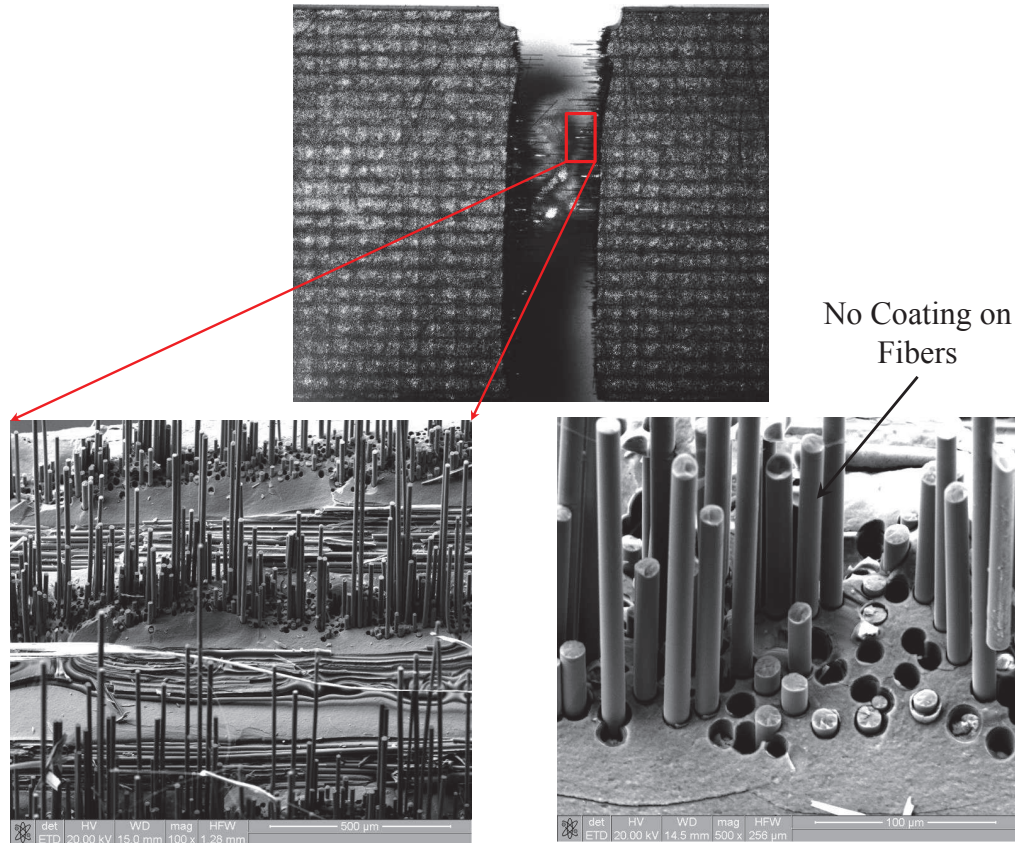


Figure 5.2: Investigation of fiber pullout of a CMC specimen tested at 1315° , the top picture shows the surface of the CMC specimen after fracture, bottom left SEM image taken at 100x magnification, bottom right SEM image taken at 500x magnification

Fiber pull-out resistance was measured after a monotonic tensile test had been conducted and the specimen had fractured catastrophically. The temperature was held constant at the same level of the tensile test until the fiber pullout resistance test was completed. The load cell data and cross head displacement were recorded for the duration of the test. In addition, images of the separation were recorded at a frame rate of 2 images/sec. The displacement rate during the pullout test was set to 0.254 mm/min. It is assumed that the fibers fractured at various locations inside the composite during the monotonic tension test. Hence, the fiber pullout test can be used to calculate the sliding resistance stress only.

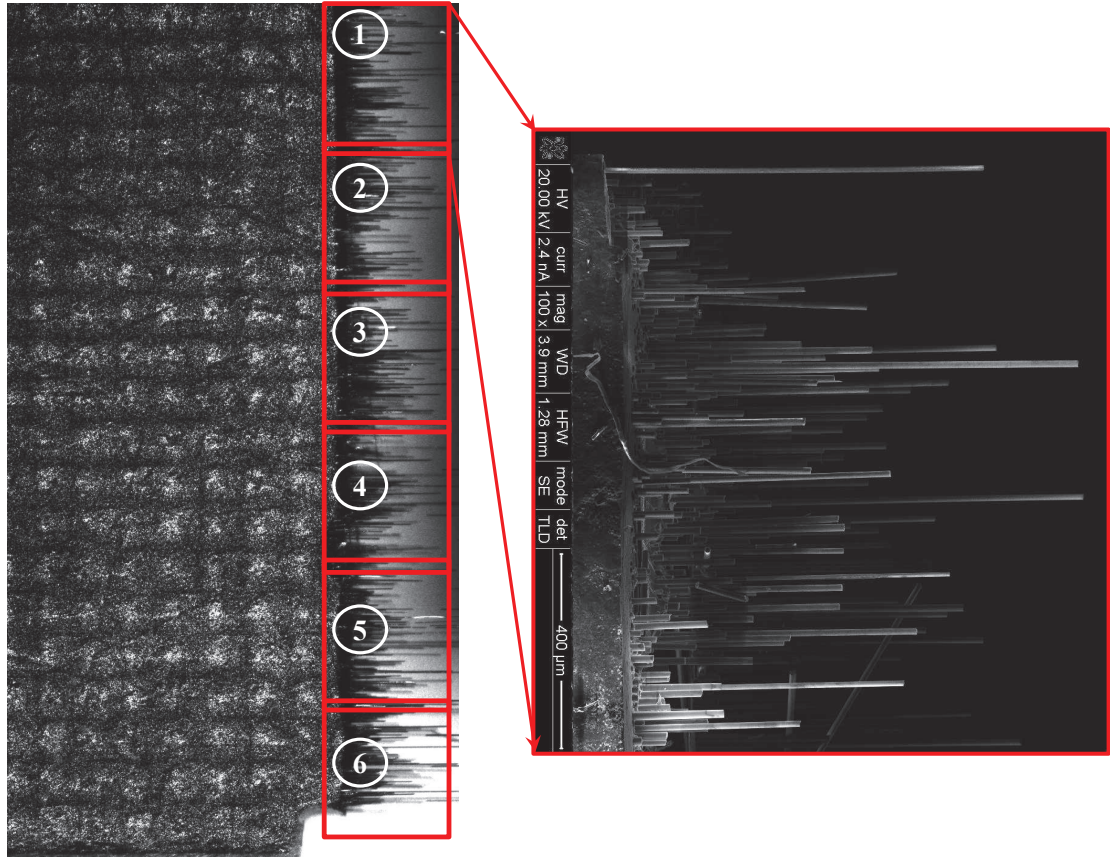


Figure 5.3: SEM micrograph used to measure fiber lengths of a specimen that was tested at 1315°

In order to measure the variations of the fiber pullout length, SEM images with a 100x magnification were taken perpendicular to the crack surface. Six images were taken to cover the entire specimen width. The images were taken with a slight overlap and eventually stitched to form a complete image of the the crack surface. Figure 5.3 illustrates an SEM image of the left edge of the crack surface. The fiber lengths of all fibers contained in the outer layer were measured. The histogram of the fiber pullout lengths is shown in figure 5.4. The histogram bin width was set to 0.05 mm. It can be observed that the majority of fibers exhibit short pullout lengths within the range of 0.1 - 0.25 mm. Larger fiber pullout lengths above 1 mm were measured, however the contribution to the load transfer is small due to the low number of fibers.

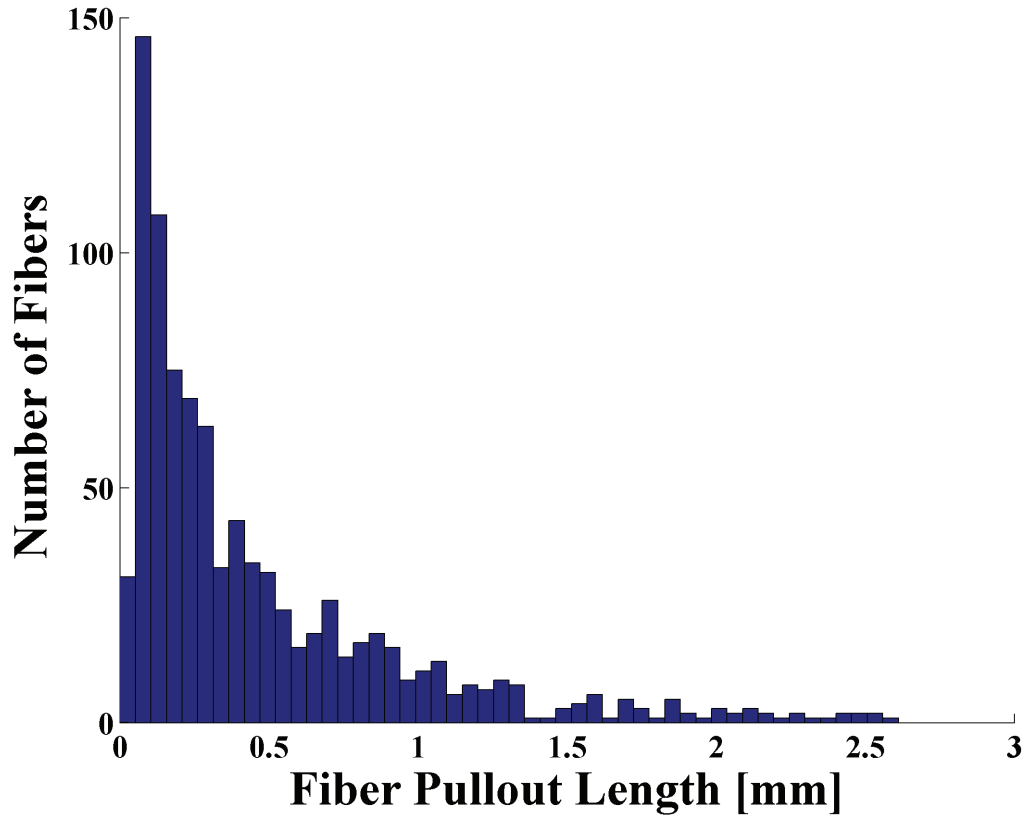


Figure 5.4: Histogram of the fiber pullout length for a single layer

5.3 Fiber-Pullout Micromechanics within the Finite Element Method

Fiber pull-out simulations were carried out in the finite element suite Abaqus. Three dimensional elements (C3D8) were used to model the constituent materials, e.g. fiber, matrix, and coating. User defined discrete cohesive zone elements (DCZM) were inserted between the nodes of the fiber and the coating material. The idea of DCZM elements is to treat the cohesive zone between two materials as a discrete spring foundation as shown in figure 5.5. In this study 1D-DCZM elements connect two initially coincidental node pairs, one node for each material. The DCZM elements adopted in this study differ from those reported in *Xie et al. (2006)*. In this work it

is assumed that no rotations occur between the fiber and coating surface. Only the relative perpendicular displacement determines the crack opening. Additional stresses due to the Poisson's expansion of the fiber are small compared to the cohesive-, and constant friction stress as was shown by *Marshall and Oliver* (1987).

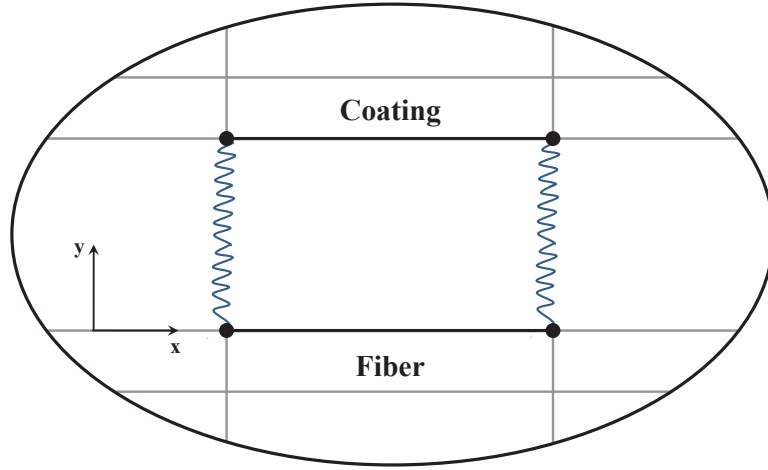


Figure 5.5: Two DCZM interface elements connecting two node pairs in the cohesive region between the fiber and coating material

In the present study a triangular cohesive law is used as shown in figure 5.6. The critical opening δ_{cr} can be calculated as,

$$\delta_{cr} = \frac{F_{cr}}{K_i} \quad (5.1)$$

where K_i is the initial stiffness which is selected to be large compared to the fiber stiffness. When the cohesive force F_{cr} and the fracture toughness g_{IC} are known the maximum crack opening δ_m can be calculated as,

$$\delta_m = \frac{2g_{IC}}{F_{cr}} \quad (5.2)$$

The post-peak tangent stiffness can be calculated as,

$$K_y = -\frac{F_{cr}}{\delta_m - \delta_{cr}} \quad (5.3)$$

The DCZM element stiffness vanishes ($K_y = 0$) for $\delta \geq \delta_{cr}$. After the DCZM elements have failed completely only frictional forces based on the Abaqus contact formulation act between the fiber and coating surfaces.

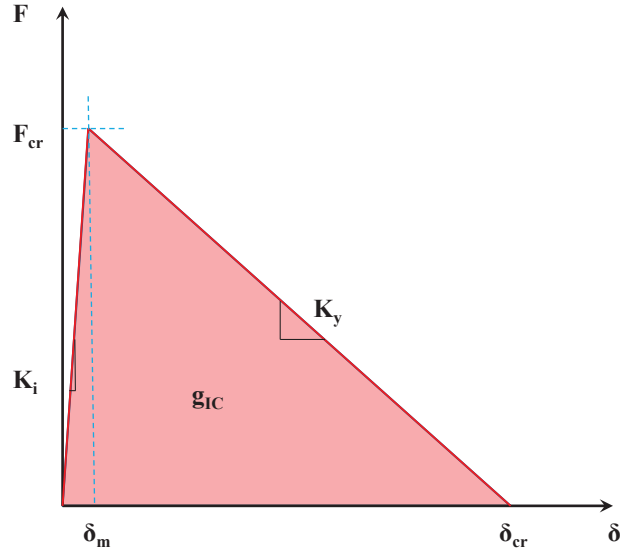


Figure 5.6: Triangular cohesive zone law for DCZM elements

The DCZM elements require the existence of initially coincidental nodes connecting the two bridging materials (fiber/coating). In order to create these node pairs on a cylindrical surface, a dummy material is introduced during the mesh creation as depicted in figure 5.7. The dummy material is meshed with a single element through the thickness. Due to the intricate geometries of the models a bottom-up mesh technique is used to create the finite element mesh in Abaqus. Subsequently a Matlab script was developed to collapse the dummy elements to zero thickness elements and to assign the DCZM elements to the coincidental node pairs. The volume fraction of the coating material had been reduced to account for the dummy material. Sub-

sequent to collapsing of the dummy element the original coating volume fraction is re-established. It is assumed based on the experimental findings that the bonding between the coating and the matrix is perfect. Debonding or frictional effects are not modeled between these two constituents.

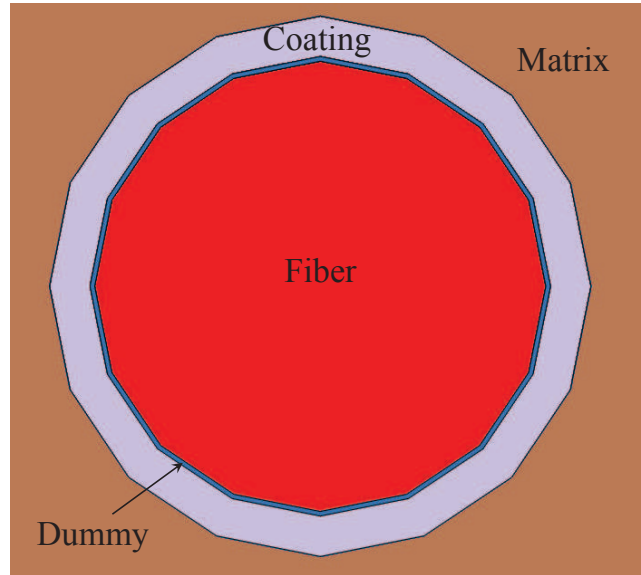


Figure 5.7: Strategy for creating DCZM elements within the 3D-FEM pullout model; Shown is a single fiber with a dummy material between the fiber and coating material

In order to achieve a good representation of the CMC microstructure, multiple fibers with varying length are included in the model based on the experimental findings discussed in chapter 5.2. The fiber lengths are: $L_1 = 40 \mu\text{m}$, $L_2 = 60 \mu\text{m}$, $L_3 = 80 \mu\text{m}$, $L_4 = 100 \mu\text{m}$, $L_5 = 120 \mu\text{m}$, $L_6 = 140 \mu\text{m}$. Variations of the fiber diameters are typical for CMC materials and therefore should be part of the model. In the current work two fiber diameters were chosen: $D_1 = 8 \mu\text{m}$, $D_2 = 10 \mu\text{m}$. The fibers are located randomly within the model. The model consisted of 153789 degrees of freedom. The modeling strategy to capture the non-linearity present during fiber pullout is characterized by three main features:

1. Three dimensional C3D8 elements with linear elastic stress-strain response for the matrix, fiber, and coating

2. One dimensional DCZM elements modeling the cohesive zone between the fiber and coating
3. Abaqus frictional contact surface elements between fiber and coating surfaces

Figure 5.8a depicts the entire model with randomly placed fibers. Two $8\ \mu\text{m}$ diameter fibers and one $10\ \mu\text{m}$ diameter fiber form a small cluster in the vicinity of the left corner. The matrix material has been removed in figure 5.8b to visualize the FEM discretization of the coating material. In figure 5.8c both the matrix and coating material have been removed. The number of nodes on the fiber surfaces matches the number of nodes on the inner coating surfaces. DCZM elements have been inserted here. The nodes on the outer coating surfaces are shared with the matrix material. The bottom of the matrix block was restricted from movement in the fiber direction while the top surface nodes of the fibers subjected to a displacement of $150\ \mu\text{m}$ which ensured a complete pullout of all fibers. A small lateral compressive displacement was applied on the vertical matrix surfaces prior to fiber pullout displacement to establish a normal force between the fiber and coating surface. A normal force is required in the frictional contact formulation utilized in this model.

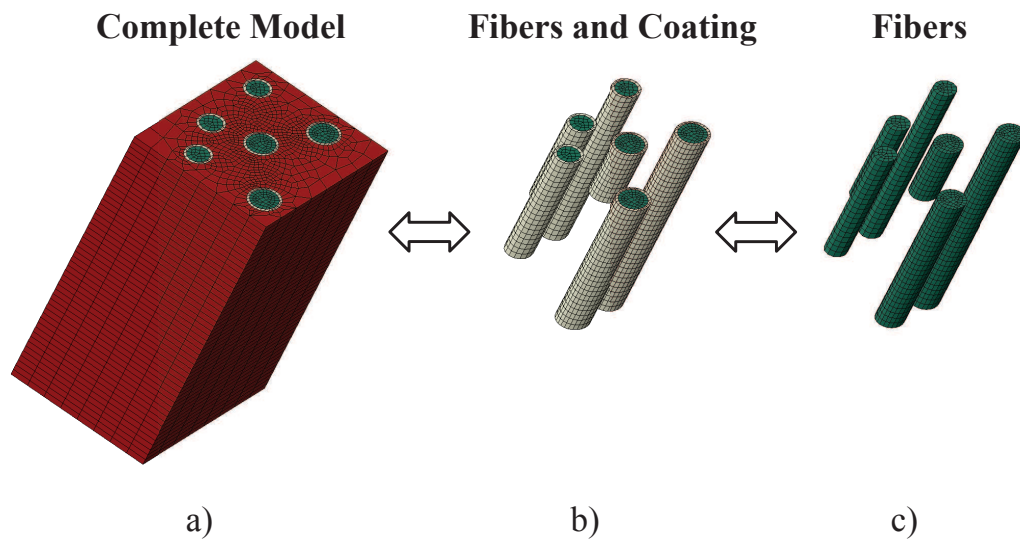


Figure 5.8: Fiber-pullout model, a) whole model b) Fiber with Coating c) Fibers only

5.4 Fiber-Pullout Results and Discussion

Fiber pullout simulations were carried out with Abaqus' implicit solver. Figure 5.9 shows the development of the pullout curve and the corresponding stress state of the fibers and the matrix for one particular case with the following properties: initial stiffness $K = 500000$ N/mm, fracture toughness $G_{IC} = 0.5$ J/m, critical force $F_c = 8e-8$ N, and the friction coefficient $\nu = 0.3$. The peak load is reached when the smallest fiber has completely debonded and only frictional resistance contributes to the energy dissipation for that particular fiber (38 MPa). The stress in that fiber continuously reduces to zero as the material remaining in the matrix block shortens.

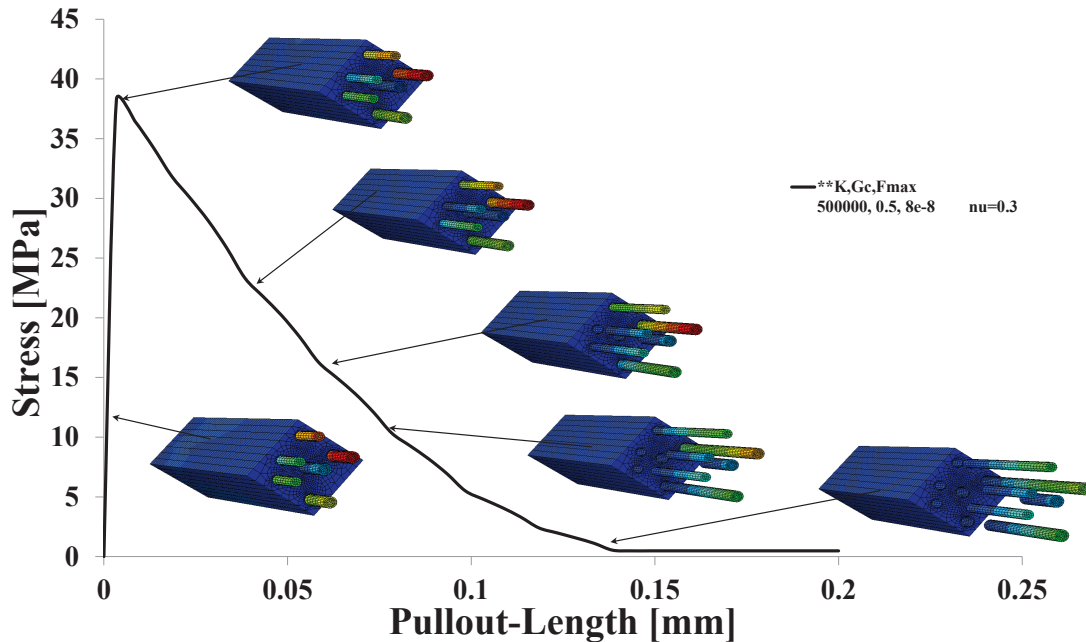


Figure 5.9: Fiber pullout response as predicted by the finite element model

A bump in the stress-displacement response was observed when the disbond length reached the length of the shortest fiber ($40\ \mu\text{m}$). As before the stress in that fiber tends to zero at this point. Multiple further dips can be observed each corresponding to a fiber being pulled out of the matrix block. A parameter study was conducted to investigate the impact of each model input parameter with the exception of the

initial DCZM stiffness. It was chosen to be larger than the highest stiffness of the constituents. Figure 5.10 shows the stress-pullout length response of all models. The first four models show the influence of the critical force F_c . The baseline model was run with $F_c = 4e-8$ N. All subsequent models will be compared to the baseline model. The critical force was doubled in the second model with no noticeable effects on the stress-pullout-length response. Increasing F_c by an order of magnitude to $F_c = 4e-7$ N resulted in a slight increase of the peak stress from 38 MPa to 40.5 MPa. Further increase of the critical load to $F_c = 4e-6$ N resulted in a drastic increase in the peak-stress to 60 MPa.

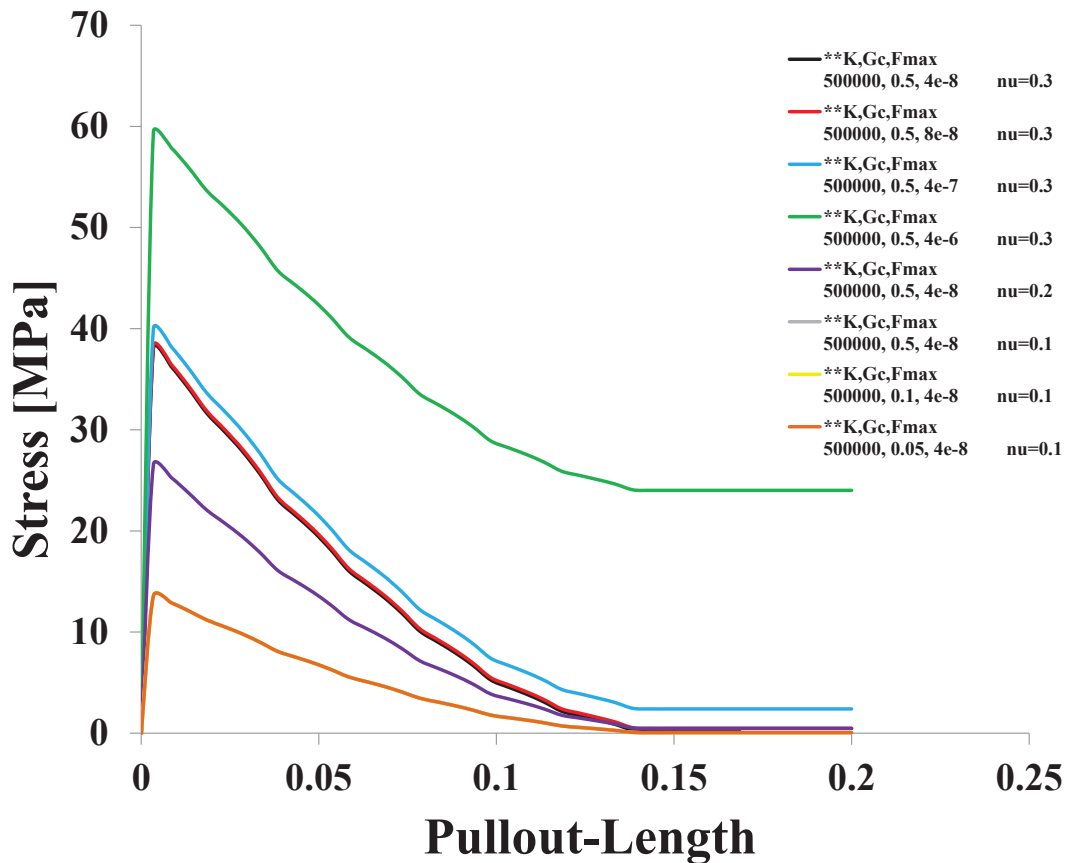


Figure 5.10: Input parameter study of fiber pullout response as predicted by the finite element model

The effect of critical load is therefore non-linear as shown in table 5.1. Next, the influence of the friction coefficient was investigated with constant values for $K =$

Table 5.1: Dependence of the pullout strength on the critical Load F_c

Critical Load F_c	Peak Stress [MPa]
4e-8	38
8e-8	38
4e-7	40.5
4e-6	60

500000 N/mm, $G_{IC} = 0.5$ J/m, and $F_c = 4e-8$ N. The purple stress-pullout length response shows a decrease in peak-load to 37 MPa with $\nu = 0.2$. The peak-load is further reduced to 13 MPa with a smaller friction coefficient of $\nu = 0.1$ represented by the grey stress-pullout length response. Furthermore, the influence of the critical energy release rate G_{IC} was studied. The last two responses shown in yellow and orange, respectively in figure 5.10, represent predictions with $G_{IC} = 0.1$ and $G_{IC} = 0.05$. A change of the critical energy release rate did not have an effect on the stress-pullout length response as the last three responses are coincidental.

5.5 Conclusions

A first step toward understanding the effects of fiber pullout on the mechanical behavior of CMCs was discussed in this chapter. Full three-dimensional finite element model with multiple fibers at various lengths was used to investigate the influence of critical fracture parameters. The fiber diameters and lengths were based on test data. Discrete cohesive zone elements were employed to capture the released energy during fiber-interface debonding. In order to capture the released energy during the pullout process due to friction Abaqus' frictional contact model was used. The two critical parameters were determined through a parameter study. The friction coefficient and the critical load to fracture need to be carefully determined through experimental testing such as fiber-pushout tests. The energy release rate did not effect the stress-pullout length response.

Future work should reflect a statistical variation of the critical load F_c along the

fiber length. This would represent impurities and variations in the bonding quality between the fiber and the coating.

CHAPTER VI

Concluding Remarks

6.1 Conclusions

In this dissertation the response of melt infiltrated SiC/SiC ceramic matrix composites with continuous fibers was studied. A novel experimental setup was developed that utilizes a low power blue light laser for both the illumination of the specimen surfaces and the creation of a suitable speckle pattern for DIC analysis. Multiple lay-ups were investigated and the crack propagation of single edge notch tensile samples was investigated at four different temperatures. It was shown that the high-temperature DIC method can be used to detect crack initiation before a non-linearity in the stress-strain response occurs. This emphasizes the need of optical non-contact measurements to determine the damage state of the material.

The microstructural response and damage behavior was investigated in Chapter III. Small RVE sized models based on micrographs of the CMC material were used to identify geometrical stress risers within the microstructure. A micromechanics model, the energy based crack-band formulation, was used to predict the post-peak response of each constituent. Based on the numerical predictions, fiber clusters with thicker than average fiber coatings have been found to increase the local stress field. Hundreds of fibers were explicitly modeled in large finite element models in order to investigate the crack propagation within the microstructure. The model was large enough to capture

multiple macro-cracks. The FEM predictions revealed that small microcracks initiate throughout the structure and join up on continued loading to form the macroscopic cracks. The model predicted the arrest and deviation of crack tips at fiber interfaces. The response of coupon level notched and un-notched specimens was studied in chapter IV. Two finite element simulations were interlinked to concurrently predict the response of a macroscopic model based on the response of a microstructural RVE. The RVE finite element code was developed in Fortran and entirely integrated in Abaqus' user defined material subroutines. It was shown that a high level of fidelity was achieved with a moderate computational effort. Stress-strain responses as well as details of the crack propagation were captured and compared to experimental results. Mesh objectivity was achieved on the RVE model through the incorporation of a characteristic element length into the fracture mechanics mathematical model. Finite element models without geometrical stress risers, such as smooth bar tensile specimens, require the incorporation of a minimum level of randomness. Two methods were investigated, e.g. geometry and material property based randomization. Geometrical randomization of the microstructure, which is found extensively in low volume fraction composites (e.g. CMC), was simulated through the use of multiple geometrically distinct subcells. Material property based randomization was achieved through the introduction of statistically varying critical stresses. A two parameter Weibull distribution was employed and it was shown that the shape factor n is a non-critical parameter and therefore does not need to be determined experimentally. The onset of non-linearity was predicted accurately. Discrepancies were found for the post-knee behavior.

Fiber-pullout was observed experimentally in $[0/90]_{2S}$ specimens. Fiber pullout is likely to have a major impact on the stress-strain response of the material after crack saturation in the matrix developed. In order to understand the impact of critical parameters associated with fiber-pullout, a finite element model was developed. Dis-

crete cohesive zone elements were used to describe the crack development along the fiber-coating interface. Frictional sliding was utilized to predict the released energy during the pullout process. It was established that the friction coefficient is among the critical parameters. Results and observations can be used in the future to incorporate fiber-pullout in a multi-scale fracture mechanics code.

6.2 Future Work

Experimental testing is essential to determining the post-peak stress-strain response of ceramic matrix composites (CMC). In the previous work single edge notch monotonic tensile tests were conducted on symmetric cross-ply $[0/90]_{2S}$ laminates. One main focus of future work should be the role of damage propagation in the zero layers in a composite after crack saturation in the ninety layers has occurred. The occurrence of crack growth along the interface in longitudinal layers has been proposed. However, experimental verification is needed. Multiple other layups, e.g. $[90/0]_{2S}$, $[+45/-45]_{2S}$, etc., should be investigated in the future to further strengthen the understanding of damage behavior and validate numerical models. Enhanced toughness of CMCs results from the ability of the fibers to bridge matrix cracks traversing the composites before fiber breakage occurs. The extent of fiber debonding and subsequent energy dissipation through frictional sliding determines the toughness enhancement of the composite. But how this toughness increase depends on the constituent parameters such as elastic properties of the matrix, coating, and fiber, coating thickness and fracture toughness, residual stresses due to the manufacturing process, has not yet been established. The existence of residual compressive stresses acting across the fiber interfaces needed for frictional sliding has not been shown experimentally. It is assumed that fiber pull-out occurs in the wake of a matrix crack. Understanding the debonding mechanics of the matrix/coating and coating/fiber interfaces is essential. Fiber-pushout tests could be developed to determine fracture properties

that are needed for analytical or numerical predictions. Unidirectional CMC coupons, subjected to transverse tension, could be used to investigate crack propagation as a validation of the numerical predictions. Digital Image Correlation (DIC) on small fields of view on the order of a few hundred microns could reveal crack paths and crack propagation. Influences of geometrical obstacles, e.g. fiber clusters or residual silicon pockets, could be studied. CMCs have the advantage of small degradation of material properties at elevated temperatures. A DIC system for very high temperatures has been developed in this work. It was shown that it delivers the ability of measuring full-field strain maps at temperatures of 2400 F. Temperature dependent properties can be studied for various composite layups. The systems should be extended for smaller fields of view to observe the influence of temperature on crack initiation and propagation. Other specimen geometries, e.g. c-shaped specimens, should be investigated to further broaden the knowledge of crack development along interfaces. CMCs will eventually be introduced to components that are subject to high cycle fatigue loading. Typically, strain-controlled experiments are conducted to determine S-N curves. Full field strain measurements for these experiments are prone to a number of challenges especially at elevated temperatures. Oxidation might affect the image and speckle quality. Image recording devices, for DIC analysis, must to be coupled with the applied loading and therefore new recording systems need to be developed. Automatic detection of damage initiation and propagation are essential to the practicality of DIC analysis.

Previous studies have focused on three main areas: macroscopic damage evolution, microscopic crack propagation, and fiber debonding. A multi-scale code has been developed and shown to predict realistic results of monotonic tensile coupons with various layups. Single edge notch and smooth bar tensile coupon geometries were studied. Future work should incorporate temperature dependent constituent material models. Incorporation of residual stresses due to crystallization and expansion

during cool down could be included. The macroscopic scale, e.g. component level, in this particular multi-scale methodology is informed by a finite element model that predicts constituent level damage. In general, representative volume elements (RVE) are chosen such that correct damage mechanics are captured. Studies on the influence of the size of the RVEs should be conducted in the future to establish a methodology to quickly determine the required RVE size for a particular macroscopic problem. The current multi-scale code preserves the released energy in post-peak response regardless of the discretization size used for the RVE model. This is achieved by incorporating a characteristic length of every element within the RVE in the post-peak damage formulation (crack-band). This idea needs to be developed further to ensure mesh objectivity is carried up to the macroscopic scale. One proposed method would be to introduce a second characteristic length based on the element size of the macroscopic model. The RVE size could be scaled to that length or the energy release rate of the elements within the RVE could be adjusted accordingly. Typically, multi-scale models increase the accuracy of the material models significantly but increase the required computational cost.

Future research could entail the development of methods that are able to predict the response variables, e.g. stress and stiffness, based on a surrogate model such as the Kriging method. These models can interpolate a limited set of numerical models or experimental data and rapidly predict the response in any other design point. A careful study to determine the required number of training sets should be conducted in order to minimize the error. The micromechanics models developed in the previous studies have predicted crack spacing in transverse plies accurately. However, they lack the ability to capture damage mechanics in the longitudinal plies correctly. Based on the experiments suggested earlier, analytical or numerical models focused on fiber-debonding and fiber/interface frictional sliding during pull-out should be developed and incorporated in the micromechanics models. The question if and how cracks

propagate along fibers has not been resolved. Two dimensional models would serve as a starting point to investigate the transition from mode I dominated matrix cracks to mode II and mixed mode damage along the fiber. Ultimately, three-dimensional models must be developed that include multiple fibers and have the ability to predict the onset of damage in the matrix, further release of energy through fiber/interface debonding (e.g. cohesive elements), predict fiber cracking and finally fiber-pullout mechanics. After establishing the model ability to capture these mechanisms, it should be extended and included in the multi-scale methodology. In order to validate these models, experimental results from fiber-pullout or pushout tests are required. Developing component level models subjected to cyclic thermal and mechanical loading is essential for the design process. High cycle fatigue models should be introduced into the multi-scale and micromechanics methods. Simple material models could be based on the classical S-N curves. More advanced models that can predict crack propagation of pre-existing cracks could be based on cycles of crack-opening (COD) rather than stress cycles. High cycle fatigue formulation could be implemented in the crack-band method. Further research could entail the influence of oxidation on the crack development. All numerical models should encompass a study of the influence of material impurities in the composite. Residual carbon or silicon in the matrix, variations in the fiber diameter or variations in the coating thickness might induce weak material points prone to early initiation of damage.

APPENDICES

APPENDIX A

Determination of Randomness Parameters

A.1 Probability Density Function

In multi-scale or micromechanics finite element models it would be helpful to quickly probe randomly generated subcells in order to establish if realistic damage behavior can be expected. Two different methods will be discussed here which need to be tested and verified in future research. One possible measure of randomness could be the probability of fiber to fiber distances within a subcell model. Figure A.1a shows a baseline subcell which is based on a micrograph of a CMC microstructure. A randomly generated model is shown in figure A.1a. Although both appear to be similar each subcell will exhibit different damage evolution when subjected to a e.g. transverse load. Subcells with random fiber locations could potentially show non-physical behavior due to various reasons. Damage models, especially at low volume fractions, are sensitive to the location of the constituents as discussed in chapter 3.6.

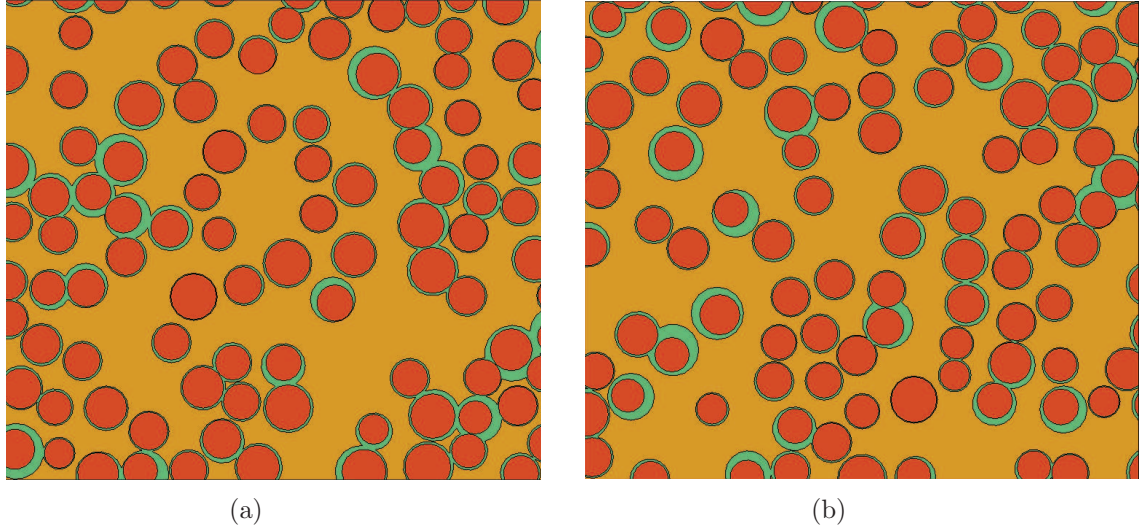


Figure A.1: *a*) Baseline RVE *b*) randomly generated RVE

A Matlab script has been developed to automatically determine the distances between fibers. Every distance is only considered once as shown in Figure A.2. The fiber distances are then binned and plotted as a probability density function (PDF). Calculation of the mean square error between two PDFs could then be used to establish an error measure as shown in figure A.3.

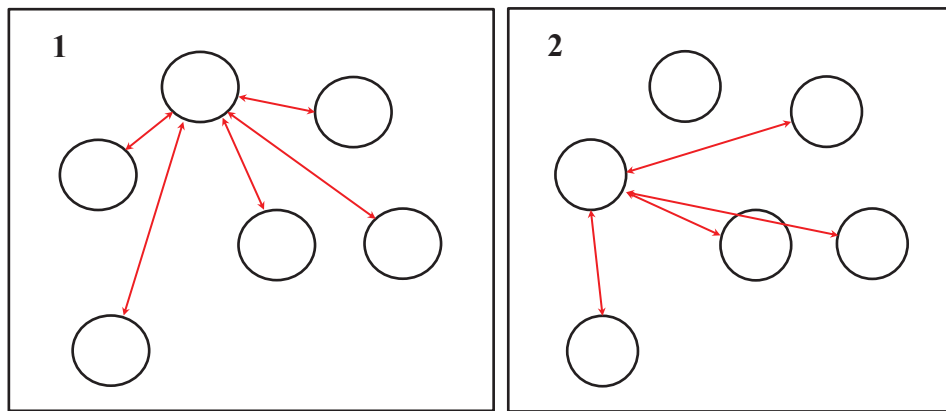


Figure A.2: Fiber distance calculation for probability density function

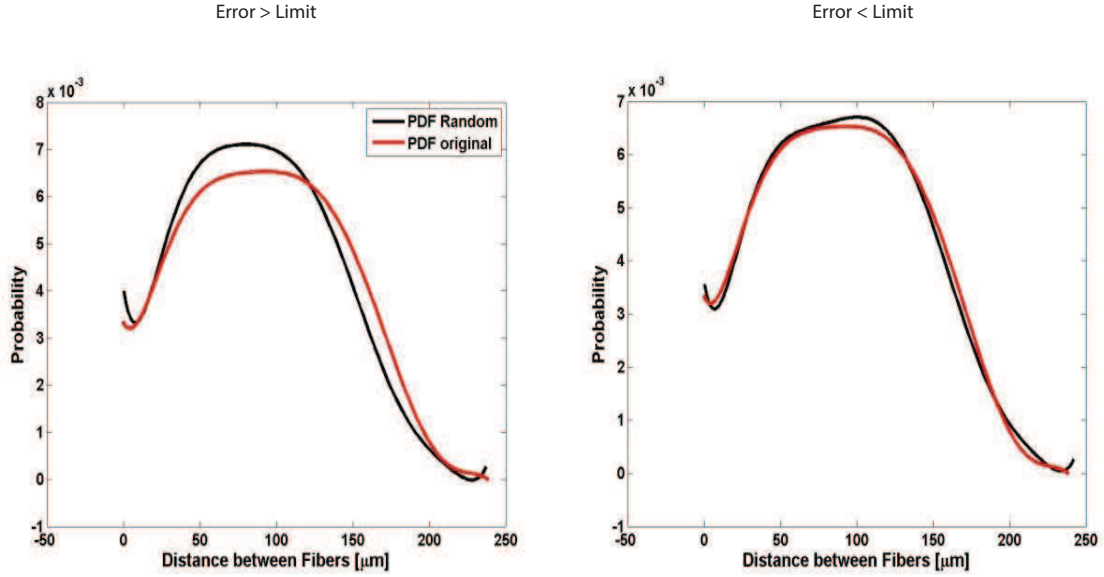


Figure A.3: Probability density functions of a baseline RVE and a randomly generated RVE

A.2 Mean Intercept Length Tensor

Another approach to measure the properties of a subcell with random fiber locations is the mean intercept length tensor. The intercept length between fibers and radial lines emanating from the center outward is normalized by the total length of the radial line. This concept is schematically shown in figure A.4. The data is then plotted in polar coordinates. For a perfect geometrically isotropic subcell the resulting shape will be circular. Any non-circularity indicates a bias in one or more directions.

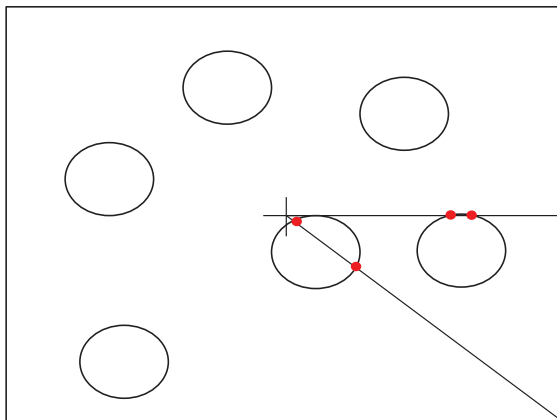


Figure A.4: Schematic Drawing of the Mean Intercept Length

Conic sections can then be fitted to the data with a least square fit. Equations A.1 represent a conic section in Cartesian coordinates.

$$Ax^2 + Bxy + Cy^2 + Dx + Ey + F = 0 \quad (\text{A.1})$$

Equation A.1 can be solved for the coordinate y,

$$y_{1,2} = -\frac{(Bx + E)}{2C} \pm \sqrt{\frac{(Bx + E)^2}{4C^2} - \frac{Ax^2 + Dx + F}{C}} \quad (\text{A.2})$$

All solutions to equation A.2 need to be real which poses a restriction on the variable x,

$$x_{1,2} = -\frac{(BE + -4DC)}{2(B^2 - 4CA)} \pm \sqrt{\left(\frac{(BE - 4CD)}{2(B^2 - 4AC)}\right)^2 - \frac{E^2 - 4CF}{B^2 - 4AC}} \quad (\text{A.3})$$

The coefficients A, B, C, D, E, and F can be determined from the least squares fit of the measured mean intercept lengths. Figure fig:SchematicMeanInterceptExample shows the raw data of a base subcell (thin black line) and a randomly generated subcell (thin red line) which are displayed in figure A.1. In addition, the Conic Sections of both subcells are plotted (bold black and red lines). A possible error measure could be the mean square error between the conic sections. This method could possibly be used to compare the geometry of subcells and confirm that a randomly generated

subcell will exhibit comparable damage characteristics. Further work has to be done to establish the maximum error.

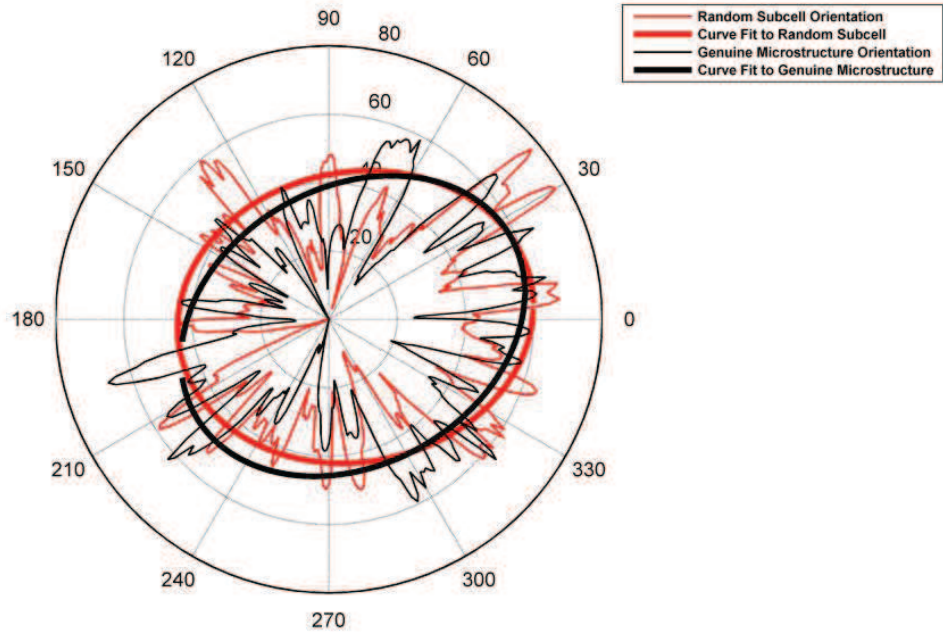


Figure A.5: Example of mean intercept length of a base RVE and a random subcell

BIBLIOGRAPHY

BIBLIOGRAPHY

- Abaqus (2008), *Abaqus User's Manual*, vol. 1-3, Dassault Systemes Simulia Corp.
- Aboudi, J., M.-J. Pindera, and S. Arnold (2001), Linear thermoelastic higher-order theory for periodic multiphase materials, *J. Appl. Mech.*, *68*, 697–707.
- Aveston, J., and A. Kelly (1973), Theory of multiple fracture of fibrous composites, *Journal of Materials Science*, *8*, 352–362.
- Awander, M., B. Weiss, and H. Weiss (2000), Noncontacting Strain Measurements at High Temperatures by the Digital Laser Speckle Technique, *Experimental Mechanics*, *40*, 98–105.
- Bacarreza, O., M. Aliabadi, and A. Apicella ((2012)), Multi-scale failure analysis of plain-woven composites, *J. Strain Analysis*, *47*, 379–388.
- Bažant, Z. (1983), Crack band theory for fracture of concrete., *Materials and Structures*, *16*, 155–177.
- Bažant, Z., and L. Cedolin (1991), *Stability of Structures: Elastic Inelastic, Fracture and Damage Theories*, Oxford University Press.
- Berger, H., S. Kari, U. Gabbert, R. Rodriguez-Ramos, J. Bravo-Castillero, and R. Guiovert-Diaz (2005), A comprehensive numerical homogenization technique for calculating effective coefficients of uniaxial piezoelectric fibre composites, *Mater. Sci. Eng. A*, *412*, 53–60.
- Beyerle, D., S. Spearing, F. Zok, and A. Evans (1992), Damage and Failure in Unidirectional Ceramic-Matrix Composites, *J. Am. Ceram. Soc.*, *75*.
- Bornert, M., et al. (2008), Assesment of Digital Image Correlation Measurement Errors: Methodology and Results, *Experimental Mechanics*, *49*, 353–370.
- Boyer, H. (2002), *Atlas of Stress-Strain Curves*, ASM International.
- Bruck, H., S. McNeill, M. Sutton, and W. Peters (1989), Digital image correlation using Newton-Raphson method of partial differential correction, *Experimental Mechanics*, *29*, 261–267.
- Budiansky, B., J. Hutchinson, and A. Evans (1986), Matrix Fracture in Fiber-Reinforced Ceramics, *J. Mech. Phys. Solids*, *34*, 164–189.

- Chandrupatla, T., and A. Belegundu (2002), *Introduction to Finite Elements in Engineering*, Pearson Education Inc.
- Charalambides, P., and A. Evans (1989), Debonding Properties of Residually Stressed Brittle-Matrix Composites, *J. Am. Ceram. Soc.*, *72*, 746–753.
- Chen, X., L. Yang, and D. Xiang (2012), High temperature displacement and strain measurement using monochromatic light illuminated stereo digital image correlation system, *Meas. Sci. Technol.*, *23*, doi:10.1088/0957-0233/23/12/125603.
- Corman, G., and K. Luthra (2005), Silicon Melt Infiltrated Ceramic Composites (HiPerComp), *In handbook of ceramic composites*, pp. 99–115.
- Corman, G., K. Luthra, and M. Brun (2003), Silicon melt infiltrated ceramic composites - processes and properties, in *Progress In Ceramic Gas Turbine Development, Vol. II, Ceramic Gas Turbine Component Development and Evolution, Fabrication, NDE, Testing and Life Prediction*, vol. 2, edited by M. van Roode, M. Ferber, and D. Richardson, chap. 16, ASME Press, New York.
- Dal Corso, F., and L. Deseri (2013), Residual stresses in random elastic composites: nonlocal micromechanics-based models and first estimates of the representative volume element size, *MECCANICA*, *48*, 1901–1923.
- Drugan, W., and J. Willis (1996), A micromechanics-based nonlocal constitutive equation and estimates of representative volume element size for elastic composites, *J. Mech. Phys. Solids*, *44*, 497–524.
- Dunn, D. G. (2010), The effect of fiber volume fraction in hipercomp sic-sic composites, Ph.D. thesis, Alfred University.
- Efendiev, Y., and T. Hou (2009), *Multiscale Finite Element Methods*, vol. 4, Springer.
- Evans, A. (1988), The Mechanical Performance of Fiber-reinforced Ceramic Matrix Composites, *Materials Science and Engineering*, *107*, 227–239.
- Evans, A., and F. Zok (1994), The physics and mechanics of fiber-reinforced brittle-matrix composites, *J. Mater. Sci.*, *29*, 3857–3896.
- Fago, M., and A. Waas (1998), Experimental Investigation of the Behavior of Edge Delaminations Using Holographic Interferometry, *Opt. Eng.*, *37*, 1420–1428.
- Feyel, F., and J. Chaboche (2000), Fe2 multiscale approach for modeling the elastoviscoplastic behavior of long fiber sic / ti composite materials, *Computer Methods in Applied Mechanics and Engineering*, *183*, 309330.
- Fish, J., and Q. Yu (2002), Computational mechanics of fatigue and life predictions for composite materials and structures, *Computer Methods in Applied Mechanics and Engineering*, *43*, 4827–4849.

- Fish, J., Q. Yu, and K. Shek (1999), Computational damage mechanics for composite materials based on mathematical homogenization, *Int. J. Numer. Methods Engrg.*, *45*, 1657–1679.
- Forrest, C., P. Kennedy, and J. Shennan (1972), The Fabrication and Properties of Self-Bonded Silicon Carbide Bodies, *Special Ceramics*, *5*.
- Garret, K., and J. Bailey (1977), Multiple transverse fracture in 90° cross-ply laminates of a glass fibre reinforced polyester, *J. Mater. Sci.*, *12*, 157–168.
- Ghosh, S., and Y. Liu (1995), Voronoi cell finite element model based on micropolar theory of thermoelasticity for heterogeneous materials, *International Journal for Numerical Methods in Engineering*, *38*, 1361–1398.
- Ghosh, S., and S. Mukhopadhyay (1993), A material based finite element analysis of heterogeneous media involving dirichlet tessellations, *Comp. Meth. Appl. Mech. Engrg*, *104*, 211–247.
- Ghosh, S., L. Kyunghoon, and S. Moorthy (1995), Multiple scale analysis of heterogeneous elastic structures using homogenization theory and voroni cell finite element method, *Int. J. Solids and Struct.*, *32*, 27–62.
- Gowayed, Y., J. Ojardi, R. Morscher, G. and Miller, U. Santhosh, J. Ahmad, and R. John (2011), Accumulation of time-dependent strain during dwell-fatigue experiments of iBN-Sylramic melt infiltrated SiC/SiC composites with and without holes, *Composites Part A: Applied Science and Manufacturing*, *42*, 2020–2027.
- Grant, B., P. Wihters, and M. Preuss (2009), High-Temperature strain field measurement using digital image correlation, *The Journal of Strain Analysis for Engineering Design*, *44*, 263–271.
- Gusev, A. (1997), Representative volume element size for elastic composites: a numerical study, *J. Mech. Phys. Solids.*, *45*, 1449–1459.
- Hashin, Z., and B. Rosen (1964), The Elastic Moduli of Fiber-Reinforced Materials, *J. Appl. Mechanics*, *31*, 223–232.
- Heinrich, C., and A. Waas (2013), Investigation of Progressive Damage and Fracture in Laminated Composites using the Smearred Crack Approach, *CMC-Computers Materials & Continua*, *35*, 155–181.
- Heinrich, C., M. Aldridge, J. Kieffer, A. Waas, and K. Shahwan (2012), The influence of the representative volume element (RVE) size on the homogenized response of cured fiber composites, *Modelling Simul. Mater. Sci. Eng.*, *20*, doi:10.1088/0965-0393/20/7/075007.
- Hill, R. (1964), Theory of Mechanical Properties of Fiber-Strengthened Materials: I. Elastic Behavior, *J. Mech. Phys. Solids*, *12*, 199–212.

- Hutchinson, J., and H. Jensen (1990), Models of fiber debonding and pullout in brittle composites with friction, *Mech. Mater.*, *9*, 139–163.
- Johnson, S., and P. Mangalgiri (1985), Influence of the resin on interlaminar mixed-mode fracture, *NASA/TM*, *87571*.
- Kanit, T., S. Forest, I. Galliet, V. Mounoury, and D. Jeulin (2003), Determination of the size of the representative volume element for random composites: statistical and numerical approach, *International Journal of Solids and Structures*, *40*, 36473679.
- Kanoute, P., D. Boso, J. Chaboche, and B. Schrefler (2009), Multiscale methods for composites: A review, *Arch. Comput. Methods Eng.*, *16*, 31–75.
- Key, C., M. Garnich, and A. Hansen (2004), Progressive failure predictions for rib-stiffened panels based on multicontinuum technology, *Composite Structures*, *65*, 357–366.
- Kwon, Y., D. Allen, and R. Talreja (2008), *Multiscale Modeling and Simulation of Composite Materials and Structures*, Springer.
- Ladeveze, P., and A. Nouy (2003), On a multiscale computational strategy with time and space homogenization for structural mechanics, *Computer Methods in Applied Mechanics and Engineering*, *192*, 30613087.
- Laws, N., and G. Dvorak (1988), Progressive Transverse Cracking in Composite Laminates, *Journal of Composite Materials*, *22*, 900–916.
- Li, L., Y. Song, and Y. Sun (2014), Modeling the Tensile Behavior of Unidirectional C/Sic Ceramic Matrix Composites, *Mechanics of Composite Materials*, *49*.
- Lissart, N., and J. Lamon (1997), Damage and failure in ceramic matrix minicomposites: Experimental study and model, *Acta Materialia*, *45*, 1025–1044.
- Liu, J., J. Lyons, M. Sutton, and A. Raynolds (1998), Experimental Characterization of Crack Tip Deformation Fields in Alloy 718 at High Temperatures, *J. Eng. Mater. Technol.*, *120*.
- Lyons, J., J. Liu, and M. Sutton (1996), High-temperature deformation measurements using digital-image Correlation, *Exp. Mechanics*, *36*.
- Mahmoodia, M., and M. Aghdamb (2011), Damage analysis of fiber reinforced Ti-alloy subjected to multi-axial loading a micromechanical approach, *Mater. Sci. Eng. A*, pp. 7983–7990.
- Marshall, D., and W. Oliver (1987), Measurement of Interfacial Mechanical Properties in Fiber-Reinforced Ceramic Composites, *J. Am. Ceram. Soc.*, *70*, 542–548.
- Marshall, D., B. Cox, and A. Evans (1985), The Mechanics of Matrix Cracking in Brittle Matrix Fiber Composites, *Acta Metall.*, *33*, 2013–2021.

- McCartney, L. (1987), Mechanics of Matrix Cracking in Brittle Matrix Fiber-Reinforced Composites, *Proc. R. Soc. London, Ser. A*, 409.
- Mehan, R. (1978), Anisotropic Behavior of Si/SiC Ceramic Composites, *Am. Ceram. Soc. Bull.*, 57.
- Meyer, P., and A. Waas (2015), Measurement of In Situ-Full-Field Strain Maps on Ceramic Matrix Composites at Elevated Temperature Using Digital Image Correlation, *Experimental Mechanics*, doi:10.1007/s11340-014-9979-7.
- Michel, J., H. Moulinec, and P. Suquet (1999), Effective properties of composite materials with periodic microstructure: a computational approach, *Computer Methods in Applied Mechanics and Engineering*, 172, 109143.
- Moorthy, S., S. Ghosh, and Y. Liu (1994), Voronoi cell finite element model for thermo-elastoplastic deformation in random heterogeneous media, *Appl. Mech. Rev.*, 47, 207–220.
- Nairn, J. (1989), The strain-energy release rate of composite microcracking - a variational approach, *J. Comp. Mater.*, 23, 1106–1129.
- Novac, M., and F. Zok (2011), High-Temperature Materials Testing with Full-field Strain Measurement: Experimental Design and Practice, *Rev. Sci. Instrum.*, 82.
- Pan, B., D. Wu, Z. Wang, and Y. Xia (2011), High-Temperature digital image correlation method for full-field deformation measurement at 1200°C, *Meas. Sci. Technol.*, 22, doi:10.1088/0957-0233/22/1/015701.
- Pankow, M., B. Justusson, and A. Waas (2010), Three-dimensional digital image correlation technique using single high-speed camera for measuring large out-of-plane displacements at high framing rates, *Applied Optics*, 49, 3418–27.
- Pineda, E., B. Bednarczyk, A. Waas, and S. Arnold (2013), Progressive failure of a unidirectional fiber-reinforced composite using the method of cells: Discretization objective computational results, *IJSS*, 50, 1203–1216.
- Popper, P. (1960), The Preparation of Dense Self-Bonded Silicon Carbide, *Heywood and Company*.
- Rajan, V., M. Rossol, and F. Zok (2012), Optimization of digital image correlation for high-resolution strain mapping of ceramic composites, *Experimental Mechanics*, 52, 1407–1421.
- Sauder, C., A. Brusson, and J. Lamon (2010), Influence of Interface Characteristics on the Mechanical Properties of Hi-Nicalon type-S or Tyranno-SA3 Fiber-Reinforced SiC/SiC Minicomposites, *Applied Ceramic Technology*, 7, 291–303.
- Settles, G. (2001), *Schlieren and Shadowgraph Techniques*, Springer-Verlag.

- Shoukry, S., R. Prucz, R. Eluripati, P. Shankaranarayana, and G. William (2007), Multi-fiber unit cell for prediction of residual stresses in continuous fiber composites, *Mech. Adv. Mater. Struct.*, *14*, 531–540.
- Sigl, L., and A. Evans (1989), Effects of residual stress and frictional sliding on cracking and pull-out in brittle matrix composites, *Mechanics of Materials*, *8*, 1–12.
- Smit, R., W. Brekelmans, and J. Meijer (1998), Prediction of the mechanical behavior of nonlinear heterogeneous systems by multi-level finite element modeling, *Computer Methods in Applied Mechanics and Engineering*, *155*, 181–192.
- Song, S., and A. Waas (1993), A Nonlinear Elastic-foundation Model for Interlaminar Fracture of Laminated Composites, *Composites Engineering*, *3*, 945–959.
- Soni, G., R. Singh, M. Mitra, and B. Falzon (2014), Modelling matrix damage and fibre-matrix interfacial decohesion in composite laminates via a multi-fibre multi-layer representative volume element, *International Journal of Solids and Structures*, *51*, 449–461.
- Stein, E., and G. Sagar (2008), Convergence behavior of 3d finite elements for neo-hookean material, *International Journal for Computer-Aided Engineering and Software*, *25*, 220–232.
- Sutton, M., W. Wolters, W. Peters, W. Ranson, and S. McNeill (1983), Determination of displacements using an improved digital correlation method, *Experimental Mechanics*, *1*, 133–139.
- Sutton, M., J. Orteu, and H. Schreier (2009), *Image Correlation for Shape, Motion and Deformation Measurements*, Springer.
- Talreja, R., and C. Singh (2012), *Damage and Failure of Composite Materials*, Cambridge University Press.
- Thouless, M., and A. Evans (1988), Effects of pull-out on the mechanical properties of ceramic matrix composites, *MActa Meallurgica*, *36*, 517–522.
- Totry, E., C. Gonzalez, and J. LLorca (2008), Prediction of the failure locus of C/PEEK composites under transverse compression and longitudinal shear through computational micromechanics, *Composites Science and Technology*, *68*, 3128–3136.
- Tracy, J. (2014), Multi-scale investigation of damage mechanisms in sic/sic ceramic matrix composites, Ph.D. thesis, Univerity of Michigan.
- Vendroux, G., and W. Knauss (1998), Submicron deformation field measurments: Part2. Improved gigital image correlation, *Experimental Mechanics*, *38*, 86–92.
- Vest, C. (1979), *Holographic Interferometry*, John Wiley and Sons, Inc.

- Vest, C., H. Stone, P. Withers, and M. Preuss (2009), High-temperature strain field measurement using digital image correlation, *The Journal of Strain Analysis for Engineering Design*, 44.
- Xia, Z., Y. Zhang, and F. Ellyin (2003), A unified periodical boundary conditions for representative volume elements of composites and applications, *International Journal of Solids and Structures*, 40, 1907–1921.
- Xie, D., and A. Waas (2006), Discrete cohesive zone model for mixed-mode fracture using finite element analysis, *Engineering Fracture Mechanics*, 73, 1783–1796.
- Xie, D., A. Salvi, C. Sun, A. Waas, and A. Caliskan (2006), Discrete cohesive zone model to simulate static fracture in 2d triaxially braided carbon fiber composites, *Journal of Composite Materials*, 40, 2025–2046.
- Yuan, Z., and J. Fish (2008), Towards realization of computational homogenization in practice, *IJNME*, 73, 361–380.
- Zhang, D., D. Patel, and A. Waas (2015), A novel two-scale progressive failure analysis method for laminated fiber-reinforced composites, *AIAA SciTech, 56th AIAA/ASCE/AHS/ASC Structures, Structural Dynamics, and Materials Conference, Kissimmee, Florida, Jan 5-9, AIAA, 0969*.
- Zok, F., and S. Spearing (1992), Matrix Crack Spacing in Brittle Matrix Composites, *Acta metall. mater.*, 40, 2033–2043.